[redacted]

116p

*X64 80647a

Code 5

[redacted]

Space Programs Summary No. 6

for the period 15 September 1959 to 15 November 1959

[redacted]

CLASSIFICATION CHANGE

TO - UNCLASSIFIED

[redacted]

By authority of [redacted] No. E.O. 11652

Changed by O. L. Dewitt Date 2/1/72

[redacted]

jpl

JET PROPULSION LABORATORY

4800 OAK GROVE DRIVE, PASADENA, CALIFORNIA

CALIFORNIA INSTITUTE OF TECHNOLOGY

RECEIVED NASA STI FAC. MAR 1975

1 December 1959

"Available to U.S. Government Agencies and U. S. Government Contractors Only."

[redacted]

(NASA-CR-143318) SPACE PROGRAMS SUMMARY NO. 6, 15 SEPTEMBER - 15 NOVEMBER 1969 (Jet Propulsion Lab.) 123 p

N75-75603

Unclas

00/98 11193

D. D. Wyatt

NATIONAL AERONAUTICS AND SPACE ADMINISTRATION
(NASA CONTRACT NO. NASw-6)

Space Programs Summary No. 6

for the period 15 September 1959 to 15 November 1959

(NASA CR --- ; JPL-SPS-6)

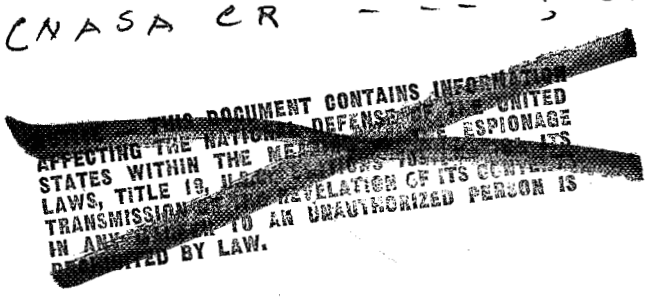
AFFECTING THE NATIONAL DEFENSE OF THE UNITED
STATES WITHIN THE MEANING OF THE ESPIONAGE
LAWS, TITLE 18, U.S.C., SECTIONS 793 AND 794, ITS
TRANSMISSION OR THE REVELATION OF ITS CONTENTS
IN ANY MANNER TO AN UNAUTHORIZED PERSON IS
PROHIBITED BY LAW.

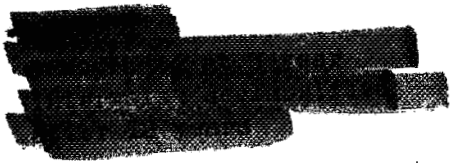

1304823

jpl
JET PROPULSION LABORATORY
CALIFORNIA INSTITUTE OF TECHNOLOGY
4800 OAK GROVE DRIVE, PASADENA, CALIFORNIA

1 December 1959

Copy No. JA 3

"Available to U.S. Government Agencies and U. S. Government Contractors Only."

Preface

The *Space Programs Summary* is a bimonthly publication of the Jet Propulsion Laboratory. Research and development activities conducted by JPL, having specific application to space programs under the sponsorship of the National Aeronautics and Space Administration, are reported in this publication.

The projects reported herein were undertaken in partial fulfillment of National Aeronautics and Space Administration Contract No. NASw-6.

W. H. Pickering, *Director*
Jet Propulsion Laboratory

This document contains information affecting the national defense of the United States within the meaning of the Espionage Laws, Title 18, U.S.C., Sections 793 and 794, the transmission or revelation of which in any manner to an unauthorized person is prohibited by law.

Copyright © 1959
Jet Propulsion Laboratory
California Institute of Technology

[redacted]

Contents

Page

I. Introduction 1

II. Spacecraft 2

A. Data Encoding 2
B. Communications 5
C. Electrical Power 6
D. Guidance 8
E. Controller 9
F. Assembly and Test 9

III. Tracking and Communications 13

A. Project Echo Communications 13
B. Goldstone Tracking and Communications 16

IV. Guidance and Control 34

A. Injection Guidance Analysis 34
B. Injection Guidance Mechanization 37
C. Attitude Control Analysis 57
D. Attitude Control Mechanization 58
E. Space Navigation and Terminal Guidance 66
F. Trajectory Studies 68
G. Trajectory Programs 73
H. Flight Evaluation 77

V. Vehicle 78

A. Structure 78
B. *Vega* Third-Stage Propulsion System 82
C. Instrumentation 94
D. Electrical Power 97

VI. Field Operations 100

A. *Juno II*, Round AM-19A 100
B. *Juno II*, Round AM-19B 103

VII. Associated Studies 107

A. Communication Techniques 107
B. Space Guidance 114
C. Photographic Experiment 116
D. Lunar Magnetic Field 118

References 120

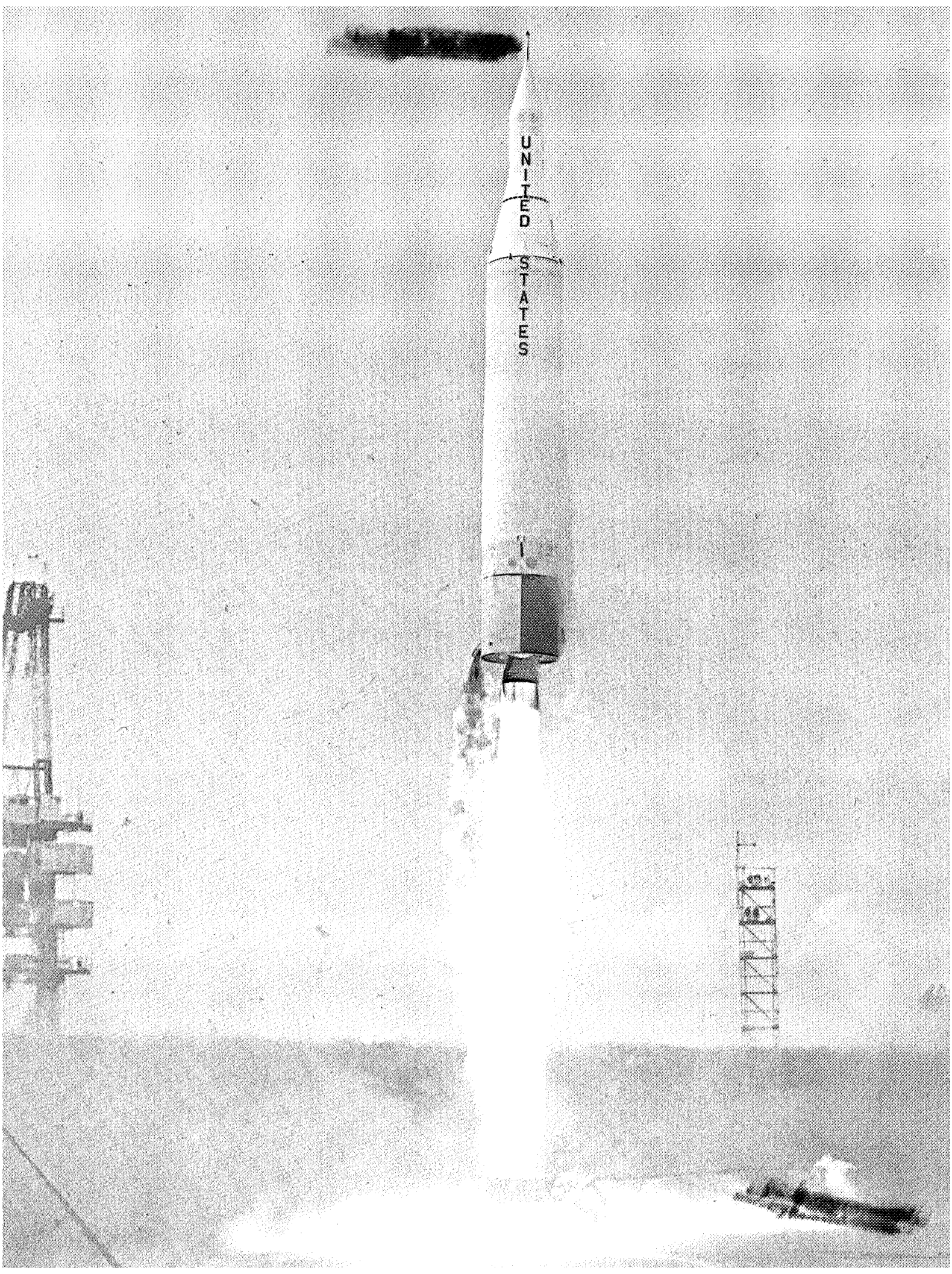
UNITED STATES

I. INTRODUCTION

Aside from some early studies on satellite trajectories carried out for the Navy in 1945 and 1946, the first direct participation of the Jet Propulsion Laboratory in space-flight activities occurred in the *Project Orbiter* studies of 1954 and 1955. The first application of these studies resulted in the development of a high-performance re-entry test vehicle for the *Jupiter* IRBM program. The first flight was made in September 1956 and the project was successfully completed on 8 August 1957, with the recovery at sea of a nose cone which had satisfactorily executed the IRBM trajectory.

In November 1957, after the second successful Russian satellite launching, the Army was instructed to prepare some of the remaining *Jupiter-C* vehicles, which had not been required for the re-entry test program, and to make two satellite launching attempts. The work was undertaken as a joint ABMA-JPL effort. The first launching attempt on 31 January 1958 was successful and *Explorer I* was placed in orbit. The second attempt on 5 March 1958 was unsuccessful; however, a spare vehicle was available and was used to launch *Explorer III* into orbit on 26 March 1958.

On 1 April 1958 the newly formed Advanced Research Projects Agency (ARPA) took over the responsibility within the Department of Defense for all space-flight activities. ARPA approved a program for utilizing the three remaining *Jupiter-C* vehicles for satellite launchings. This program was called the *Juno I* program and its status is presented in *Space Research Summaries 1* through 3.

With the unsuccessful firing of *Explorer VI* (officially designated *Beacon*) on 22 October 1958, the *Juno I* program was brought to completion. Of the six satellite firings attempted, three resulted in placing payloads into satisfactory orbits.

The next phase of the JPL space effort was the *Juno II* program. The *Juno II* vehicle consists of a *Jupiter* booster and a modified JPL high-speed assembly. Use of this new configuration substantially increased the capabilities of *Juno II*.

On 1 October 1958, the *Juno II* program and all other nonmilitary space programs were transferred by ARPA to the National Aeronautics and Space Administration (NASA).

The first *Juno II* launching on 6 December 1958 was a lunar probe, designated *Pioneer III*, which did not succeed in achieving escape velocity. However, it reached an altitude of 63,500 miles from earth and obtained valuable radiation data.

Pioneer IV, the second experiment in the *Juno II* series, was successfully injected into a trajectory (3 March 1959) which carried it past the moon and into a heliocentric orbit. *Space Programs Summaries 1* and *2* contain details of *Pioneer III* and *IV*, respectively.

The *Vega* program, under the supervision of JPL, has as its mission the development of a vehicle capable of placing a several-hundred-pound payload into the vicinity of the moon, Mars, or Venus.

JPL will operate its Goldstone facilities as an official part of Project Echo. This project has as its principal objective the determination of the feasibility of using passive reflective satellites (100-foot-diameter balloon) for global communications.

Documentation of this Laboratory's participation in the NASA *Vega* program, Project Echo, and their associated studies is presented in this summary.

II. SPACECRAFT

The acquisition of new knowledge in space technology and space science is the design objective of the *Vega* program. Although the first several *Vega* vehicles will have as their primary objective the testing of the vehicle itself, a considerable variety of scientific experiments will be carried in the spacecraft.

A. Data Encoding

Telemetry data to be transmitted from the spacecraft falls into two general categories. One of these is engineering data, which covers spacecraft structural, guidance, and propulsion systems data for use in the logical development of spacecraft technology and components. The second type of data is that taken primarily for scientific reasons; that is, to study the nature of space and its components.

On early flights emphasis will be given to obtaining engineering data where there is a question of available bandwidth, weight, or time.

The encoded telemetry signals will modulate the spacecraft-to-earth transmission of the spacecraft transponder system. The spacecraft data quantity and encoding mechanization is dictated by the communication bandwidth. First estimates of the moon-distance information channel bandwidth is less than 2 cps for a 0.25-watt omnidirectional transmitter. This narrow bandwidth makes it undesirable to frequency multiplex many parallel channels together, as the information rate per channel would be prohibitively low for practical purposes. Instead, a time sequence sampling plan (commutation) must be used which will accommodate frequency requirements of the various data in an optimum manner.

Mechanization. Figure 1 is a block diagram of a typical proposed mechanization for data encoding the engineering telemetry signals for the *Vega-I* spacecraft. This mechanization will change for different spacecraft objectives but the basic philosophy presented is flexible and typical. Three modes of encoding and data routing are employed: (1) powered flight, (2) attitude acquisition, and (3) free or coasting flight. These modes are employed to meet the varying data requirements and system bandwidth capabilities.

Basically, the commutation of the engineering measurements is a process of selecting and transmitting successively one of several high-rate information channels, and mixing in at longer intervals, samples of other slow-rate data channels. This method of time sharing enables a large number of low-data rate channels to be accommodated.

The mechanization of this switching logic may be accomplished in many ways. Since it is almost always desirable to perform all switching functions on low-level signals before amplification (to eliminate the need for a separate amplifier for each channel), low contact potential switches must be used. Semiconductor switches are not at this time well suited for low-level switching, so relays or motor-driven contacts seem the most probable answer.

The problem of limited power makes undesirable the use of relay motors (coils) which must be continuously energized. Polarized magnetic latching relays answer this problem, but weight becomes large because a relay is necessary for every signal switched.

Probably the most expedient and immediately reliable answer is a type of contacting mechanical counter which is available from several companies. The devices consist of up to five-digit wheels each with ten contacts brushed by a rotating brush to indicate the wheel position.

In the mechanization shown (Fig 1), the election has been taken to pin the first three wheels together. The switching assignments shown are those which seem desirable under the following requirements: (1) Attitude control equipment data is most important; (2) transponder equipment data is next; (3) the primary communication system is probably the more reliable of the two; and (4) scientific experiments are not to preclude the return of engineering data. The use of other refinements may well be in order, and will change the switching priority in future vehicles.

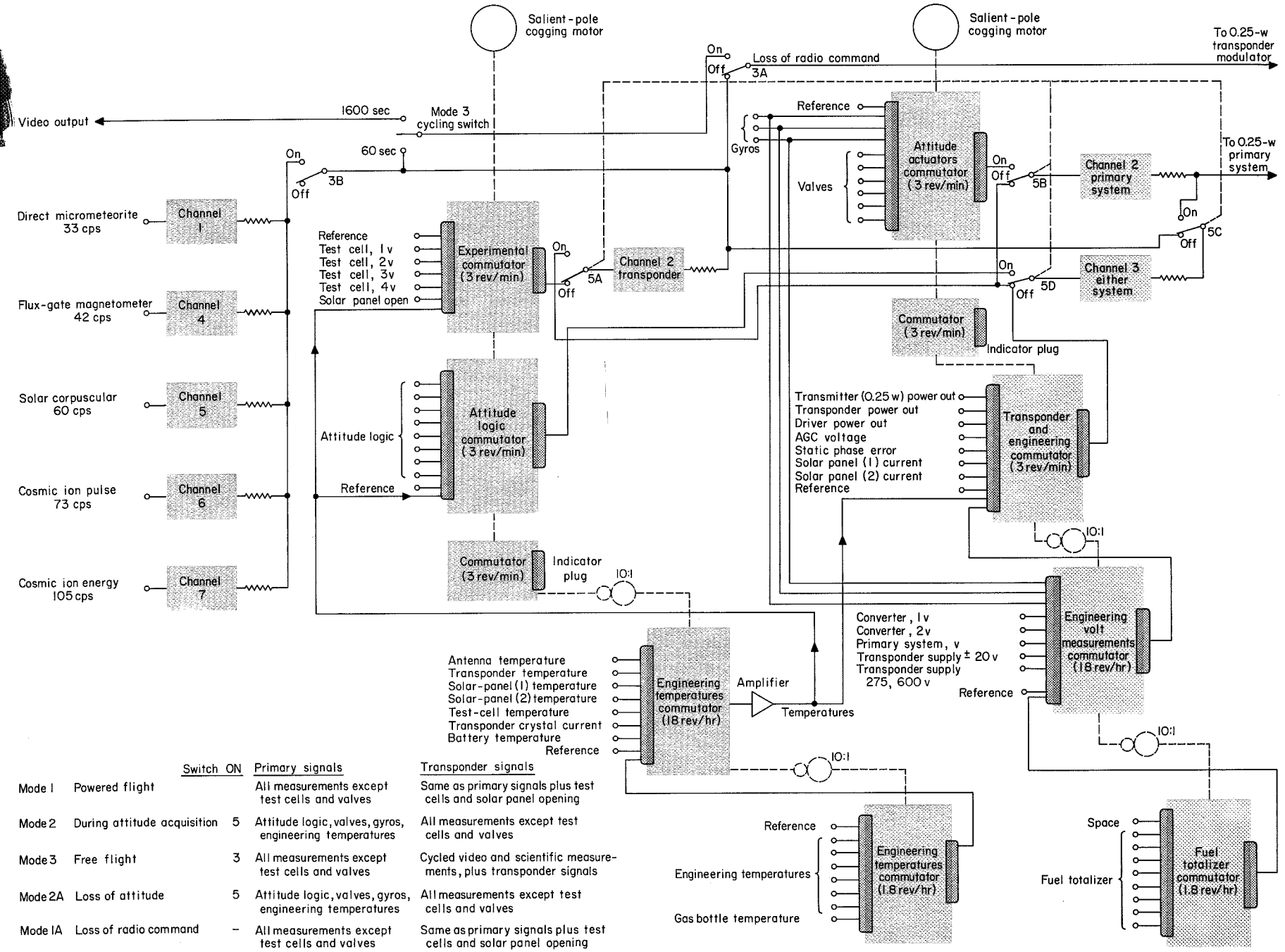

		Switch ON	Primary signals	Transponder signals
Mode 1	Powered flight		All measurements except test cells and valves	Same as primary signals plus test cells and solar panel opening
Mode 2	During attitude acquisition	5	Attitude logic, valves, gyros, engineering temperatures	All measurements except test cells and valves
Mode 3	Free flight	3	All measurements except test cells and valves	Cycled video and scientific measurements, plus transponder signals
Mode 2A	Loss of attitude	5	Attitude logic, valves, gyros, engineering temperatures	All measurements except test cells and valves
Mode 1A	Loss of radio command	–	All measurements except test cells and solar panel opening	Same as primary signals plus test cells and solar panel opening

Figure 1. Spacecraft telemetry and data encoding systems

Present feelings toward reliability and simplicity indicate that compromises should be made wherever possible to eliminate, or at least simplify, the switching.

All switching commands, including timing for the cogging motors, are expected to come from the spacecraft controller equipment.

The scientific experiment data will be handled by utilizing an FM subcarrier for each experimental channel into the common mixed-signal line which modulates the transmitter. Ground reduction of these signals is accomplished by separating the subcarriers through bandpass filters and frequency discriminators. The decommutation of the engineering data will then be accomplished by a mechanization similar to that shown in Figure 2.

The subcarriers are separated in the usual manner with bandpass filters, and the commutated subcarrier is discriminated by a phase-lock-loop discriminator.

The synchronizing pulses appear on the data channel as bursts of a high-frequency audio tone at the beginning of each frame of information. This tone is too high in phase velocity to be followed by the loop action of the phase-lock-loop discriminator, so it appears at the summing junction of the loop as an error voltage mixed with the loop-excluded noise.

The signal-to-noise ratio of the pulses is quite low at this point, but the pulses are a steady frequency, and are separated from the noise by a narrow-band filter. There will be a delay associated with any high-Q filter at this point, but this will be constant, and can be easily compensated in the rest of the decommutation mechanization. After separation, the synchronization pulses are used to synchronize a local pulse generator which operates at the data-sampling rate. This pulse generator drives a ten-step data sorter which gates the data frequency successively to ten different three-digit decimal data displays.

The data is simultaneously gated for exactly 1 second per sample so that the frequency count in each storage display is a count of the frequency of that commutated sample in cps. Not indicated on the figure are the display reset lines from the data sorter which resets each display unit just prior to gating into it another sample.

The data sorter is kept in sample step by the local data-rate pulser, and it is kept in frame synchronization (so that data sample No. 1 always goes to display No. 1) by a reset line actuated by the incoming synchronizing pulses at every frame.

The mechanization of the one-tenth rate decommutation is effected by gating the appropriate readout line

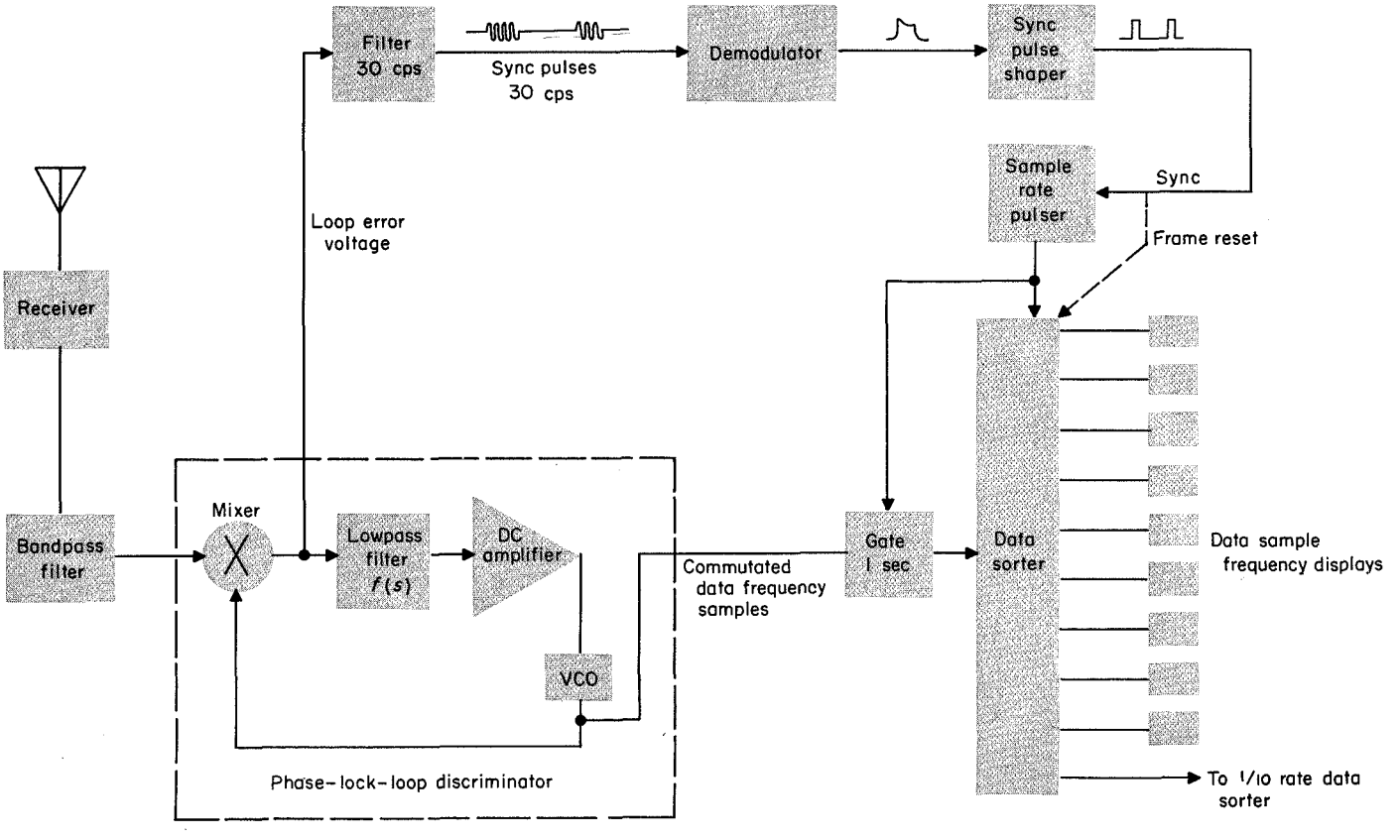

Figure 2. Ground telemetry decommutation system

to another data sorter operating at one-tenth the stepping speed, and synchronization is accomplished by a double-sync pulse which is appropriately discriminated and used to reset the one-tenth sorter, just as the fast-frame sync pulse resets the fast deck decommutator.

The decommutated data will be displayed as a subcarrier frequency. The display panel will sample and hold a measurement until the next sample is taken. Thus, the latest indication of a specific measurement is always available by viewing this display panel.

B. Communications

Communication between the *Vega* payload and the earth is to be via a radio system utilizing phase-modulated continuous wave signals. The purpose of the system will be: (1) to telemeter commands to the payload as well as scientific and equipment performance data back to the earth, (2) to coherently receive and transmit signals for radio measurements of doppler velocity, range, and angular position to the earth, and (3) to angle-track the signal received from the earth. For the earlier experiments, the system will be relatively simple and will perform only the functions of command and data telemetry, along with the measurement of doppler velocity. Each successive experiment will be designed to further develop the functional capabilities and reliability of the communications system.

1. Transponder

The initial transponder developmental effort was started at the Laboratory (*SPS 3*) and, subsequently, a joint developmental effort was established with the Motorola Western Military Electronics Center, Phoenix, Arizona, who will manufacture all the units. Before the individual modules are put into production, however, the system will be evaluated as thoroughly as possible to determine in what areas problems exist and what modules must be modified to correct these problems. To begin this evaluation, a complete RF loop was assembled using prototype or breadboard models of the individual modules. This loop (Fig 3) consisted of a 50-mc IF amplifier and second mixer, 10-mc IF amplifier, phase detector, loop filter,

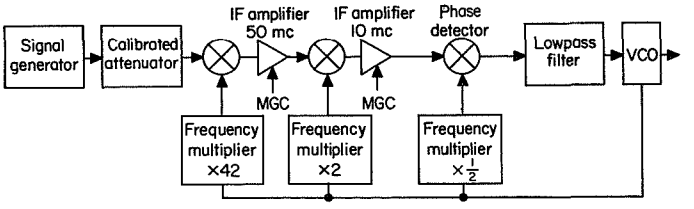

Figure 3. RF loop test setup

voltage-controlled oscillator, frequency divider, local oscillator multiplier chain (×42), and a strip-line directional coupler mixer having balanced outputs. The 890-mc source was a crystal-controlled Mosley SG-45A signal generator followed by a calibrated PRD 198 attenuator.

The system evaluation, at present, is being performed with an RF loop noise bandwidth ($2\ B_{L_0}$) of 100 cps, a 19-db noise figure (no effort was made to minimize this figure for the test) and a manual AGC system. The theoretical threshold under these conditions is −135 dbm. The purpose of these tests was to determine if any unwanted coherent signals were present which might deteriorate the performance of the system. The first attempt to lock the RF loop indicated that spurious sideband signals in the local oscillator chain degraded the receiver threshold by 5 db. An evaluation of the effect of local oscillator sideband signals indicated that the level of these sidebands must be down 40 db below the level of the local oscillator signal. Consequently, the local oscillator was redesigned to meet the required amount of sideband rejection. With the improved local oscillator signal the RF loop was capable of acquiring a signal at the threshold level of −135 dbm.

Frequency multiplier chains. To obtain the sideband rejection in the local oscillator, it was necessary to include 20- and 40-mc traps at the output of the tripler stage (Fig 4). The inclusion of these traps reduced the level of the largest sideband to more than 50 db below the 840-mc signal.

The transmitter multiplier chain is identical to the LO up to the 120 mc point. At this point an additional transistor ×2 frequency multiplier is required to derive the 240-mc signal which enters the ×4 Varactor multiplier. 2N706 high-frequency silicon transistors are used throughout the chains to improve the temperature characteristics.

The modulation is performed in the 60-mc amplifier stage, rather than a multiplier stage, to obtain linear phase modulation characteristics. Its response when used with range coding must be flat from dc to 5 mc. The desired sensitivity of the modulator is 1 v/rad of modulation at the final frequency.

Packaging. The basic transponder, which consists of a single channel phase-coherent receiver and a transmitter

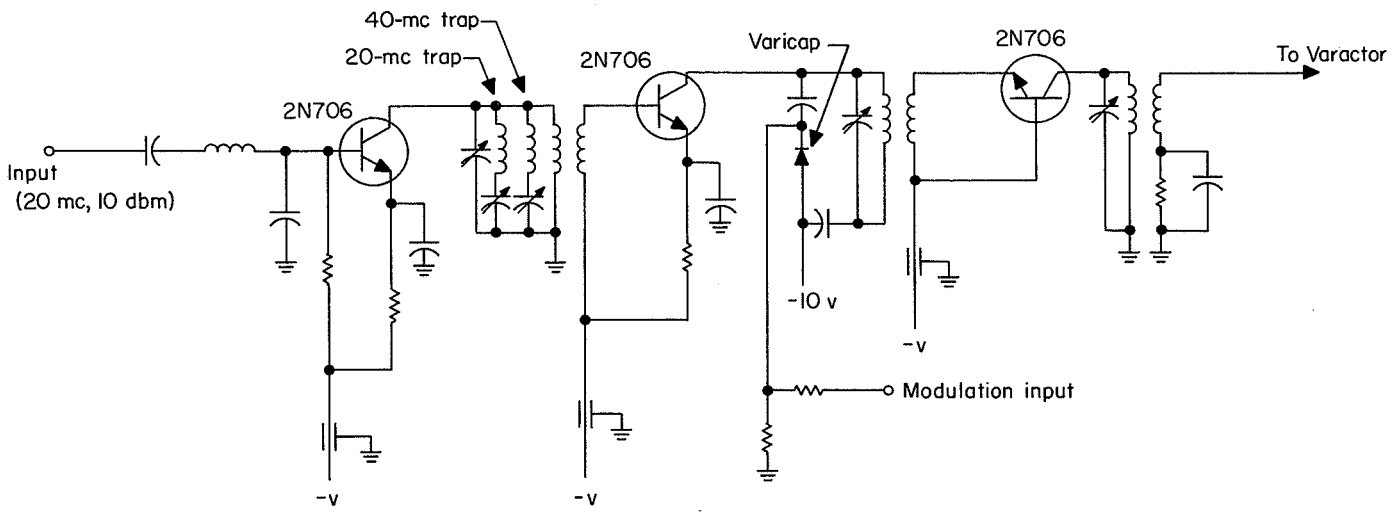

Figure 4. Multiplier chain

delivering 5 to 10 mw has been packaged in one container. The higher power cavity amplifiers will be located externally to provide heat dissipation. This basic transponder is scheduled to be flown on the earlier flights. For later flights, which will contain a more extensive communications system including range coding and angle tracking, this unit will be redesigned to house these additional modules. Figure 5 shows the modules used in the RF loop test when installed in the basic transponder housing.

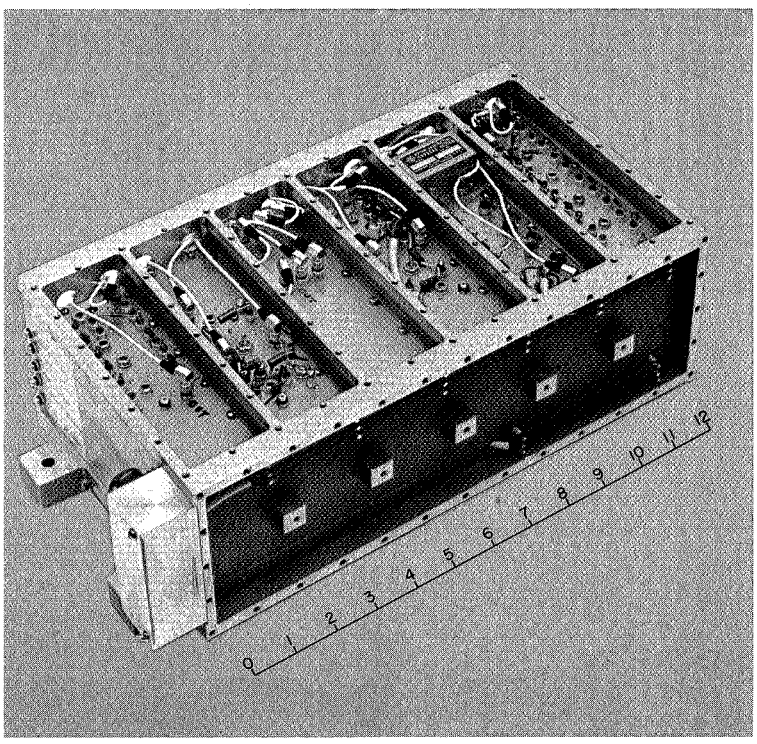

Figure 5. Transponder

C. Electrical Power

The spacecraft electrical power system has undergone a number of design changes in recent weeks. This series of design exercises has reduced the amount of solar power available aboard the spacecraft. A critical requirement exists for engineering manpower to develop the attitude control system necessary for the sun-oriented solar panels.

1. System Design

A reduction in power has taken place between the completion of the guidance system study spacecraft design and the current spacecraft design. The regulated power available (Fig 6) from the oriented solar panel has been reduced from 250 to 35 watts. An additional 13.5 watts of power is available for 140 hours from battery power carried aboard the spacecraft. This power tabulation does not include the power that is allocated to scientific instruments. This power will be provided from an integrated electrical power system, but for planning purposes is tabulated separately. A critical evaluation of the requirements of the communication and telemetry systems has

reduced their power from 120 to 21 watts and from 40 to 5 watts, respectively. A block diagram of the new system is presented in Figure 7. For reliability, the receiver is operated from a separate battery.

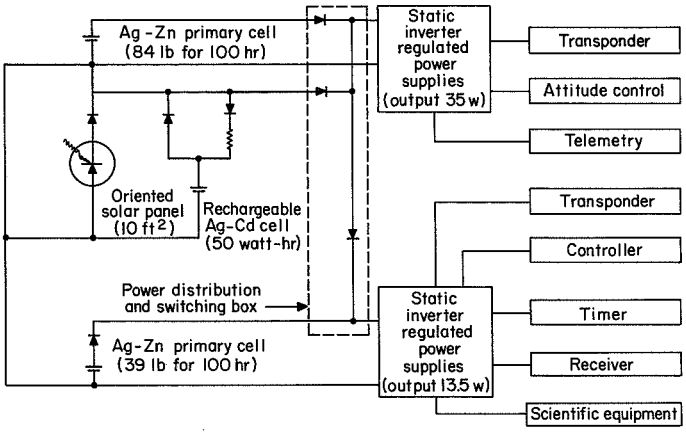

Figure 7. Spacecraft electrical power system

2. Solar Cell Development

Considerable effort has been devoted to the solar cell glass-slide adhesive problem. A large number of epoxy adhesives has been evaluated and tested. Based on tests conducted with 6-mil thick glass slides having the ultraviolet rejection filter deposited on them, this problem now seems to be nearing a solution. Additional tests have been conducted to develop solar cell matching techniques to achieve maximum efficiency using *E-I* curves obtained on an *X-Y* plotter.

Tests have been run in a 14-inch-bell-jar space environment simulator, with a calibrated black body to control the energy in a carbon arc light source to a pyroheliometer referenced value. Life tests to determine the emissivity stability of solar cell coatings in a simulated space vacuum environment have also been conducted. Based on the variation in cell temperature and output as a function of time, there has been no significant change in the emissivity of these special solar cell coatings.

System tests to determine the best manner in which to interconnect solar cells, rechargeable batteries, and transistor static inverters are being conducted. There are many factors to be considered in selecting the optimum system, such as the dynamic response of the solar cells, the impedance-matching characteristic of the battery, and the need to limit the charging rates of batteries connected in parallel with solar cells.

3. Static Power Supply

Two static inverters (50 volt ampere) have been built which are identical with the exception that one incorporates germanium and the other silicon transistors. Heat transfer tests are being conducted in the 14-inch-bell-jar space environment simulator to evaluate which design has the largest thermal margin. The recent spacecraft design has eliminated the provision of a cooling fan to blow gas over the electronic components in the static inverter modules. These modules will be as much as 8 inches thick, and it will be necessary to conduct heat from the semiconductor junctions to the outer radiating

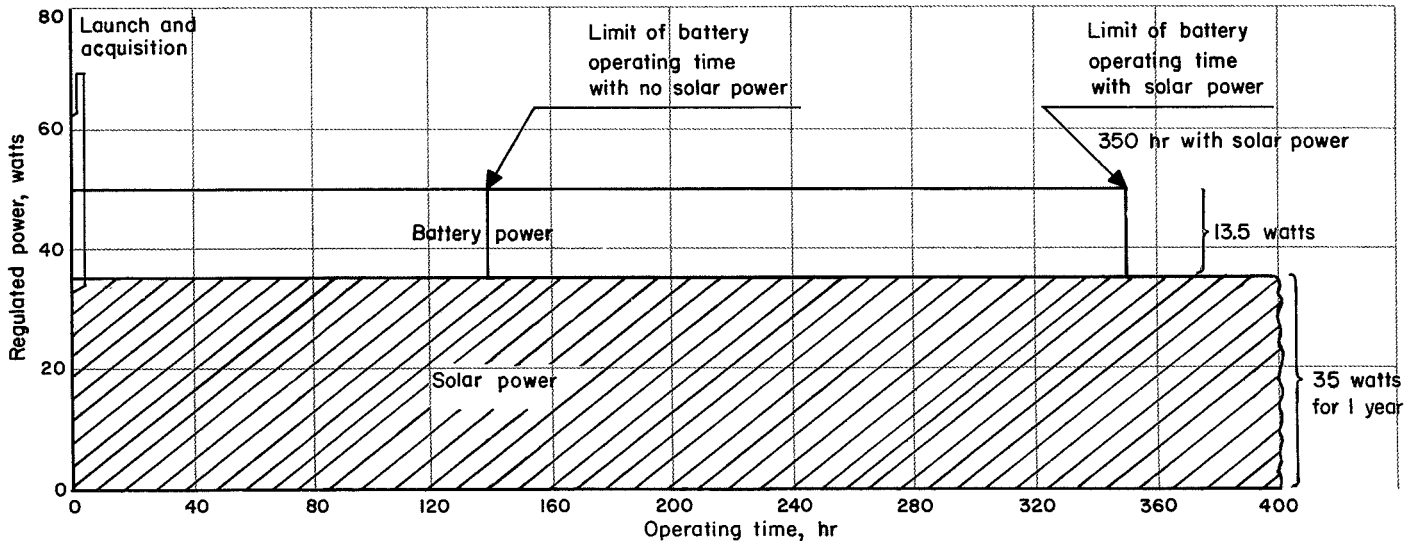

Figure 6. Spacecraft power requirements

surface to dissipate heat. The heat transfer characteristics of insulators such as mica are being evaluated. The system tests in connection with the solar cell panels will substantially influence the design of the static inverters because the dynamic response characteristics of the solar cell panel may substantially increase the switching time of the power transistors. System studies are being conducted to determine if it will be necessary to develop a transistorized battery charger. This battery charger could degrade the impedance-matching function of the battery when placed in parallel with the solar cell panel.

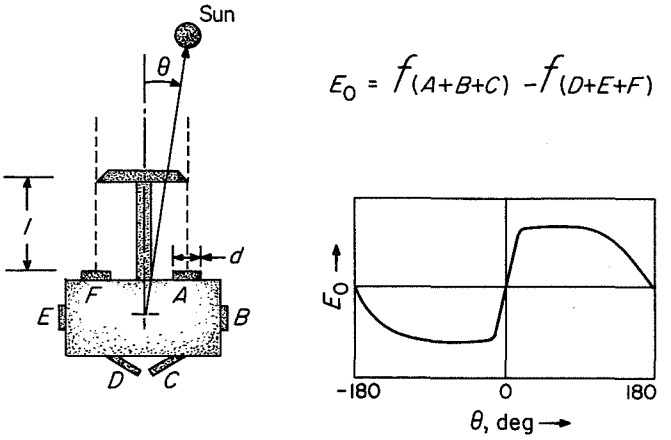

Figure 8. Single-axis sun seeker

D. Guidance

Attitude stabilization and mid-course guidance maneuver require the accurate determination of earth and sun lines. The required accuracy is highest just prior to a retro-maneuver. For example, in a typical lunar orbiter mission, at about 80,000 miles from the earth a correcting maneuver will be used. The sun and earth lines are required to be within ±0.8 degree and anticipated to be ±0.2 degree at this point. A second maneuver will be made in the vicinity of the moon. At this point, the sun and the earth lines are required to be within ±0.4 degree and expected to be within ±0.1 degree. At all other times the required accuracy is much less stringent, principally being used to point the antenna and stabilize the spacecraft.

1. Sun Seeker

A sun can provide an angular reference in two axes through the use of two single-axis sun seekers. A single-axis sun seeker is shown in Figure 8. Note that the output of this unit rapidly passes through zero as θ goes through zero and that

$$\left.\frac{\Delta E_0}{\Delta \theta}\right|_{\theta=0}$$

can be made very large by increasing the length l while holding d constant. This mechanization offers many advantages: ruggedness, simplicity (no optics required), reasonably accurate center-finding ability, relative insensitivity to gain changes, and a 360-degree field of view.

The detector for this device will be of the photoconductive type, probably cadmium selenide. A mockup of the sensor has been made and null stability on the order of 0.2 degree was achieved. Flight-type hardware will be ready for test by 30 November 1959.

Tests on three types of detectors were made to determine stability with temperature and time: (1) cadmium selenide (Clarex 403 glass encapsulated), (2) cadmium selenide (Clarex 3 epoxy encapsulated), and (3) Hoffman silicon solar cells (58C). All cells were tested in both a simulated seeker and individually. The Clarex 403 cells were much more stable than the Clarex 3 both with temperature and time. The silicon solar cells were about the same as the Clarex 403 cells in the simulator. Since the cadmium selenide has the lowest impedance in this application, it will probably be used in the final system.

2. Earth Seeker

The earth-seeker accuracy requirements are much the same as the sun seeker. Mechanization will be similar in that no optics and that shadow-bar-type construction are used; however, the error signals on both yaw and pitch are developed in one two-axis device. (Note that yaw is redundant between sun seeker and earth seeker, the sun seeker is dominant for attitude control; however, the earth seeker is dominant for antenna pointing.) Field of view on each axis is only required to be ±15 degrees. After spacecraft sun acquisition has been effected, the spacecraft will begin to roll about the sun line. Simultaneously the earth seeker will scan in yaw to find the

earth. When the earth is detected, scan-mode will switch to servo-mode and the seeker will be slaved to the earth.

The detector used can be either the Clarex 403 photoconductive type or Dumont K1664 photomultiplier tubes. While adequate for *close-in* use, the Clarex 403 does not offer as much growth potential as the photomultiplier. Photomultiplier detectors are now considered the most logical choice; however, it is intended to build three flight-type units using the Clarex cells as a backup to the photomultiplier design.

Parts are being procured and detail prints are ready for construction of the first flight model prototype earth seeker. It is anticipated that the first model will begin tests by 10 December 1959.

E. Controller

Because the various spacecraft systems often perform functions in which several systems are affected by the same conditions, and because routing and processing of intersystem commands must be done in a manner which does not interfere with the functions of any system, it is desirable to have a central information and command processing unit which will contain the necessary logic to meet these requirements. This unit will be called the spacecraft controller.

The controller will perform the following functions:

(1) Generate timing information.

(2) Receive information and/or commands from: (a) earth-based control during preflight system tests, (b) earth-based control during flight, (c) timer, and (d) on-board systems to indicate the existence of conditions requiring action by other systems.

(3) When required, generate commands based upon information from the sources shown in item (2).

(4) Route the received and generated commands to the appropriate spacecraft systems for action.

The preliminary functional design of a spacecraft controller is in process and will be reported on in future issues of the *SPS*.

F. Assembly and Test

The assembly of the spacecraft is scheduled to occur during the month of June 1960. During this period, the basic truss structure, the intermediate structure joining the spacecraft to the *JPL-6K* third stage, the six instrument cases, antenna parabaloid, attitude control jets, extensible booms, cabling and all other components will come together, forming the flight spacecraft. Concurrently, shortcomings in fit, clearance, mechanical interchangeability, finish and constructional details, in general, will be substantially eliminated. The delivery schedule (Table 1) relates the assembly program to the *Vega* schedule.

Flight spacecraft assembly will be preceded by construction of mockups and an Engineering Model. Intended uses of these items are tabulated in the disposition schedule, Table 2. As the disposition schedule makes clear, the assembly of the mockup will inaugurate a period of intensive design evaluation. The construction of mockups and Engineering Model will be of benefit in three areas:

(1) In establishing standards for assembly procedure and workmanship in advance.

(2) In facilitating recognition of suboptimum elements in the spacecraft design and introduction of improvements.

(3) In constructing the Engineering Model which will be altered more or less continually to model, in all major respects, the spacecraft design for following missions.

Assembly operations will be conducted in the JPL missile building main assembly area. An area of 1400 square feet of floor space has been assigned for assembly. A service tower will be erected on the north end of the missile building. This tower is primarily intended for structural tests on the JPL third stage but will be on secondary call for mating tests of third stage and spacecraft. Assembly operations may be transferred from the missile building to the new assembly building scheduled for completion in August 1960, when the new building is ready for use.

[redacted]

Table 1. Delivery of spacecraft components for assembly

Schedule of events[a, b]	1959	1960																									
	Dec	Jan				Feb				April				June				Sept									
Basic structure	←					M				E				401				S									
Attitude jets and valves[c]						M				E				401				S									
Gas bottles						M				E				401				S									
Backup battery[d]						M					E				401			S									
Separation fittings						M					E				401			S									
Antenna drive mechanism						M					E				401			S									
Solar panels[d]						M					E				401			S									
Instrument boom No. 1						M					E				401			S									
Instrument boom No. 2						M					E				401			S									
Dish antenna						M						E				401		S									
Nondirectional antennas						M						E				401		S									
Cabling harness							M					E				401		S									
Attitude electronic cases[e]																											
Case 1	M											E				401		S									
Case 2	M												E				401	S									
Case 3	M												E				401	S									
Case 4	M												E				401	S									
Case 5	M												E				401	S									
Case 6	M												E				401	S									
Spacecraft assembly fixture	←					M				E				401													

[a] Symbols used are as follows: M = mockup, E = Engineering Model, 401 = flight, and S = flight spare.
[b] Only those months are listed in which an event is scheduled.
[c] If external.
[d] Stand-in.
[e] Nomenclature is interim and may be supplanted.

In contrast to some previous space programs, only one flight spacecraft will be assembled for each mission. Nominally interchangeable replacement spares will be maintained for most of the components.

Following the assembly and preliminary checkout of the spacecraft, systems testing will commence in the missile assembly building at the Jet Propulsion Laboratory. Following successful completion of systems testing in the assembly building, the complete spacecraft will be transferred to the environmental facility where abbreviated type systems tests will be performed under several different environments. Upon successful completion of these and mechanical mating tests with the *JPL-6K* third stage, the spacecraft will be shipped to Cape Canaveral where a systems test, virtually identical to the one run in the missile assembly building at JPL, will be performed. Subsequent to successful systems tests in the hangar checkout area of Cape Canaveral, the spacecraft together with the *JPL-6K* third stage will be mated to the first and second stages at the launch area.

[redacted]

Table 2. Disposition schedule

Item	Use
Mockup spacecraft (plus additional mockups of portions, only)	Packaging evaluation Movable components tests Structural loading tests Vibration tests (nondestructive) Pattern for routing of electrical fluid lines test Separation from JPL third stage Development of assembly procedures
Engineering Model spacecraft	Environmental tests Structural tests Electrical tests Development of assembly procedures
Flight spacecraft	Atlantic Missile Range
Spare components	Support of flight spacecraft

The systems test configuration to be utilized in the missile assembly area at JPL and the hangar area at the Cape will consist of the spacecraft mounted on a tilting-type fixture with the solar panels extended into the open position. This basic configuration will be surrounded by a semicircle of test equipment consoles and racks comprised of that needed by each of the individual major subsystems groups having units in the spacecraft. Operation of these individual racks and consoles will be the responsibility of the cognizant engineering design group for each particular development section. (Present thinking indicates that approximately eight of these test consoles will be needed to monitor the power functions, attitude control, communications, scientific experiments, etc.)

This modus operandi will allow the operator a good view of the spacecraft while he is monitoring and operating the various control panels and consoles. Figure 9 shows the plan view of the present concept for this system test configuration. It will be observed from this drawing that all operators and participating observers have as unrestricted a view of the spacecraft and the programmer timer face as is possible to obtain with the equipment necessary for this operation.

The whole systems test will be based upon a published procedure wherein testing of almost all of the units will be accomplished by stimulating each through the range it is likely to encounter during actual flight. This is to be performed in a predetermined sequence and time schedule. Many of these functions will be time-programmed, thereby insuring their actual occurrence at the times called out in the test procedure. Certain other functions which cannot be conveniently programmed will be manually operated. This latter type of operation will likely have to be performed to stimulate some of the proposed scientific experiments and attitude control light sensors by movements of magnets, radioactive materials, light sources, etc. Performance of these scheduled functions will be closely coordinated by means of the stimulus operator observing the large timer dial face associated with the programmer. Conformance to a rigid sequence of time scheduling such as provided by this prescribed setup adds greatly in later reduction of the information pertinent to acceptances or rejection of the overall test. Besides the functions that can be directly recorded and time-correlated on an oscillograph, various phenomena may have to be observed on oscilloscopes or by observers watching for mechanical phenomena such as the opening of solar panels, extension and retraction of Vidicon or magnetometers, motion of the dish antenna, etc.

The whole test will be coordinated by a systems test conductor who will be in charge of integrating the operation and making various decisions relative to the performance and continuation of testing in the event of any malfunctioning or other contingency. Figure 9 shows that the proposed test area allows the test conductor to rapidly move from one console position to another to observe and assist in making decisions in various readings as they progressively occur throughout the complete procedure.

Following completion of the systems test, the test conductor is to coordinate the gathering and analysis of all data pertinent to the acceptance or rejection of the test. Data obtained during the test will be filled in on systems test procedure data sheets for the various recordings, visual observation of meters and oscilloscopes, observations of physically moving phenomena on the spacecraft

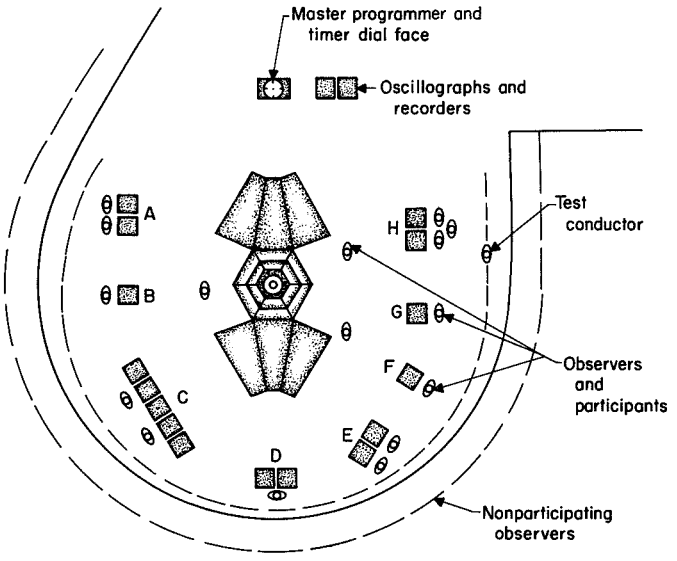

Figure 9. Test assembly setup

and other items as necessary. The various cognizant engineers who have the responsibility for the subsystems test equipment will contribute to the analysis of the test affecting their respective units and to the overall analysis and subsequent rejection or acceptance.

Environmental testing of the complete spacecraft will be performed in two different basic areas within the JPL environmental test facility. The first of these, a large vacuum chamber, will contain the spacecraft with the solar panels removed and will allow operation within the chamber at pressures considerably less than 1 micron (with the chamber wall temperatures maintained at a low level by circulating liquid nitrogen through tubing contained therein). Four access windows at the top of the chamber will be provided through which four 15 kw, high intensity, arc projection lamps will irradiate the spacecraft during this operation. It is anticipated that relatively complete systems testing can be accomplished within the chamber under the simultaneous environments of vacuum, very low wall temperature and irradiation close to the spectrum and intensity of the sun.

Following the completion of a successful test in the described facility, complete vibration tests of the assembled spacecraft (while performing a regular or possibly abbreviated systems test) will be performed. It is presently anticipated that available equipment will allow vibrating the complete spacecraft under noise and sine wave conditions at maximum accelerations somewhere between 5 and 10 *g*. These tests are planned to be repeated for approximately a 10-minute duration in each of three planes. Though the individual packages comprising the spacecraft will be subjected to accelerations as high as 25 *g*, it is believed that accelerations in the region of 5 to 10 *g* for the total time of 30 minutes should suffice for the whole system. This amplitude and duration should reveal any system vibration resonances.

Following acceptance at JPL, the spacecraft and *JPL-6K* third stage will be shipped to Cape Canaveral where systems testing very closely approximating that initially performed in the missile assembly building will be carried out. After completion of an acceptable complete systems test in the hangar area, the spacecraft and third stage will be mated to the first- and second-stage boosters at the launch area. In the event of failure of one of the units during test, a spare can be installed from the complete set of tested operating spares that will accompany the spacecraft to the Cape. If so utilized, the complete systems test will be re-run.

An overall test of the spacecraft is to be performed during the missile countdown starting at approximately X − 7 hours. This test is to be a very streamlined version of the basic systems test wherein various functions will be monitored via the test plug during power-on operations of the spacecraft and by stimulating the portions of the equipment that can be, through the RF link. Presentation of much of the monitored telemetry data will be accomplished by means of a data display panel located with the spacecraft master control console in the blockhouse and showing output frequencies for each of the commutated functions. The outputs from the telemeter discriminators will present information for each RF interrogation to assure that the communications equipment as well as the end instruments and the functions being mointored are in proper working condition. Besides these overall loop tests, certain other elementary functions can be monitored by means of the spacecraft test plug and the RF link, such as basic dc supply voltages, frequency and stability of RF, sensitivity, power output, etc. Due to the limited room in the blockhouse, it is not anticipated that a transmitter or phase-lock receiver will be situated there. Any operation and checkout of the RF link would have to be commanded by RF from the launch station facility, but monitoring of all telemetered functions can be performed by running the spacecraft transmitter modulator output to the blockhouse by means of a cable, thus bypassing the space consuming equipment of the RF link.

The principal objective of Project Echo is to determine the feasibility of reflecting sphere satellites for global communications. Radio signals will be sent from the East Coast of the United States to the West Coast, and vice versa, via a 100-foot-diameter balloon in a 1000-mile satellite orbit. The Jet Propulsion Laboratory will operate its Goldstone deep-space instrumentation facility for Project Echo as the official NASA West Coast transmit/receive station. The East Coast station will be operated by the Bell Telephone Laboratories and is located in Holmdel, New Jersey.

III. TRACKING AND COMMUNICATIONS

A. Project Echo Communications

The utilization of Earth satellites has been proposed as a possible technique for improving global communications. These communications satellites fall into two general categories: passive repeaters and active repeaters. Project Echo utilizes a passive repeater in the form of a 100-foot-diameter balloon. Project Echo is a NASA program; however, other agencies and organizations have been invited to utilize the 100-foot balloon to perform communications experiments. The official NASA transmit/receive stations are located at Goldstone, California, and Holmdel, New Jersey (Fig 10). The Goldstone station is operated by the Jet Propulsion Laboratory, and

The TRAC(E) system as developed for the initial *Juno II* experiments was described in *SPS 1* through *4*. This system is an integral part of the Goldstone tracking station which was used to track the signals from *Pioneer* probes *III* and *IV*.

The present TRAC(E) system is a one-way link consisting of a vehicle-borne transmitter and a ground-based receiver. A two-way TRAC(E) system is now under development for the *Vega* program. This two-way system will consist of the present 960-mc receiving system with its 85-foot-diameter antenna plus a new 890-mc, 10-kw transmitting system operating into another 85-foot-diameter antenna located approximately 7 miles from the receiving station. Elements of the two-way TRAC(E) system will be utilized in the Passive Communications Satellite Program (Project Echo) before the equipment will be needed for the *Vega* program. Therefore, many of the detailed activities reported in this summary will refer to Project Echo rather than *Vega*. However, it should be borne in mind that the Goldstone station and the deep space instrumentation facility are being designed principally to satisfy the tracking and communications requirements of deep space exploration programs such as *Vega*.

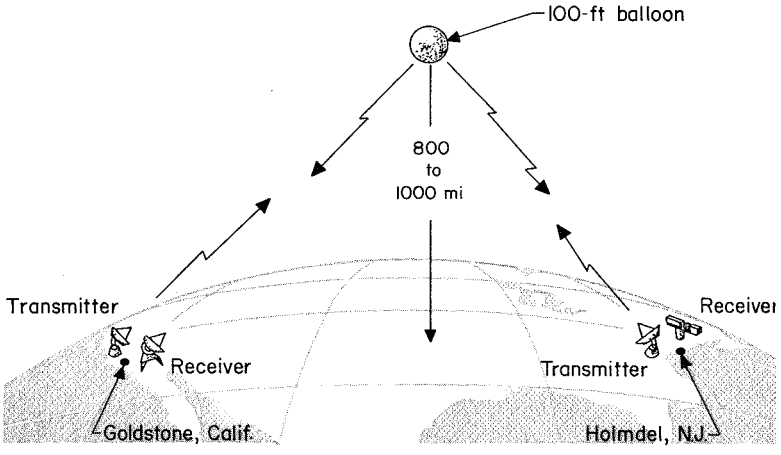

Figure 10. Passive communications satellite experiment

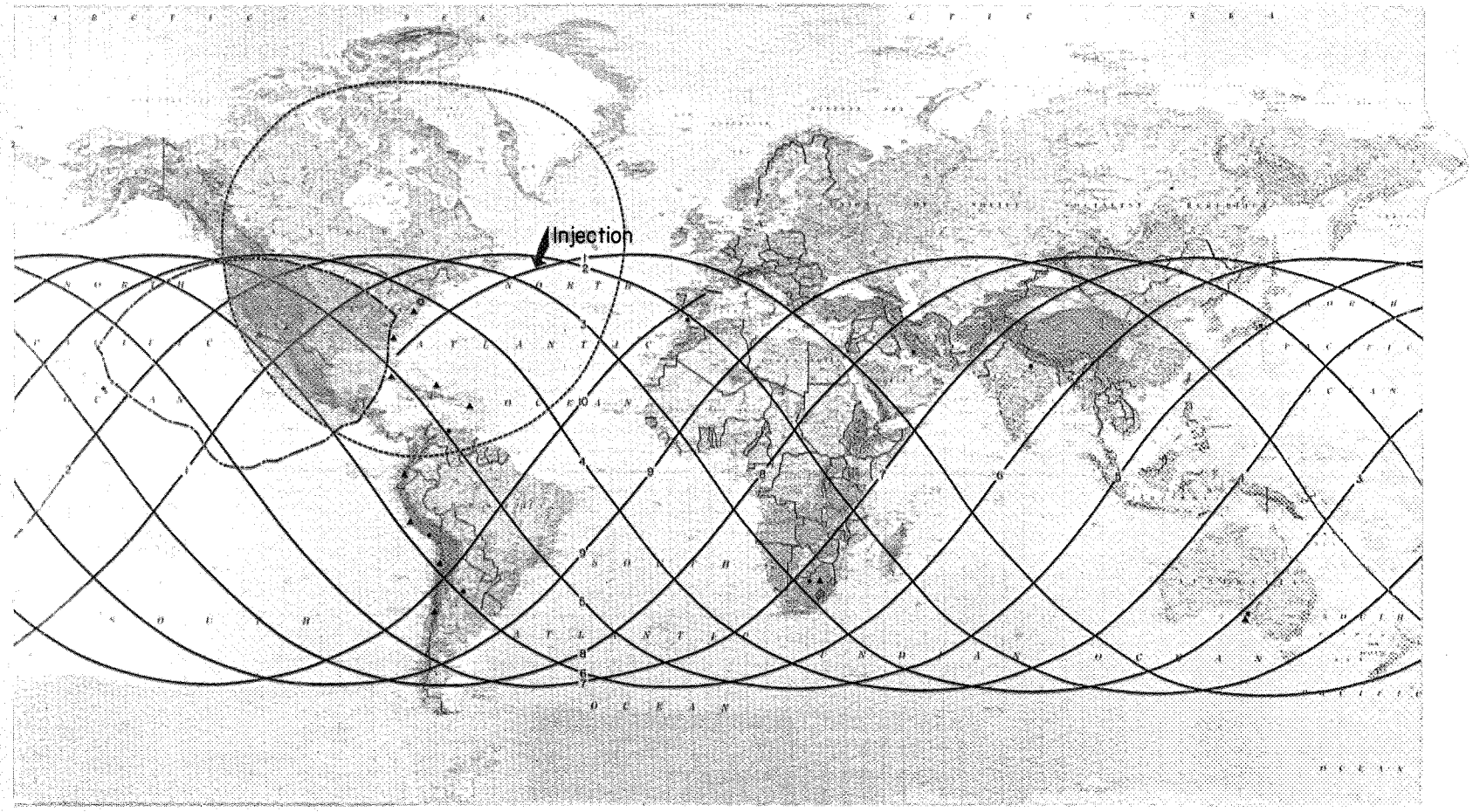

——— Preliminary Echo coasting trajectory

– – – – Perimeter of visibility from Goldstone, Calif. (JPL) ◎

– – – – – Perimeter of visibility from Holmdel, N.J. (BTL) ◎

Satellite height: 900 nautical miles

49° inclination of orbit plane

▲ Minitrack Stations

Blossom Point, Maryland	Santiago, Chile
Ft. Stewart, Georgia	San Diego, California
Havana, Cuba	Antigua, BWI
Quito, Ecuador	Woomera, Australia
Lima, Peru	Johannesburg, South Africa
Antofagasta, Chile	Grand Turk, BWI (Mark II)

● Baker-Nunn Satellite Cameras

Organ Pass, New Mexico	West Palm Beach, Florida
Olifantsfontein, South Africa	Haleakala, Hawaii
Woomera, Australia	Arequipa, Peru
Cadiz, Spain	Villa Dolores, Argentina
Tokyo, Japan	Shiraz, Iran
Curacao, NWI	Naini Tal, India

Figure 11. Mutual visibility zone for Goldstone-Holmdel

the Holmdel station is under the cognizance of the Bell Telephone Laboratories (BTL).

The satellite will be launched northeast from Cape Canaveral (Fig 11) and will be injected into a 1000-mile circular orbit inclined approximately 49 degrees to the equator. The balloon is expected to appear above the Goldstone horizon for the first time when it is over the Pacific Ocean southwest of the station. Optical and radio tracking will begin as soon as possible after the balloon is visible from Goldstone. A short time later the balloon should be visible to both Goldstone and Holmdel, and radio communications may be initiated. Figure 11 shows the region of mutual visibility for the two sites; it also shows that radio communications should be possible during the first, second, fourth and fifth passes of the balloon over the United States. The zone of visibility for the Goldstone station is smaller than that for the Holmdel station because the Goldstone receiving antenna is equatorially mounted and cannot be positioned in declination below the North Star.

The Goldstone and Holmdel transmit/receive stations are described functionally in Figures 12 and 13, respectively. The two Goldstone antennas operate together, and according to the block diagram they may be positioned (1) optically, (2) digitally, from computed trajectory data, or (3) by radio means, automatic tracking on the reflected RF signal. The Holmdel antennas also operate together, and they can be positioned optically or digitally. The Goldstone transmitter frequency is 2390 mc, whereas the

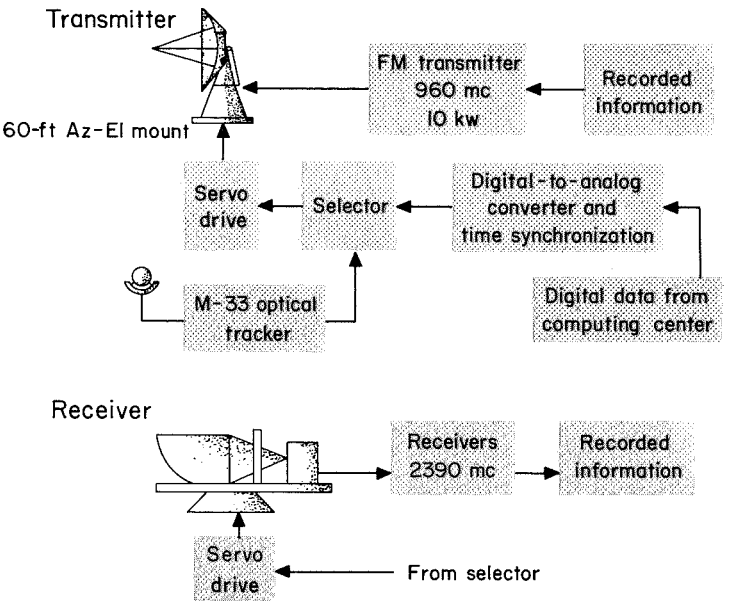

Figure 13. Holmdel tracking station

Holmdel transmitter frequency is 960.05 mc. Therefore, the East-to-West Coast link is on 960.05 mc, and the West-to-East Coast link is on 2390 mc.

The expected values of received signal level, as reflected from the 100-foot balloon, were calculated from the known radar equation

$$P_R = P_T G_T G_R \left[\frac{c}{4Rf_c}\right]^2 \left(\frac{D}{4R}\right)^2 \frac{\eta_T \eta_R}{L} \text{ milliwatts}$$

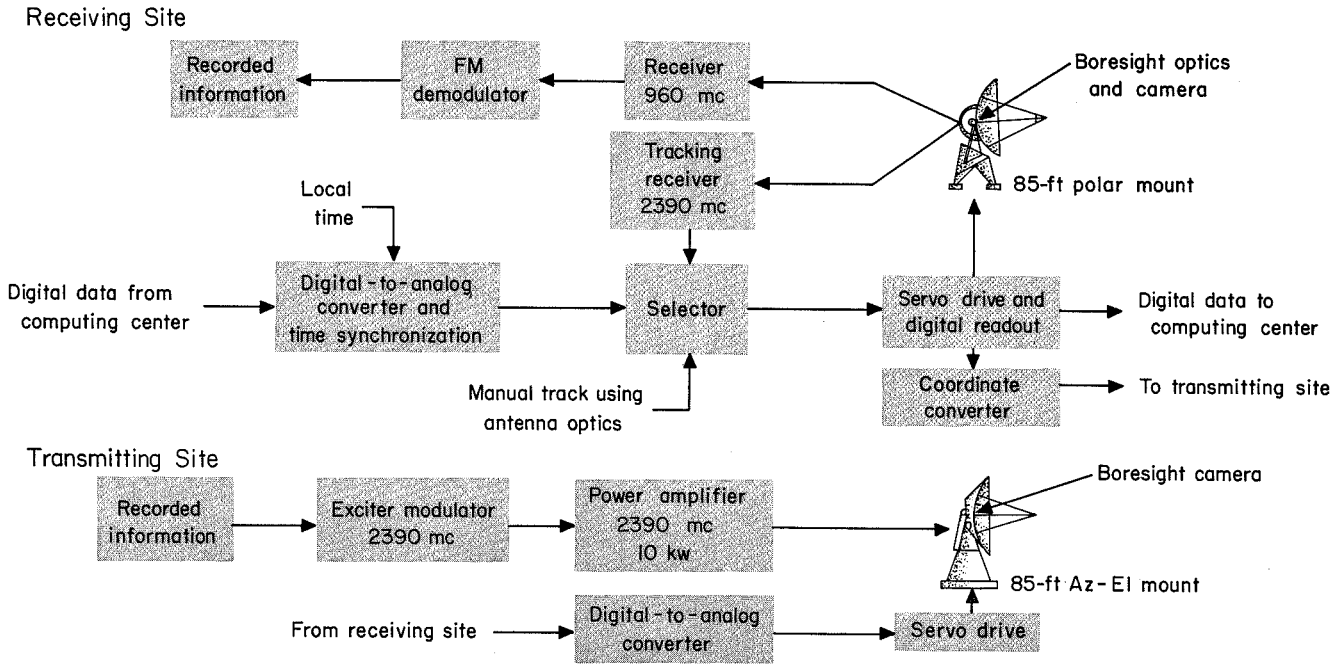

Figure 12. Goldstone tracking station

where

P_T = transmitted power in milliwatts

G_T = transmitter antenna gain relative to isotropic based on uniform illumination of the parabolic reflector

G_R = receiver antenna gain relative to isotropic based on uniform illumination of the parabolic reflector

c = velocity of propagation in mi/sec

R = radial range from the transmitter/receiver to the target in miles (assumes satellite is midway)

f_c = carrier frequency in cps

D = diameter of the balloon in miles

η_T = efficiency of the transmitting antenna

η_R = efficiency of the receiving antenna

L = all other losses such as feed loss, transmission line loss, reflection loss, polarization loss, propagation anomalies, etc.

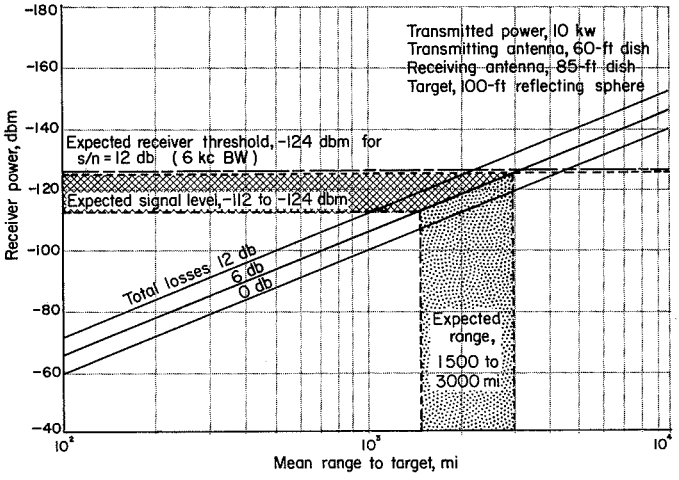
Transmitted power, 10 kw
Transmitting antenna, 60-ft dish
Receiving antenna, 85-ft dish
Target, 100-ft reflecting sphere
Expected receiver threshold, -124 dbm for s/n = 12 db (6 kc BW)
Expected signal level, -112 to -124 dbm
Total losses 12 db
6 db
0 db
Expected range, 1500 to 3000 mi
Receiver power, dbm
Mean range to target, mi

Figure 14. East-to-West transmission at 960 mc

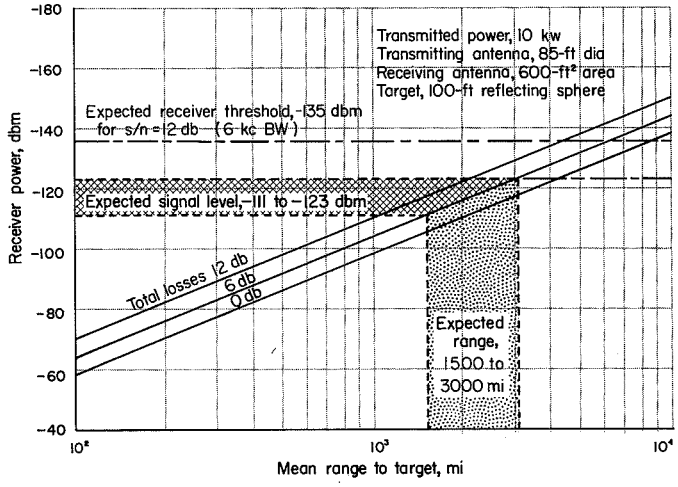
Transmitted power, 10 kw
Transmitting antenna, 85-ft dia
Receiving antenna, 600-ft² area
Target, 100-ft reflecting sphere
Expected receiver threshold, -135 dbm for s/n = 12 db (6 kc BW)
Expected signal level, -111 to -123 dbm
Total losses 12 db
6 db
0 db
Expected range, 1500 to 3000 mi
Receiver power, dbm
Mean range to target, mi

Figure 15. West-to-East transmission at 2390 mc

The received signal level is plotted in Figure 14 as a function of range for the East-to-West 960-mc communication link. It is assumed that the transmitter power is 10^7 milliwatts, or 70 dbm, and that the satellite is effectively midway between the two stations. The antenna efficiencies and other losses are indicated as parameters in the graphs. For the expected range, 1500 to 3000 miles, the signal level is −112 to −124 dbm when the total losses are 6 db. Since the receiver predetection bandwidth is 6 kc and the receiving system noise temperature is 290°K, the expected receiver threshold is −124 dbm for 12 db signal-to-noise ratio.

The received signal level vs range for the West-to-East 2390-mc communication link is shown in Figure 15. The expected signal level varies from −111 to −123 dbm when the total losses are 6 db. If the receiving system noise temperature is assumed to be 20°K, the expected receiver threshold is −135 dbm for a 12-db signal-to-noise ratio in a 6-kc bandwidth.

B. Goldstone Tracking and Communications

The present Goldstone system contains a 960-mc tracking receiver. The future Goldstone system (for *Vega* in 1961) will contain a 960-mc tracking receiver plus a 10-kw, 890-mc transmitter. In 1960 Goldstone will be used as the West Coast transmit/receive station in Project Echo. For Project Echo, Goldstone will contain a 960-mc listening receiver, a 2388-mc tracking receiver, and a 2390/2388-mc, 10-kw transmitter. The 960-mc listening receiver will amplify and demodulate the voice signal transmitted from Holmdel and reflected by the balloon. The 10-kw, 2390-mc transmitter will be voice-modulated, and its signal will be beamed at the balloon for reception at Holmdel.

The 2388-mc signal is used for tracking only. Approximately 1 kw of RF power will be transmitted to the balloon from the Goldstone transmitting site to derive a balloon-reflected signal for the 2388-mc tracking receiver at the Goldstone receiving site. The 2388-mc tracking receiver in conjunction with the tracking-feed will provide the control signals to the servosystem for automatic positioning of the antenna in angle.

A functional block diagram is shown in Figure 16. It may be seen from the diagram that the communications

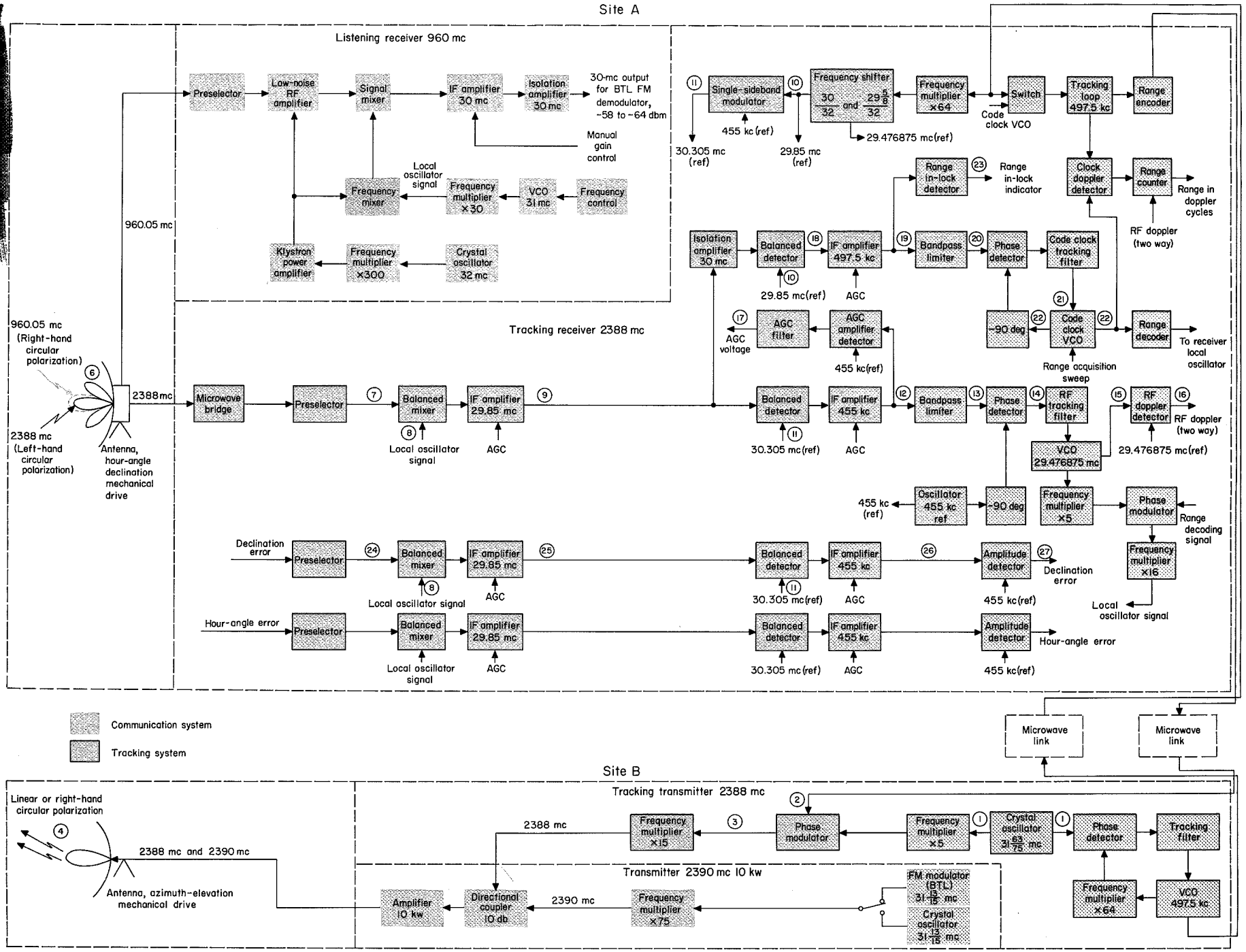

Figure 16. Goldstone setup for Project Echo

portion of the system (the 2390-mc voice-modulated exciter and the 960-mc listening receiver) is small compared to the tracking portion. This situation points up the fact that the technical problems associated with aiming the narrow (0.4 to 1 degree) antenna beams directly at the target, to within one-tenth of a beamwidth (0.04 to 0.1 degree), are significantly more complex than the problems associated with communications alone. The parameters of the 2388-mc tracking system are listed in Table 3, and the expected signal level is shown in Figure 17 as a function of range.

From the diagram in Figure 16 it is seen that the 2388-mc tracking system is actually a CW doppler-radar which is capable of measuring two angles, range, and range rate. The waveform equations which describe the operation of the 2388-mc CW doppler-radar are listed in Table 4. The numeral preceding each expression refers to the corresponding numerals in Figure 16.

1. Tracking Receiver (2388 mc)

The 960-mc Goldstone tracking receiver is being modified to receive signals at 2388 mc. Changes are being

Table 3. Preliminary characteristics, 2388-mc system

Transmitter power, dbm	60
Carrier power (0.9 kw), dbm	59.5
Range code power (0.1 kw), dbm	50
Transmitter antenna gain, db	53.5
Transmission line loss, db	0.4
Reflection loss at 2000 miles, db	−112.5
Space loss at 2000 miles, db	−170.2
Receiver antenna gain, db[a]	49.0
Transmission line loss, db	0.7
Receiver noise figure, db	7.5
Receiver bandwidth ($2B_{L_0}$), cps	60
Receiver threshold, dbm	−149.4
Range code loop bandwidth ($2B_{L_0}$), cps	1
Range code loop threshold, dbm	−167.1
Angle tracking loop bandwidth ($2B_L$), cps	0.3
Angle tracking loop threshold, dbm	−172.3
AGC loop bandwidth ($2B_{L_0}$), cps	0.03
AGC loop threshold, dbm	−182.3
At 2000-mile range	
Received RF carrier, dbm	−121.8
S/N for RF loop, db	20.9
S/N for AGC loop, db	57.3
S/N for angle loop, db	50.5
Received range code power, dbm	−131.3
S/N for range code, db	21.7

[a]The antenna gains are based on the assumption that the polarizations of the two antennas are matched.

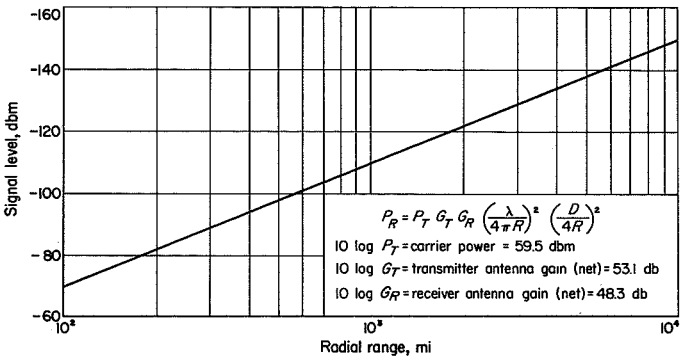

Figure 17. Expected signal levels for Project Echo

made in the local oscillator and the receiver front-end assembly. This tracking receiver in conjunction with a new 2388-mc antenna-tracking feed will provide an additional tracking capability for the Goldstone station.

A block diagram of the 2388-mc receiver front-end assembly is shown in Figure 18. Figure 19 is a photograph of the actual equipment as it will be mounted on the rear of the antenna reflector structure. The equipment includes the 2388-mc preselectors, balanced mixers, and IF preamplifiers for the reference, hour angle, and declination error channels. Local oscillator signals are derived from a single UHF frequency multiplier chain which multiplies the input signal from 147 to 2388 mc. A variable UHF attenuator is provided in the local oscillator channel to optimize the bias current supplied to the balanced mixer crystals. The output from the attenuator feeds a three-way power splitter which then supplies RF power to each balanced mixer through individual 16-db attenuator pads. The fixed attenuator pads are used to provide spurious signal isolation between mixers of at least 60 db. The 2388-mc front-end components are mounted in a weather-tight box. Provision has been included for monitoring the crystal bias currents in each of the three balanced mixers within the front-end box as well as remotely monitoring at the hydro-mechanical building.

Preliminary performance tests of the 2388-mc tracking receiver system have been conducted utilizing a closed-signal path. Noise figure measurements were made using a test setup similar to that described in *SPS 3* (p 32). The noise figure as a function of crystal bias current for each balanced mixer is shown in Figure 20. Sensitivity measurements were made recording AGC voltage as a function of input signal level to the reference channel. The signal level was varied over a range of approximately −55 to −140 dbm. The results are shown in Figure 21. An improved balanced mixer is being developed at JPL to replace the present 2388-mc mixers installed at Goldstone for the purpose of reducing the noise figure.

Table 4. Project Echo waveform equations for 2388 CW doppler radar system

① $\text{Cos}\ \omega_c t$

② $PN_1(t)$

③ $\text{Cos}\left\{5\,\omega_c t + \frac{M_P}{15} PN_1(t)\right\}$

④ $A_1\,\text{Cos}\,\{75\,\omega_c t + M_P PN_1(t)\}$

⑤ $A_1'\,\text{Cos}\,\{75\,(\omega_c t - \phi_c) + M_P PN_1(t - \tau_1)\}$

⑥ $A_2\,\text{Cos}\,\{75\,(\omega_c t - 2\phi_c) + M_P PN_1(t - \tau_2)\}$

⑦ $g_\Sigma(\alpha)\,A_2\,\{\text{Cos}\,75\,(\omega_c t - 2\phi_c) - M_P PN_1(t - \tau_2)\,\text{Sin}\,75\,(\omega_c t - 2\phi_c)\}$

⑧ $\text{Cos}\left[\left(75 - \frac{30}{32}\right)\omega_c t - 75\,(2\phi_c)^*\right] - M_P PN_1(t - \tau_2^*)$
$\times\,\sqsubset\text{os}\,(\omega_R t - \phi_R^*)\,\text{Sin}\left[\left(75 - \frac{30}{32}\right)\omega_c t - 75\,(2\phi_c)^*\right]$

⑨ $g_\Sigma(\alpha)\,A_2\,M_1(U)\,[1 + M_P^2\,\psi(\tau)\,\text{Cos}\,(\omega_R t - \phi_R)]$
$\times\,\text{Cos}\left\{\frac{30}{32}\,\omega_c t + 75\,[(2\phi_c)^* - (2\phi_c)]\right\}$

⑩ $\text{Cos}\,\frac{30}{32}\,\omega_c t$

⑪ $\text{Cos}\left(\frac{30}{32}\,\omega_c t + \omega_m t\right)$

⑫ $E\frac{A_2}{A_2^*}\,\text{Cos}\,\{\omega_m t - 75\,[(2\phi_c)^* - (2\phi_c)]\}$

⑬ $\text{Cos}\,\{\omega_m t - 75\,[(2\phi_c)^* - (2\phi_c)]\}$

⑭ $75\,[(2\phi_c)^* - (2\phi_c)]$

⑮ $\text{Cos}\left[\frac{1}{80}\left(75 - \frac{30}{32}\right)\omega_c t - \frac{75}{80}\,(2\phi_c)^*\right]$

⑯ $\text{Cos}\,\frac{75}{80}\,(2\phi_c)^*$

⑰ $U = \left[\frac{A_2^* - A_2}{A_2^*}\right]E$

⑱ $g_\Sigma(\alpha)\,A_2\,M_1(U)\,\text{Cos}\,75\,\{(2\phi_c)^* - (2\phi_c)\}\,[1 + M_P^2\,\psi(\tau)\,\text{Cos}\,(\omega_R t - \phi_R)]$

⑲ $E\frac{A_2}{A_2^*}\left[\frac{M_P^2\,\psi(\tau)}{1 + M_P^2\,\psi(\tau)\,\text{Cos}\,\omega_R t}\right]\text{Cos}\,(\omega_R t - \phi_R)$

⑳ $\text{Cos}\,(\omega_R t - \phi_R)$

㉑ $(\phi_R - \phi_R^*)$

㉒ $\text{Cos}\,(\omega_R t - \phi_R^*)$

㉓ $E\frac{A_2}{A_2^*}\left[\frac{M_P^2\,\psi(\tau)}{1 + M_P^2\,\psi(\tau)\,\text{Cos}\,\omega_R t}\right]$

㉔ $g_\Delta(\alpha)\,A_2\,\text{Cos}\,\{75\,(\omega_c t - 2\phi_c) + M_P PN_1(t - \tau_2)\}$

㉕ $g_\Delta(\alpha)\,A_2\,M_1(U)\,[1 + M_P^2\,\psi(\tau)\,\text{Cos}\,(\omega_R t - \phi_R)]$
$\times\,\text{Cos}\left\{\frac{30}{32}\,\omega_c t + 75\,[(2\phi_c)^* - (2\phi_c)]\right\}$

㉖ $\frac{g_\Delta(\alpha)}{g_\Sigma(\alpha)}\frac{A_2}{A_2^*}\frac{E}{\text{Cos}\,75\,\{(2\phi_c)^* - (2\phi_c)\}}\,\text{Cos}\,\{\omega_m t - 75\,[(2\phi_c)^* - (2\phi_c)]\}$

㉗ $E\frac{A_2}{A_2^*}\frac{g_\Delta(\alpha)}{g_\Sigma(\alpha)} \approx E\,g_\Delta'(0)\,\alpha$

A_1 = amplitude factor of the signal radiated from the transmitter antenna, volts
A_1' = amplitude factor of the signal incident on the satellite, volts
A_2 = amplitude factor of the signal at the receiver input, volts
c = velocity of propagation, meters/sec
E = dc reference in the receiver AGC loop, volts
$g_\Sigma(\alpha)$ = voltage pattern of the main-beam antenna normalized so that $g_\Sigma(0) = 1$
$g_\Delta(\alpha)$ = voltage pattern of the split-beam antenna normalized with respect to $g_\Sigma(0)$
$g_\Delta'(0)$ = slope of the $g_\Delta(\alpha)$ curves near $\alpha = 0$, mils^{-1}
$M_1(U)$ = voltage gain of the 30-mc IF amplifiers
$M_2(U)$ = voltage gain of the 455-kc and 497.5-kc IF amplifiers
M_P = phase modulation index of the range code modulator
$PN_1(t)$ = pseudonoise range code waveform
R = radial range to the satellite, meters
s = complex variable of frequency
t = time, seconds
U = AGC error signal, volts
α = tracking error of the antenna servo, mils
ϕ_c = doppler phase shift on ω_c, $= \frac{\omega_c}{c}\int_0^t \dot{R}\,dt$, radians
ϕ_R = doppler phase shift on ω_R, $= \frac{\omega_R}{c}\int_0^t \dot{R}\,dt$, radians
τ_1 = one-way time delay of the range code $PN_1(t)$, seconds
τ_2 = two-way time delay of the range code $PN_1(t)$, seconds
$\tau = \tau_2^* - \tau_2$
$\psi(\tau)$ = autocorrelation function of the pseudonoise
ω_c = angular frequency of the transmitter crystal oscillator
$= 2\pi$ (31.84 mc), radians/sec
ω_m = angular frequency of the 455-kc reference crystal oscillator
$= 2\pi$ (455 kc), radians/sec
ω_R = angular frequency of the range code clock, $= \omega_c/64$, radians/sec
$\frac{1}{A_2^*}$ = a measure of the voltage gain of the receiver so defined that the incoming signal A_2 multiplied by the receiver gain figure $1/A_2^*$ equals unity
$= \frac{G_\Sigma(\alpha)\,M_1(U)\,M_2(U)\,\{1 + M_P^2\,\psi(\tau)\,\text{Cos}\,(\omega_R t - \phi_R)\}\,\text{Cos}\,75\,\{(2\phi_c)^* - (2\phi_c)\}}{E}$
$\sqsubset\text{os}$ = expression for a square wave centered about the origin
$[\ ]^*$ = servo response to the quantity $[\ ]$
$\dot{x}$ = time derivative of the quantity x

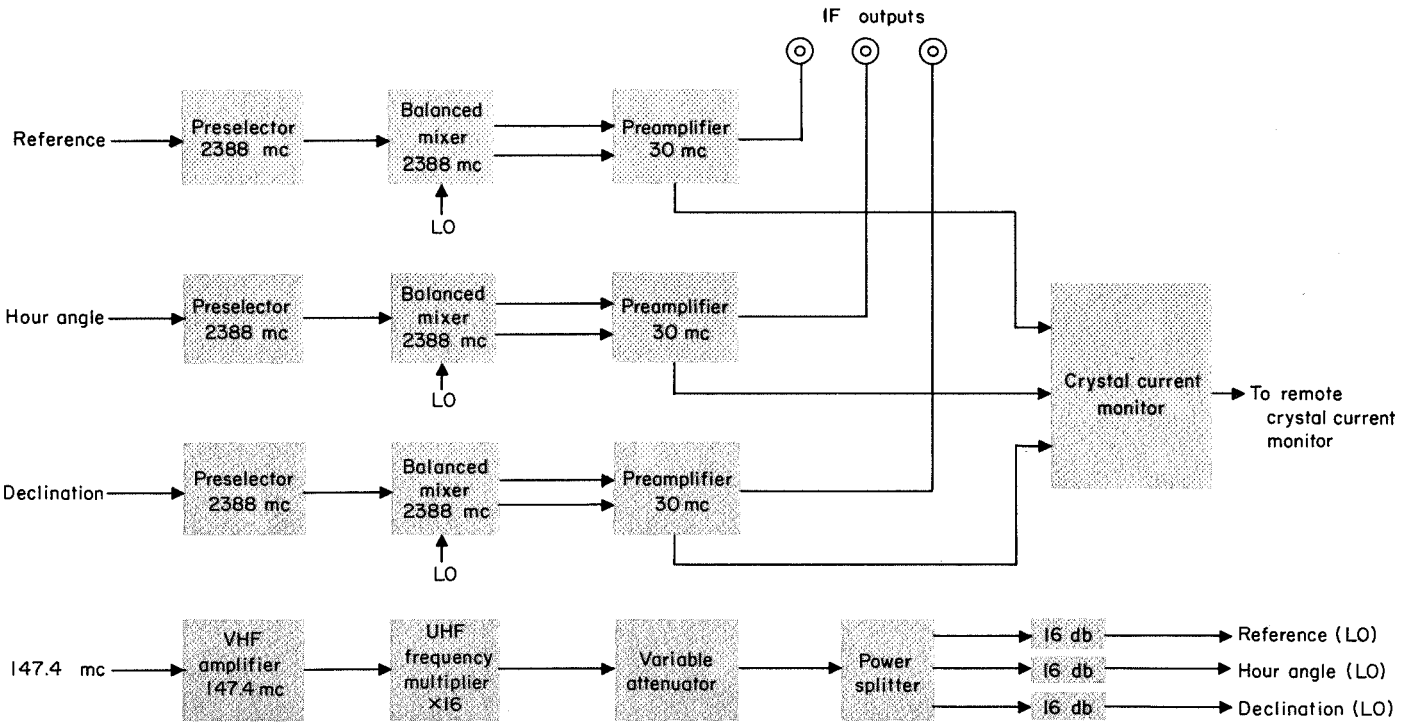

Figure 18. Block diagram of receiver front end

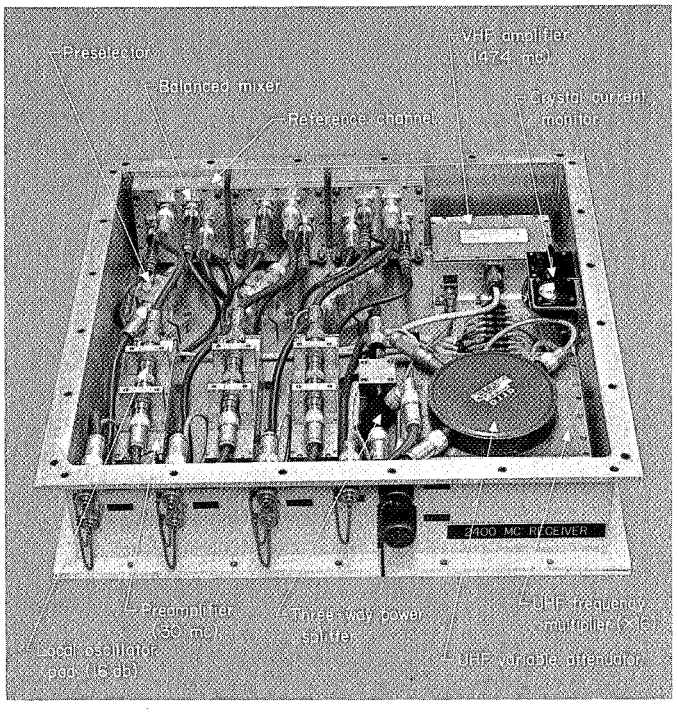

Figure 19. Receiver front end

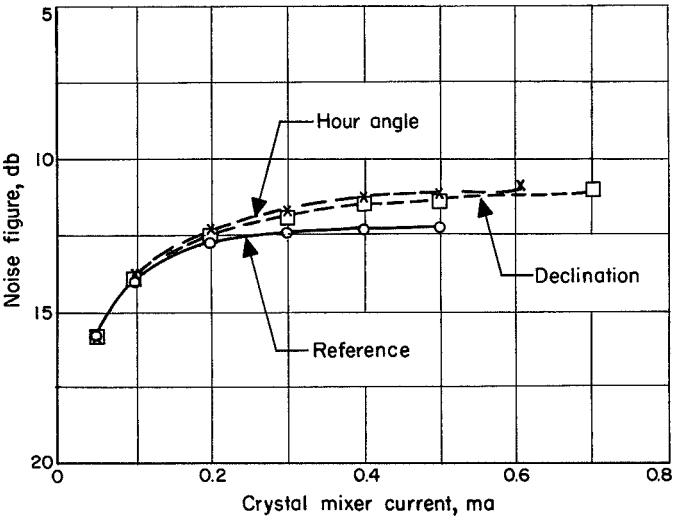

Figure 20. Noise figure vs crystal current

The gain tracking and differential phase-shift performance of the three-channel 2388-mc receiver was measured using a test setup similar to that described in *SPS 3*. The results of the gain tracking and differential phase-shift tests at 2388 mc are plotted in Figure 22. The differential gain tracking of the error channels relative to the reference channel remains constant within ±2 db over a signal level range of −60 to −125 dbm. The differential phase-shift in the error channels relative to the reference channel shows a maximum deviation of ±5 degrees over a signal level range of −55 to −125 dbm. However, at signal levels below −125 dbm, the declination channel differential phase-shift error increases rather abruptly to approximately 40 degrees and the gain tracking error of both channels increases to approximately 6 db at a signal

level of −140 dbm. The modules involved are being rechecked in an effort to determine the cause of gain tracking error and excessive phase-shift in the declination error channel.

2. Low-Noise Receiver (960 mc)

A low-noise 960-mc receiver has been developed and installed at the Goldstone tracking station. The receiver incorporates a parametric amplifier which operates in an up-converter mode as shown in the block diagram of Figure 23. The Varactor diode is pumped at a frequency of 9600 mc from a crystal-controlled source. In order to maintain a stable amplifier gain the pump power is regulated by means of a current-controlled ferrite attenuator, power monitor and feedback circuit. The amplified upper sideband signal at 10,560 mc is demodulated in an X-band balanced mixer. The X-band local oscillator signal is obtained by up-converting 930 to 10,530 mc in a second parametric amplifier channel which is pumped with the same 9600-mc source.

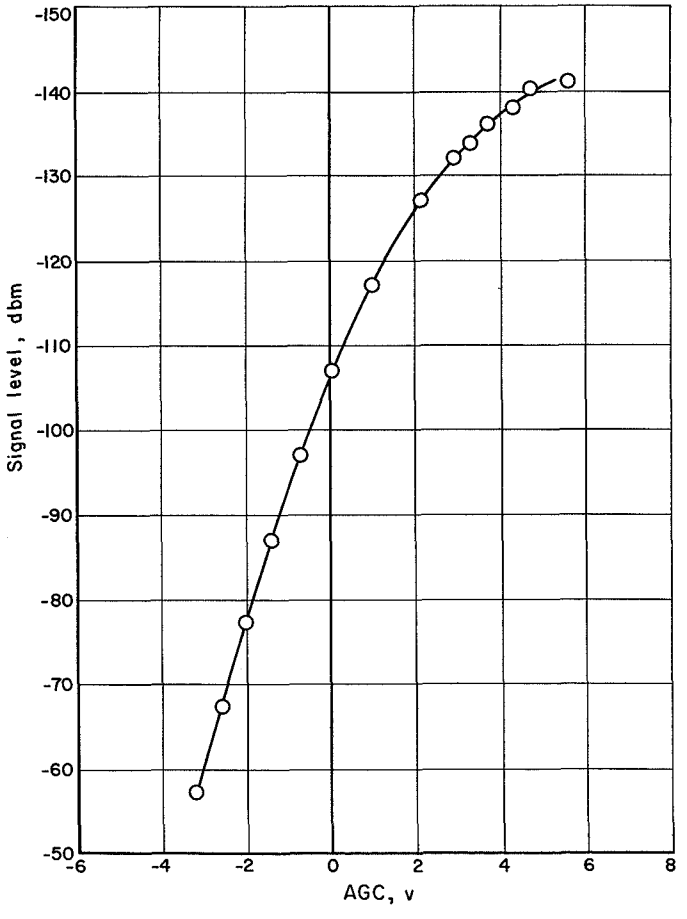

Figure 21. Receiver front-end performance

The X-band mixer noise figure measured 9.2 db. The theoretical maximum gain of the upper-sideband amplifier is 10,560/960 or 11 times (10.42 db). If the assumption were made that the Varactor alone had a 1.0-db noise figure, then the theoretical overall figure would be 2.84 db with 10.42-db gain. In order to take advantage of the low noise figure of the Varactor, more gain is necessary to override the relatively noisy X-band mixer. The tuning controls were adjusted in such a manner as to permit the lower sideband, as well as the upper sideband, to exist and enter into the operation of the up-converter. Significantly higher conversion gains were realized by this means.

The parametric amplifier has been installed in a new electronics cage assembled on the rear structure of the Goldstone receiving antenna. A photograph of the installed amplifier assembly is shown in Figure 24. The interiors of the amplifier and pump assemblies are shown in Figures 25 and 26, respectively.

The noise figure of the receiver referred to the input jack of the parametric amplifier box was measured to be 2.3 db at an optimum pump drive of 22 dbm on the Varactor element. The total attenuation of the components between the input jack and the Varactor element was measured to be 1.2 db. These components are the directional coupler, the preselector cavities, the circulator

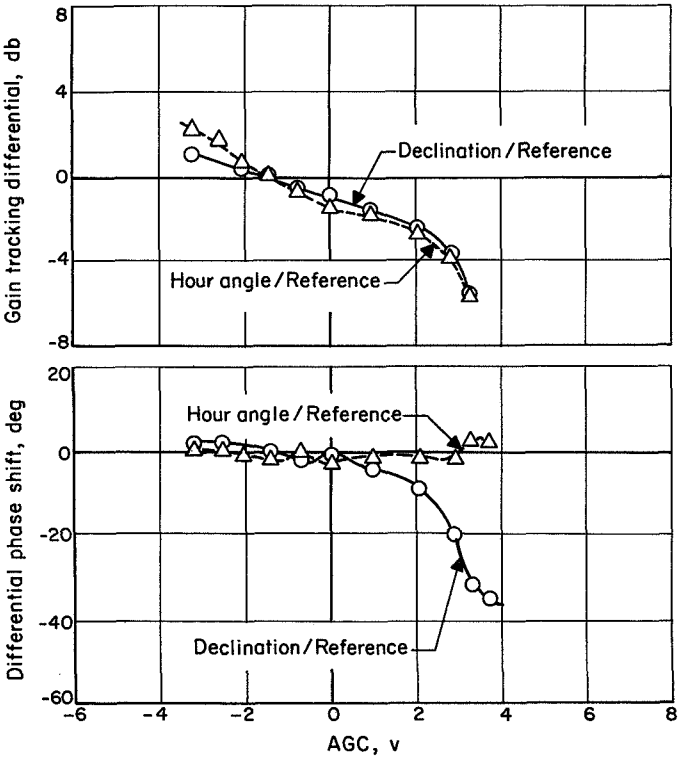

Figure 22. Received differential phase and gain tracking

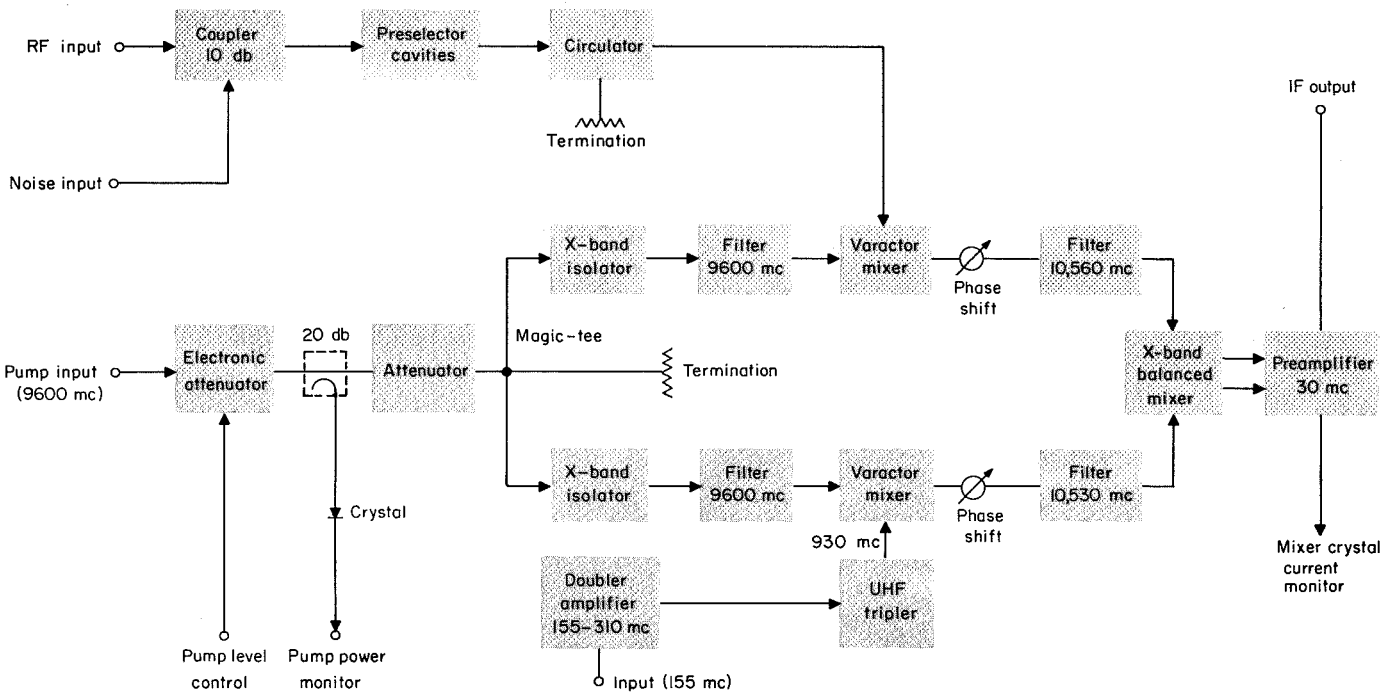

Figure 23. Low-noise RF amplifier, 960 mc

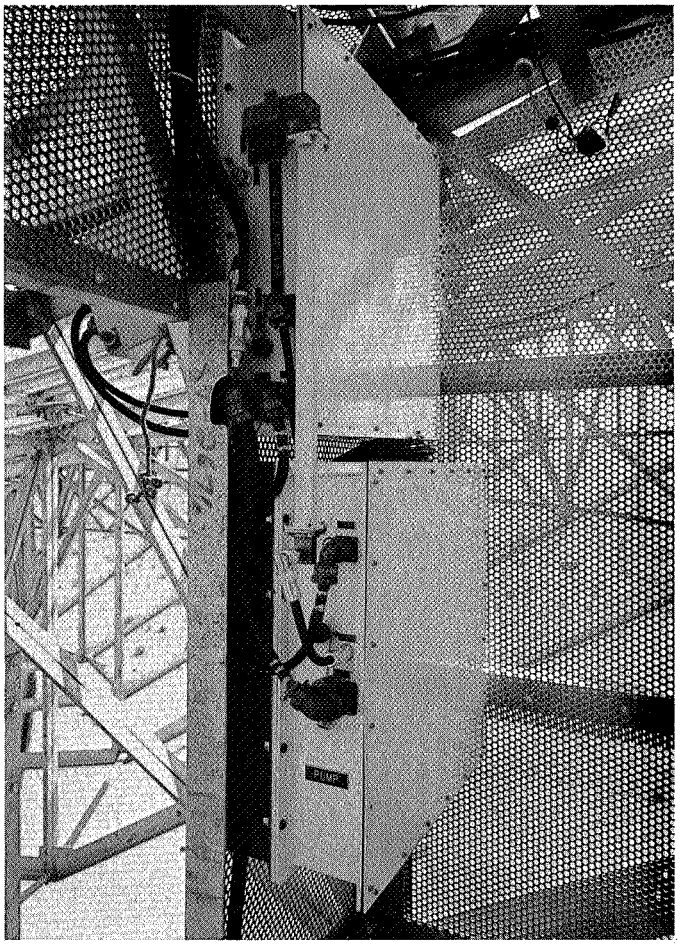

Figure 24. Low-noise amplifier installation

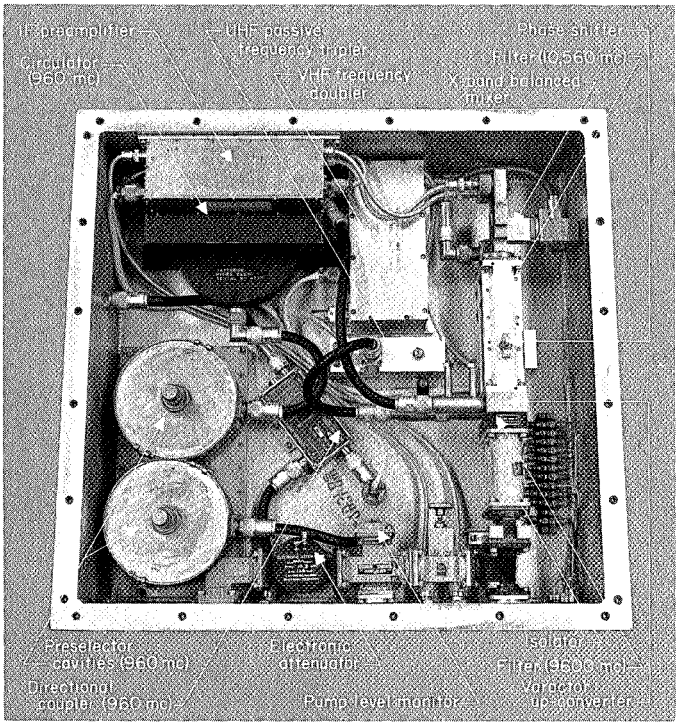

Figure 25. Low-noise amplifier

and the interconnecting coaxial cables. The indicated minimum noise figure referred to the Varactor was therefore 1.1 db. The 3-db bandwidth measured through the 30-mc IF amplifier was 0.4 mc. The variation of conversion gain with pump level is also plotted in Figure 27.

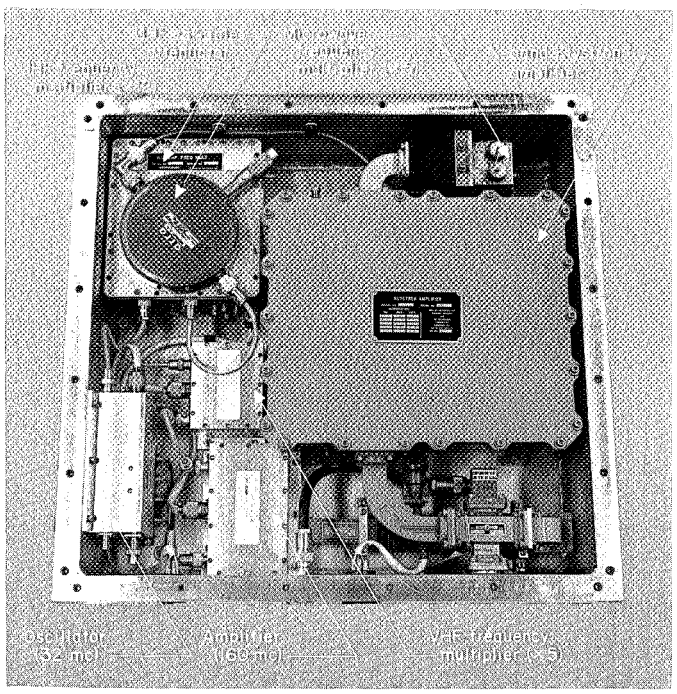

Figure 26. Pump assembly

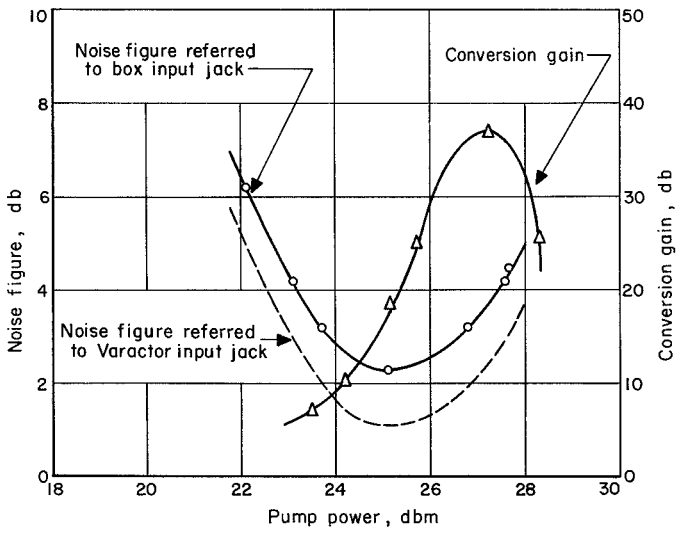

Figure 27. Noise figure and conversion gain vs pump level

The automatic gain control (AGC) voltage of the 960-mc receiver was measured as a function of the input signal levels using a closed signal path between the RF signal generator and the input to the parametric amplifier (Fig 28). Due to spurious RF leakage, usually encountered during closed path tests of this type, an accurate measurement of the receiver threshold could not be made. The threshold of the receiving system will be measured following the installation and calibration of a new 960-mc antenna feed and low-loss transmission line.

The feasibility of operating the parametric amplifier without the 10-db directional coupler for noise insertion and the 960-mc preselector cavities will be determined at a future date. The attenuation associated with these two components is 0.7 db; if the system can be operated successfully without them, the receiver noise figure will be 1.6 db.

3. Angle Encoding

Description and functional specifications for the angle encoding systems to be installed on the Goldstone antennas were given in *SPS 5*.

The encoding system consists of three angle-encoding discs for each angle measured, which convert 360 degrees of angular rotation into 180,000 digitally coded increments. These discs are sampled at time increments controlled by the sample-rate selector; the code number is stored by digital circuits included in the code converter.

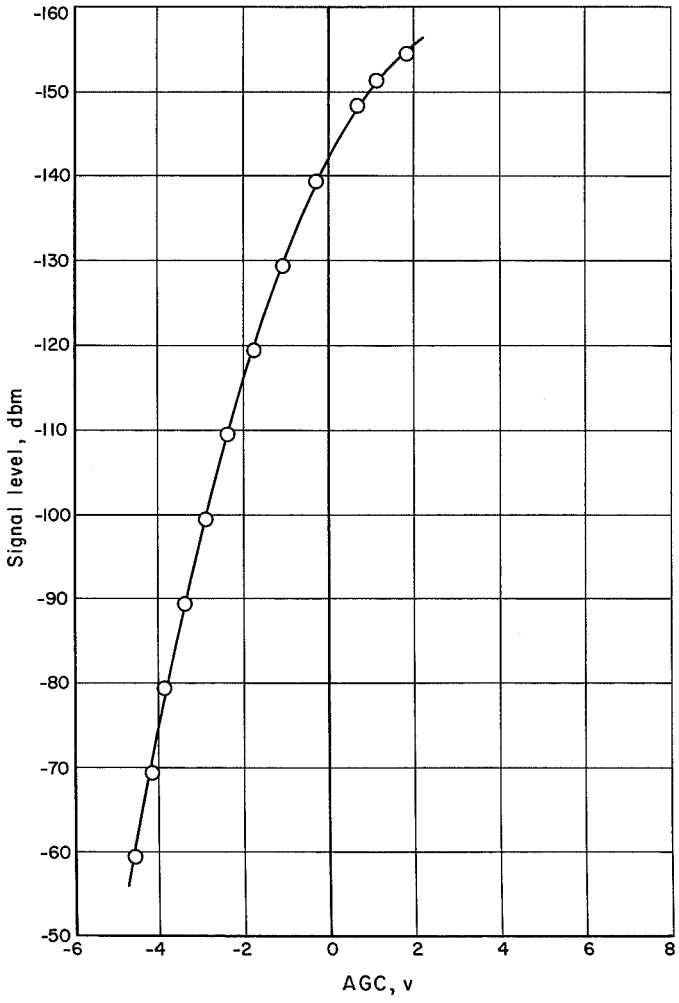

Figure 28. Receiver gain performance

Because the BCD code can lead to ambiguities in the readout of the code discs, a special cyclic-decimal code is used in the encoder and code conversion is used to obtain the BCD code required by the data commutator. Two separate systems are used to read the two antenna angles and both are sampled simultaneously.

Design and fabrication of the encoding equipment is proceeding in accordance with these specifications and is on schedule. Photo engraving of the encoding discs has been completed; assembly and wiring of the encoding logic and the servo followup units have been initiated. It is therefore anticipated that the scheduled installation of the angular encoding system will begin during the first week of December, 1959.

The following accuracy test will be made at the Datex Corporation (manufacturers of the angular encoding systems) with JPL participation. Some of the tests will be repeated on portions of the angular encoding systems at JPL. Input shaft angular measurements will be made by a calibrated indexing head at Datex. JPL will employ a T-3 Wild theodolite and a pseudo-collimation technique to determine input shaft angles.

The accuracy tests to be performed on all the angular encoding systems are:

(1) The input shaft of the multipoled synchro-resolver (sensor of antenna axis rotation) will be positioned throughout 360 degrees to provide a minimum of 100 output counts (in equal increments) for each encoder disc assembly and its associated servo followup drive.

(2) The difference between the angle represented by each count (at the transition from the next lower count to the count in question) and the angle position of the input shaft will be determined.

(3) Input shaft angles will be measured with a device having an absolute accuracy of 2 seconds of arc or better. A calibrated indexing head or a T-3 Wild theodolite will be used to meet this requirement.

(4) Steps (1) through (3) will be used to calculate the sample mean and the rms errors from these equations:

$$X^* = \frac{1}{n}\sum_{K=1}^{n}(X_{KS} - X_K)$$

$$D^* = \left(\frac{1}{n}\sum_{K=1}^{n}[X^* - (X_{KS} - X_K)]^2\right)^{1/2}$$

where

X^* = sample mean error

X_{KS} = kth reading of angle represented by encoder output count

X_K = kth reading of the angular position of input shaft of multipoled synchro-resolver

D^* = rms error about the sample mean

n = 100 or greater

(5) Tests (1) through (4) will be repeated for each disc assembly separately.

(6) The angular position of the input shaft of the encoder assembly will be measured in the same manner as prescribed for the multipoled synchro-resolver. This measurement will be referenced to the antenna axis assuming ideal coupling and ideal gearing such that:

$$X_K = 90X_{K_e} \text{ for decimal encoding}$$

$$X_K = 128X_{K_e} \text{ for binary encoding}$$

where X_{K_e} = kth reading of the angular position of the encoder disc assembly.

A test fixture is being modified at JPL to mate a T-3 Wild theodolite with either of the two types of encoding disc assemblies or the multipoled and single-poled synchro-resolver assemblies. To optically test the accuracy of the Thomas flexible couplers to be used to engage the sensor with the antenna axis, a second test fixture is being designed. Accuracy tests will be performed for various angular and lateral misalinements and longitudinal offsets.

4. Coordinate Computer

The digital computing equipment to be described is being generated for installation at the Goldstone tracking site. The purpose of the computer is to perform coordinate transformations necessary to the simultaneous positioning and tracking of the two spatially separated antennas at the Goldstone facility. The general organization of the system required to execute the control of the antennas and the modes of control to be provided were previously described in *SPS 5*.

The digital equipment is being developed by the Computer Control Company (CCC) in accordance with JPL requirements and specifications. Standard CCC static and dynamic logic circuit modules are being used to mechanize the computing system. Digital operations are performed at a 1-mc clock rate. Memory is obtained by the use of magnetostrictive delay lines.

A block diagram of the computer equipment is shown in Figure 29. The major sections of the computer are the arithmetic, the memory, the control, and the timing units.

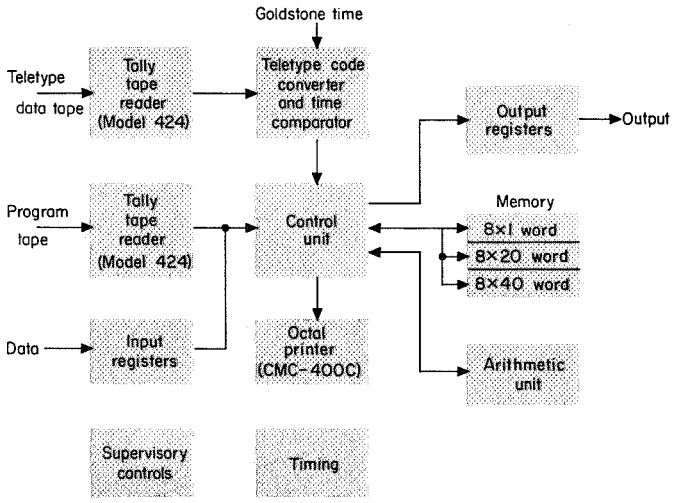

Figure 29. Coordinate converter computer

Additional equipment is required for the conversion of the teletype data, the insertion of data, supervisory control and monitoring of computer performance. The digital predictor and comparator equipment utilizes the output information of the computer.

a. Arithmetic unit. The arithmetic unit contains the circuitry necessary to perform the operations of addition, subtraction and multiplication. This unit consists of a serial accumulator, multiplicand and multiplier register, registers for product overflow and carry propagation, and circuits for control and complementing. Subtraction is performed by using the 2's complement for representation of negative numbers.

b. Memory section. The memory section of the computer consists of magnetostrictive delay lines. There are three types of memories used. There are eight 1-word quick access lines, eight 20-word data lines and eight 40-word order lines. A word consists of 25 bits and is 25 microseconds long. There are two types of words. The data word consists of a sign bit and the additional bits for expression of the data magnitude. The order word structure is shown in Figure 30. To permit more command operations, micro-programming has been incorporated into the order word.

c. Control unit. The control unit of the computer provides the control of computer by the proper channeling and execution of data and commands. This unit contains the comparison circuits, registers, and the logic circuits required to interpret the order words, to modify the course of action by index registers, and to provide the control signals for the arithmetic unit and address selection circuits.

Operations occur serially and synchronously under control of signals obtained from the timing unit. The basic clock is a 1-mc oscillator which will be synchronized to the Goldstone 1-mc signal. Other timing signals for recognition of the beginning of words and the start of data in the memory units are provided to the computer.

Additional computer circuitry is needed to insert and remove the data, to provide mode control and to insure monitoring and supervisory control. Angle position data, range, and time will be taken in at the site in standard 60 wpm teletype code and tape recorded. Angle data will be decimal numbers in increments of 0.002 degree. The teletype tape information will then be converted to binary-coded decimal. Angle data will be further converted to serial binary and scaled to binary circle information in the computer arithmetic unit. The angle information is processed through the computer in this representation. Data from the antenna angular encoders is also presented in binary circle readings. This representation appears particularly suited to the sensing of zero crossover of angles and in performing the subsequent arithmetic operations.

Control data from the computing center will be inserted into the computer through a *tally* tape reader. The program will be permanently stored on tape and will be read into the computer at the beginning of a day's activity by the use of another tally reader. This information will be stored in the 40-word memory section. The program code will be one which will permit the preparation of programs from Flexowriters. The computer memory will be safeguarded against transient power failures by coupling standby battery power across the computer's primary dc supply.

The logical design of the computer is nearly completed. Construction is well advanced. Including the digital servo predictor and comparator, a total of five 7-foot racks of equipment is involved. Four of these will be located in

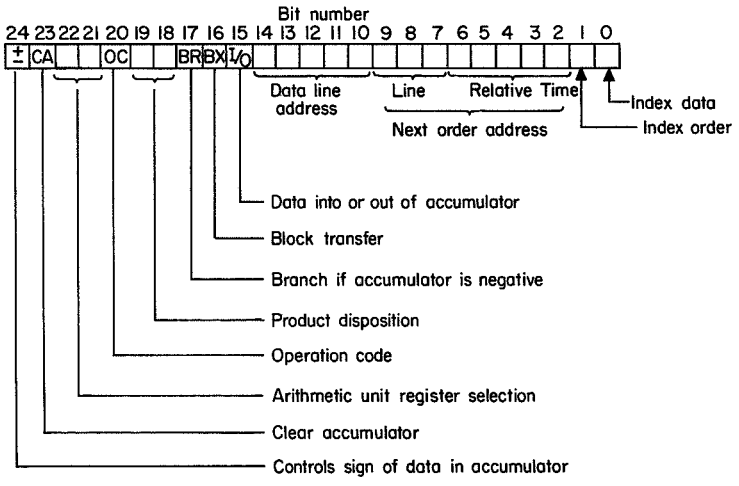

Figure 30. Order word structure

the main control building at the present hour angle-declination (Ha-Dec) antenna site. The remaining rack will be located in the new azimuth-elevation (Az-El) antenna control building some 7 miles removed from the Ha-Dec site. Transmission of position control data between the two sites will be achieved through a two-way microwave radio link which is scheduled to become operational prior to 1 January 1960.

Functional testing of computer subsystems is currently in progress. The digital predictor and comparator design has been completed and one unit has been tested at JPL with an analog simulation of the Ha-Dec antenna. System testing of the equipment at the contractor facilities will begin in the near future. Installation of the equipment at Goldstone is expected to begin during the first week of December 1959.

5. Digital Predictor and Comparator

Evaluation of the digital predictor and comparator system was accomplished through the hybrid simulation of the Goldstone antenna digital servosystem on the analog computer. Simulation of a single axis of the receiver antenna in the high-speed mode was considered sufficient to evaluate system performance. The effected simulation is indicated in Figure 31.

The Datex antenna position encoding was simulated with the Datrac analog to digital converter. The compatibility of the Datrac and the CCC equipment was accomplished by a simple buffer. The Datrac was operated on a ± 100 volt range and the 10 binary digits in the Datrac were used for inputs to the least significant 10 digits of the comparator. This arrangement resulted in a gain through the digital system of less than one, which was compensated for in the differential analyzer. (The transfer function of the comparator with the Datex encoders will be 4 v/0.17 deg.)

The 10 binary place capacity of the Datrac was at first thought to be a disadvantage; however, the analog computer noise really established the limit on useful binary places in the encoding. The range of the analog computer extends from the noise level to 100 volts. Assuming a noise level of 5 millivolts, this would yield a range of 20×10^3 which corresponds to a binary range in excess of 10 places. However, the noise level in the analog computer with the digital equipment running was more like 100 millivolts which necessitated elimination of the tenth or least significant place to reduce jitter out of the Datrac. The open loop transfer function of the receiver antenna

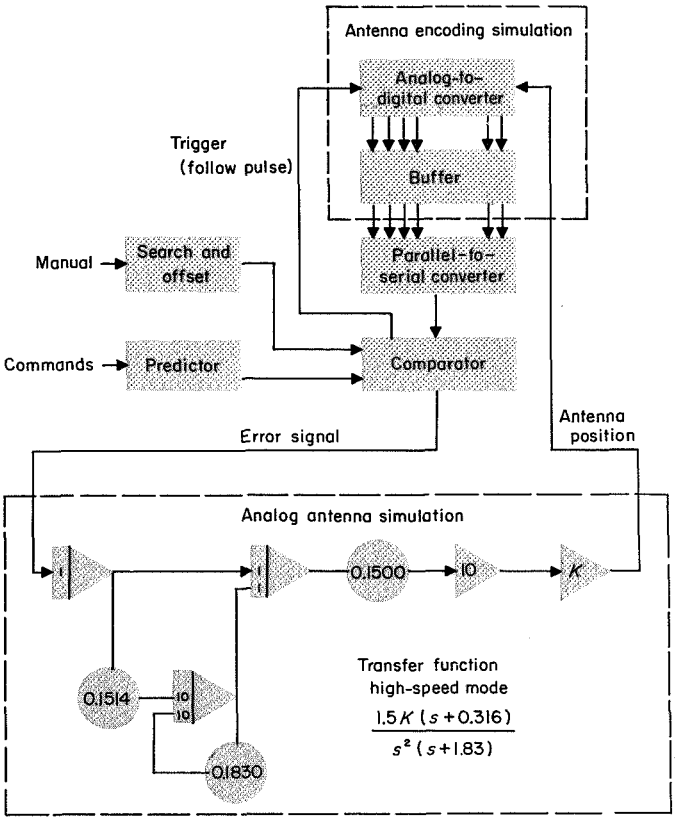

Figure 31. Digital servo and antenna simulation

was simulated on the differential analyzer. One of the actual digital servo units to be used at Goldstone was provided by CCC for the test.

The response of the digital system to steps and search patterns at the search pattern input to the comparator is presented in Figure 32. A plot of the response of the analog system is also presented for comparison. It may be seen by the step response of the two systems that introduction of the digital comparator has made no appreciable change in the damping or the roots of the system. The response to search ramps, holds, and steps is also seen to be well behaved.

An attempt to check the pointing command channel of the digital equipment by driving it with the search pattern generator led to some interesting results. The command channel includes a predictor which operates on data one sample time old to generate a ramp approach to next point. This prediction scheme corresponds to the first-order hold of sampled data theory and as such does not respond well to inputs whose first derivatives are discontinuous. The system response of the command channel to step and ramp inputs is presented in Figure 33. This will not be a problem in operation, however, since command signals will always have continuous first derivatives.

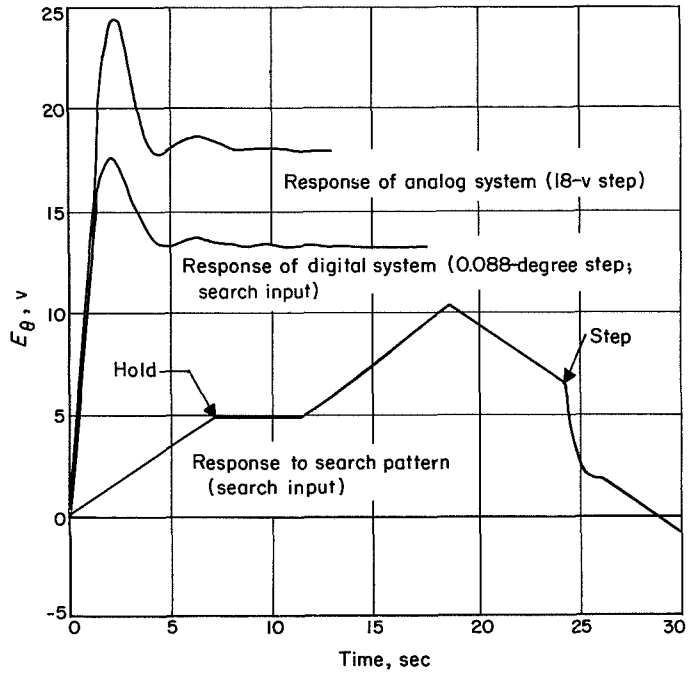

Figure 32. Simulated antenna response curves

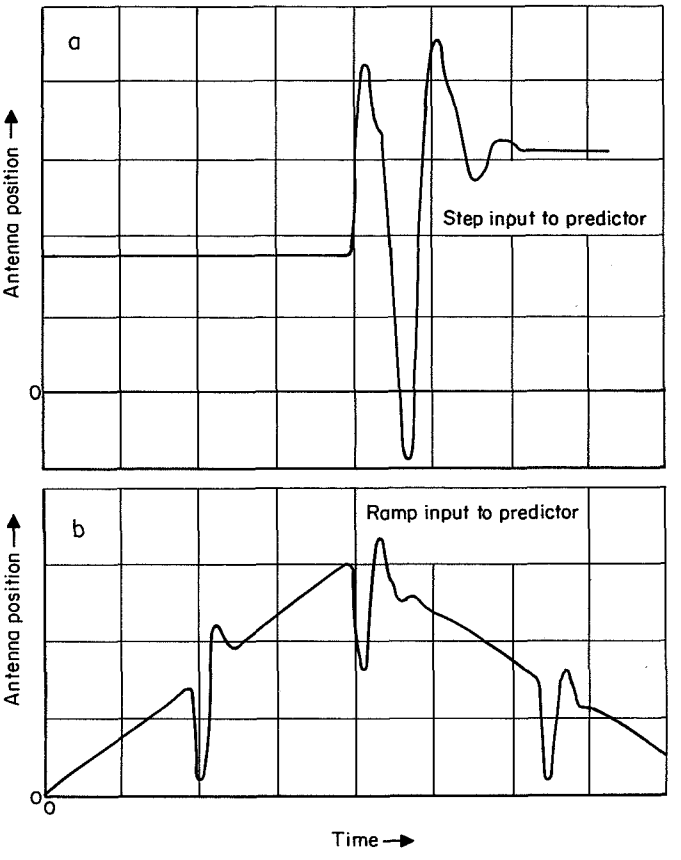

Figure 33. Antenna response

6. *Tracking Data Handling*

The data handling system for Goldstone Site B was described briefly in *SPS 5* and that description will be expanded here to include the various subsystems which form the complete data system.

The block diagram for the complete system is shown in Figure 34 to indicate the interconnections between the various subsystems.

a. System capabilities. The data system will initially have the capabilities of recording the following:

(1) Time, Greenwich Mean Time: 6 decimal digits—00:00:00 to 23:59:59 in hours, minutes and seconds.
(2) Azimuth angle: 0 to 360 degrees in 6 decimal digits with a resolution of 0.002 degree.
(3) Elevation angle: 0 to 360 degrees in 6 decimal digits with a resolution of 0.002 degree.
(4) Program and station identification: 10 decimal digits in any combination.
(5) Teletype commands: carriage return, line feed, figures, space, and period, in any combination as required to produce the desired data readout on teletype machines.

The system will initially be set up to handle those inputs indicated, which totals to 28 teletype characters (1 character per decimal digit or teletype command), but will be capable of expansion to 60 characters of recorded information as new data inputs are required, with minor additions to the system. By slight modification, the capacity can be increased to 100 characters, but this is not desirable with the present teletype transmission capabilities. The teletype tape format is shown in Figure 35.

The present teletype transmission system can only transmit data at the rate of 60 teletype wpm (6 characters per second), which is 1/10 the speed at which it can be recorded. Because of this limitation, data samples of 60 characters in length require a 10-second transmission time and sampling intervals of less than one sample per 10 seconds will cause a buildup of untransmitted tape. This buildup of tape cannot be readily handled if the recording period is of extended length. Increasing the number of characters to something greater than the 60 per sample would also cause a tape buildup and would require the sample rate to be reduced to 1 sample per 20 seconds (next slower rate) to prevent this. A slower sampling rate is not desirable for most trajectory computations.

If the teletype transmission system is converted to a 100 wpm (10 characters per second) capability, the data system capacity could be increased to the 100 characters and still maintain the 1 sample per 10 second recording rate.

b. Timing system. To coordinate the data generated at Site B with data generated at other sites, a time label

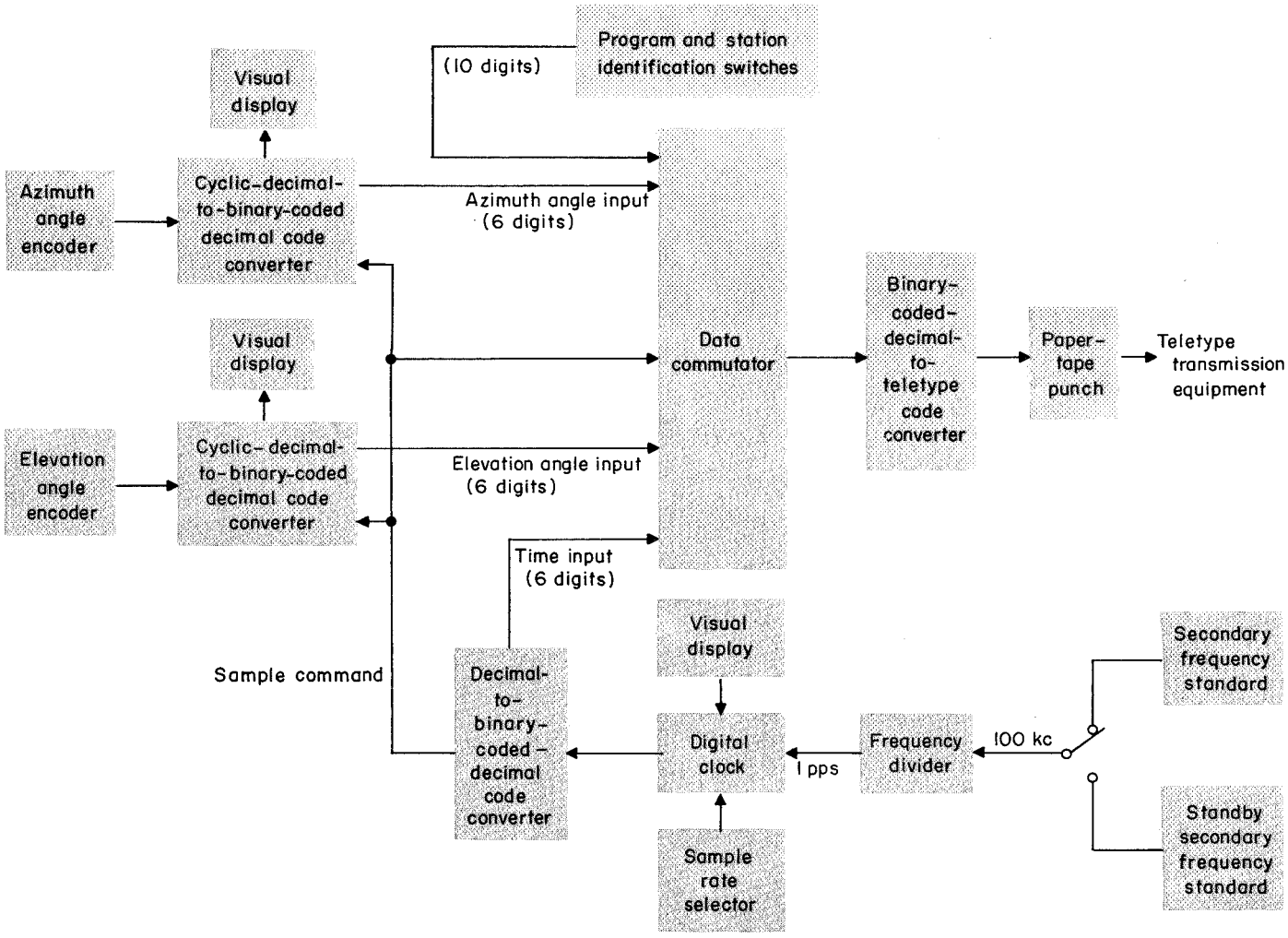

Figure 34. Data handling system

must be applied to each data point, which indicates the time at which the point was taken in Greenwich Mean Time. This timing information is generated at each site and is required to be synchronized with the timing at other tracking sites to less than 10 milliseconds time difference, with 1 millisecond time difference desirable, when all stations are referenced to WWV radio transmissions.

To obtain the time information, a secondary frequency standard is used as the basic time reference from which a 100-kc signal is obtained. This unit is a James Knight (FS-1100 T) precision reference oscillator which operates at a frequency of 1 mc with a frequency stability of 5 cycles in 10^{10} cycles per day. An internal regenerative frequency divider divides this basic frequency by a factor of 10 to produce the 100-kc signal used by the timing system. The timing system is shown in Figure 36.

To derive the 1 pulse per second (pps) required by the digital clock, five digital frequency dividers are used to divide the 100-kc frequency in five decade steps. These dividers are a ring-counter type which will be explained as part of the sample rate selector. To allow the 1 pps to be shifted in time for synchronization with WWV, an add-delete circuit is included which can add pulses into the second, third or fourth decades to advance the 1 pps pulse in time, or delete pulses in the second decade to retard the 1 pps pulse. The addition of pulses to the third and fourth decades allows rapid advance of the pulse to the desired time and the addition or deletion of pulses to the second decade allows a fine setting. Table 5 lists the rates at which the 1 pps pulse can be advanced or retarded.

Table 5. Stepping rates

Switch position	Advance, msec/sec	Retard, msec/sec	Increments, msec/sec
Fast	100	—	10
Medium	10	—	1
Slow	1	1	0.1

The procedure for synchronizing the time and correcting the oscillator frequency has been described in *SRS 2*. Because the calibration procedure for the oscillator requires several days of uninterrupted operation of the oscillator and the frequency divider unit, these units will be operated from a power supply having a floating battery. In case of primary power failure, the battery will function as the power source for a period up to 48 hours, to insure normal oscillator operation and prevent loss of system calibration.

To prevent a malfunction in the primary oscillator from destroying the timing system accuracy for extended periods of time, a standby oscillator (Collins 40K1) having a stability of 1 part in 10^8 is maintained as an operating spare and can assume operation as the frequency source until the primary oscillator is stabilized and adjusted again.

The digital clock contains additional digital frequency dividers which divide the 1 pps by the appropriate count

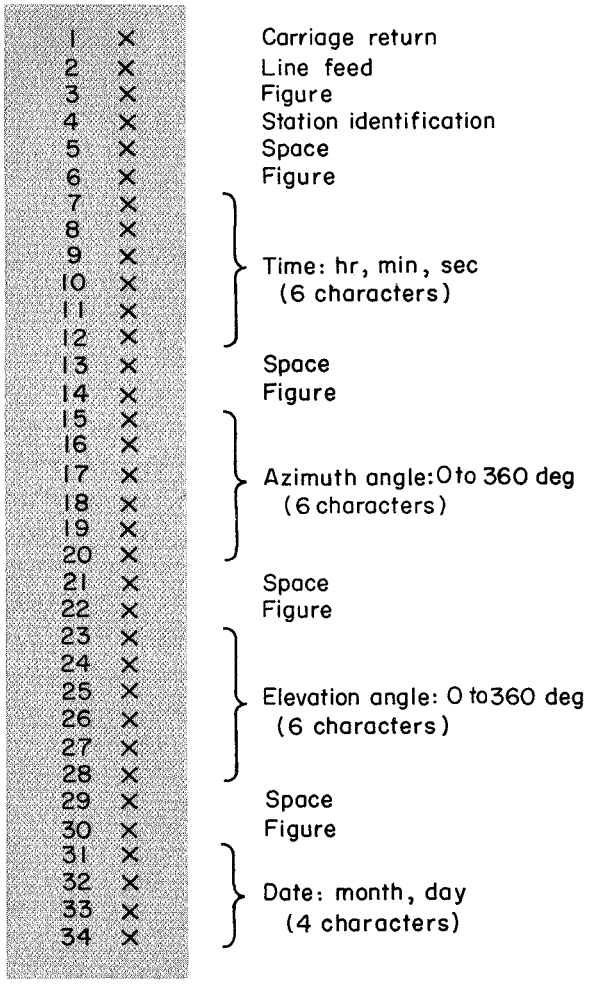

Figure 35. Teletype tape format

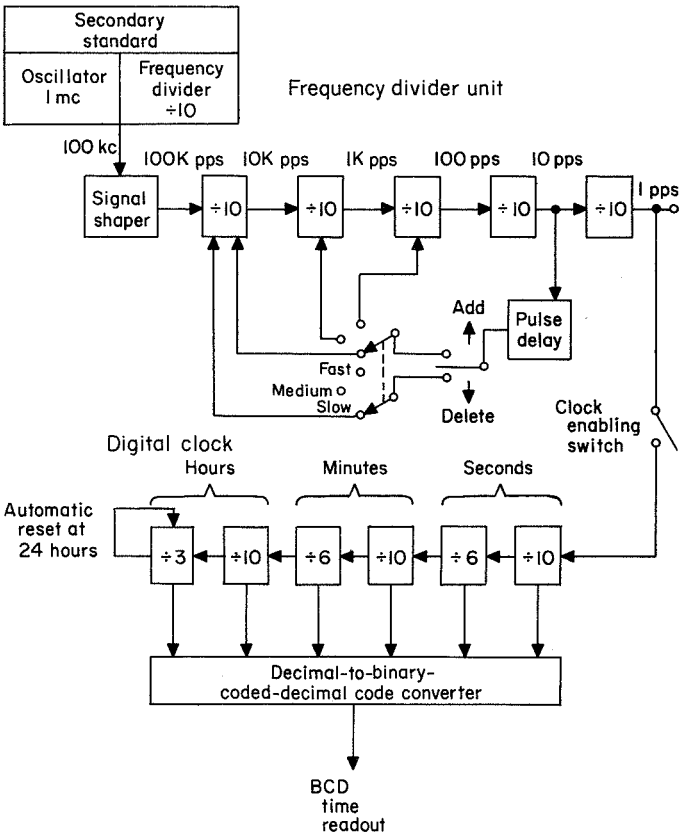

Figure 36. Timing system

to produce a time readout in hours, minutes, and seconds. These dividers contain manual controls for setting the clock to the desired time and a clock enabling switch to start the clock at the proper time. To allow recycling of the clock to 00 hours at the 24th hour, an automatic reset circuit is included in the hours decades to sense 24 hours and reset these dividers to zero. Because the data commutator requires a binary-coded-decimal (BCD) input and the clocks produce a decimal output, the clock is connected to the data commutator through a code converter.

c. Sample rate selector. The sample rate selection circuit allows the time interval between data points to be selected as indicated in Table 6 and is controlled by the digital clock.

Table 6. Selector sample rates

Time interval	Increments
1 to 9 seconds	1 second
10 to 90 seconds	10 seconds
1 to 9 minutes	1 minute
10 to 90 minutes	10 minutes

Figure 37 shows the circuit by which these intervals can be selected. The coarse control selects the clock output signal to be counted by the ring counter and sets the basic increment of time that can be selected. The fine control adjusts the number of increments between each sample by selecting the proper output from ring counter. This output serves to command the angle sampling circuits and to start the data commutation cycle for recording.

The ring counter operates by advancing one count for each input (advance) pulse until the selected count is reached. At the selected count an output pulse is produced and this pulse after a short delay resets the counter to zero and starts a new cycle.

d. Program and station identification. A program and station identification unit provides a means of inserting identification data into the recorded data as required. This unit consists of 10 selector switches, each of which can be set in any one of 10 positions. These switches then encode the inserted number into the BCD code and this information is recorded along with the angle and time information. Quantities such as program number, station identification number, and date can be manually selected for recording.

e. Data commutator. The data commutator is used in the system to convert all the data, which is available in a parallel form, to a serial form for punching on paper tape, since the tape punch is capable of punching only one character at a time.

Figure 38 shows the block diagram of the data commutator. When a sample command is received, the control gate is opened and the ring counters proceed to count

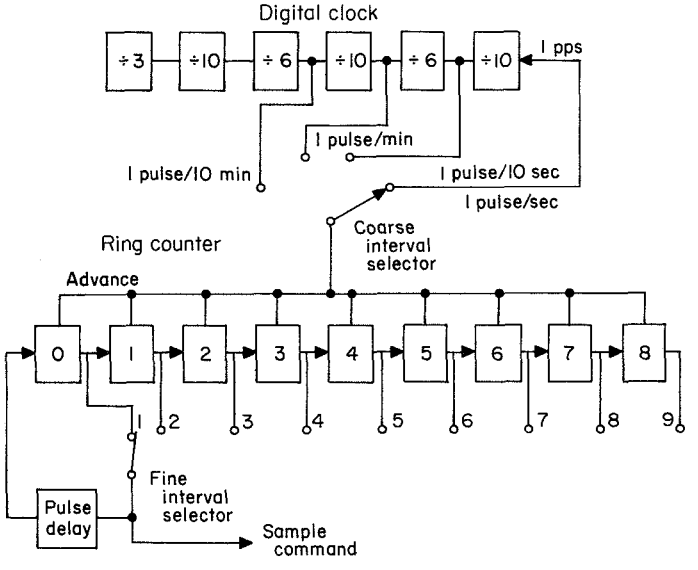

Figure 37. Sample rate selector

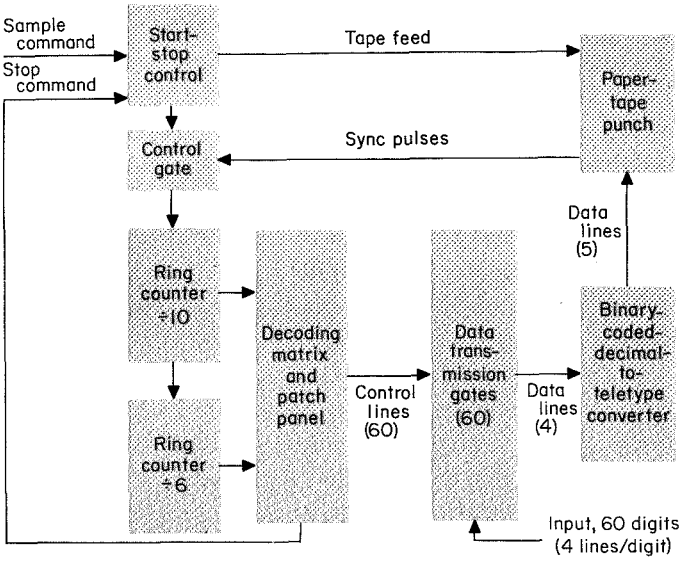

Figure 38. Data commutator

the sync pulses. A sync pulse is generated by the punch at the completion of each punching cycle. As the ring counter counts the sync pulses, the decoding matrix decodes the count that is stored in the counter and one output line of the 60 output lines from the matrix will be energized for each count. As each line is energized, a data transmission gate is opened and the BCD digit associated with that gate is allowed to pass to the code converter and on to the punch for punching. When all the digits have been punched, a stop command is generated, which closes the control gate and resets the counter in preparation for the next recording cycle.

To allow flexibility, a patch panel is included as part of the decoding matrix to allow the 60 output lines to the transmission gates to be energized in any order desired, and to generate the stop command after any number of characters are punched, up to the maximum of 60 characters. The patch panel also contains provisions for inserting special teletype characters required by the teletype machines to give the proper data readout. These special characters can be inserted at any point in the punching cycle to command the teletype machines as desired.

A code converter is inserted before the punch to convert the data into the standard commercial teletype code for punching. This code is not required for teletype transmission, but is desirable because commercial teletype machines will give a printed copy of the data and any other code would require special machines.

f. Paper-tape punch. The paper-tape punch is a mechanically operated unit capable of punching 60 characters per second. The unit is driven by a 3600 rpm motor and a punching cycle occurs for every revolution of the motor.

The punching operation and the paper-tape feed are controlled by relays which are actuated by the information coming from the data commutator. During operation, the feed control relay is energized by the start-stop control in the commutator and advances the tape after each punching operation until a stop command is received. The code relays cause a hole to be punched in the tape for each relay that is energized and any combination of five holes can be punched in one punch cycle.

7. Antenna Structure

Recent activities at the Goldstone tracking facility, on or in support of the antenna structures investigations encompassed the following activities:

a. Polar shaft bearing radial movement measurements. On 23 September 1959 and 22 October 1959 measurements were made of the polar shaft bearing radial movement of the receiving antenna. Tests were run with the dish at various declinations through the complete hour angle traverse. Figure 39 shows typical results of these tests. The entire results indicate that at no time does the total excursion of the bearing movement exceed 0.011 inch and in the general tracking area is in the neighborhood of 0.006 inch.

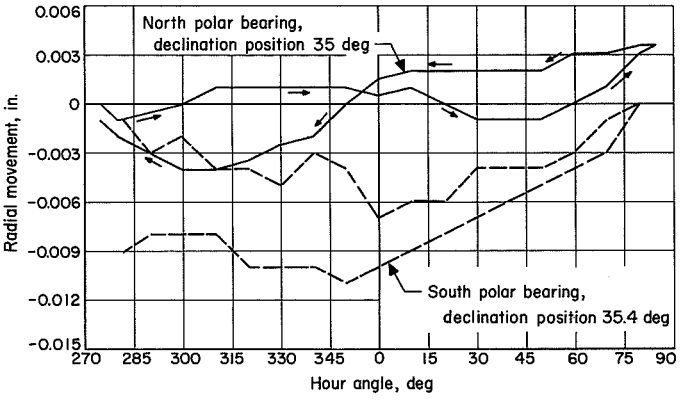

Figure 39. Antenna polar bearing radial movement

b. Optical star track data. Figures 40 and 41 are representative of the results of the reduced star track data for the period 7 August 1959 through 10 October 1959. This

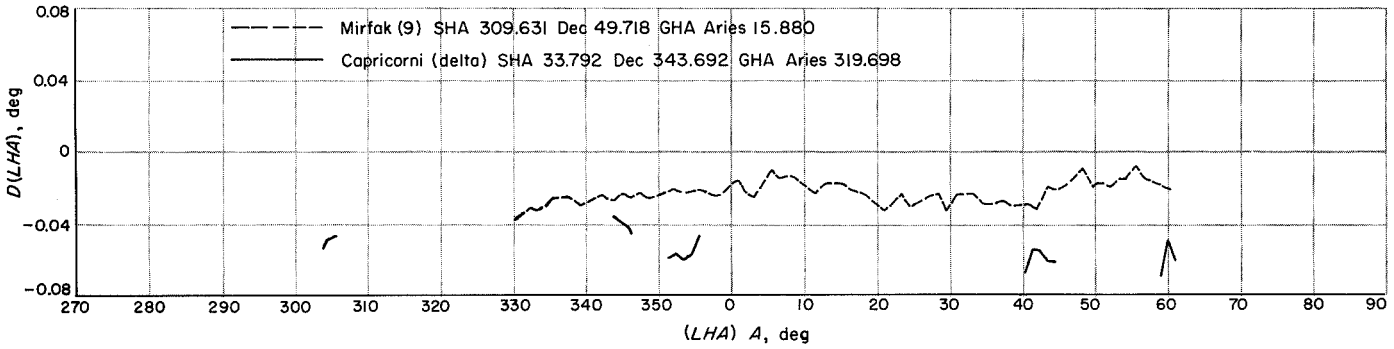

Figure 40. Goldstone star tracks

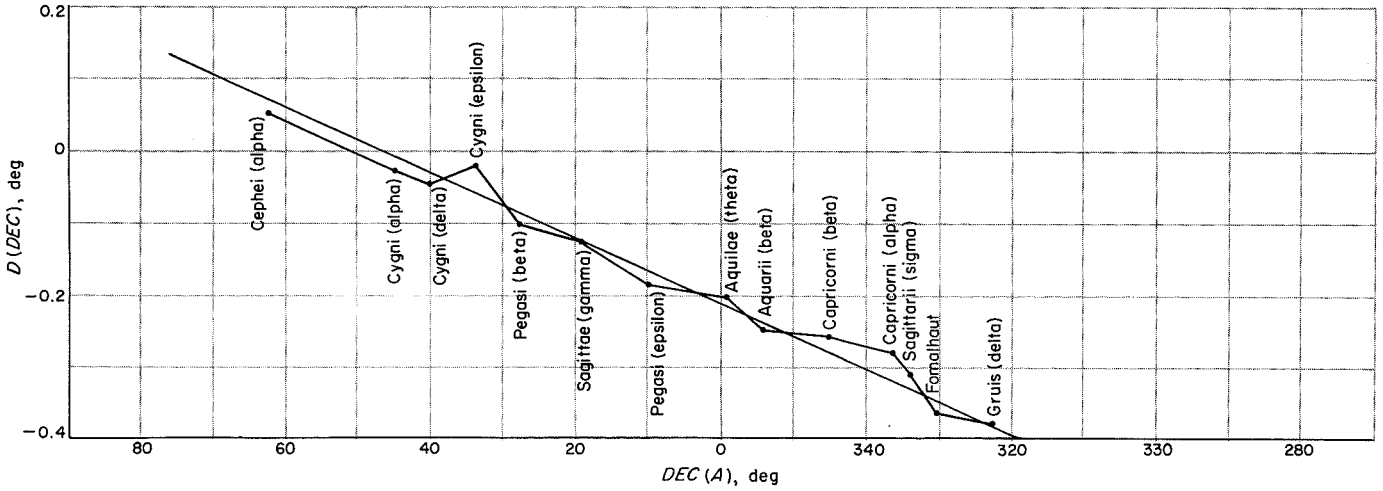

Figure 41. Reduced star tracks

data, gathered at the Goldstone tracking station, was acquired via the closed-loop television system mounted on the antenna as a visual tracking aid. The overall data gathering system (the TV camera, position readouts, antenna structure and computer reduction) has an apparent data noise width of approximately 0.02-degree peak.

Within the limitations imposed by the system data noise and accuracy, the reduced star track data infers the following:

(1) No apparent slope in hour angle readout data (Fig 40).
(2) A data slope in declination of approximately 0.0044 deg/deg (plus and minus of 35.389° N in declination, Fig 41).
(3) No apparent change in angular readout biases or accuracy due to opening of the bow gear mesh at the extremities of bow gear travel.
(4) No apparent change in angular readout biases or accuracy due to structural deformations within the limits of the investigated areas.
(5) A mechanical accuracy, for the antenna, of 0.02 to 0.04 degree in both coordinates.

c. Installation of permanent theodolite piers. The polar shaft alinement and latitude adjustment checks, the polar shaft-declination shaft orthogonality measurements, and the tie-in with the local survey, required the installation of permanent orientation reference points and theodolite piers. Figure 42 shows these piers as installed at the Goldstone tracking station receiver site. The piers carry a bronze (bench mark) monument in the slot on top of the pier below the theodolite mounting plate. The piers are striped black and orange to aid in prevention of damage by external forces.

d. Second electronics cage. During the period of 28 September 1959 to 5 October 1959 a new electronics cage was installed at the west end of the declination shaft of the Goldstone tracking station receiving antenna. The installation of the new cage was necessitated by the pending installation of new electronic equipment on the antenna. The installation of the new cage involved several associated activities besides the cage installation; that is, the removal of the existing optical cage, the relocation of the reference telescope, and the modification during installation of the cage structure, and the rebalancing of the declination and polar wheels with lead bullets.

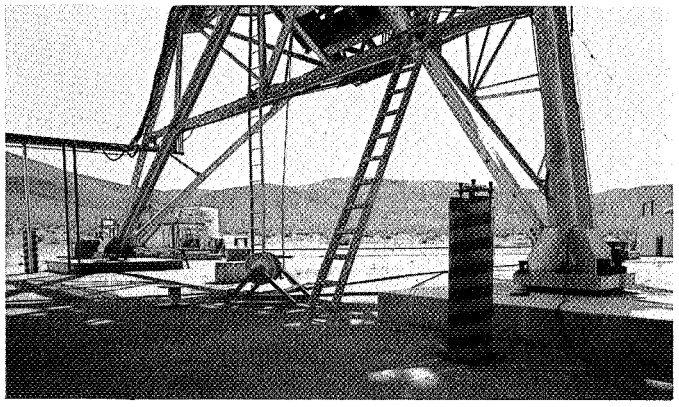

Figure 42. Bench mark/theodolite piers

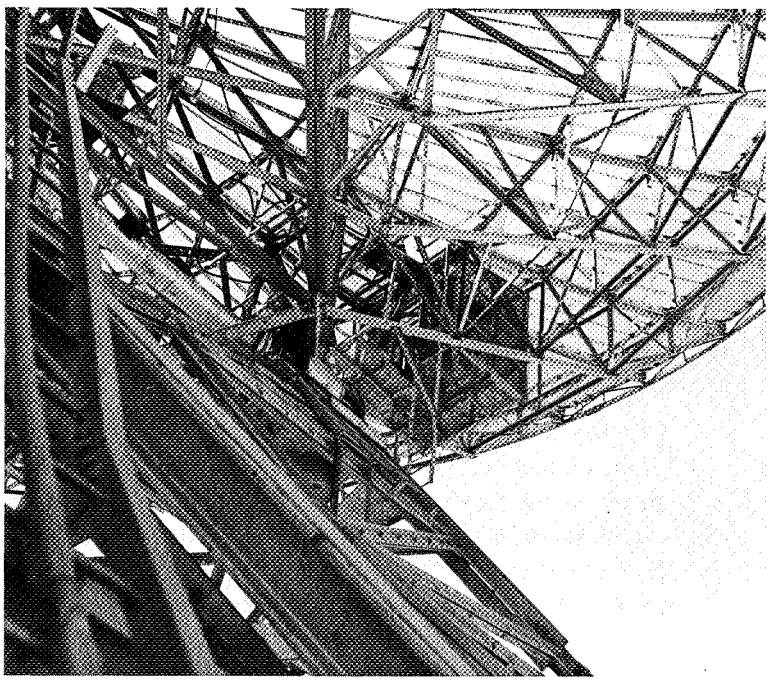

Figure 43. West electronics cage

The new cage differs from the existing east-end electronics cage primarily in its panel material. The existing east-end cage uses expanded metal mesh *skywalk* and the new west-end cage uses perforated aluminum plate. The orientation of the new cage is the mirror image of the east-end cage and its configuration and dimensions are similar (Fig 43).

e. Installation of feed lift. During the month of September the existing interim feed lift assembly utilized in changing the various feeds in the receiving antenna was modified. An assembly which is more convenient and safer to operate was installed. Figures 44 and 45 show the new feed lift assembly in operation. The feed is being lifted from its storage position on the SW perimeter of the antenna next to the servicer (Fig 44) and with the dish at zenith (Fig 45) the feed is hoisted into position into the quadripod.

f. Antenna electronics cage vibration tests. On 17 and 18 October 1959 limited vibration tests were made on the receiving antenna at the Goldstone tracking site. The

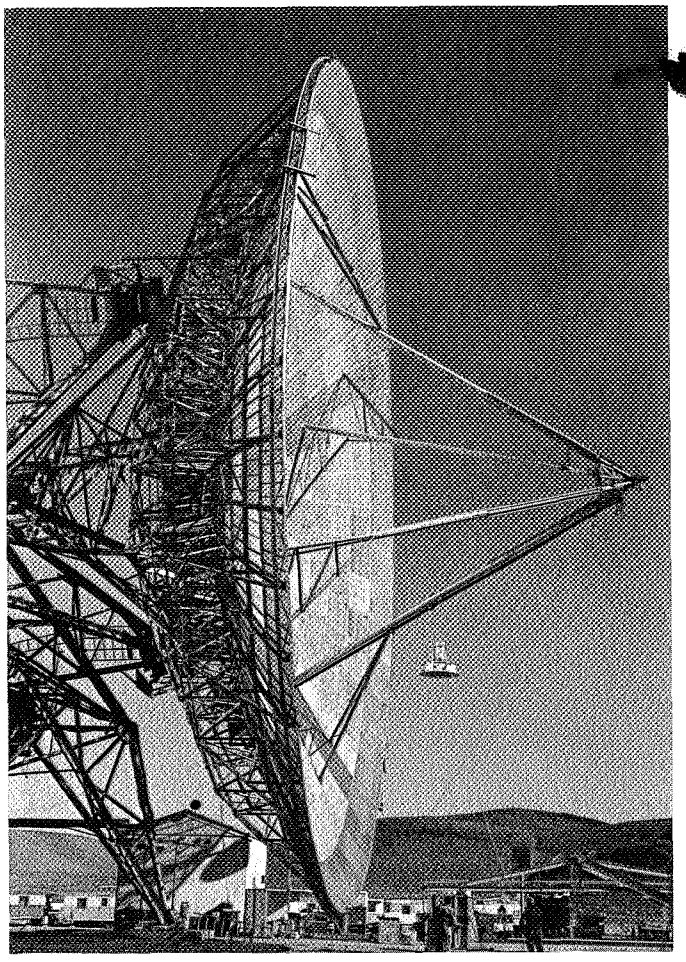

Figure 44. Feed-handling system in ground-lift position

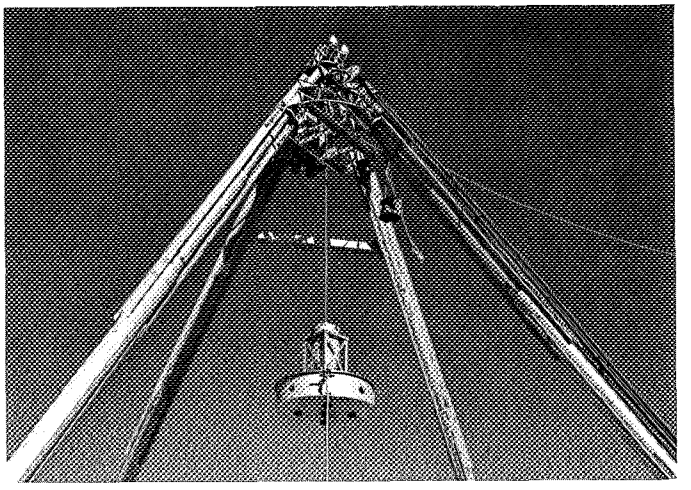

Figure 45. Feed-handling system in zenith position

purpose of these tests was to obtain data on the possible vibrational frequencies and acceleration (g) levels that might be experienced by electronic equipment located in the receiving and transmitting antenna electronics cages.

The results of the tests indicated the worst condition in the scan mode (spiral). Switching into and out of this mode was done to simulate sudden stops, sudden acquisition, or servo troubles. This series of tests has revealed the following:

(1) On the klystron mounting plate, a dominant frequency of 10 cps and a maximum g of 0.5.
(2) On the antenna truss members supporting the mounting plate, a dominant frequency of 100 cps and a maximum g of 0.4.
(3) On the central structure member of the west cage, a dominant frequency of 50 cps and a maximum g of 0.5.

It is understood that methods used have produced data which can only be considered as qualitative information.

IV. GUIDANCE AND CONTROL

It is convenient to divide the space guidance and control problem into three categories: these categories are injection guidance, which is the guidance of the vehicle during the boost phase from launch to injection into orbit; attitude control, which is the control of the angular orientation of the vehicle; and space navigation, which is the guidance of the vehicle after injection into orbit.

The *Vega* injection guidance system (VIGS) is an analog-inertial guidance system which has been adapted from the *Sergeant* guidance system. The VIGS provides guidance for the entire three-stage *Vega* vehicle.

The function of attitude control is to maintain some preferred angular orientation of the vehicle. The *Vega* spacecraft will be oriented by reference to observations made optically upon the sun and the earth. Such orientation will serve to meet the requirements of obtaining scientific data, for maneuvering, for radio communication, and for gathering power from the sun.

The space navigation requirements of the *Vega* spacecraft will be met by a mid-course maneuver, which will correct for errors remaining after injection; the VIGS is not sufficiently accurate to alone meet the mission needs. A mid-course guidance maneuver will be based on an orbit determination obtained from radio tracking information; a command will be sent to the vehicle over the radio link instructing the vehicle as to the direction, magnitude and time of application of the maneuver.

A. Injection Guidance Analysis

Injection guidance commands the motion of the launching vehicle from liftoff to injection into orbit. A majority of space vehicle missions requires coasting periods between applications of thrust; the total interval during which injection guidance must operate may be as much as 15 hours or more. Injection may occur over many points on the surface of the earth, the injection point location being strongly dependent on the mission, the vehicle, and the exact time of launch. The injection point frequently is not in sight of the launcher. Thus, earth-based guidance, such as radio guidance, is rarely suitable for all of the injection phase and inertial guidance must be used.

Error analysis. A preliminary guidance-error analysis for typical satellite, slow and fast lunar trajectories is almost complete. Results will become available during the next reporting period. A more complete analysis that includes the effects of closed-loop elevation guidance is also in progress.

1. Launch-Time Considerations

Presently planned rocket vehicles, such as the *Vega*, will be able to successfully complete extra-terrestrial space exploration missions only if launched within certain restricted intervals of time, called *firing windows*. The boundaries of these time-windows are determined by the interaction between the time-varying trajectory geometry and the limitations of the vehicle system and launching complex.

Because the launching of a rocket vehicle is an extremely complicated operation involving many systems and personnel over a period of many hours, it is difficult to demand that a vehicle lift off at a precise instant in time. With the proper attention to system design and operation, however, it appears possible to make the interval, within which the vehicle launching time falls, smaller than the available *firing window*. Certain missions, such as interplanetary probes, can only be fired in windows of a few minutes duration each day over a period of a few weeks. After this period has passed, efficient firings are not possible until many months have elapsed. For lunar missions, the windows may be an hour or more in duration and available a few days in each month.

The firing-window problem may be illustrated by some examples, tracing the relationship between changes in trajectory coefficients and the resulting changes in vehicle and launching-system parameters. Basically, changes in the trajectory coefficients as functions of the sidereal time at launch are required by the relative motion between the launch and destination points. The major component of this motion is the daily rotation of the earth, which can be partially counteracted by the use of coasting-orbit injection trajectories. Unfortunately, however, the operational problems in evaluation of the launch-vehicle performance, from a reasonable number of ground stations, limit the usefulness of the coasting-orbit technique. The changes in the trajectory coefficients in turn require changes in parameters of the vehicle and launching system. These latter parameters can be varied only over relatively restricted ranges. The times at which the limiting values are reached are boundaries of the firing windows. For example, the relationships exist as given in Table 7.

The acceptable ranges of some parameters can be varied more easily than others. In Table 7, range safety is essentially immutable. The payload capability is fixed by the vehicle design. The coverage of ground stations is limited. On the other hand, it is relatively easy to change the guidance-system parameters within a matter of seconds, minutes, or at most hours, depending on the design of the guidance system. Thus, the gross limits for the firing windows of a particular vehicle and range complex for a given mission are not determined by guidance parameters.

The guidance parameters are dependent upon the trajectory and hence still place restrictions on firing time. In the *Vega* injection guidance system (VIGS), it is difficult to take directly into account the effects of varying launch time in the guidance computations performed during flight, or even to vary the parameters during the countdown as a continuous function of expected launch time. Consequently, the guidance parameters are designed for a particular launch time. If the vehicle is launched with a set of parameters at some time other than the design value, a terminal error will result unless there is the capability of reducing this error later with a mid-course guidance system. Typically, the terminal error for a 36-hour lunar voyage increases at the rate of about 650 mi/min of uncompensated firing time delay. As a result, a given set of guidance parameters will limit this window to about 2 minutes.

The probability of performing the entire prelaunch countdown of a *Vega* vehicle in such a way that the vehicle will be launched within ± 1 minute of a preselected firing time is relatively low. In order to have a reasonable probability of successfully launching the vehicle on a given day, it must be possible to adjust the

Table 7. Gross limits for firing window as determined by trajectory-coefficient changes

Trajectory coefficient changed	Vehicle and launching-system parameter affected	Limiting factor
Inclination of the orbital plane	Azimuth at injection related to azimuth of launch	Range safety
Path angle of trajectory above horizontal at injection	Propellant required to reach required injection energy	Payload capability
Time of exit from a parking orbit	Location of vehicle track on the surface of the earth	Visibility of ground telemetering and tracking stations
Any coefficient	Guidance system parameters	Terminal accuracy or midcourse correction capability

guidance parameters during the countdown (preferably as late as possible) when the probability of launching within a particular 2-minute window is acceptably high.

The approach being taken in the VIGS is to provide remote adjustment of the important guidance parameters from the blockhouse through the umbilical cables. Sufficient adjustment will be provided to enable the guidance parameters to be set for any mission that the vehicle system is capable of accommodating; a complete change of parameters requires about 15 minutes. Minor changes can be accomplished in about 5 minutes. It presently appears that the *Vega* vehicle system is such that a hold for readjustment of the guidance parameters could be initiated as late as 30 seconds prior to launch in the countdown; further investigation of this capability is required.

2. Injection Guidance Equations

The *Vega* Phase I injection guidance system mechanizes a motor shutoff equation and an elevation-guidance equation to control thrust attitude. These two guidance signals are independent and allow the capability of nulling two linear combinations of measured coordinate deviations at shutoff of a given stage. The goal of the system for a lunar mission is to null the miss distance at the moon. This might be accomplished by controlling angular momentum and path angle during powered flight, or by directly mechanizing the predicted target error equations. A study is now underway to determine the best way of accomplishing this goal, assuming no azimuth or component errors. Any miss at the moon will therefore be due to approximation error, which arises from using only linear terms in the guidance equations, and approximating velocity and position deviations by the corresponding measured values obtained from the accelerometers (which do not sense gravity). The true coordinate deviations will change since the acceleration due to gravity will not be standard on a perturbed trajectory.

Elevation guidance consists of nulling an error signal V_N, defined as

$$V_N(t) = \delta\dot{P}_m(t) + \frac{1}{\tau_E}\delta Q_m(t)$$

where

$$\delta\dot{P}_m(t) = \dot{P}_m(t) - \dot{P}_m(t)_{std}$$

is the measured velocity deviation from standard in an arbitrary P direction, and

$$\delta Q_m(t) = Q_m(t) - Q_m(t)_{std}$$

is the measured displacement deviation from standard in an arbitrary Q direction. The quantities $\dot{P}_m(t)$ and $Q_m(t)$ are obtained in the vehicle by integration of the outputs of the A and B accelerometers in the trajectory plane and by multiplying these integrator outputs by the appropriate direction cosines. The corresponding standard values are obtained from the elevation guidance program.

The shutoff equation is similar in form. The shutoff signal V_S is given by

$$V_S(t) = \dot{S}_m(t) - \dot{S}_m(t_{SS})_{std} + \frac{1}{\tau_S}[N_m(t) - N_m(t_{SS})_{std}]$$

where t_{SS} is the standard shutoff time. The motor is shut off when $V_S(t)$ reaches zero, so that on a standard trajectory $V_S(t_{SS}) = 0$. Analogous to P and Q in the elevation guidance equation, S and N are arbitrarily selected axes along which it is desired to null deviations in velocity and position. A time-varying program is not required because the V_S equations need only be satisfied at motor shutoff. The quantities $1/\tau_E$ and $1/\tau_S$ can be interpreted as weighting factors between position and velocity deviations. Since τ has the dimensions of time, it can be seen that both V_N and V_S have the dimensions of velocity.

The most promising guidance scheme investigated to date uses the same directions and weighting factors for sustainer and second stage with the shutoff equations determined such that angular momentum at sustainer shutoff is standard; the elevation guidance is chosen so that the path angle at second stage shutoff is standard. This requires that the S direction be parallel to the local horizontal and N be perpendicular to the velocity vector at sustainer shutoff on a standard trajectory. The P direction must be perpendicular to the velocity vector and Q parallel to the local horizontal at second-stage shutoff on the standard trajectory. The value of τ for both equations is distance to earth center/missile speed, where τ_S is evaluated from standard sustainer shutoff values and τ_E, from standard second-stage shutoff values.

The third-stage equations are determined by mechanizing the first-order, lunar-impact-parameter equations. This is done by using the shutoff to null one component of the impact error vector and elevation guidance to null the other. The linear-impact-parameter equations are obtained from perturbation studies; the guidance directions and weighting factors can be computed directly. It is possible to always have the P direction perpendicular to the thrust vector by properly choosing the coordinate system to define the impact parameter. A computer evaluation of this guidance scheme will be reported in SPS 7.

B. Injection Guidance Mechanization

The *Vega* injection guidance system (VIGS) is an analog system which is similar to that used in the *Sergeant* but increased in versatility and complexity, and reduced in weight. VIGS provides guidance signals from launch for the *Atlas* sustainer and second-stage autopilots, and provides guidance for the third stage and attached spacecraft during the burning or injection phase.

Orbital coast times of up to 1 hour may be expected between second-stage burnout and third-stage ignition depending upon the mission; the purpose of the coast interval will be to place the vehicle at an optimum injection point above the earth for that mission. During the coast period, the guidance computer is re-zeroed, and a new set of constants is inserted for third-stage guidance.

Considerable versatility is required to provide guidance and control for missions varying from direct ascent to those involving coast distances extending ¾ or more of the way around the earth.

1. Guidance Compartment

The components of VIGS are attached to a separate compartment (Fig 46) which occupies the space immediately above the third-stage propulsion unit, and below

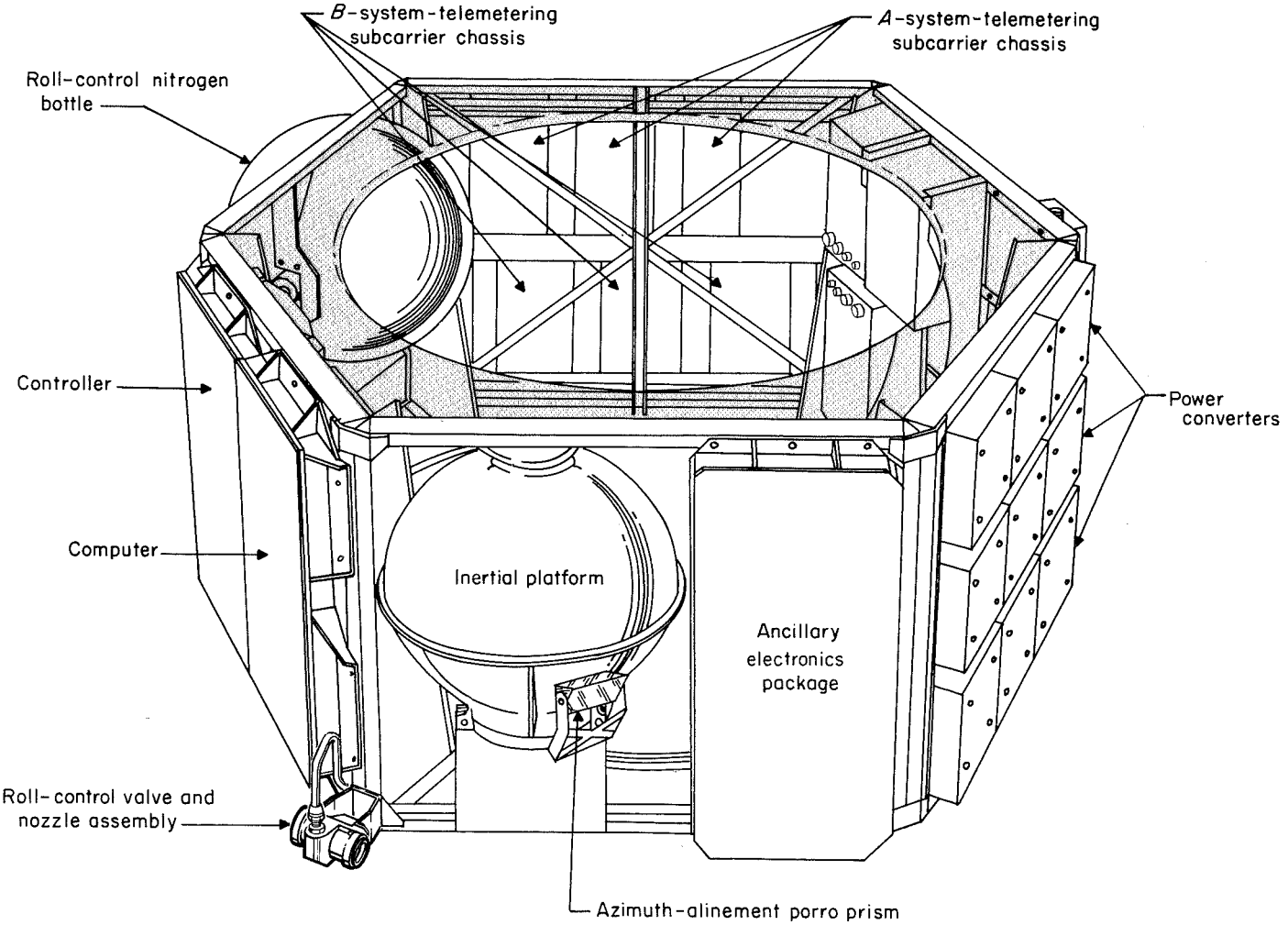

Figure 46. *Vega* injection-guidance-system compartment

the spacecraft of the *Vega* three-stage vehicle. The compartment structure continues the design philosophy of the third-stage propulsion unit. It is a lightweight, open framework, hexagonal in cross-section, with T-shaped longitudinal members connecting end bulkheads and shear bracing, and is 18 inches from top to bottom.

Lightweight cast boxes are used for the individual packages containing the components which are packaged according to function. Each box is sealed, RF shielded, and has provisions for temperature control where necessary. All packages are bolted to the periphery of the hexagonal compartment in such a manner as to augment the stiffness of the compartment structure, and to present the maximum radiating surface outward. The compartment and packages may be assembled and checked out as a unit prior to mating with the propulsion and spacecraft units.

Equipment contained in the guidance compartment consists of: (1) the three-axis inertial platform and associated electronics, (2) guidance computer, (3) controller and parameter storage unit, (4) third-stage autopilot, (5) roll-control nitrogen bottle, jets, and associated regulators and servovalves, (6) power supplies, including converters and batteries, (7) A and B telemetry systems, and (8) cabling and interface connections to the first- and second-stage autopilots, and the third-stage motor-gimbal actuators.

For the first few flights, the guidance compartment will be instrumented to telemeter temperature information obtained in a space environment. This information will be compared with ground simulation tests.

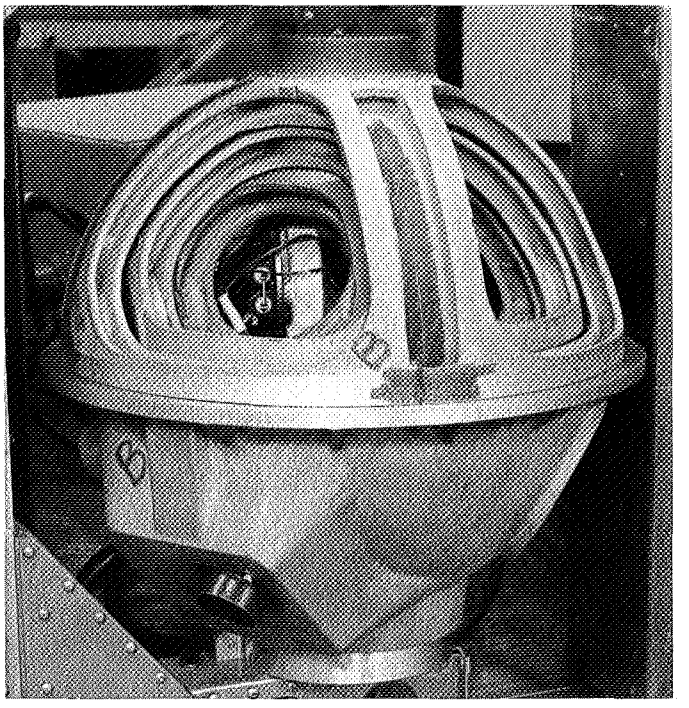

Figure 47. *Vega* inertial platform

2. Inertial Platform

The inertial platform (Fig 47) is a scaled-down version of the *Sergeant* platform. It has a three-axis gimbal system, a generally spherical shape, 12½ inches in diameter and weighing about 32 pounds. Size and weight reductions compared to *Sergeant* configuration have been accomplished by removing bulky electronic components from the inner (pitch) element, and by using an improved, smaller Bell accelerometer. The platform consists of: (1) an inner pitch element, (2) a yaw gimbal, (3) a roll gimbal, (4) an outer case, and (5) a cover.

a. Inner pitch element. The inner element (Fig 48) provides a mounting for three Minneapolis-Honeywell miniature integrating gyros, three Bell IIIB-5 accelerometers, three accelerometer amplifiers, three gyro-heater amplifiers, and three stabilization preamplifiers. The three gyros are arranged with their axes mutually perpendicular and at an angle with the horizontal which minimizes the effects of mass unbalance during the powered portions of the trajectories.

One accelerometer (transverse) is alined with its sensitive axis parallel to the pitch axis (transverse to the guidance plane). The sensitive axes of the other two accelerometers are perpendicular to each other in the plane of the flight path, and at an optimum average angle to the trajectory. The outputs of these two accelerometers are integrated, and then summed.

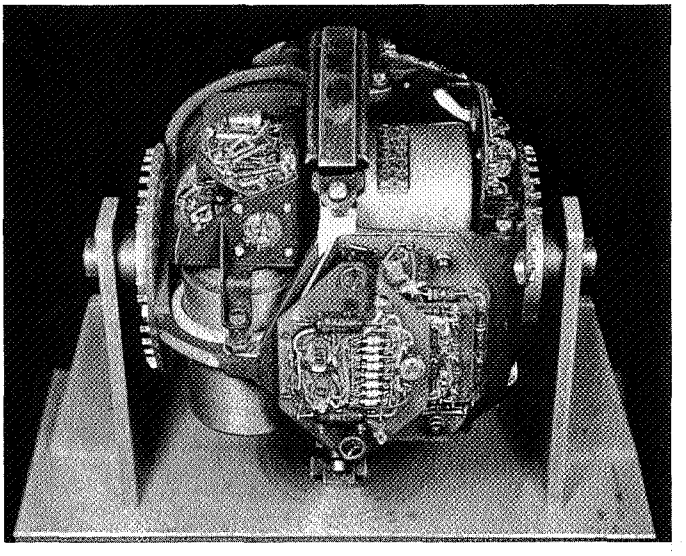

Figure 48. Inner pitch element of inertial platform

The axis of the inner element is horizontal and normal to the flight path, permitting a single degree of freedom in the pitch plane. A carbon-film potentiometer (angle pickoff) is mounted on one end of the axis, and a coding resolver on the other.

b. Yaw and roll gimbals. The yaw and roll gimbals are similar in construction, being open (spoked), spherical aluminum castings.

The yaw axis is horizontal when the vehicle is on the launch pad, and is parallel to the flight path. The roll axis is alined parallel to the vehicle axial centerline, and is the axis on which flight azimuth angle is inserted. Carbon film potentiometers are used as angle pickoffs on the yaw and roll axes.

The lower end of the roll-axis spindle carries the rotor of an Inductosyn which is a precise, inductively-coupled, angle-measuring device. The Inductosyn is one element in a servoloop which measures and controls the flight azimuth angle.

Each gimbal axis is supported on two ball bearings, one at each end of each axis, operating as opposed, preloaded pairs. All signals and power are carried through the gimbal-axis spindles in flexible leads, eliminating slip rings. Gimbal torquers are located at the greatest diameter of each gimbal, and are of the ac air-gap type.

c. Outer case and cover. The outer case supports the roll axis; provides the upper and lower trunnions for attachment to the guidance compartment; and contains the Inductosyn stator, electrical connectors, and air circulation fan. With the cover in place, the outer case serves as a RF-shielded, sealed container.

The azimuth-orientation porro prism is located on the outside, lower portion of the case. A line-of-sight opening is provided in the vehicle shroud for viewing the prism.

d. Accelerometers. The primary guidance accelerometer used in the *Vega* inertial platform is the Bell Aircraft Corporation Model IIIB-5 (Fig 49). This instrument is very similar in operating principle and basic internal construction to the Bell accelerometer used in the *Sergeant* platform. The main differences are that the IIIB-5 unit is about half the size and about a third the weight of the former *Sergeant* type.

The IIIB-5 accelerometer is of the inverted-pendulum, force-balance, closed-loop-servo type. The proof mass and torquer are supported by means of small flexure springs in a strong, radial magnetic field. The unit is unfloated; the required damping is supplied by eddy currents generated in the torquer support form which is a beryllium spool. The edges of this same spool are used as movable plates of a variable-capacitor position pickoff. This position pickoff is excited by an 8.4-kc signal.

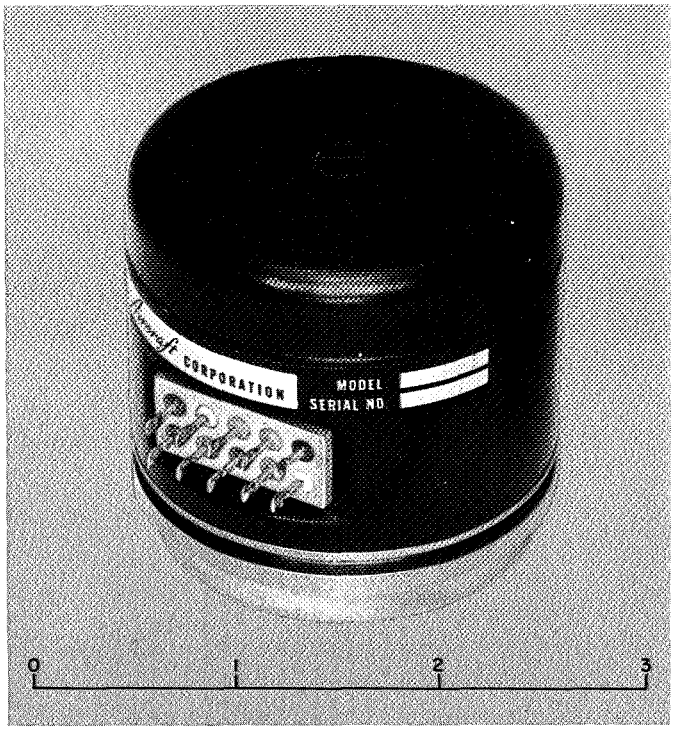

Figure 49. Accelerometer used in inertial platform

Operation. An error signal is produced when the pickoff is off null. This error signal is amplified in the loop-closing amplifier, full wave demodulated, and returned to the torquer; current flowing in the torquer is proportional to acceleration applied. The necessary voltage signal required by the guidance computer is developed by sending this same current through a precision resistor located in the guidance computer.

The gain of this capture (rebalance) loop is very high, resulting in a deflection of the pendulum proof mass of about 0.1 mrad/g (applied). Capture is maintained by the servosystem to about 45 g applied acceleration. The lower limit of sensitivity has never been determined and is below the present measuring limit of 10^{-6} g. This gives the accelerometer system a dynamic range of greater than 4.5×10^{7}. Frequency response of the system is also very high, being about 700 cps in an unfiltered mode and about 100 cps in the filtered mode as used in the platform.

Performance. The first unit of the IIIB-5 type evaluated at JPL was a hand-built prototype. This unit was subjected to a long-term test extending over a period of 3 months. The study was to determine effects of daily temperature cycling on null offset (error) and scale factor. Readings were taken at a constant temperature. The last 40 days showed a null stability of 4 parts in 100,000 total change. The scale factor showed the expected logarithmic increase due to the decrease in magnetic field strength in the accelerometer.

Status. The first six production units have not demonstrated the same stability of null offset as the hand-built prototype. Day-to-day variations as large as 0.1% have been observed, with the average error spread being 5×10^{-4} *g*. As a result of an improvement effort, the last two units under test are showing a definite trend toward increased stability. Every other area under investigation has been satisfactory and proven adequate for the VIGS.

Testing. Considerable environmental and accuracy testing is performed on these instruments at JPL before being installed on the platform. These tests are performed to determine the following characteristics:

(1) *Null error:* that amount of output the accelerometer shows for 0 *g* input.
(2) *Drift:* change of the null error as a function of time, temperature, and vibration.
(3) *Scale factor:* the amount of v dc/*g* produced at the series resistor.
(4) *Scale-factor change:* the change in scale factor as a function of time and vibration.
(5) *Scale-factor compensation:* accuracy and range of the scale-factor temperature-compensation network.
(6) *Linearity:* the relation of input *g* to output voltage over the range of ± 1 *g*, and of high range to ± 30 *g*.
(7) *Rectification:* the amount of error produced as a function of vibration applied.

All of the tests for null error, scale factor, and 1-*g* linearity are taken by turning the instrument in such a manner that a variable amount of gravity is coupled into the accelerometer sensitive axis. This turning is accomplished with the necessary accuracy by means of a Lietz optical dividing head. This dividing head is capable of a readout accuracy of 2 seconds of arc and can be reset to any given position to better than 0.5 second of arc. With the accuracy of 2 seconds of arc, the zero *g* point can be established to 1 part in 100,000, and the 1 *g* point can be established to better than 1 part in 10^6. The dividing heads are mounted on cast concrete piers extending several feet below floor level and isolated from the building.

The output voltage from the accelerometer is read on a Tinsley Type 4363D vernier potentiometer. The Tinsley potentiometer has a linearity of 2 parts in 10^6 and reading capability of better than 1 part in 10^6. The potentiometer is standardized against a bank of four temperature-controlled, saturated standard cells that hold a stable voltage to about 3 parts in 10^6.

The 30-*g* linearity test is performed on a modified Genisco centrifuge Type C-159. This machine was developed by JPL for use in calibrating *Sergeant* accelerometers to ± 30 *g* and is capable of establishing the accelerometers' linearity to about 0.02%.

Vibration effects are studied on the shake tables in the JPL environmental test laboratory.

e. Gyros. The *Vega* inertial platform gyros (Fig 50) are of the miniature, floated-rate, integrating type. The units presently being used are the miniature integrating gyro (MIG) developed for the *Sergeant* program by the Aero Division of Minneapolis-Honeywell. JPL has supported this development effort and has maintained a continuous technical aide program which included the evaluation of their latest production units.

Description. The MIG is 1.75 inches in diameter by 2.75 inches in length and weighs 0.55 pound. A flange located at the center of gravity provides the mounting. The unit has two heater elements wound around the case: one a 100-watt warmup element, the other a 25-watt heat-sustaining unit. A sensor element is also wound around the case and provides the signal source for the proportional heat control. The outer cover is chromed *mu*-metal,

Figure 50. Inertial platform gyro

providing an electromagnetic shield with some heat retaining characteristics. The unit is mounted with the flange engaging a phenolic ring (heat barrier) mounted in the gyro support structure. Terminals are located on the rim at the bellows end of the gyro.

The gyro has a 1×10^5 gm-cm²/sec angular-momentum wheel which rotates at 24,000 rpm. Its 26-volt, 3-phase, 400-cps synchronous motor draws 85 ma/line at synchronous speed. The gimbal, although common to one line, is electrically isolated from the case with power being delivered to the motor through three flex leads.

The signal generator and torquer (Dualsyn) are wound on the same core. The signal generator is excited with 4200-cps signal at 5 milliamperes resulting in a signal sensitivity of 5 mv/mrad.

The torquer has two windings. The first (pattern field) is excited by a dc current (e.g., 5, 10 or 50 milliamperes). The second (control field) can be driven from a servo-amplifier as a closed-loop servo during testing of the gyro, or for orienting or leveling the platform. High pattern currents are used during orientation or alinement to precess the platform gimbal system. During flight lower current levels are used to aid in improving the overall performance by reducing reaction torque drift resulting from the torquer excitation current.

Performance. The MIG has medium accuracy performance characteristics, which for the *Vega* program are marginal when the environmental effects such as heat, cold, vacuum, acceleration and estimated vibration are taken into account. Figures 51 and 52 approximate the vibration and the acceleration profiles. An intensive effort is being made to perfect the gyros and to provide a unit which will meet the requirements of the *Vega* system.

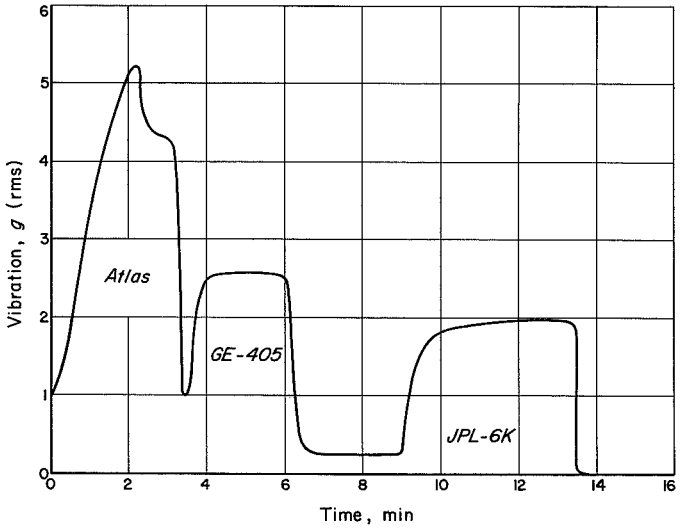

Figure 51. Approximate Vega vibration level vs time

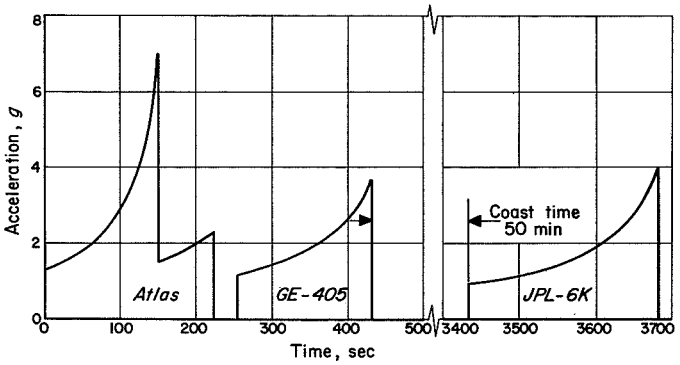

Figure 52. Approximate acceleration profile of *Vega*

The MIG is referenced as a medium-performance gyro since it has higher performance capability than the HIG-4 and HIG-5 designs but lower performance than the larger gyros employed in high-performance inertial systems such as the 2FBG and HIG-6. However, the MIG has proven to be very rugged under environmental test conditions while being smaller than other gyros of similar performance capability. The presently procured MIG for the *Sergeant* program demonstrates the characteristics as shown in Table 8.

An improvement effort has been undertaken which includes the evaluation of performance resulting from selecting the gyro orientation, changing the excitation currents, and trimming the unit to the highest degree possible. An increase of pickoff excitation frequency to 4200 cps has permitted a reduction in excitation current, resulting in the elimination of most of the signal generator reaction torques and the associated variations.

Table 8. MIG performance characteristics

Characteristics	Specified[a]	Sample lot
Mass unbalance		
Input axis	±2.0 deg/hr/g (max)	0.5 deg/hr/g
Spin axis	±2.0 deg/hr/g (max)	0.6 deg/hr/g
Mass unbalance shift, either axis during rated life	±1.0 deg/hr/g (total)	0.7 deg/hr/g
Mass stability, day-to-day		
Input axis		0.32 deg/hr/g
Spin axis		0.36 deg/hr/g
Fixed torques	±2.0 deg/hr (max)	0.8 deg/hr/g
Anisoelasticity	0.02 deg/hr/g²	0.008 deg/hr/g²
Vibration drift	0.15 deg/hr/g	0.1 deg/hr/g
Null repeatability	0.4 deg/hr (max)	—
Random drift	0.2 deg/hr	0.1 deg/hr

[a]All listings are for 1 — σ values.

The orientation of the gyros on the inner element of the platform has been determined to give a minimum degradation resulting from thrust-acceleration effects. Pattern and control-field currents are being held to a minimum to reduce reaction torques, and an effort is being made to improve temperature control and reduce temperature gradients.

An evaluation of the stability characteristic of some sources of drift is presently being made. These sources include mass balance, fixed torques, etc. The mass shifts and changes of fixed torques contribute significantly to the inaccuracy of the system. These shifts, if large and if a function of vibration, shock, acceleration, temperature cycling, or running time, greatly reduce and in some cases may prevent, the use of a compensation system to control or minimize drift-rate error. Preliminary results show the shifts to be significant although the final results are not yet available.

3. Platform Ancillary Electronics

The *off-platform* electronics are packaged as individual modules, and assembled in a 15½ × 9½ inch, cast-magnesium box which is sealed, RF shielded and weighs about 17 pounds complete.

Electronic units within the package include the level, erection, orientation (LEO) preamplifiers, the remainder of the stabilization electronics, Inductosyn signal amplifier, and power and signal switching circuits. The box lends structural support to the guidance compartment.

The *Vega* reference system (inertial platform and ancillary electronics) contains four types of control systems:

(1) The *leveling, erection, and orientation (LEO)* system is required to initially aline the platform to the required system of inertial coordinates for the assigned mission.

(2) The *stabilization* system is responsible for maintaining the platform rotationally fixed with respect to a system of inertial coordinates.

(3) The *gyro temperature-control* system maintains the gyros at their required temperature.

(4) The *acceleration measuring* system holds the accelerometer pendulums at a null position with a current-controlled torque that is proportional to acceleration.

All of the platform and ancillary electronics are involved in either the operation or monitoring of at least one of these control functions.

a. Leveling, erection, and orientation system. The leveling, erection, and orientation system (LEO) is responsible for initial alinement of the three platform axes to the desired directions. The operations of leveling and erection utilize the plane perpendicular to the local gravity vector as a reference. The orientation alinement is referenced to a surveyed ground line.

The LEO operations are broken down into four modes.

Coarse cage is a fast, high-gain mode designed to accomplish most of the necessary angle correction to within about 0.5 degree.

Fine cage is considerably slower and more accurate and is designed to reduce the angular alinement errors to within 1 minute.

The *hold mode* is used for a number of seconds just prior to launch to prevent misalinement during booster ignition. In this mode, the integrators are connected to the gyro torquers and continue to deliver earth-rate precession and drift-compensation currents which have been stored during fine cage. The integrator inputs are disconnected, however, which opens the LEO loops. In this condition, the platform is being precessed at earth rate (as in the caging mode) and stabilized (as in the flight mode). It is therefore, capable of withstanding the booster ignition shock.

The *flight mode* is used from $t = 0$ (2 in. motion point) on. In this mode, the platform remains alined to a true inertial-coordinate system rather than the earth coordinates. A predetermined current is applied to each gyro torquer to compensate for fixed torque drifts.

Leveling is the simplest of the three alinement operations to physically mechanize. It is this operation that positions the sensitive axis of the C accelerometer perpendicular to the local gravity vector, resulting in a null accelerometer reading. Leveling is accomplished as follows: (1) the signal from the C accelerometer is mixed with the orientation signal in two mixing networks; (2) both signals are then amplified in transistorized chopper amplifiers, referred to as the LEO preamplifiers; (3) the preamplifiers are followed by chopper-stabilized operational amplifiers. These operational amplifiers are the same amplifiers that are used during the flight by the controller for generating the angle, velocity and τ programs. This economy of amplifiers was possible since LEO is a preflight operation, and the controller has no use for these amplifiers prior to flight.

The function of the operational amplifiers changes as a function of the platform mode. During coarse cage the amplifiers are used as high-gain summing amplifiers. In the fine cage and hold modes they are used as integrators with lead compensation. The integration is desirable in fine cage to eliminate steady-state errors due to gyro drifts.

Second in order of mechanization complexity is the erection operation. It requires positioning of the pitch gimbal about the pitch bearings, perpendicular to the local gravity vector. The erection operation is accomplished with the help of the A and B accelerometers. These accelerometers are mutually orthogonal and at a mission-dependent angle with respect to the pitch plane. For erection caging, the A and B acceleration signals are electrically mixed so that, at the desired erection angle, their sum is 0. This mixed signal is amplified by a LEO preamplifier and an operational amplifier, which in turn excites the pitch-gyro torquer. The gyro torquer precesses the output axis of the No. 1 pitch gyro, which causes the input axis of the gyro (the platform pitch axis) to drive to the erected position.

Orientation of the *Vega* platform is the most difficult of the three caging operations. It involves accurately setting the rotational position of the inner element with respect to a ground-surveyed line. Since the sealed platform case prevents any direct optical sighting on the platform inner element, the inner-element-to-surveyed-line angle (θ_1) must be measured indirectly.

The angle (θ_2) between the platform case, as defined by a porro prism, and the surveyed line is measured with an automatic, optical-tracking device known as the azimuth orientation unit (AOU). The coarse caging of the θ_2 portion of the total angle can be considered to be the placing of the missile on the pad. This can be accomplished to within 0.25 deg.

The remaining portion of the total angle (θ_1) is the platform-case-to-inner-element or roll-gimbal angle (θ_3). This angle is measured, for coarse caging purposes, with the roll-gimbal pickoff potentiometer. This potentiometer is nulled against the remotely controlled, orientation master pot located in the controller and provides the coarse caging of θ_3.

The Inductosyn is employed to provide a vernier reading of the roll-gimbal angle θ_3. In the fine-cage mode, the Inductosyn is compared to a Reeves 601 master resolver. Since the Inductosyn is a 360-pole device, the roll gimbal must be set to the correct cycle of the Inductosyn during coarse cage to enable the fine-cage operation to proceed correctly.

The master resolver has two mechanical inputs. The first is its nominal setting, which is defined as θ_3, standard (θ_{3S}). Since the missile frame, and in turn the platform case, may twist, the resolver setting must be modified by the amount of the twist angle, so that the total angle between the roll gimbal and the surveyed ground line remains constant. This correction is the second input to the master resolver. It is mechanized with a positional servosystem that rotates the resolver in response to the AOU information on missile twist.

The above operation would normally be sufficient to successfully orient the platform; however, in *Vega* there is one additional problem. Since the platform is located about 120 feet above the ground in the third stage, the sighting angle from the AOU to the porro prism is about 9 degrees. As a result, the AOU is actually measuring twist about an axis perpendicular to the sighting angle instead of about the vertical roll axis. A sway cross-coupling error ($\phi \tan \theta$) is produced in the AOU reading, where ϕ is the sway angle, and θ is the approximate 9-degree look angle.

To eliminate this effect, a leveling accelerometer is used to measure the twist angle, ϕ. After appropriate scaling, this angle is summed with the demodulated output of the Inductosyn signal amplifier. The resultant signal is mixed with the leveling signal in two mixing networks. These two resulting signals feed the LEO preamplifiers and integrators for Gyros 2 and 3.

b. Stabilization system. There are two requirements for constant platform attitude: (1) it is necessary to maintain the sensitive axes of the accelerometers in the proper direction, independent of vehicle motion, and (2) the platform gimbal angles, as monitored by pickoff potentiometers, serve as the attitude reference for the autopilot systems. The stabilization system counteracts any external torques that act on the platform inner element to produce errors in its alinement with respect to an inertial coordinate system. These torques are principally bearing-friction and flex-lead torques.

In principle, the operation of the *Vega* platform is fairly conventional. Angular errors of the platform produce errors about the input axis of the corresponding gyro, since the gyro's input axis is measured by the gyro's microsyn pickoff.

In the *Vega* platform, the gyro-microsyn excitation frequency has been raised from 400 to 4200 cps. This was due primarily to noise and bandwidth considerations. As the size of platforms decreases, greater bandwidths become possible, and higher carrier frequencies are desirable. If the carrier frequency is too close to the highest signal frequency, adequate filtering of the demodulated carrier is difficult without introducing destabilizing phase lags within the systems' pass band. Since platform systems generally require phase-lead compensation which amplifies the high-frequency noise, adequate carrier filtering is highly important.

The 4200-cps gyro-microsyn signal, representing the output-axis error, is passed through an ac preamplifier (Fig 53). The roll and yaw signals are then passed through

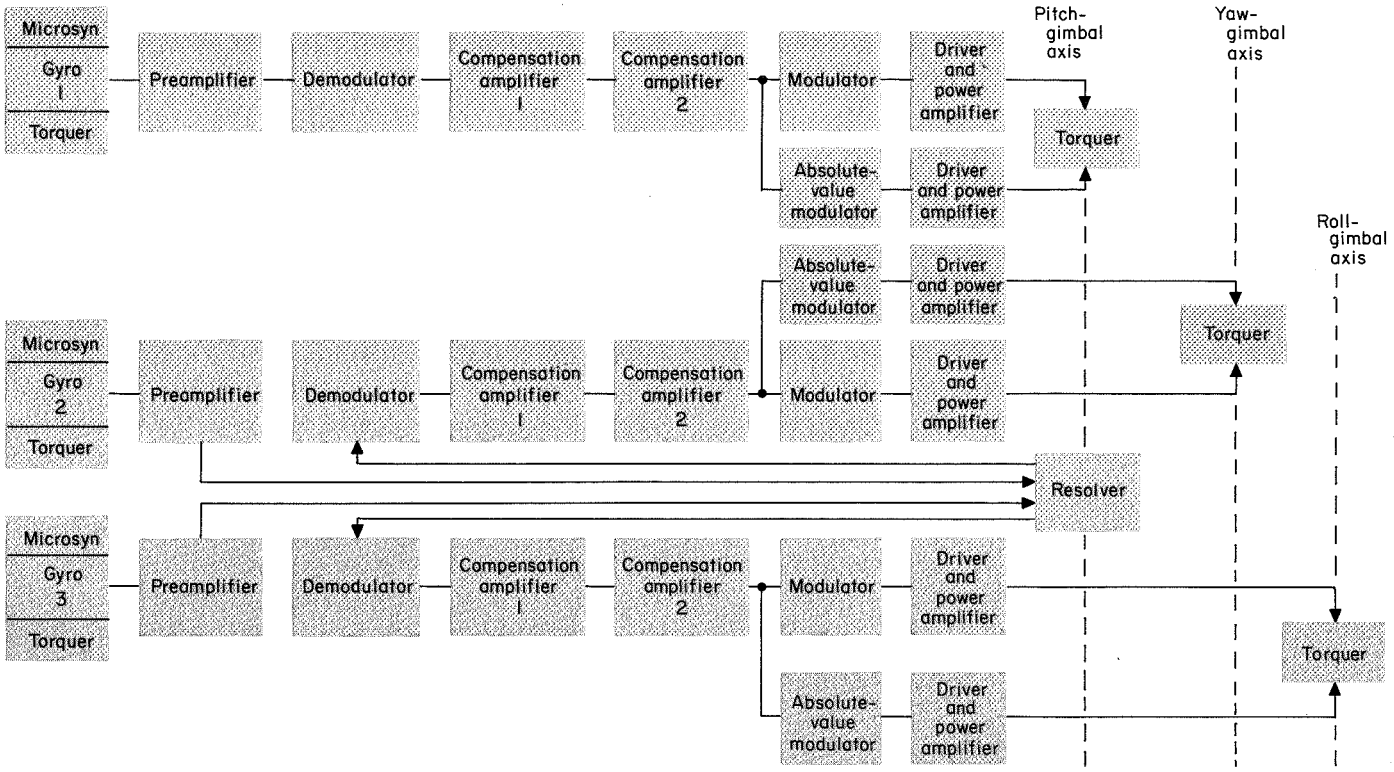

Figure 53. *Vega* platform stabilization system

a pitch-coding resolver to perform a coordinate conversion of the signals to the appropriate gimbal torquers, as a function of the pitch angle. (The pitch gimbal is the innermost gimbal and thus requires no resolving). The signals are then demodulated to permit the loop compensation to be performed on dc information.

The compensation scheme includes both linear and nonlinear operations. The need for the nonlinear compensation is a result of the gimbal-torquing scheme. The linear compensation consists of two real-axis zeros and a pair of complex poles. From a physical-realization standpoint, it was more convenient to add an additional pole and zero to the system. Although this pole and zero should theoretically cancel, they are used to obtain a small amount of additional phase lead to counteract filtering lags.

The compensation and torquing scheme used on the *Vega* platform is somewhat novel. Normally, 2-phase, ac torquers have two fields: (1) a reference field, which is produced by a constant ac current, and (2) a control field, which responds in direction and magnitude to the torque demands of the system. In the *Vega* platform, both phases of the torquers are controlled. This technique is used principally as a result of thermal problems.

At the outset of the program, an examination of the thermal problems in the *Vega* platform, based on *Sergeant* platform experience, indicated that a serious overheating problem would exist if significant power reductions (with respect to the *Sergeant* platform) were not made in the *on-platform* electronics. This was due principally to two factors: (1) the *Vega* missions involve considerably longer flight times than were experienced on the *Sergeant* program, and (2) the smaller size of the *Vega* platform results in a smaller radiating surface as well as a lower thermal capacity.

As a result of this examination several changes were instituted to help alleviate the thermal problem:

(1) Much of the heat-producing electronics was removed from the platform inner element.
(2) Insulating jackets and phenolic mounting rings were employed to reduce the heat transmitted from the gyros to the inner element.
(3) Dual-channel control was used on the platform torquers.

The dual-channel operation of the platform torquers significantly reduces the platform heating problem. Formerly a constant power of 120 watts was used to excite the torquer reference field. In the *Vega* platform, the reference fields are excited only when torque is required.

Dual-channel torquing results in a torque proportional to the square of excitation voltage. This presents two

problems: torque is always in a positive direction, and torquer gain is a nonlinear function.

The sign-change problem is overcome by using an absolute-value modulator in one of the torquer channels. This device produces a 400-cps, suppressed-carrier, modulated output that is proportional in magnitude to the input signal but constant in phase. The second channel is permitted to change phase with the input-signal phase which produces a torque in the commanded direction.

The gain change problem is overcome by using a nonlinear compensation scheme. It is physically realized by diode circuitry located in the feedback loop of the second dc compensation amplifier.

The torquers apply a torque to the platform, restoring the gyro input axis to its desired position. At this point, the gyro output axis is at a null, resulting in a null output from the gyro microsyn pickoff.

c. Gyro temperature-control system. The *Vega* platform contains three miniature integrating gyros (MIG). Many of the important gyro parameters are temperature sensitive. Both the damping and the input-to-output axis gain, which is inversely proportional to the damping, are functions of the Fluorolube viscosity, a temperature dependent variable. In addition, many components of gyro drift exhibit a variation with temperature.

In order to maintain the gyros at their required temperature, the following system is employed. A sensing resistor is located inside the gyro, and its resistance is adjusted such that it is 780 ohms at the temperature required to make the gyro gain of 14. The sensing resistor is in a bridge circuit which is in a balanced condition when the gyro temperature reaches the value necessary to yield a sensor resistance of 780 ohms. The bridge is placed across the differential input of the high-gain gyro-heater amplifier. The output of this amplifier excites the gyro-control heater. For initial warmup, a second higher powered heater is also employed. It is controlled by a magnetic amplifier which monitors the current demands of the control heaters. This heater system is very similar to the system used in the *Sergeant* system.

d. Accelerometer measuring system. The *Vega* injection guidance system utilizes Bell Model IIIB-5 force-balance accelerometer, the operation of which is as follows:

A small coil is suspended between the poles of a permanent magnet. This coil assembly has two purposes. First, a current applied to the coil produces a force capable of moving the assembly. Second, the coil assembly is the center plate of a double-ended capacitor. The double-ended capacitor forms two legs of a capacitive bridge. The bridge is adjusted so that, if the pendulum is at its mechanical center, it will be electrically balanced.

Any acceleration that displaces the pendulum from its null position unbalances the bridge, which produces a signal into the accelerometer amplifier. This signal is ac amplified, power demodulated, and then applied to the torquer coil in order to reposition the pendulum to its null. Since the coil current is proportional to torque, and torque is proportional to acceleration, acceleration can be measured by measuring the rebalance current.

The *Vega* accelerometer amplifier is a slightly modified version of the amplifier used with the Bell 2B accelerometer in the *Sergeant* system. It is modified only to the extent necessary to make it compatible with the scaled-down Bell IIIB-5 accelerometer.

4. Azimuth Orientation Unit

The azimuth orientation unit (AOU), which monitors the platform-case porro prism, is an autocollimation device. A linear readout angle of ± 5 minutes of arc from the reference zero position is provided. This angle reading is a necessary input to the orientation circuitry to compensate for possible twisting of the vehicle after initial alinement has been accomplished.

Operation of the orientation unit is best described with reference to Figure 54 which is a top view of the alinement monitoring system. In this figure is sketched the AOU front-end mechanism for the *Vega* system. Two 60-inch fluorescent tubes are set horizontal and excited 90 degrees out-of-phase; this causes the fluorescent tubes to illuminate alternately. Along the centerline is mounted a theodolite which receives the fluorescent light reflected from the platform's porro prism on the *Vega*. A belt shutter, on the prism side of the fluorescent tubes, covers alternate portions of the tubes, as shown. The optical system works into phototube detectors which are separately phased to one of the alternately excited fluorescent tubes. The phototube detectors drive a phase-sensitive servosystem. The servosystem is phased such that light from one fluorescent tube will cause the belt shutter to drive in one direction, and light from the other tube will drive the belt shutter in the opposite direction. The servosystem operates in saturation and, although it is slightly oscillatory, is thereby insensitive to variations of light intensity.

Assume a platform prism angular-offset-error (ϕ) of 2 minutes, on the vehicle, as approximately shown. Light from the uncovered fluorescent tube at a point displaced 11.5 inches from center will reflect back to the shutter phototube elements. The servosystem will drive the belt shutter to the 11.5-inch point in order to cut off the light. As it drives past the 11.5-inch point, the opposite

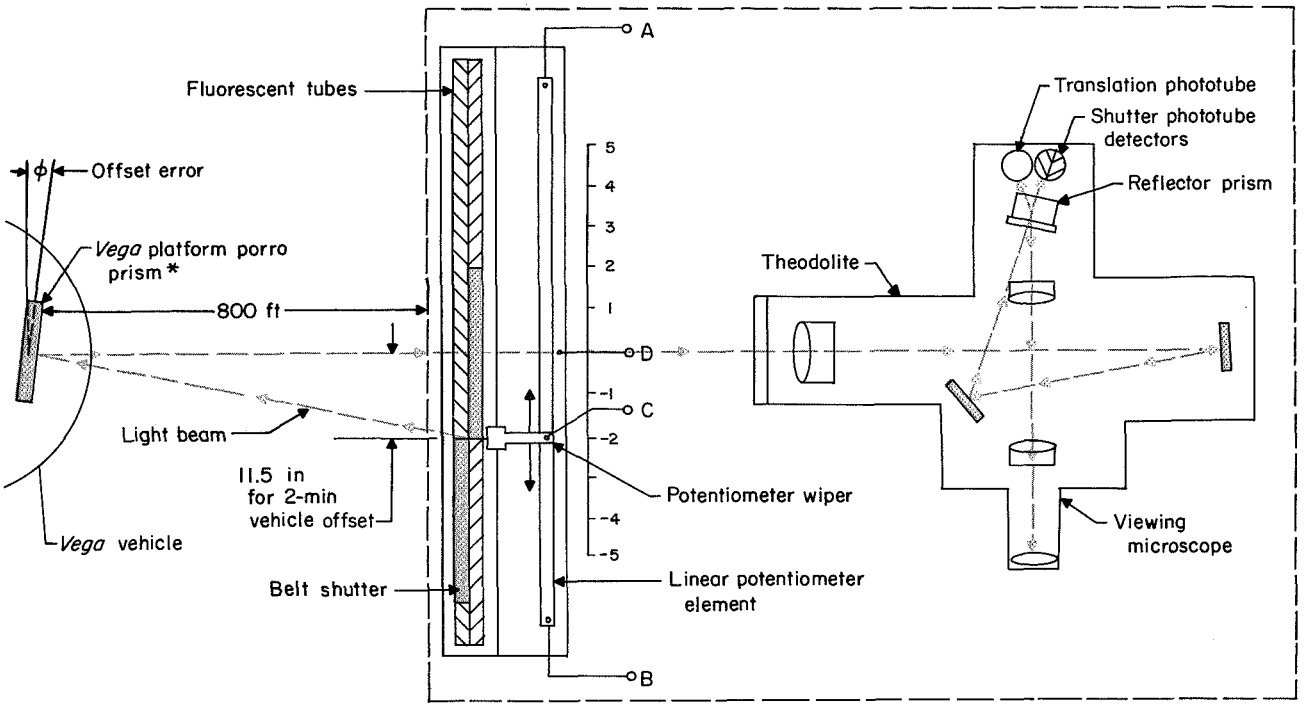

*The shutters are in an offset position since the prism is shown out of alinement with the theodolite

Figure 54. Azimuth orientation unit

fluorescent tube will be uncovered, causing the belt shutter to reverse direction. As long as the platform prism angle remains at 2 minutes of error, the belt shutter will oscillate around the 11.5-inch position. Because of the mechanical advantage of the 800-foot lever arm, very small angles can be discriminated.

Attached to the belt shutter is a potentiometer contact. This contact rides on a 60-inch linear potentiometer which is excited from a reference voltage source at A and B. In this manner, a voltage proportional to shutter position is generated and brought out at terminals C and D, indicating the orientation error.

Sway compensation is accomplished by the translation phototube sighting on the edge of the platform prism and driving the entire AOU along a precise set of ways as the prism moves. This sway (transverse to the sighting plane) will, however, contribute an azimuth error in the system. In addition to translation of the platform case prism, there will also be a tilt to the prism. If the vehicle is assumed to be rigid, a sway of 3 inches will cause a tilt of the prism of 2 milliradians. This error will be compensated for by the leveling accelerometer.

5. Injection Guidance Computer

a. Functional description. A functional description of the *Vega* computer was given in *SPS 5*. Subsequently, two additional functions were incorporated in the computer. These two are booster shutoff and the incorporation of position information in the elevation guidance computation. The amended functional diagram is shown in Figure 55.

Booster shutoff is accomplished by mixing the $\ddot{A}$ and $\ddot{B}$ acceleration signals and comparing them with a predetermined constant K_5 in the zero detector. When the sum of the three signals produces a null, the zero detector sends a shutoff command to the booster.

The addition of position data in the elevation guidance computation channel is accomplished by taking the output signals from the A and B channel second integrators, scaling the signals by using potentiometers as voltage dividers, and either sending the properly scaled signals directly into the elevation mixer, or first inverting the signals and then sending them into the mixer. The combination of scaling potentiometers and the inverter permits the resolving of the measured position data into any direction within the plane defined by the $\ddot{A}$ and $\ddot{B}$ acceleration vectors.

b. Error analysis. The parameter insertion procedure, associated with the shutoff portion of the guidance computer, makes it necessary to differentiate between errors which are present during both the parameter insertion and flight computations, and errors which are present during either parameter insertion or flight, but not both.

Absolute errors are considered to be present during both parameter insertion and flight. Stability errors are present during either parameter insertion or flight, but not both.

The estimated errors are based upon nominal component values and tolerances. In the case of the shutoff and elevation-computer scale factors, it is possible to obtain considerable reduction in the estimated errors by measuring the components used in each computer to determine the deviation from the nominal value, and adjusting the initial conditions and scale-factor potentiometer settings in the programmer to compensate for the deviations. The use of measured scale factors would result in each computer being essentially different and would require the computation of nonstandardized parameters.

c. Computer development. The computer consists of eight operational amplifiers, a relay amplifier, and a remotely controlled servosystem. The shutoff computation section of the computer utilizes four operational amplifiers as integrators, one operational amplifier as a mixer-inverter, and a relay amplifier as a zero detector. The elevation computation section of the computer utilizes one operational amplifier as a mixer-inverter and another operational amplifier as a mixer. The azimuth guidance computation section of the computer utilizes a single operational amplifier to perform multiple integrations and a summation. The remotely controlled servosystem is used to zero the operational amplifiers and also to set up initial condition voltages on the storage potentiometers.

The computer consists of nine distinct subassemblies as follows: four identical operational amplifier subassemblies (each consisting of two operational amplifiers), a relay-servoamplifier assembly, a switching subassembly, a servo subassembly, a cover subassembly, and a housing subassembly.

The computer development will be accomplished in three phases. The first computer will be an Engineering Model (EM) which is being fabricated using machined structural parts. The first computer will be utilized primarily to evaluate mechanical and electrical performance in the packaging configuration under *Vega* type-approval testing requirements.

The second computer will be a production prototype and will be fabricated using investment-casting structural parts. The wiring and assembly will incorporate modifications resulting from the evaluation of the EM. The production prototype will also be evaluated under *Vega* type-approval testing requirements.

The third and subsequent computers will be flight models which will be fabricated, wired, and asssembled using production techniques. The flight model computers will incorporate all of the modifications resulting from the evaluation of the EM and the production prototype. Each of the flight model computers will be required to pass the *Vega* flight-acceptance tests.

d. Computer-component development.

Operational amplifier. The operational amplifier (Fig 56) is chopper stabilized and has a gain of approximately 2×10^7. Bench tests of the amplifier in an inverter and in an integrator computing configuration have been completed. As an inverter with the input grounded and with

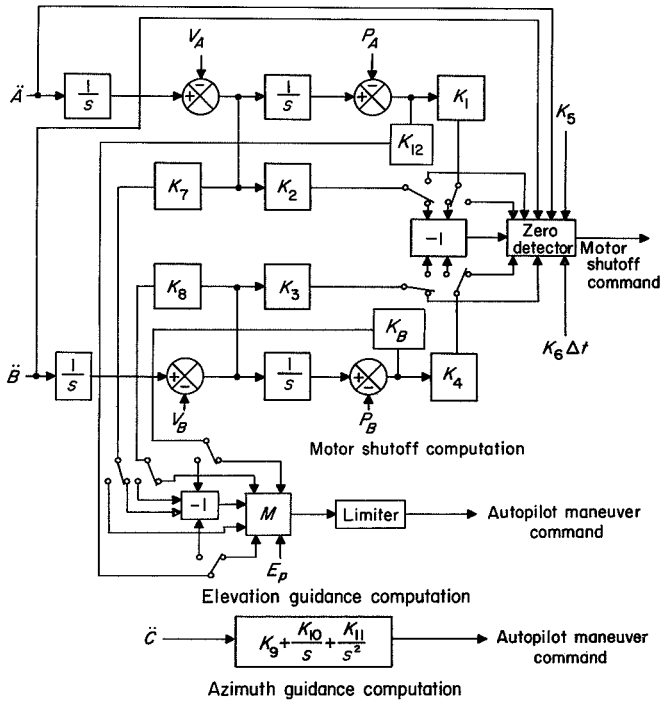

Figure 55. Injection-guidance-computer amended [illegible]ctional diagram

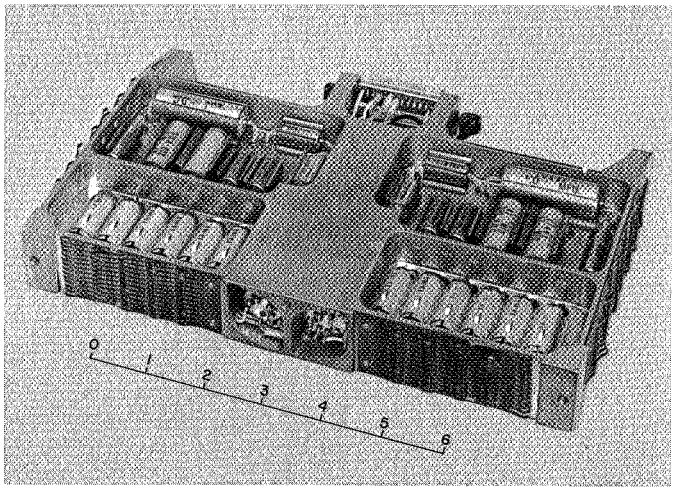

Figure 56. EM operational amplifier assembly

1-megohm resistors in the input and feedback paths, output zero offsets on the order of $\pm 10^{-5}$, or less, were consistently obtained and maintained. As an integrator with the input grounded and with a 1-megohm resistor in the input path and a 1-microfarad capacitor in the feedback path, output drift rate on the order of $\pm 10^{-4}$ v/min, or less, were consistently obtained.

An operational amplifier chassis loaded to simulate component weights and properly mounted was subjected to a 12.5-*g* vibration survey over a 15-to-1500-cps frequency range. A fundamental resonance in a direction normal to the two largest dimensions, with an amplification factor of 12, occurred at 810 cps. Operational tests under combined random noise and sine-wave vibration, as specified in the *Vega* type-approval specifications, will be conducted in the near future.

The beryllium-copper contact stock riveted to the sides of the operational amplifier (Fig 56) is for the purpose of conducting heat from the chassis to the computer housing. Tests are planned to evaluate this method of cooling in the absence of convection. Weight of the EM operational amplifier assembly is 2.42 pounds.

Relay-servo amplifier. The relay amplifier (Fig 57) is being tested at the present time to evaluate its performance characteristics. The servoamplifier is a three-stage device consisting of two cascaded stages each with a gain of approximately 50 and a power stage with a unity gain. For zeroing the operational amplifiers or for setting the dual initial-condition potentiometers, a servoamplifier voltage gain of unity is required. For setting the 10-turn initial-condition potentiometers a servoamplifier voltage gain of 2500 is required. The above gain change is accomplished by switching out one stage of voltage gain and inserting a voltage divider at the amplifier input.

The servoamplifier was bench tested in a servosystem with simulated inertia and backlash conditions. The test results indicated that the servosystem was stable under both gain conditions. In the low-gain condition the servosystem open-loop zeroed the operational amplifiers or set the dual potentiometers to within ± 1.0 volt or less. In the high-gain condition the servosystem set the 10 turn potentiometers to within ± 0.0007 volt or less.

A relay-servoamplifier chassis loaded to simulate component weights and properly mounted was subjected to a 12.5 *g* level vibration survey over a 15 to 1500 cps frequency range. A fundamental resonance in a direction normal to the two largest dimensions with an amplification factor of 13.3 occurred at 1300 cps. Operational tests will be conducted on the relay amplifier with the assembly subjected to the *Vega* type-approval environment. The

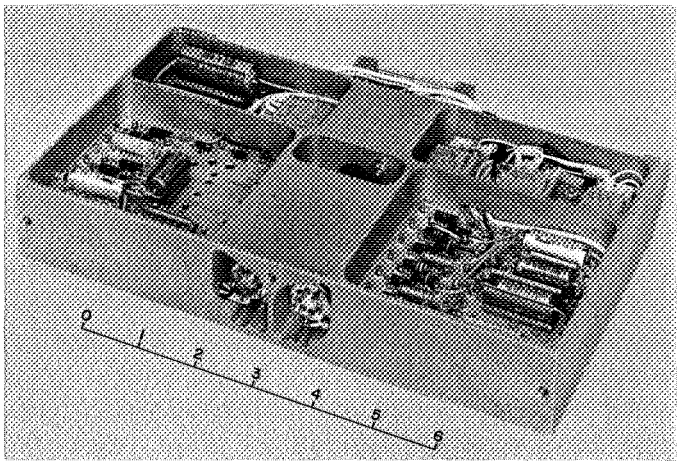

Figure 57. EM relay amplifier assembly

weight of the EM relay-servoamplifier assembly is 2.31 pounds.

Switching assembly. The switching assembly (Fig 58) contains all of the programming Ledex switches, some of the programming relay switches, all of the integrating capacitors and most of the input network resistors associated with the integrators.

The integrating capacitors are made of aluminum foil separated by 1-mil teflon dielectric and are being developed specifically for the *Vega* program. Tests performed to date indicate that the capacitors have the following functional characteristics: leakage resistance of 10^{13} ohms, temperature characteristics of 0.002%/°C or less over the temperature range 25 to 75°C, absorption of 0.015% or less, piezoelectric-like effect of 0.0005 v/°C or less. The input network resistors have temperature characteristics of ± 0.0005%/°C or less.

A switching assembly chassis loaded to simulate component weights and properly mounted was subjected to

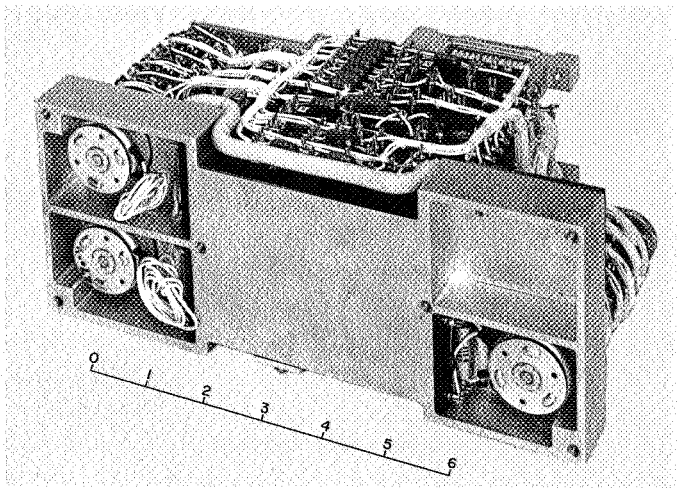

Figure 58. EM switching assembly

a 1-g level vibration survey over a 15- to 1500-cps frequency range. The lowest resonance occurred at 375 cps in a direction parallel to the axis of the Ledex motors. The loaded switching assembly was subjected to the *Vega* type-approval vibration test six times in succession. No evidence of structural damage was apparent at the conclusion of the type-approval tests. The weight of the switching assembly is approximately 7.5 pounds.

Servo assembly. The EM servo assembly is in the process of being assembled. The assembly contains the zeroing potentiometers; the dual and 10-turn, initial-condition storage potentiometers; a transformer which supplies chopper, servo-reference phase and relay-amplifier voltages; reference diodes and associated networks.

Cover assembly. The EM cover assembly is being wired at the present time. The cover contains all of the interconnecting wiring between the various subassemblies, some of the program-switching relays, the computing resistors associated with the mixers and inverters, ground boards, power boards, external connectors, etc.

Computer housing. The EM computer housing is being fabricated at the present time. The computer housing is the primary structural element of the computer. The housing contains two boilers located in the vicinity of the operational amplifiers. The boilers will be used to maintain a constant computer temperature during flight in order to minimize scale-factor stability errors.

A computer-housing structure slightly larger than the EM computer and loaded with 40 pounds of dummy weights was supported at the two small ends and subjected to a 2-g vibration survey over the frequency range 15 to 1500 cps. A fundamental resonance with an amplification factor of 18 occurred at 493 cps in a direction normal to the two largest dimensions. The dummy loaded structure was subjected to the *Vega* type-approval vibration test six times in succession. No evidence of structural failure or damage was apparent at the conclusion of the tests.

The weight of the simulated structure including the top and bottom covers was approximately 5 pounds and was fabricated entirely from magnesium.

e. Test and blockhouse control equipment. The first set of computer test equipment is being assembled and wired at the present time. The test equipment will be contained in a single relay rack and will have the capability of performing the complete checkout of the computers in the field by utilizing only the external computer connectors.

Three abbreviated sets of test equipment are being supplied for trailer use. The trailer equipment is essentially the same as the standard test equipment except it contains no power supplies and is permanently wired into the trailer cabling. The trailer equipment does not require power supplies, since it is used only when missile power is supplied to the computer.

The blockhouse control equipment utilizes the same control panel as the test equipment and is essentially identical to the trailer test equipment with the possible exception of the mounting rack.

6. Controller

The *Vega* controller provides or initiates the majority of all inflight control operations, sequences, and trajectory references for the three injection stages of the vehicle. Inasmuch as all such functions originating in the controller are to be accomplished at prescheduled, specific times between launch and injection, the controller must include an accurate time-from-launch base, and a memory device in which the required events can be stored and then reproduced on schedule. Since a few discrete operations, and all trajectory reference data, are dependent upon both mission and launch time, the controller must also include both the flight and ground equipment necessary to allow remote insertion of schedule and parameter changes. Therefore, the term controller refers to a system consisting of six major parts: (1) program storage unit, (2) program generators, (3) parameter storage equipment, (4) actuators, (5) ground program insertion equipment, and (6) ground parameter insertion equipment. Also contained within the flight-controller assembly are the autopilot amplifiers, and the integrators for leveling, erection, and orientation of the inertial platform. These integrators also serve a dual role as program generators during flight.

a. Flight controller. The flight controller for the VIGS is a modularly constructed assembly containing the following modules:

(1) Velocity-program generator.
(2) Constant angle and time-to-go generators.
(3) Three parameter-potentiometer modules.
(4) Integrator-capacitor assembly.
(5) Three autopilot amplifiers.
(6) Switching-deck assembly.
(7) Cabling-harness assembly.
(8) Controller housing and cover.
(9) Programmer.
(10) Frequency standard for programmer.
(11) Isolation power supply for programmer.

When assembled for flight the entire package will weigh approximately 30 pounds and occupy 1010 cubic inches.

The *velocity-program generator* consists of an operational amplifier with capacitor feedback, a precision voltage divider, and relay logic for selecting various levels of the divider. The basic operational amplifier is the same as used in the VIGS flight-data computer. It is a chopper stabilized, five-tube dc amplifier with an open circuit dc gain of 2×10^7. Operation as an integrator is accomplished by the use of a 1-microfarad feedback capacitor of high quality.

The voltage divider will provide five levels of positive or negative voltage accurate to 0.01%. Precision voltage for the divider is obtained by zener regulation of ± 150 volts dc. Relay logic is used to select the first-derivative changes (FDC), first-derivative sign changes (FDSC), and the second-derivative sign changes (SDSC) when referenced to the output of the integrator.

Three velocity programs will be generated in flight: for *Atlas* sustainer, *GE-405*, and *JPL-6K* burning. Each program will require 25 time slots. Twenty of the time slots will be used as first-derivative changes. The remaining five slots will be used for first-derivative sign changes and second-derivative sign changes.

In order to compensate for scale-factor errors in the integrator, all units are precalibrated during checkout by trimming the input resistor with a small carbon resistor of 25K nominal value. Evidence to date indicated that this precalibration can be accomplished in such a manner as to hold long-term stability of the integrator to less than 0.1%.

The *constant angle* and the *time-to-go generators* use the same type of operational amplifiers as are used for velocity-program generation. Neither of these programs requires logic for multiple selection of derivatives and can therefore be mechanized with fixed voltages at the integrator input whenever an output is required. These program generators will also be precalibrated during checkout and should maintain this calibration permanently. There will be two time-to-go and three constant angles generated during flight.

Three *parameter-potentiometers modules* are included in the flight controller. Each module contains 10 clutch-brake-potentiometers of JPL design, a Kearfott motor-generator, and gearing. All 10 potentiometers in the module are driven simultaneously by the motor-generator, and individual potentiometers can be selected for setting by energizing the associated 28-volt magnetic clutch-brake. After setting and removing clutch power the wiper of the potentiometer is locked in position for flight by a built-in brake.

The 30 potentiometers are set to an accuracy of 0.01% by a parameter insertion servoamplifier located in the ground insertion equipment. Voltage used for exciting the potentiometers while setting is derived from a ground source and is also used to excite the ground-based reference pots. Utilization of the 30 potentiometers in the system is shown in Table 9.

The *integrator capacitor assembly* contains, in addition to its normal capacitor complement, components and associated switching relays necessary to utilize the program generators for leveling, erection, and orientation integrations.

Several problems were encountered, and it was found that the output load resistor of the integrator had to be reduced from 15K to 6.8K in order to obtain a desired 20 milliampere output instead of a normal 5 milliampere maximum output. A gain of 100 was also desired. Therefore, it was necessary to reduce the input resistance of

Table 9. Potentiometer functions of VIGS controller

Identification symbol	Function		Burning period
S_{11}	A	Shutoff coefficient	First (*Atlas* sustainer, *GE-405*)
S_{12}	A		
S_{13}	$\dot{B}$		
S_{14}	B		
S_{15}	τ_1		
S_{16}	K_S		
S_{17}	K_{405}		
S_{21}	$\dot{A}$	Shutoff coefficient	Second (*JPL-6K*)
S_{22}	A		
S_{23}	$\dot{B}$		
S_{24}	B		
S_{25}	τ_2		
S_{26}	K_{6K}		
E_{11}	$\dot{A}$	Elevation guidance coefficient	First (*Atlas* sustainer, *GE-405*)
E_{12}	A		
E_{13}	$\dot{B}$		
E_{14}	B		
E_{15}	$\dot{P}_{1C}$[a]		
E_{21}	$\dot{A}$	Elevation guidance coefficient	Second (*JPL-6K*)
E_{22}	A		
E_{23}	$\dot{B}$		
E_{24}	B		
E_{25}	$\dot{P}_{1C}$[b]		
θ_{01}	θ_{1C}	Autopilot program	First (*Atlas* booster and sustainer)
$\dot{\theta}_{02}$	$\dot{\theta}_S$		
θ_{11}	θ_{1C}	Autopilot program	First (*GE-405*)
$\dot{\theta}_{12}$	$\dot{\theta}_{405}$		
θ_{21}	θ_{1C}	Autopilot program	Second (*JPL-6K*)
$\dot{\theta}_{22}$	$\dot{\theta}_{6K}$		
ϕ_S	Roll standard angle		(Preflight orientation)

[a]First elevation-guidance initial condition.
[b]Second elevation-guidance initial condition.

the integrator to 220K and to add a 22M resistor in series with the 1 microfarad capacitor.

Autopilot amplifiers. The third-stage autopilot consists of three plug-in amplifier modules mounted in the controller. The approximate outline dimensions of the three-channel package are 2¼ × 3¼ × 6⅜ inches, with a weight of 2.5 pounds. Two summing junctions are provided: one for the dc guidance, program, and angular position signals; and one for the suppressed-carrier angular rate and local feedback signals. The dc summing junction is accomplished by the use of a starved-current diode modulator with an equivalent input drift to the ac amplifier of less than 4 millivolts over the temperature range of −10 to 60°C. The ac summing junction is provided by a high-gain ac amplifier. In pitch and yaw, the dc actuator control current is supplied by an active half wave demodulator, while in roll a low-power, full-wave demodulator and a Class B, push-pull stage supplies dc current to the series connected valves. The total power required by the autopilot electronics amounts to 2.5 watts for each plus and minus 65 volt supply; .5 v-amp from the 115 volt, 400 cps supply; and negligible current (1 milliampere) from the 6.3 and 26 volt, 400 cps supplies.

The autopilot actuator in pitch and yaw is the Lear magnetic-particle clutch, in which the output force is proportional to the input differential current. The maximum control force available with this actuator is 600 pounds acting at a lever arm of approximately ½ foot. This torque level requires a differential input current of 85 milliamperes and is required to accelerate the gimbaled-motor-load inertia of 35 slug-ft². The velocity limit of the ram is 1.8 ft/sec. Figure 59 contains a block diagram of the autopilot minor loop. The system may be represented as a position-control servo with the following transfer characteristic:

$$\frac{\delta}{\theta} = \frac{kM}{K_m} \frac{AK_1 K_m / I}{s^2 + \frac{AK_1 K_T}{I} s + \frac{AK_1 K_m}{I}}$$

where kM is the equivalent modulator-ac-amplifier-platform-pickoff gain in v (rms)/rad, A is the current gain in ma/v (rms), K_1 is the actuator gain in ft-lb/ma, I is the load inertia in slug-ft², K_m is the position feedback gain in v (rms)/rad, K_T is the velocity feedback gain in v (rms)/rad/sec, δ is the motor angle in radians, and θ is the missile angle in radians. The autopilot gains are adjusted for 1.055 position gain, 0.6 damping, and a 5 cps natural

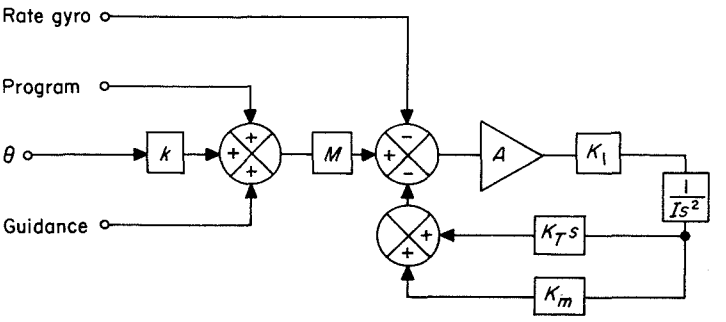

Figure 59. Pitch and yaw autopilot minor loop

frequency, which results in the following transfer characteristics:

$$\frac{\delta}{\theta} = 1.055 \frac{986}{s^2 + 37.7\,s + 986}$$

The measured frequency response is shown in Figure 60.

Roll control is accomplished by use of nozzles placed on the periphery of the guidance section. The Atchley pneumatic valve is used as the basic actuator. The Atchley unit is a spring-force-rebalance, flow-control valve in which the spindle position is proportional to the armature current to within ±5% from valve-to-valve. The valve is operated at a regulated pressure of 400 psi, and the nozzle is capable of 8-pound thrust, acting at a lever arm of 2.5 feet. The control torque available is 40 ft-lb, with a maximum sideways-unbalance force of 0.8 pound.

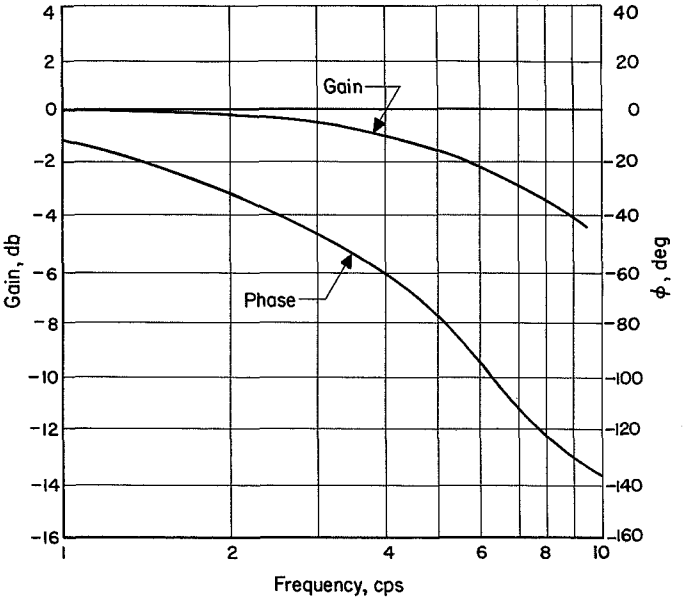

Figure 60. Pitch and yaw autopilot frequency response

The block diagram and root locus of the roll system are shown in Figures 61 and 62, respectively. The missile inertia is represented by J in slug-ft^2, k and k_T are platform angle and rate gyro sensitivity in v/rad and v/rad/sec, S is the autopilot current gain in ma/v, kl is the lever arm length in feet, and n is the nozzle gain in lb/lb/sec. The valve and gyro may be represented as second-order systems where ω_n and ω_0 are the respective undamped natural frequencies and τ and ρ are the damping ratios. From the values tabulated on Figure 61 it can be seen that the valve dynamics may be eliminated from the root locus without markedly changing the locus at low frequencies. Operating at an electronic gain of 1775 ma/v in the position channel, the resultant steady-state error for a disturbance equal to the full capability is 0.1 degree and the system damping factor is 0.6 with a 3.4 cps natural frequency. The gain margin is 4.5.

As in the roll system the compensation for pitch and yaw is derived from a Detroit Controls GR-43 rate gyro. The rate gyro package containing three gyros is approximately $4 \times 4 \times 3$ inches and weighs 1¾ pounds. The gyro damping factor is 0.9 $\pm$0.1, the natural frequency is 24 $\pm$2 cps, the sensitivity is 9.55 v rms/rad/sec $\pm$5%, and the inphase null is 15 mv rms. The power required per gyro for the spin motor is 3 phase, 26 volts at 5 v-amp and for the pickoff, 115 volts, 6 v-amp, single phase.

In the initial stages of system testing, the rate gyros that will be utilized for autopilot stability information will be those which were used in the pitch and yaw channels of the *Sergeant* system. In all three channels (roll, pitch, and yaw) 15 deg/sec gyro units will be employed. A contract has been issued with American Standard Corporation for the production of (34) 15 deg/sec rate gyros of an advanced design which are to be employed in flight

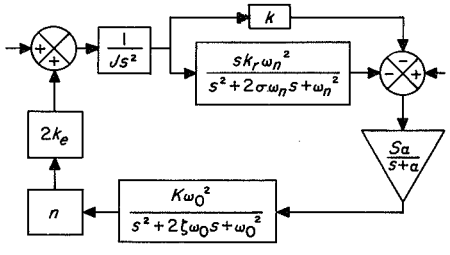

α = 50 rad/sec
k = 5.73 v/rad
k_r = 0.799 v/rad/sec
σ = 0.9
ζ = 0.6
K = 5.5×10^{-3} lb/sec/ma
n = 75.5 lb/lb/sec
k_e = 2.5 ft
ω_n = 150 rad/sec
ω_0 = 468 rad/sec

$$g = \frac{S\alpha}{s+\alpha} \cdot \frac{k}{Js^2} \cdot \frac{s^2+\left(2\sigma+\frac{kr}{k}\omega_n\right)\omega_n s+\omega_n^2}{s^2+2\sigma\omega_n s+\omega_n^2} \cdot \frac{2k_e n K\omega_0^2}{s^2+2\zeta\omega_0 s+\omega_0^2}$$

$$= \frac{(0.547\times10^6)\,S(s+4500)(s+5)}{s^2(s+50)(s^2+270s+22{,}500)(s^2+564s+222{,}000)}$$

$$\approx \frac{(0.0111\times10^6)\,S(s+5)}{s^2(s+50)(s^2+270s+22{,}500)}$$

Figure 61. Roll system functional diagram

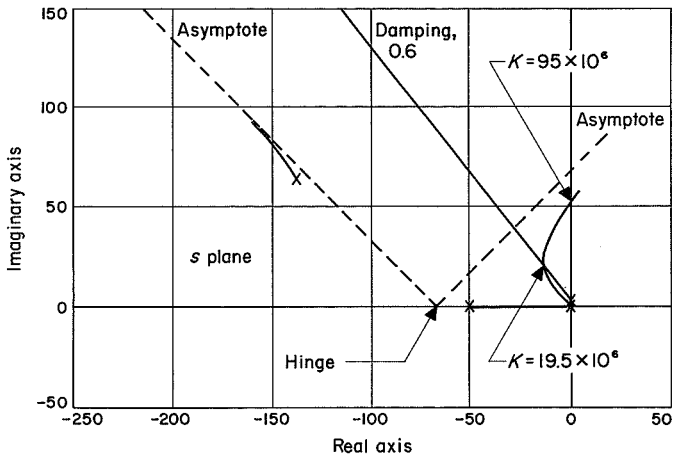

Figure 62. Autopilot-roll-system root-locus plot

systems. The advanced design units are of the same size and weight as the *Sergeant* rate units and have the same electrical characteristics; however, their performance degradation under environmental conditions will be an order-of-magnitude less. These new type gyro units will have a torsion bar of smaller cross-sectional area which will reduce the threshold level and increase the resolution.

The rate-gyro package consists of a cast-aluminum housing containing three miniature rate-gyro units, three sensitivity compensating toroid chokes, one terminal board, and two small connectors. The package will utilize O-rings to seal the unit.

Test equipment for testing the individual gyro units and equipment for testing the completed package consists of two control panels and their associated cables. An angle bracket will be designed and built as soon as the location of the package in the airframe is firm. Rate-of-turn tables and other necessary test equipment are presently available at JPL. Testing the completed package will consist of checking for proper polarity of output signals for a given input direction and a five-point check of output-voltage amplitude vs input-rate amplitude.

Field system checks will utilize a small, portable, rate-of-turn table. The table operates on 115 volts, 400 cps, single phase power and has a constant turning rate of 0.1 rad/sec in clockwise and counterclockwise directions.

The *switching deck assembly* furnishes inflight switching for the entire VIGS. All commands for time switching are derived from the programmer, power amplified and then used to either energize relays or step rotary switches. Presently the switching deck contains six 5-wafer BD-2 rotary switches manufactured by G. H. Leland Incorporated and 34 2P2T relays of both latching and normal types. The BD-2 Ledexes have been environmentally tested and performed quite satisfactorily

after being disassembled and then reassembled with rigid quality control. No pulse greater than 17 volts, 30 msec duration was required to step the switch over a temperature range of from −30 to 180°F.

Three of the rotary switches are associated with switching the parameter potentiometer modules for preflight operations: one for switching commands from ground to airborne control, and the remaining two are used for inflight sequence switching. The relays are used for sequencing of the controller and for inflight switching where one command must be switched at a given time.

The *wiring harness* of the flight controller will have 12 Bendix Pigmy connectors for wiring external to the controller, and 15 Cannon connectors to be used internally for plug-in of modules. This type construction allows all wiring to be accomplished in a wiring jig where rigid quality control and inspection can be maintained.

The *controller housing and cover* are cast magnesium, using thin wall construction. Ribbing is added where necessary to give added support. The inside dimensions of the box are 9¾ × 15⅜16 × 7 inches with approximately 1000 cu in. of usable volume. This volume is subdivided into three compartments for ease of mounting and isolation of the modules.

All external connectors are mounted in two rows of six each through the bottom of the housing, and mounting rails are provided lengthwise down the center.

Externally, on both sides of the compartment containing the program generators, boiler areas are provided for temperature control of that compartment during flight. It is anticipated that boiler relief valves will be calibrated to maintain the internal temperature of 135°F.

Programmer and associated ground equipment. The programmer unit forms an integral part of the *Vega* controller. The program storage unit is used to hold preset operation times for the switched elements necessary to the flight of the *Vega*. The program storage unit has 96 time-storage channels. Each channel has the capability of storing any time from 0 to 4 hours in 0.1-sec increments. Approximately 60 to 75 of the time-storage channels will be devoted to nonlinear program channels. The remainder of the 96 channels will hold actuator times. The actuators may consist of either relays or rotary switch units. The actuation times for each stage are stored and acted on as local times; i.e., each stage operational times will be determined by the shutoff of the preceding stage.

The program storage unit utilizes the latest techniques of ferrite-core storage and logic. The memory system is a nondestructive system using multi-aperture cores. The drive switches and counters are constructed of multi-aperture and conventional core circuits with appropriate transistor drives. The high-accuracy timing signals are derived from a transistorized, crystal-controlled master oscillator.

The ground equipment used for inserting times into the airborne unit is divided into two basic groups: (1) laboratory test and insertion equipment; and (2) field test and insertion equipment. The laboratory equipment will be similar to the field equipment in that both have the same basic test and insertion capabilities. The equipments differ in that the laboratory units will be capable of more detailed system analysis and test. One laboratory test unit will be installed at JPL; the second will be used by the programmer subcontractor. There will be an additional box of electronics which can be carried into the field and connected to a field-test and insertion set, making it capable of performing complete laboratory-type tests. Three field units will be installed in test trailers and one unit will be installed in the blockhouse. The time inputs will be derived from either a keyboard installed in the test rack or from an IBM-card reader.

The ground units are designed to utilize standard computer-logic modules. The ground logic is used to set up the stored programs, transfer the stored data from the ground to the airborne unit, and perform the system test functions. The ground units contain four multi-aperture core matrices for the storage as alternate programs. The master time reference for the synchronous ground equipment is derived from the airborne clock.

The storage element consists of the multi-aperture matrix, and its read and load switches. A particular core in the matrix is interrogated by the coincidence of two currents derived from switches, each of which by itself is not capable of producing a read signal. In order to obtain maximum economy of operating elements, the two read switches are advanced at the same time. With this type of operation it is necessary that the number of cores in each switch be mutually prime so as to insure that, in one scan, each core is interrogated only once, and that the scan starts at the same point each time. It is for this reason that the switches are chosen as 51 and 22. Using two matrices driven from the selected switches, a capacity is obtained of 96 operation times and two test times stored with a resolution of 0.1 second for a maximum of 24-hour periods. The time is stored as binary-coded decimal (4 hours in 0.1-second increments takes 20 bits). If both switches are advanced simultaneously, the matrix is scanned in a diagonal fashion.

The 22-way read switch consists of 11 cores on each of two drive lines, and the 51-way switch consists of 17 cores on each of three drive lines. To simplify the switch

driving problems, the equipment is tied by five separate driving pulses.

Each of the 51 rows of each matrix in one direction contains 21 cores corresponding to the 20 bits of the binary-coded decimal (BCD) time rotation; the remaining two positions are used to code the four local time sequences. These two sets of 51 rows correspond to the 96 actuators in the missile, two test outputs and four spare rows. If a matrix scan begins at position (1, 1), due to its diagonal nature it will end at position (22, 51) and will then recommence at (1, 1). Positions (1,1) and (22, 51) are used to generate two interrogate times. These two times are used to transfer to the time register from the time counter and to interrogate the 50-bit register.

Loading of the storage element is controlled from the ground. When it is desired to load a program, the matrix is first cleared by energizing a winding that links all the matrix cores through their major hole. The load switches are then operated in conjunction with a digit-inhibiting winding which links all write holes so that each core is written into its required state.

To allow a simplification in the time counting, entering and display mechanism, time is carried throughout in terms of hours, minutes, seconds, and tenth seconds. In BCD notation 20 bits are required: 2 bits for hours, 3 bits for 10 minutes, 4 bits for 1 minute, 3 bits for 10 seconds, and 4 bits each for seconds and tenth-seconds. The counter is composed of core flip flops set to count in BCD. The counter is stepped by an α pulse which is generated when the matrix has reached the (22,51) position of its scan and a β pulse which is generated when the scan of the matrix begins at (1,1). By this method the counter progresses every tenth second. In order to provide local time counting the counter is cleared to zero as each stage is shut off. The twenty-first and twenty-second bits are used to hold the coding to indicate which stage is being timed.

The matrix contains the programs times. If each bit of a matrix row is compared with the corresponding bit in the counter and any two bits do not compare, the bit in the 96-bit register corresponding to that row is cleared. Instead of examining all the bits of a given row, and then going to the next, the diagonal scan of the matrix causes a bit of one row to be compared and then another bit of another row, eventually scanning every bit of every row within the tenth-second increment. If the two bits being compared are not the same, the read-compare-and-drive circuit generates a drive current which half-selects the cores in the output register. The other half-select drive for the output register is derived from the 51-way read switch. If the BCD circuit sees a match between the bit from the time register and the matrix, it does not put out a half-select pulse and the output register is not cleared. At β time (the start of a matrix scan) all the output register cores are set on. As the scan progresses the cores are cleared due to noncomparison. Any output core in the *on* state at the end of the scan is sensed by the α pulse (end of scan), and the pulse out of this core is used to drive a silicon control switch, which in turn sets a relay and thereby performs a given operation at the desired time.

A precision crystal oscillator with an output frequency of 11.22000 kc is used to drive the clock-pulse generator, which in turn drives the 22-way and 51-way switches.

The operation of the ground equipment is similar to the airborne unit except that all of the synchronization is derived from the airborne-clock pulse generator, and α and β signals. System test is run in two stages. First, the ground equipment is loop checked automatically and a *go, no-go* light is displayed. Second, the airborne unit is checked in a loop with the ground. The program stored in the ground or the airborne matrix, or the difference between ground and airborne matrix are displayed on a 17-inch cathode ray tube. This allows the operator to find the area which is malfunctioning.

b. Ground parameter inserter. The function of the ground parameter inserter will be to furnish precision timing for preflight autocalibration of the flight-data computer, parameter calibration for scale-factor errors, position flight potentiometers to make automatic compensations for accuracy, and to monitor all flight controller switches.

Autocalibration of the flight-data computer is accomplished by precisely timing standard integrations and then transferring the integrated value onto potentiometers for storage. The precision timing for this operation is accomplished by means of a low-resolution preset counter. The preset counter is set for a predetermined readout from information stored on IBM punched cards. The computer will start the counter and integrators on command and an automatic stop signal is returned to them at the end of a timed period. This process is repeated until initial conditions are obtained for both the α and β channels, for a total of eight operations.

Each of the eight data-computer initial conditions obtained may be in error by as much as 1%. A parameter calibration technique will therefore be employed to correct the missile ratio-potentiometer settings. The correction applied will be the negative of the scale-factor error expressed in percentage. If a scale factor is in error by -1%, then the corresponding ratio potentiometers will have these values increased by 1%. This is accomplished in the following manner: A prepunched card containing

the calculated values for each initial condition is inserted in an IBM Model 526 punched-card reader. The information on the punched card sets up two precision voltage dividers whose voltage outputs are of opposite polarity and equal to the calculated initial condition. The calculated divider output, the initial condition from a data-computer integrator, and the output from a potentiometer are summed in a servoamplifier. An associated motor generator is geared to the potentiometer such that the output of the potentiometer is equal and opposite in sign to the absolute scale-factor error when the servo is nulled. If the potentiometer is excited with the calculated initial-condition voltage, then angular shaft position of the potentiometer is proportional to the integrator scale-factor error. A second potentiometer is ganged to the first one and is wired into the voltage reference source used to position the gain potentiometers. This voltage reference is then changed by a voltage increment of the same percentage as the scale-factor error but opposite in sign.

After this operation is completed, a *go* signal sets up relay logic so that gain potentiometers corresponding to a particular integrator initial condition can be positioned. The card reader again sets a precision voltage divider to a predetermined value. Another servo operation is performed against a potentiometer located in the missile. After the servo has driven to a 5 mv null, the clutch on the potentiometer being positioned is dropped but a voltage comparator continues to sample the null. If this null is less than 30 mv, a *go* signal now steps the card reader and the entire operation is repeated.

A control panel will have facilities for position readout of all controller rotary switches. All rotary switches will also be capable of manual operation in order to perform autopilot and system checkout. Interlocks will also be made with the reference unit and the computer before a *ready* command to launch can be given.

Preset counter. The preset counter used in the ground parameter inserter is a dual-channel, transistorized unit that may be remotely reset. Each channel is independent of the other with the exception of a mutual ±30-volt power supply. Reference sources are 32-kc crystals with 2^5 countdown contained in a thermostatic-controlled oven giving a 1 kc ±0.001% output signal of 3-volt amplitude.

The 1-kc signal is then fed through a starting gate, amplified, squared, and introduced into a 2^{20} countdown chain. All 20 stages are capable of being preset from information contained on an IBM punched card. The reset signal is a −30-volt pulse of at least 10 msec duration. Presetting all 20 stages before introducing the start signal gives a counter resolution of 1 msec and a total counting time of 17.476 minutes.

The basic circuits contained in the preset counter are the same as those used in the *Sergeant* firing station except for the following changes:

(1) Two additional stages have been added to increase the total counting time.
(2) All stages may be preset instead of leaving the first two free running.
(3) The start signal is delayed until after presetting instead of both being introduced simultaneously.

In addition, the counter has been repackaged into a standard 19-inch rack panel using plug-in, modular construction and printed circuitry. All leads are brought out of Bendix connectors in the rear of the panel, making the counter completely capable of remote operation.

Servoamplifier panel. The servoamplifier panel consists of five plug-in, modular assemblies packaged in a standard 19-inch rack. All signal, power, and control leads are brought out of Bendix connectors in the rear of the panel making it capable of remote operation. This was done in order to physically locate the panel in the instrumentation room under the launching pad. Lead lengths at this location will be less than 200 feet rather than 1500 feet if the panel were placed in the blockhouse. Much data is known about noise levels and accuracies at the shorter distances from *Sergeant* flights, but no experience with lines approaching 1500 feet is presently available.

7. Roll Control System

The roll-control system (Fig 63) has been designed as a simple, proportional-control, gas-flow system, utilizing ambient-temperature nitrogen gas to produce the required thrust couple. Approximately 8 pounds of nitrogen will be stored in a spherical lightweight, titanium-aluminum-alloy bottle, pressurized to 3550 psig. Pressurization of

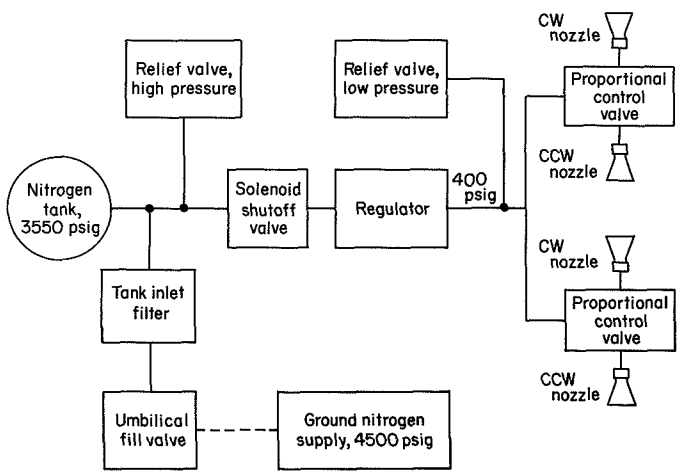

Figure 63. VIGS roll-control system

the bottle will be accomplished from a remotely located pressurization control unit and a 4500-psig ground nitrogen supply through a quick disconnect coupling in the third-stage umbilical plug.

The high-pressure nitrogen from the bottle will be regulated to a pressure of 400 psig before entering the proportional control valves. The regulator is one part of a combined package which also includes a solenoid-operated shutoff valve; high- and low-pressure relief valves; and a bottle-inlet filter. This combined package, manufactured by Sterer Engineering Company, threads into the inlet of the bottle and forms a part of the compartment mounting scheme. The other component of mounting utilizes a JPL-designed slip coupling that permits growth of the nitrogen bottle during pressurization.

Nitrogen leaves the regulator package through a dual output and is piped into two manifold nozzle assemblies. The two manifolds are mounted diametrically opposed on each side of the guidance compartment. Each manifold has two nozzles, 180 degrees opposed, thereby allowing either clockwise or counterclockwise torque couples. The gas is proportioned out of one or the other of the two nozzles by a two-stage, pneumatic servo control valve, The valves, manufactured by Raymond Atchley Company, have dual-coil torque motors that pilot the second-stage sleeve valves, routing the gas flow to the appropriate nozzle. Each nozzle is capable of producing approximately 10 pounds of thrust at maximum flow.

The high-pressure fill line will be steel, and the regulated pressure flow lines will be aluminum. All line fittings will be modified standard AN-type tube couplings. The modification will incorporate Butyl O-rings between the male and female halves of each coupling.

The first two nitrogen bottles have been received and are being evaluated at Wyle Test Laboratories of El Segundo. Prototypes of the servovalve and nozzle manifold have been fabricated and the assembly of these two items has been satisfactorily evaluated.

8. 6K-Motor-Gimbal Actuators

Early in the *Vega* program, the choice was made to pursue the development of an electromechanical rather than a hydraulic or pneumatic actuator. This decision was based on the success with the electromechanic rotary actuator developed for the *Sergeant* missile and the availability of a linear version of this same basic design. Lear, Inc., developed the *Sergeant* rotary flap actuator, and by incorporating a reciprocating ball screw to convert rotary motion to linear motion was able to adapt essentially the same design to the requirements of a gimbal actuator (Fig 64).

In this design (Lear 3107C) a dc motor drives through a powdered-metal proportional clutch and gear train to the nut of the ball screw, producing a linear thrust at stall of approximately 700 pounds. The actuator utilizes two powdered-metal clutches to produce the capability of bidirectional drive. A Belleville spring arrangement is incorporated as shock absorbers to limit the deceleration of the combined mass of the rocket nozzle and actuator to a value under 1 *g*. A Microsyn for position feedback and a tachometer for rate feedback are geared to the ball screw nut. In the 6K propulsion system the actuator is supported solely through *monoball* bearings at each end of the unit. The nonmovable end of the rod arm attaches to the bottom casting of the fuel tank, while the movable end is attached to the injector ring of the rocket nozzle.

A total of 12 3107C actuators were purchased to evaluate the design to the specified *Vega* environment and to support the development of 6K propulsion system. Four of these units have been in continual test since their receipt. This test program has consisted of bench testing to determine such running characteristics as hysteresis and load capability, and environmental testing to determine structural strength. Minor modifications such as changing the materials of the ball-screw shaft and bearing support were necessary before the vibration tests were considered satisfactory. However, the design generally exhibited an exceptionally high resistance to the severe vibration environment specified for equipment located

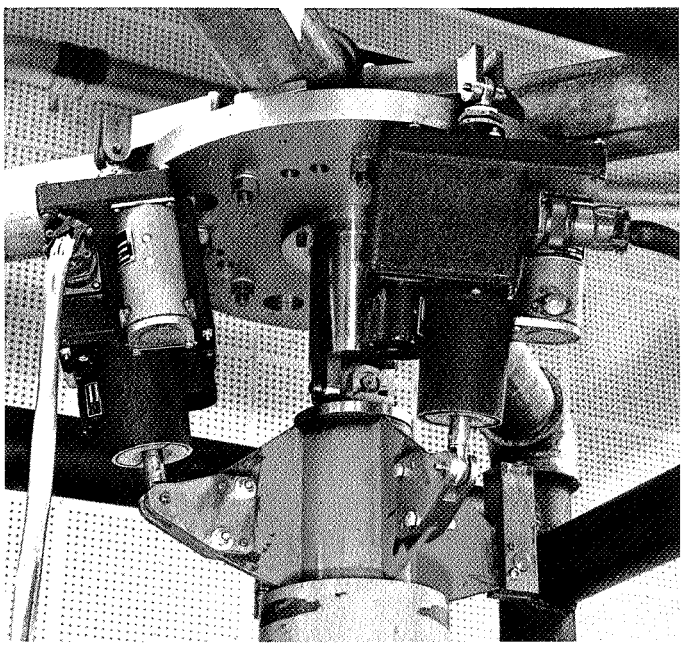

Figure 64. Motor gimbal and actuators

near the rocket nozzle. The balance of units is being readied for the firings of the 6K system scheduled for Edwards Air Force Base. These units have all been subjected to the flight-environment test specified for *Vega* third-stage equipment as a means of establishing a background of higher reliability.

Changes in the design of the flight version of the 6K propulsion system made it necessary to redesign the 3107C actuator to fit the available space envelope. Lear has accomplished the redesign using essentially the same components that were used in the 3107C and is now fabricating 28 of the new models. Two basic differences exist in the new 3135A actuator. The most important of these two differences is the use of a single dual-output clutch rather than individual clutches. The other change involves the use of a magnesium alloy for the body material. Tests show that this alloy is essentially unaffected by either hydrazine concentrate or vapor. The two changes incorporated have resulted in a considerable weight saving with the 3135A design calculated to weigh just under 10 pounds. The first units of the new design are scheduled for delivery in mid-January, 1960 and will be subjected to the same evaluation as the 3107C models.

Figure 64 shows the relative position of two 3107C actuators and the 6K rocket nozzle. The actuators are mounted on a simulated-rocket-nozzle test setup that has been used in evaluation of the gimbal actuators.

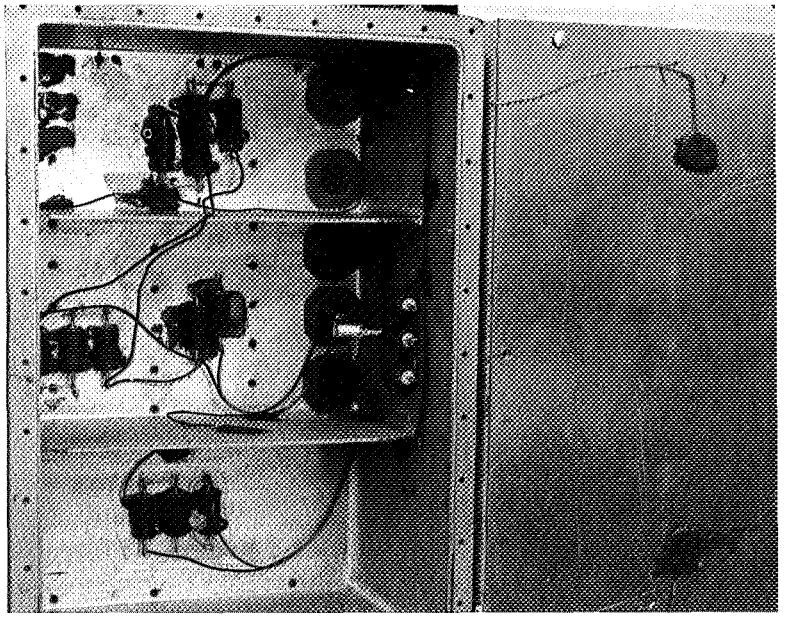

Figure 65. Guidance-compartment heat-test components

9. *Guidance Compartment Cabling and Evaluation Tests*

All cables within the guidance compartment have either single or double braided shields, primarily for RF shielding. Each major component is to be shielded with Monel rope at the parting surfaces. Extensive RF evaluation is scheduled on the Engineering Model guidance compartment for May, 1960. Optimum grounding points for the cable shields will be determined by this evaluation. A single-point grounding scheme for signal and power leads is being formulated from the detailed circuit information of the individual major components.

Preparations are being made to conduct heat tests on the entire guidance compartment to determine the requirements for both ground and flight compartment temperature control. Heat sources, based on power dissipation within each component, have been mounted in simulated flight components that were fabricated for the heat-test evaluation (Fig 65). Thermocouples have been mounted in critical areas of the compartment and in each major component to give a temperature profile during the testing. During the temperature testing, a heat source will be mounted above the guidance compartment to simulate the heat generated from the spacecraft power dissipation.

C. Attitude Control Analysis

The function of a space-vehicle attitude-control system is to maintain prescribed relationships between reference directions in the vehicle and external reference directions. Attitude control is required for at least two reasons during the periods of flight when thrust is applied: (1) the direction of rocket thrust is closely related to the direction of the vehicle axes, and (2) control torques are required to maintain the moment balance of the missile about its center of mass in the presence of misalinements or changes in the thrust direction, and in the presence of disturbances from such causes as fuel slosh or winds during passage through an atmosphere. Attitude control may

be required during periods of coasting to adjust the angular motion of the vehicle for such purposes as: performing guidance observations, aiming communication antennas, aiming power supplies dependent on solar energy, performing scientific measurements, or alining the vehicle prior to the application of thrust.

1. Powered Flight

A mathematical model describing the *Vega* third-stage vehicle dynamics has been developed. The model includes the effects of propellant sloshing, and the *tail-wags-dog* effect of motor inertia. The angular-attitude-control loop has been defined in the light of proposed guidance-system schemes. The transient response and steady-state errors of the attitude-control system have been evaluated analytically and by use of the analog-computer facility. Stability boundaries in terms of guidance gain and time constants are now being established.

The effects of bending on a simplified dynamic model are now being analyzed. The model is a three-mass representation with a parabolic, first bending mode assumed. The higher bending modes and the propellant dynamics are neglected. The guidance loop is also being neglected for the initial investigation.

2. Coasting Flight

SPS 5 contains an abbreviated functional description of an attitude-control system for the first *Vega* spacecraft. This system has been modified to provide flexibility and growth potential for use in both lunar and interplanetary probes.

a. Control system. The attitude-control system establishes and maintains the desired angular orientations of the vehicle and its major movable assemblies. The other payload systems to be oriented for *Vega* S-1 are: (1) the communications antenna, and (2) the solar panels. In the vehicle configuration chosen to facilitate relative motion between these systems, the solar panels are fixed to the vehicle hull, while the antenna is movable about one axis of the spacecraft. The system will provide two-axis control referred to the sun as a primary function. Acquisition of the earth-probe line as a third reference axis will also be performed.

b. System logic. Upon separation from the third stage, it is necessary that the spacecraft acquire the sun-probe and earth-probe primary reference lines. The initial tumbling rates about any axis are reduced by use of three rate gyros to less than 0.5 deg/sec. Simultaneously, or as soon as the probe has entered the sunlight, the sun is sought by the longitudinal (roll) axis of the spacecraft. Upon sun acquisition the vehicle is commanded to turn at a fixed rate of 0.2 deg/sec about its roll axis until the earth is acquired by the appropriate optical sensor.

Tumbling about three axes will be stopped and acquisition of the sun accomplished in less than 20 minutes after entering the sunlight, and acquisition of the earth completed within another 30 minutes.

c. Antenna orientation. The antenna rotates about one axis of the spacecraft, an axis which is perpendicular to the earth-probe-sun plane, and must be pointed toward the earth with an accuracy of about ± 8 degrees. The antenna system has its own servodrive which is actuated only after the vehicle has itself achieved 3-axis acquisition. This servosystem obtains its position signal from the earth optical sensor. The rate of rotation of the antenna and its effective reflected inertia as seen by the spacecraft are so small as to have negligible effect upon the stabilization of the vehicle and components.

D. Attitude Control Mechanization

Present planning calls for three-axes attitude control of the spacecraft in all but the earliest *Vega* missions. Although acquisition and control to the earth-probe line is designated as experimental in S-1, this and full maneuver capability become requirements in subsequent missions. To accommodate this expansion of capability, the attitude-control-system development is directed toward the creation of a basic control package that is capable of satisfying S-1 requirements and suitable for additions as needed in later missions.

An advanced system (Fig 66) having full maneuver capability consists of three rate-gyro modules, three sensor modules, three switching-amplifier modules; and the required fuel-storage tank, regulator and control jets necessary for the operation of the basic attitude control system. Added to this are the telemetry fuel totalizer and control module which instrument this system for full maneuver capability. The control module not only houses

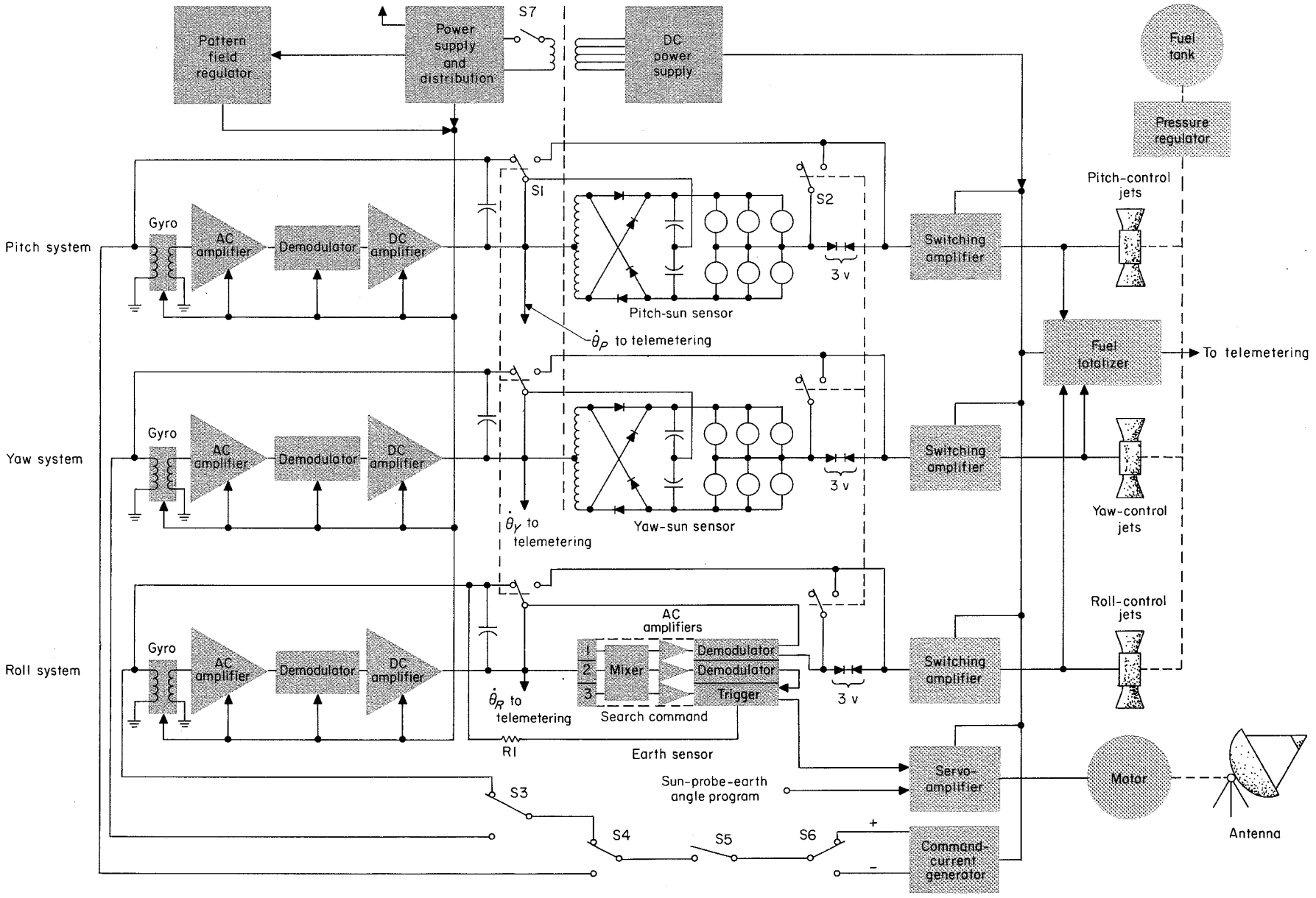

S1 Mode switch
S2 Mode switch
S3 Roll-yaw command
S4 Pitch-roll-yaw command
S5 Command execution
S6 Command polarity
S7 Solar-panel erection

Mode 1 Acquisition, cruise
Mode 2 Premaneuver
Mode 3 Maneuver

Figure 66. Attitude-control system

the control switching but serves also as a junction box and patch panel so that programming modifications can be readily accomplished without disturbing the basic-system elements.

Three modes of inflight operation are required to accomplish the acquisition, cruise, and maneuver functions to specified accuracies. During the acquisition and cruise phases (Mode 1), position- and rate-error signals are series-mixed and fed to the switching amplifier whose deadband is set to prevent valve-actuation commands until the error position exceeds 1 degree. Wide deadband limits are maintained throughout these phases of operation to prevent excessive use of fuel during long periods when precise control is not required.

In the premaneuver mode (Mode 2) deadband limits are reduced to 0.1 degree in order to cage the rate gyros more accurately to the position references prior to the maneuver phase. In Mode 3 (maneuver), the position references are dropped, and the gyro inertial references are used to perform the maneuver. In this mode, position signals are derived by integrating the rate gyros, and the switching amplifier deadbands are maintained at 0.1 degree. Maneuver commands are executed by applying a current to the gyro torquing coils. The control loops act to maintain the position errors within deadband limits. For missions which do not require maneuver capability, the control module will be simplified by omitting all switches and integrating capacitors.

1. Maneuver Command System

Attitude maneuvers of the spacecraft are accomplished by injecting a precisely controlled current into the gyro torque coil for a specified length of time. Initial-acceleration lag errors and final settling errors are reduced substantially to zero by using an integrating capacitor in the gyro torque-coil circuit. The capacitor stores the instantaneous difference between the time integral of command velocity (command position) and the time integral of actual velocity (actual position) and forces this difference to zero (within the amplifier deadband) after the command is terminated. Approximate response of the spacecraft to a commanded maneuver is shown in Figure 67.

The test setup block diagram is shown in Figure 68. All components used in the tests are breadboards of actual flight equipment (except the analog simulation of the spacecraft). The first step in testing the system was to set the command current to produce a prescribed steady-state velocity of the spacecraft. The velocity was

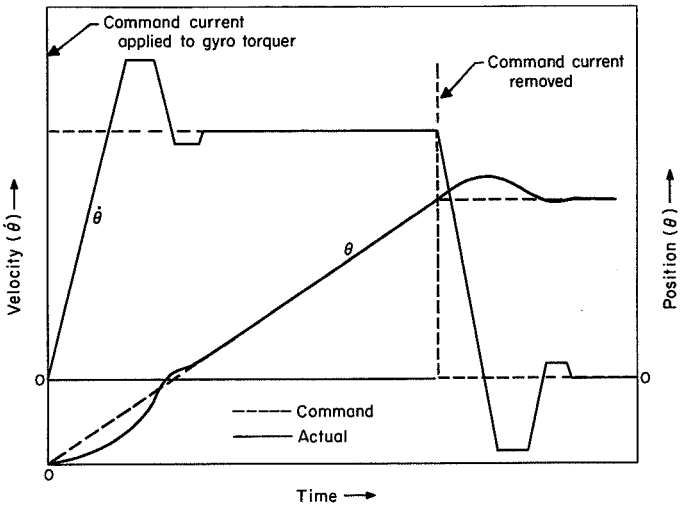

Figure 67. Approximate response of spacecraft to maneuver command

first set at 0.15 deg/sec, and several runs were made by timing the duration of the command current for corresponding angles.

Angle commands from 5 to 360 degrees, in 30 to 40 tests, showed an rms error of about 0.07 degree with a total error spread of ± 0.2 degree and no clear dependence on distance moved. Angular rates up to 0.2 deg/sec were used in the tests. Reading accuracy on the indicator dial used was about ± 0.05 degree and timing accuracy was about 0.3 second. Deadband uncertainty was removed by always taking readings when the error voltage (E_c) passed through zero.

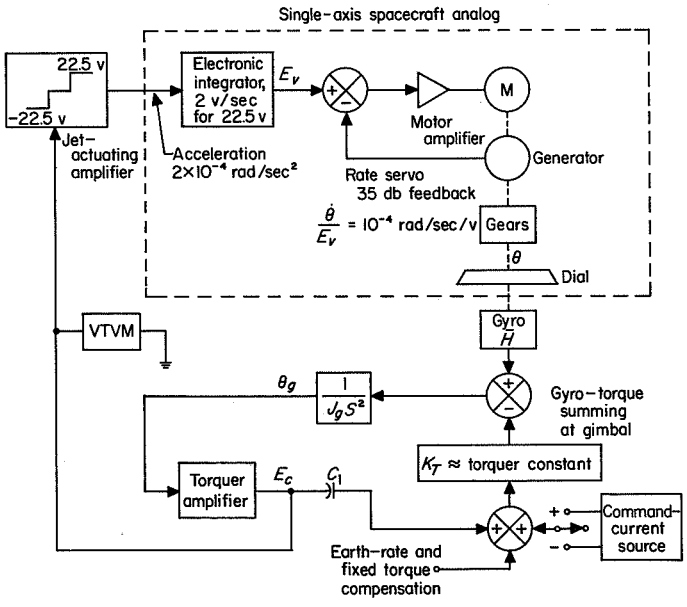

Figure 68. Maneuver-command test setup

The command maneuver system as tested has four principal sources of error:

(1) Stability of gyro-torquer constant (ratio of steady-state-input angular rate to torquer current). Torquer current here is the product of pattern field times control-field currents. Ideally, for constant pattern field current, the input rate is directly proportional to control-field current. Variations of torquer constant with gyro environment has not yet been investigated.

(2) Accuracy of timing the duration of the command current.

(3) Regulation of pattern-field current with temperature and power supply variations.

(4) Regulation of command-current source with temperature and power-supply variations.

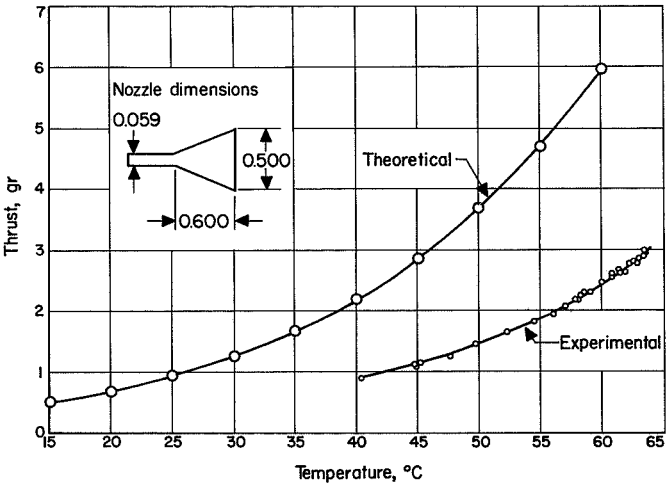

Figure 69. Theoretical and experimental thrust vs temperature for water vapor

2. *Thrust System Experiments*

A method of accurately determining low thrust was necessary in order to evaluate miniature-nozzle designs and fuels for a vapor-pressure attitude-control actuation system. Calculations indicated thrust levels up to 6 grams can be expected from a nozzle of optimum design.

The first tests utilized the water pressure vaporization as the propellent force. Water temperature, vapor temperature, and vapor pressure were monitored. This system was designed to operate in a vacuum at vapor pressures up to 5 psia. Tests have been made at temperatures up to 71°C. Test results thus far have not as yet correlated theoretical and experimental data. As shown in Figure 69, test results thus far indicate thrust levels of 50 to 60% of the calculated values. Instrumentation difficulties and orifice configuration are possible explanations for this discrepancy. For these tests, a sharp-edged entrance orifice was employed which will be rounded for further testing.

Several problems have arisen in the investigation of vapor-generation systems. The large surface areas required to supply vapor at demanded rates, thermal transfer to the evaporating surface, condensation and liquid entrapment are all problems for which satisfactory answers do not exist. As a result, emphasis on the development of these techniques has been reduced and present efforts are directed toward the design of cold-gas supply systems for early *Vega* missions.

To facilitate thrust measurements, a torque-test fixture shown in Figure 70 has been fabricated and placed into operation. The fixture measures low-thrust reaction levels in the range of 0.1 to 100 gm-cm and is designed to accommodate testing of both cold-gas and vapor-pressure systems. The measurement of force is accomplished by a torque-rebalance technique which makes use of a shaft-mounted Microsyn and permanent-magnet torquer as the loop sensor and actuator. An external electronic package provides signal amplification and demodulation of the Microsyn signal and completes the rebalance loop through

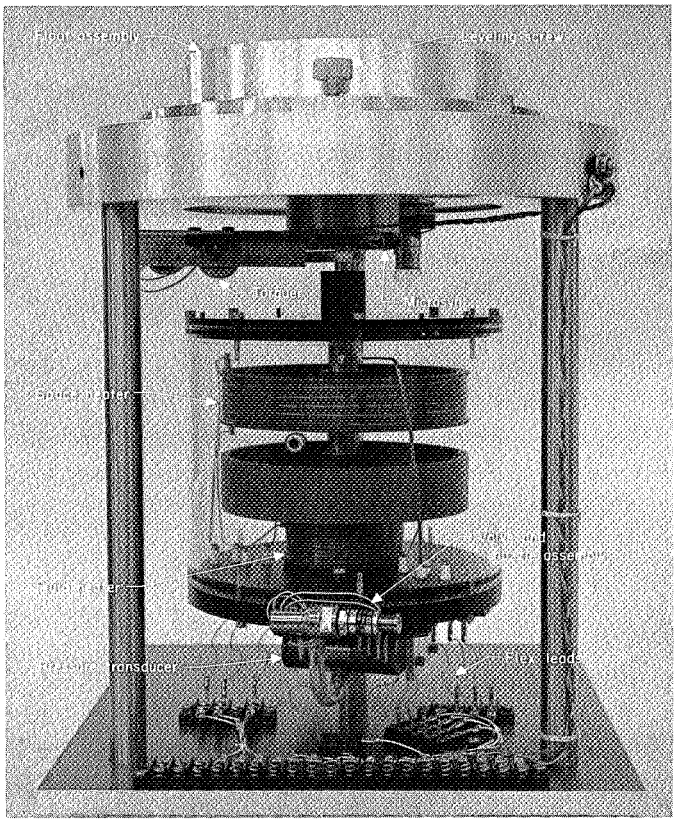

Figure 70. Torque-test fixture

a stabilization network and power amplifier. In operation, the entire assembly has a natural frequency of 5 cps with an 0.6 damping ratio. Deflection of the assembly is maintained within 1 minute of arc under full-thrust conditions.

In Figure 70, the upper assembly contains an axial and radial suspension plus the Microsyn and torquer used in the rebalance loop. Axial support is accomplished through the use of a mercury float bearing capable of supporting a 20-pound load. Two miniature instrument ball bearings provide radial support of the assembly. In operation the entire moving assembly is balanced and leveled to relieve loading of the radial support bearings and thereby reduce the coulomb friction level of the suspension to a minimum. Tests performed on the suspension indicate that coulomb friction restraint is less than 100 dyne-cm. The lower assembly contains a vapor-pressure generator with integral heater and pressure transducer. Provisions are also included for the measurement of temperature at several locations within the vessel. Flex leads located at the base of the unit carry all connections to the torque-rebalance elements, heaters, thermocouples, pressure transducer, and valve-actuator coil.

3. Electronic Development

a. Combination rate and integrating-gyro loop. For the first several *Vega* missions which do not include the requirement for a payload mid-course or terminal maneuver, the gyros will operate as rate gyros to provide rate-stabilizing signals during the acquisition phase. On later flights, however, when payload maneuver capability will be required, the gyros will be called upon to furnish positional information during the maneuver phase: i.e., they will have to function as rate-integrating gyros during this period. It was therefore decided early in the program to design a gyro loop which could provide both rate and positional information.

The gyro selected for the attitude-control application is a modified version of the Minneapolis-Honeywell, floated miniature integrating gyro (MIG). This gyro exhibits a rate sensitivity of about 2 deg/hr which is superior by more than an order-of-magnitude to conventional spring-restrained rate gyros and shows outstandingly low-drift characteristics as well. The gyro loop was made essentially independent of flotation-fluid viscous damping by substitution of a low-viscosity fluid for the conventional fluorolube in the gyro and accomplishing the necessary damping by electronic circuitry. This change made it possible to eliminate all gyro-heater and temperature-control circuitry with a corresponding saving of power and increase in gyro-loop reliability. Spin-motor-bearing preload will also be reduced in order to achieve maximum gyro life. The manufacturer has guaranteed a minimum life of 2000 hours for the modified units.

A simplified block diagram of the gyro control loop operating in both the rate and rate-integrating modes is shown in Figure 71. With the switches in Position 1, the torquer control current is proportional to gyro-input-axis rate. Prior to the maneuver phase the switches are turned to Position 2, in which case the dc-amplifier output voltage is a measure of both gyro-input axis rate and position. To prevent system saturation (loss of reference) during the transient switch-over period, and also to allow the required command rates, the capacitor size is necessarily large. Total capacity required will be approximately 4000 microfarad. Special low-leakage, non-polarized tantalytic capacitors have been ordered for this application. Capacitor volume per axis is estimated to be 7 to 10 cubic inches. Passive integration was considered more desirable than integration by using an operational amplifier with its attendant complexity and drift uncertainty. The narrow band, 400 cps filter shown in the diagram was found to be necessary due to gyro-torquer-signal-generator electrical interaction in the Dualsyn.

The loop has performed well in a gyro vibration test with the gyro subjected to sinusoidal forces of up to 20 g in all three axes. Circuit redesign with the aim of reducing the number of components required for loop mechanization is presently under way. Equipment to test the modified gyros in the control loop has been built and will be supplied to the gyro manufacturer as part of the purchase agreement. Temperature and other environmental tests will begin shortly. Gyro acceptance-test procedures are being developed, and work on the three-axis gyro package has also been started.

b. Switching amplifier. The actuating amplifier of the *Vega* attitude-control system is required to perform the

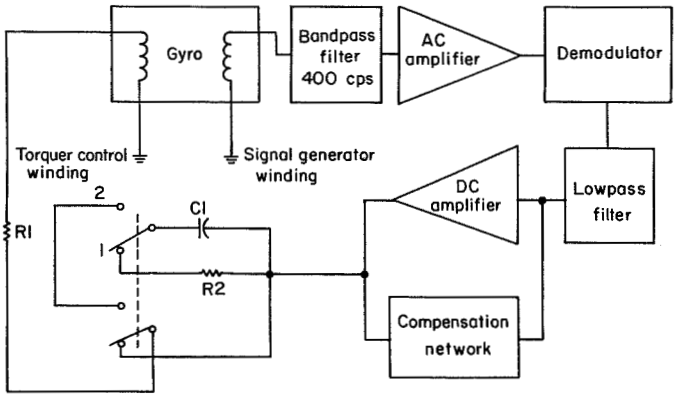

Figure 71. Gyro control loop

basic function of supplying an excitation signal to the valve solenoids when the sensor angle (or velocity) exceeds a predetermined value. It must perform this function in three distinct periods of system operation: (1) acquisition, (2) transition from acquisition to limit cycle, and (3) limit cycle.

During acquisition it may be assumed that error angle and velocity greatly exceed the desired values so that the amplifier is fully *on* as the payload moves toward the desired attitude-control angle, and the velocity decreases to its limit-cycle valve. As the payload enters one side of the deadband, the amplifier turns *off* instantaneously, and as the payload emerges on the other side of the deadband the amplifier comes *on* in the same manner.

Transition from acquisition to limit cycle occurs when the payload moves with near-limit-cycle velocity and alternately enters and leaves the deadband boundary on the same side as the system approaches limit-cycle operation. During this period the amplifier is required to prevent solenoid excitation for 0.1 second after the error angle is momentarily reduced to less than its limit-cycle value. This feature will increase valve reliability, conserve fuel, and reduce power consumption.

When the system has finally reached the limit-cycle mode of operation, the error-angle periodically reaches the limit value on opposite sides of the deadband. During this *cruising phase* of the flight the amplifier is required to provide excitation to the solenoids for at least 0.1 second (the minimum impulse time) even though the triggering pulse (0.002 second) may be short.

The circuit which mechanizes the required functions is shown in Figure 72. Triggering occurs at approximately 0.6 volt. Voltage gain of the amplifier is approximately 5×10^4. Thus, if the sensor-error voltage exceeds 0.6 volt, transistor Q3 is rapidly driven into saturation, causing breakdown of the zener coupling diode and thus triggering the positive-feedback timing circuit. As long as the error input keeps Q3 in saturation (acquisition period) the combined zener and dc feedback currents will continue to keep the timing circuit in the *on* condition.

If the error signal momentarily decreases to a value less than that necessary to keep Q3 in saturation, the dc feedback current to the base of Q4 is insufficient to hold the timing circuit in the *on* condition, and the voltage across the actuating solenoid goes to zero. The timing capacitor now applies an exponentially decreasing positive bias to the base which prevents turning *on* of the timing circuit for 0.1 second even if Q3 is again driven into saturation before the end of the lock-out period. This mode of amplifier operation is desired during

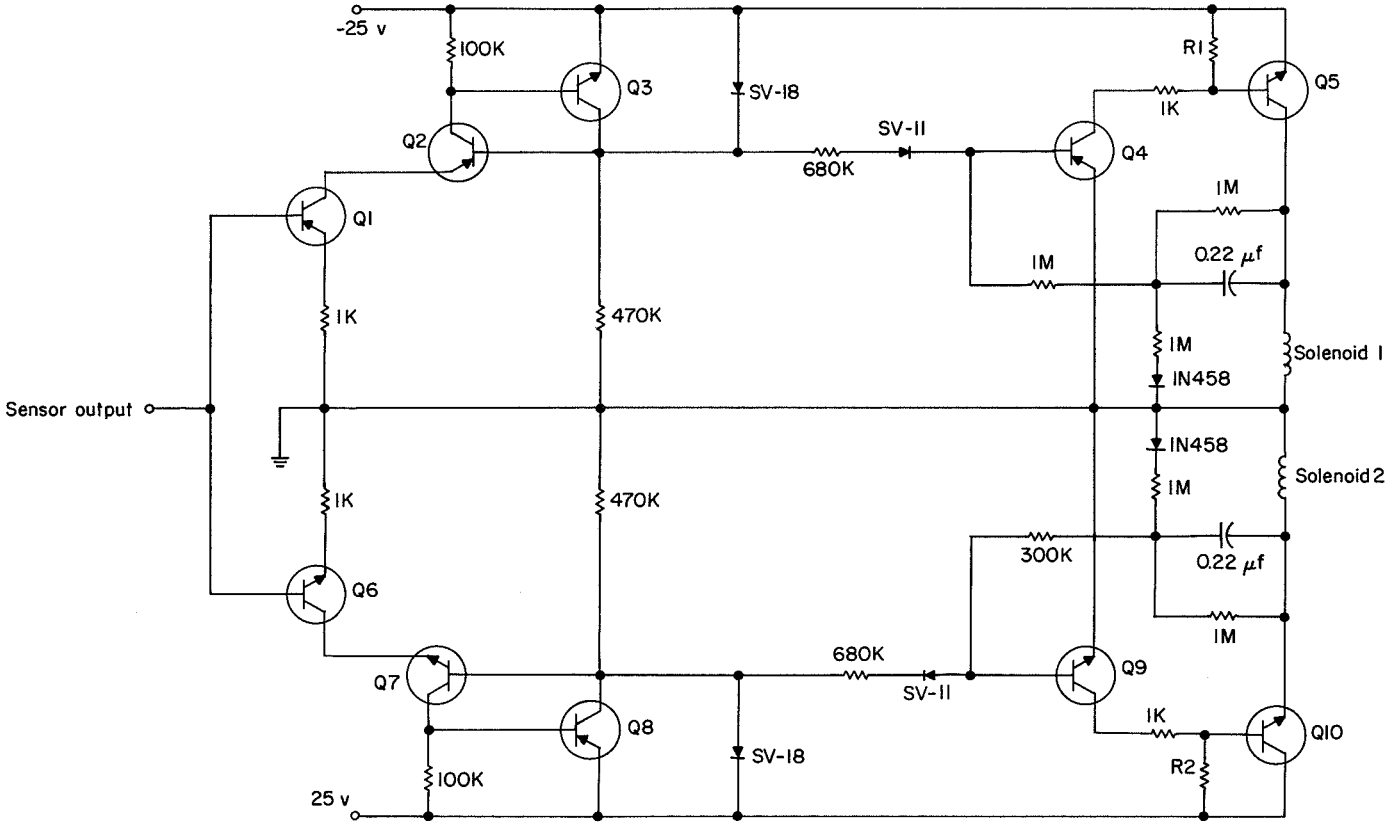

Figure 72. Switching amplifier circuit

the transitional period from acquisition to limit-cycle operation.

If an error signal exceeding the threshold value is applied for a short period of time, as during limit-cycle operation of the system, the positive-feedback timing circuit will instantaneously apply the full supply voltage to the solenoid. The ac feedback is adjusted to keep the timing circuit in the *on* condition for 0.1 second even if Q3 drops out of saturation in less than 0.002 second.

A noteworthy feature of the actuating amplifier circuit is the absence of hysteresis which would be undesirable from the system point of view. Hysteresis effects are minimized by preceding the positive-feedback timing circuit with a high-gain linear amplifier.

c. Fuel-totalizer electronics. The measurements of total fuel consumption at any time during flight will provide useful information to assess *Vega* attitude-control-system performance. Initial velocity at payload separation, payload solar-pressure unbalance, performance of the course-correction stabilization system, effect of micrometeorite impacts, and control-system limit-cycle velocity, can be determined by monitoring the fuel expenditure. Since total impulse is directly related to the amount of fuel used, an impulse totalizing system on the payload will furnish the desired information. Design specifications for the totalizing system are:

(1) The system should be completely independent of earth-probe communication in its data-storing capability.
(2) Resolution to the expected minimum impulse (0.001 lb-sec) is required for complete fuel totalization.
(3) Total storage capability of system will be 150 lb-sec.
(4) It is desirable that the totalizer be adaptable to both hot- and cold-gas actuating systems.
(5) Readout resolution is to be 0.2% of total impulse (0.30 lb-sec).
(6) Desired system accuracy is to be better than 5%.
(7) Power, weight, and volume are to be minimized without impairing system reliability.

Figure 73 presents the block diagram of a totalizer adaptable to either a hot- or cold-gas actuating system. A transducer, whose dc output is proportional to gas pressure, feeds a current-controlled oscillator through three separate relays which are normally open, but close in any combination upon actuation of the corresponding valve solenoids. Weighting of individual nozzles is accomplished by proper scaling of the current-summing resistors.

A simplified version of the totalizer, to be used with a cold-gas actuating system such as will be employed for early *Vega* flights, is shown in Figure 74. Since gas pressure is regulated here, the transducer and relays can be eliminated so that the summing resistors connect directly to the actuating solenoids via a simple voltage-regulating circuit. Yaw, pitch and roll nozzles are scaled to give 0.01, 0.014, and 0.016 pounds of thrust so that the summing resistors are in the ratio of 1.000, 0.715, and 0.625 to provide the appropriate currents to the oscillator. Oscillator output is fed to the counter-readout unit which, in turn, provides a straight binary readout to telemetry.

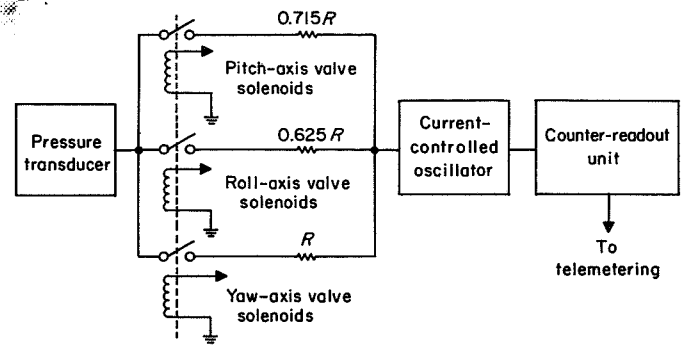

Figure 73. Hot- or cold-gas totalizer

Since minimum impulse time, corresponding to attitude-control-system limit-cycle operation is to be approximately 0.1 second, a lower oscillator frequency limit of 200 cps was selected to give 20 counts per minimum impulse period in pitch. Thus, a one-count uncertainty in the digital counter-readout unit does not degrade system accuracy beyond the desired 5%. Maximum oscillator frequency for a mode of operation during which torque is applied to all three axes is 800 cps. At room temperature the oscillator exhibits a linearity of better than 0.25% over the required 4:1 frequency range with a degradation to about 1.00% at the 60 and $-10°C$ temperature limits specified for *Vega*. Supply voltage variations of up to $\pm 20\%$ had no noticeable effect on oscillator linearity. Long-term stability tests have shown oscillator drift to be less than 1 cycle per week at room temperature.

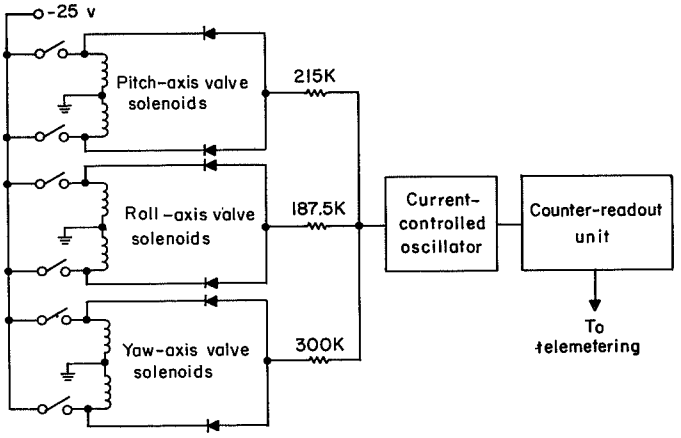

Figure 74. Simplified cold-gas totalizer

The counter-readout unit consists of twenty-two stages. The total number of stages required is determined by the ratio of total stored impulse to resolvable impulse multiplied by the number of counts per resolvable impulse. Total cumulative count to be accommodated is therefore $20 \times 150{,}000$ or three million, requiring 22 binary stages. The nine last stages will provide readout to telemetry, satisfying the resolution specification of 0.2%. A manual reset line which permits clearance of the entire register for test purposes has been included in the counter design. The counter has been temperature tested to *Vega* specifications and performed satisfactorily.

d. Reference-current sources. Two reference-current regulators are required to provide precisely controlled gyro-torquer excitation during the maneuver mode. The function of the command-current regulator is to supply gyro-control-field torquing current upon ground command. Both this and the pattern-field exciter must be accurate to 0.1% under all expected environments in order to satisfy the maneuver accuracy requirements of 0.1 degree.

A command-current regulator design has been completed and environmentally tested. As shown in Figure 75, it consists of independent positive and negative supplies which rely on the high collector resistance of silicon transistors for their operation. The output current is controlled through a comparison of the voltage across the output-stage emitter resistor with that of a reference zener diode chain. Output-transistor beta variations are compensated by passing the driver-stage collector current through the load. Because of this connection, the monitoring-resistor current differs from load current by only the magnitude of input-stage base current; hence for minimum stage betas of 50, the output stability is controlled to 0.04%. Compensation for temperature variations is achieved by providing two forward-biased silicon diodes in the reference chain whose characteristics track those of the transistor base-emitter diodes. The effect of supply-voltage fluctuations on output current is offset by the application of supply voltage to the monitoring resistance through R_c. Regulator output impedances of 200,000 ohms have been observed. Although output-voltage variations can instantaneously cause 1% regulation errors because of this finite internal impedance, maneuver accuracy is unaffected since the integrated output voltage over the entire maneuver is zero. Tests performed on these regulators have demonstrated a control stability of 0.04% under all environmental conditions.

A reference-field-regulator configuration is presently undergoing stability tests in the laboratory. With compensation techniques similar to those employed in the command-current regulator, this configuration will simultaneously provide excitation to all three reference fields connected in series.

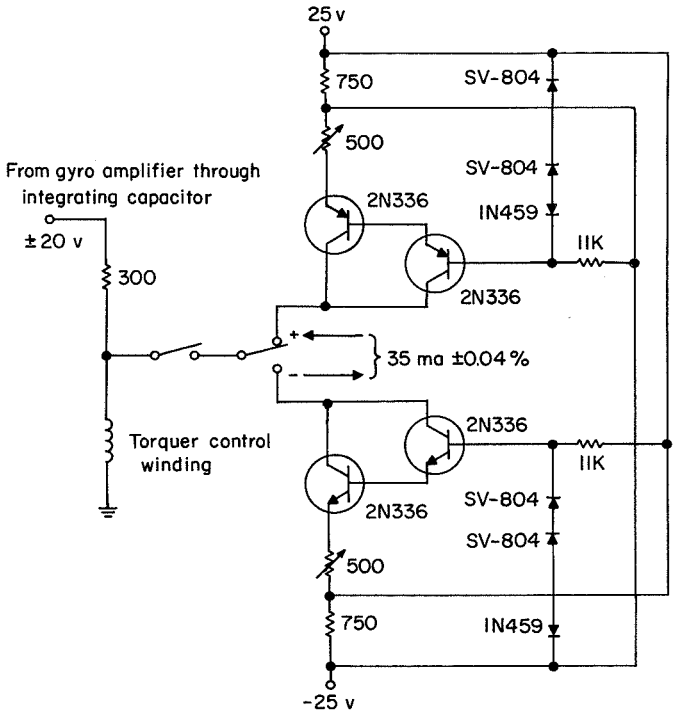

Figure 75. Command-current regulator

4. Actuator-System Development

The attitude-control actuator will employ a cold-gas system pressurized on the ground prior to flight. The mechanical components comprising the system are the gas-pressure storage tank, regulator, and six nozzle valves with interconnecting piping.

a. Valves. The actuator valves are to be an integral assembly with the nozzle. The nozzle is a separable part in order that it may be changed as required to provide different thrust levels. The valve will be a coaxial type. Because of the unknown status of plastics and non-metallic materials in the space environment, the valve seat mechanism will be constructed of metal or mineral materials. The specifications placed on the valve are as follows:

(1) The valve shall require no more than 2 watts at 28 v dc for actuation.
(2) The opening and closing times for the valve shall be less than 10 milliseconds.
(3) The valve shall be able to open against a line pressure of 50 psia.

(4) The allowable internal leakage of the valve measured by a mass-spectrometer leak detector shall not exceed 1 cc per day. (The external leakage is considered zero since the coaxial valve lends itself to hermetic sealing techniques in design.)

To satisfy these requirements, a survey of valve manufacturers was initiated. Three small coaxial valves were procured from Eckel Valve Company for evaluation. Preliminary testing disclosed reliability difficulties in the valve design; one failed to open on receipt and the second failed after 67,000 cycles of operation. The preliminary procedure employed in the testing of these and other valves consists of life cycling the valve while periodically checking leakage. To facilitate these tests, an automatic cycling fixture has been fabricated which performs a leak detector test at 300 cycle intervals. These tests performed on the Eckel valves indicated that during normal operation the leakage rates were well below the 1 cc per day specified tolerance.

To fully satisfy all requirements, proposals were invited from several manufacturers which utilized a hard-seat design. On the basis of proposals received, the Whittaker Controls Company has been selected as the flight-valve source and 36 units have been ordered. Delivery of initial units is expected in 90 days.

Concurrently, a hard-seat valve investigation has been carried on at JPL in an effort to evaluate a number of seating configurations. To date two valves have been fabricated which are presently being subjected to leak tests. Early indications are that leakage rates for the hard-seat valves are greater than those obtained on soft-seat units.

b. Regulators. For the cold-gas system, it is necessary to use a regulator. The gas under consideration, at the present time, is dry nitrogen stored at a pressure of 3000 lb/sq in. The following requirements have been established for the regulator:

(1) Regulation ratio 400 psi to 15 psi nominal.
(2) Upstream pressure decay 10 to 1.
(3) Downstream pressure tolerance ± 5 psi nominal.
(4) Internal leakage will be held to 1 cc per day. External leakage can be 1 cc per hour.
(5) The regulator will accommodate a mass flow of 10^{-3} lb/sec.

The downstream pressure for design convenience may be anywhere from 15 to 50 psi with tolerance of ⅓ of the regulated pressure. The regulator will be fitted with a relief valve in the downstream side that will be set for a pressure of twice the tolerance level. Exhaust from the relief valve will be vented so that its net thrust effect will be zero.

c. Pressure vessel. A storage pressure of 3000 psi has been selected for the cold-gas storage. The amount of gas to be stored for the control system is 2.5 pounds of nitrogen in a spherical pressure vessel approximately 8 inches in diameter. At operating temperature, the nitrogen will have a specific impulse of 76 seconds.

E. Space Navigation and Terminal Guidance

1. Lunar Mid-Course Maneuvers

Studies of the mid-course maneuver for lunar missions are continuing, with attention being given to the following problem areas: (1) the magnitude of the maneuver as a function of the choice of trajectory (slow or fast) and (2) control of additional variables at the destination (flight time or speed).

With reference to the first area, the trajectory chosen for a given mission will often be that one which gives the maximum useful payload, taking into account the boost, the mid-course, and the retro phases. Consideration of the boost and retro phases indicates that the trajectory should be as slow as possible, although the payload gain for trajectories slower than 70 hours (transit time from earth to moon) is insignificant. However, the variation of the magnitude of the mid-course maneuver with the trajectory transit time must be considered. In addition, the results may be strongly affected depending on whether or not additional destination variables are controlled.

2. Orbit Determination by Radio Tracking

The direction and magnitude of the correcting impulse for a mid-course or retro maneuver is determined from radio-tracking data. The radio-tracking data is contaminated by random noise from many sources. For example, angle-tracking data is subject to random errors caused by mechanical deformation of the tracking antennas and also to receiver noise which causes jitter in the antenna servos. A digital computer program (SPS 2) is used to

determine the injection conditions for the orbit which fits the measured data with the least-square error. These estimates of the injection errors can be used to determine the mid-course correction. Therefore, for error analysis, it is necessary to know how accurately the orbit can be determined from measured data. A method of finding the accuracy of orbit determination was described in *SPS 5*. This method has been programmed on the digital computer and some preliminary results are described here.

Before presenting the preliminary results, however, it is useful to review the assumptions concerning the characteristics of the noise contaminating the radio-tracking data. As described in *SPS 5*, it is assumed that each type of data from each station can be contaminated by several independent noise sources. The noise from each source is specified by an idealized autocorrelation function $R(t)$, where t is the correlation interval in seconds. This idealized autocorrelation function has a constant value of σ^2 from 0 to T as shown in Figure 76; where σ^2 is the variance of the particular kind of noise, and T is the time interval over which the noise is correlated. In other words, it is assumed that the noise is perfectly correlated over any interval less than T and uncorrelated over any interval greater than T. In addition, so far, it has been approximated that σ^2 and $R(t)$ do not vary with range.

A 76-hour lunar trajectory has been used for the preliminary study. The powered flight portion of this trajectory includes a coasting period between second-stage burnout and third-stage ignition. Third-stage burnout occurs over the South Atlantic Ocean. The closest approach time is 76.3 hours when the probe passes 300 miles from the surface of the moon.

It is assumed that while the probe is on this trajectory it is tracked from Johannesburg and Goldstone. Table 10 shows the assumed characteristics of the noise for each station. Note that there are several independent sources

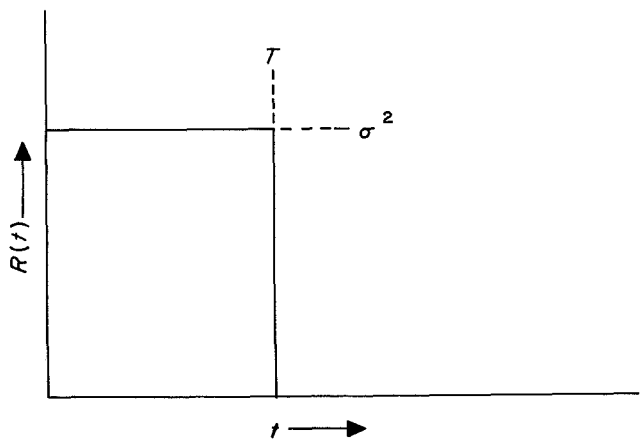

Figure 76. Idealized autocorrelation function

Table 10. Assumed noise characteristics

Station	Type of data	σ	T
Johannesburg	Elevation angle	0.10 degree	< 10 seconds
		0.01 degree	1 minute
	Azimuth angle	(same as elevation)	
	Range rate	1.0 meter/sec	< 10 seconds
Goldstone	Declination	0.01 degree	5 hours
		0.01 degree	1 minute
		0.03 degree	< 10 seconds
	Hour angle	(same as declination)	
	Range rate	0.4 meter/sec	< 10 seconds

of angle noise. For both Johannesburg and Goldstone, the angle noise with $T < 10$ seconds is mainly due to receiver noise which causes jitter in the angle servos. The low-frequency noise component for Goldstone ($T = 5$ hours) is due to structural deflections of the large antenna, which cause a random variation between the boresight axis and the electrical axis (*SPS 2*, p 38). It is assumed that all steady bias errors were measured and that the data was corrected for them. The other angular noise component ($T = 1$ minute) for Goldstone and Johannesburg is intended to roughly approximate some autocorrelation functions obtained from *Pioneer IV* data. This noise is probably due to variations in the refraction of the atmosphere. For these noise components the effectiveness of the Goldstone angle data is almost entirely determined by the low-frequency noise for which $T = 5$ hours. The effectiveness of the Johannesburg angle data is almost entirely determined by the servo jitter noise. It is assumed that the probe contains a transponder and there is a transmitter at each station so that accurate doppler measurements can be made. The doppler accuracy may be limited by transmitter frequency stability, and probe acceleration of round-off error in counting to the nearest doppler cycle.

In addition, it is assumed that each type of data from each station is sampled once every 10 seconds. The probe is considered to be above the horizon at either station when the elevation angle exceeds 5 degrees. The station at Johannesburg has a maximum range of 25,000 miles and the Goldstone station has a range greater than 250,000 miles. It is intended that the characteristics of the Johannesburg station approximate those of the JPL downrange station used at Puerto Rico for tracking *Pioneer IV* except that two-way doppler has been added.

Figure 77 shows some of the results from the preliminary study of orbit determination. The number of hours after injection is measured along the abscissa. The ordinate shows the semi-major axis of the 40% probability ellipse of the critical miss components. The critical miss

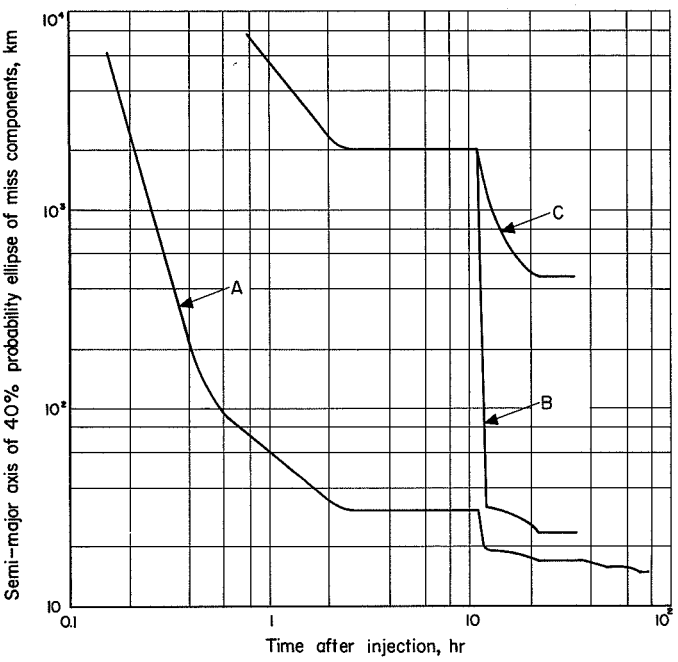

Figure 77. Accuracy of orbit determination

components are defined to be the two components of miss distance measured in the plane perpendicular to the velocity vector at closest approach. The component of miss distance measured along the velocity vector at closest approach results essentially in a time-of-flight error which is not considered here. A semi-major axis of about 20 km or 12 miles is considered satisfactory orbit determination for *Vega* missions.

Curve A in Figure 77 shows the accuracy of orbit determination on the 76-hour lunar trajectory for the above station-accuracy assumptions. Johannesburg tracks the probe from injection until 2.4 hours after injection when the probe goes out of range at a slant range of 25,000 miles. The semi-major axis remains constant at 30 km until Goldstone acquires the probe at 11 hours. When the probe goes below the horizon at 22 hours, Goldstone has reduced the semi-major axis to 17 km. Curve B shows the effect of not measuring range rate at Johannesburg. Curve C shows the effect of not measuring range rate at either Johannesburg or Goldstone. The calculations for these curves were terminated at 30 hours, since a mid-course maneuver would have been made by this time and it would be necessary to redetermine the orbit.

At the present time additional computer programming is being undertaken to include the following effects: corruption of the orbit determination by a mid-course maneuver, expected dispersion at injection, data from Baker-Nunn camera sightings, and determination of the accuracy of tracking estimates of energy and time-of-flight error of the probe.

F. Trajectory Studies

1. Lunar Studies

The simulation of the *Vega* guidance equations into the three-dimensional, powered-flight trajectory program is proceeding. It has been decided to program these equations for simulation in two different modes. Mode I will assume a perfect guidance system; i.e., no component errors, platform drift, etc. Mode II will simulate an imperfect guidance system and allow errors to be introduced at will to determine their effect on miss distance at the moon. In Mode II, the effect of leveling, erection, orientation, and autocalibration errors during preflight checkout will be included.

a. Near-earth lunar trajectories. Of particular interest are the geographic locations of the powered portions and injection points of lunar trajectories. It has been found that these locations depend strongly on the azimuth-of-fire and declination of the moon. As for the interplanetary case, given a fixed launch azimuth and firing date (which determines lunar declination), two firings per day are permissible. However, the locations of the injection point for these two firing times differ radically. This phenomenon is illustrated in Figure 78. In this figure are shown the loci of injection points as a function of launch azimuth (σ_L) for lunar declinations of minimum, zero, and maximum. Launchings for injection in the Pacific Ocean area occur 14 to 17 hours later (depending on launch azimuth) than launchings for injection in the South Atlantic and Indian Ocean areas.

It is reasonable to reject all cases of injection in the Pacific area because of the numerous practical problems of missile design, guidance, and tracking which arise when considering them. By restricting launchings to those cases of injection in the South Atlantic area (within the dotted area, Fig 78) and further restricting launch azimuths to the southeast (90 to 114 degrees), a number of advantages are apparent: (1) the coast time of the second/

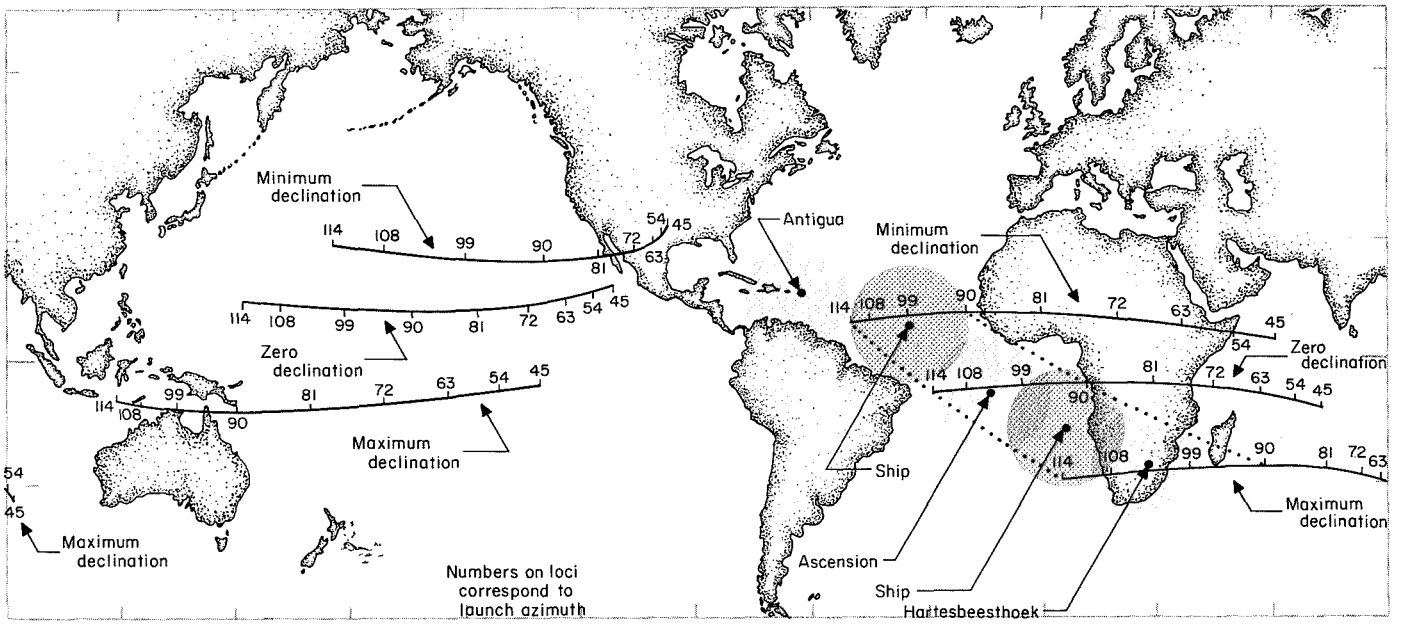

Figure 78. Injection loci for lunar trajectories

third-stage parking orbit is minimized, and (2) the range instrumentation facilities of the Atlantic Missile Range can be utilized for tracking and telemetering purposes.

b. Circumlunar trajectories. A possible future *Vega* mission would be to send an instrumented probe around the far side of the moon and have it return to the near vicinity of the earth. The chief purpose of such a mission would be to photograph the unseen (by earth) part of the lunar surface. The standard trajectory for this mission would necessarily have to satisfy several constraints. Perhaps the three most important constraints are that the probe: (1) pass around the far side of the moon; (2) miss the lunar surface by a specified amount; and (3) miss the earth by a specified amount on returning from the moon.

A tentative circumlunar trajectory has been obtained which satisfies these constraints. In Figure 79 the positive z axis of the earth-centered, space-fixed coordinate system lies along the spin-angular-velocity vector of the earth. The angle ϕ is the declination of the moon when the probe arrives at the distance of closest approach (perigee) to the moon. The distance R is measured from the center of the moon to perigee, and α is the angle between $\vec{R}$ and the earth-moon center-line. ψ is the angle between the orbital plane of the probe and the orbital plane of the moon around the earth. The probe's orbit is retrograde, as shown in Figure 79. Conditions (1) and (2) are satisfied by virtue of the fact that $\alpha = 11$ degrees and $R = 2.750 \times 10^6$ meters. The earth miss distance of the probe on returning from the moon is 5.5×10^6 meters; i.e., a collision with the earth. Also $\psi = 2°53'$ and $\phi = -5°55'$, where $d\phi/dt > 0$.

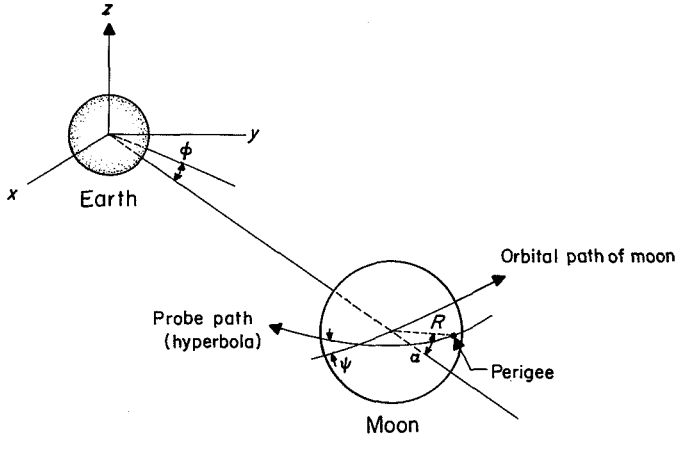

Figure 79. Definition of ϕ, R, α, ψ

Injection into orbit occurs at a latitude of -3.98 degrees, and a longitude of 19.53 degrees west. The azimuth direction of the probe at injection is 124.25 degrees east of north. Finally, travel time from earth to moon is 63.085 hours, and travel time from earth to moon to earth is 139.072 hours.

2. Homing Programs

In *SPS 1* through 5 a system of coordinates ($\vec{B}\cdot\vec{T}$ and $\vec{B}\cdot\vec{R}$) was described which makes use of the impact parameter ($\vec{B}$) of the osculating hyperbolic path near the target. The vector $\vec{B}$ is taken to originate at the center of the target planet and is directed perpendicular to the incoming asymptote of the hyperbola. The coordinate

system that is used makes use of a unit vector in the direction of the incoming asymptote ($\vec{S}$), a vector ($\vec{T}$) perpendicular to $\vec{S}$ that lies in the earth's equatorial plane, and a vector ($\vec{R}$) defined to form a right-handed system, or $\vec{R} = \vec{S} \times \vec{T}$. The miss components of $\vec{B}$ are then $\vec{B} \cdot \vec{T}$ and $\vec{B} \cdot \vec{R}$, since $\vec{B} \cdot \vec{S} = 0$.

These coordinates are useful in homing or finding a trajectory which misses the target in a satisfactory manner. However, for a trajectory in which the vehicle goes near the moon and then comes back to the earth in an elliptical path, the previous definitions do not apply since there is no longer any impact parameter vector $\vec{B}$ which would approximately represent the vector miss if the target (the earth) had no mass. For in the elliptic case the vector miss would depend on where the vehicle is started on the ellipse, unlike the hyperbolic case where the miss distance is independent of the point on the hyperbola where the vehicle is started, provided that the starting distance is reasonably far away from the target. However, if it is assumed that the approach path to the earth will be highly eccentric and that the vehicle will start near the center of the ellipse, the $\vec{B}$ vector can be defined to be along the semi-minor axis of the ellipse as shown in Figure 80. The vector which replaces the asymptote is now the vector shown along the perigee direction. The same method can now be used to compute $\vec{B} \cdot \vec{T}$ and $\vec{B} \cdot \vec{R}$.

It can be shown that in this case the semi-minor axis (b) is given by

$$b = \sqrt{2aR_M - R_M^2} = |\vec{B}|$$

where a is the semi-major axis, and R_M is the distance at perigee. The use of these coordinates in homing on the earth has been highly satisfactory.

3. Satellite Turning Maneuvers

The orbital inclination of a satellite is strongly determined by the powered-trajectory launch azimuth. For firings from Cape Canaveral, the possible inclinations of a satellite orbit are restricted by range-safety limitations on launch azimuth. To exceed this restriction on inclination, a turning maneuver must be executed sometime during powered flight. A method of performing this maneuver with a two-stage *Vega* configuration is as follows: (1) fire the *Atlas* stage in the usual manner, (2) fire the *GE-405* stage until it achieves the conditions required to produce an elliptical orbit with an apogee altitude equal to the desired circular orbital altitude, and (3) re-start the *GE-405* at apogee, applying the thrust increment out of the trajectory plane, and burn long enough to bring the speed up to the value required for a circular orbit. The angular change of orbital inclination will be primarily a function of three quantities: (1) the magnitude of the thrust component out of the initial trajectory plane, (2) the magnitude of the angle of the thrust component out of this plane, and (3) the location of the apogee point over the earth's surface. The greatest change in inclination occurs when the thrust increment is perpendicular to the trajectory plane and apogee is over the equator. To determine the effect on payload and obtain quantitative results for inclination changes, the following study was completed.

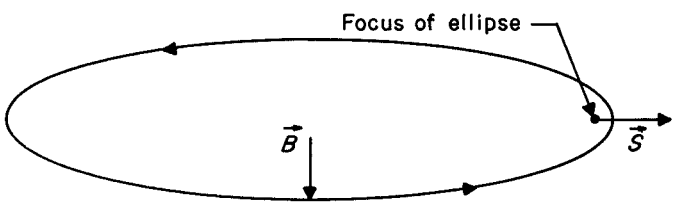

Figure 80. Definition of $\vec{B}$ and $\vec{S}$ for an ellipse

Four *Atlas* first-stage trajectories with 46-degree launch azimuths and varying degrees of trajectory flatness were selected. Of these, the *Atlas* flight having the flattest trajectory gave rise to the largest payload weight for a 700-mile altitude, circular orbit. This latter *Atlas* trajectory was then chosen as the first stage for a set of second-stage trajectories. By applying different thrust attitude angles at second-stage ignition and using various *GE-405* burning times, apogee locations were produced 40 degrees before and 10 degrees past the equator (Fig 81). All second stages were flown at constant attitudes following applied pitch-up angles at second-stage ignition.

The missile is assumed to be turned just prior to re-starting the *GE-405* so that the turning maneuver and subsequent acceleration to circular velocity occur over a short period immediately preceding and following arrival at apogee. It is necessary to determine the velocity increment Δv required to attain circular velocity for various thrust-direction-change angles (θ) between the velocity-at-apogee direction and the thrust vector producing Δv. These quantities, as viewed along the position vector at apogee (normal to their plane), are shown in Figure 82. Solving for $|\Delta\vec{v}|$ from the relation

$$(V_{apogee} + \Delta v \cos\theta)^2 + (\Delta v \sin\theta)^2 = V_{circular}^2$$

one obtains

$$|\Delta\vec{v}| = -V_{AP}\cos\theta + [V_c^2 - (V_{AP})^2 \sin^2\theta]^{1/2}$$

where $V_c = 7289$ meters/sec at 700-mile altitude.

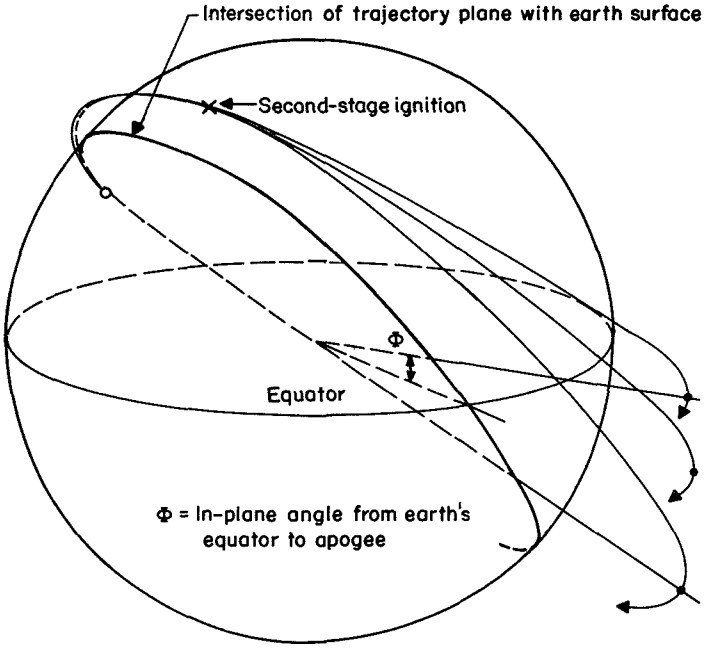
Intersection of trajectory plane with earth surface
Second-stage ignition
Φ
Equator
Φ = In-plane angle from earth's equator to apogee

Figure 81. Earth-satellite geometry

The amount of orbit-inclination angular change (Δi) which can actually be obtained at the equator depends upon the turning angle (α) at apogee shown in Figure 82 as well as apogee location relative to the equator. An orbit turn when directly over the equator undergoes a greater change in inclination angle for a given turning angle than if turned at other latitudes. Effectively,

$$\Delta i = \sin^{-1}\left[\frac{\Delta v \sin\theta}{V_c}\right]\cos\Phi$$

where Φ is the in-plane angle from the equator to apogee location and is positive measured to the north. Figure 83 shows that the inclination angular change (Δi) is primarily a function of the change in thrust direction (θ), and secondarily of apogee location (Φ) relative to the equator.

Although orbit inclination can be changed by almost 17 degrees for a thrust increment at apogee, perpendicular to the initial satellite plane, obviously this would cost heavily from a payload standpoint. The amount of missile weight remaining after accelerating to circular velocity may be found from

$$W_F = W_o e^{\frac{-k\Delta v}{F}}$$

where W_o equals missile weight after first *GE-405* shutoff, Δv is velocity increment required to attain circular velocity, k is mass flow rate of *GE-405*, and $F = 35{,}140$ pounds thrust of the *GE-405* second-stage engine.

Figure 84 depicts missile weight (W_F) after circular velocity as a function of apogee location Φ. Curves of constant thrust-direction angular change (θ) have been sketched. It can be seen that a considerable reduction in payload results for large θ. (Structural weight has not yet

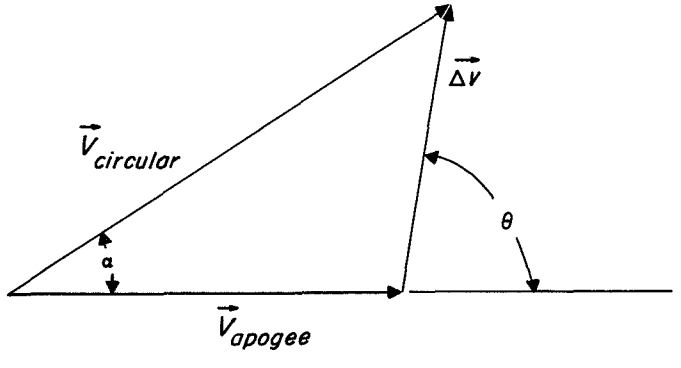

Figure 82. Apogee-velocity-vector geometry

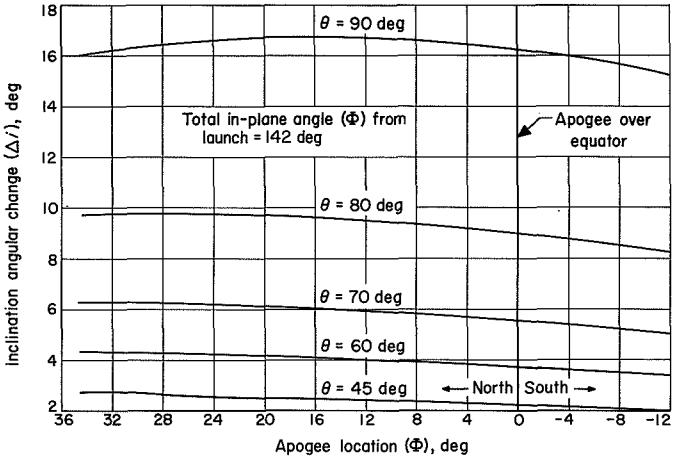

Figure 83. Orbital inclination change

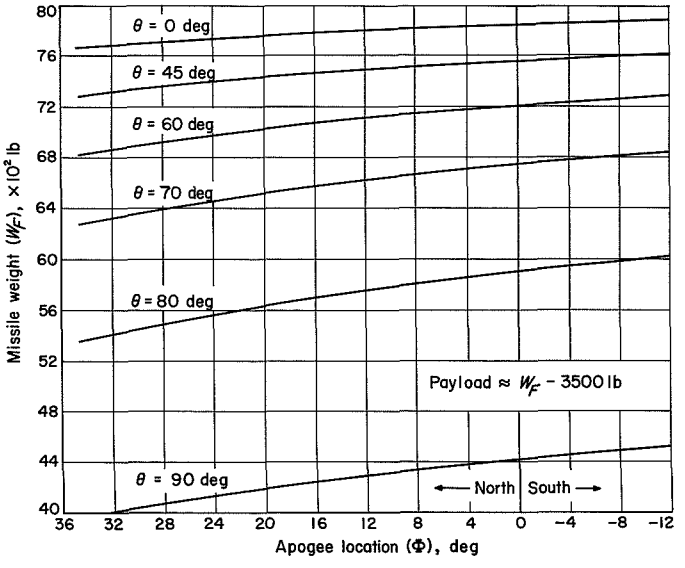

Figure 84. Missile weight after turning maneuver

been fixed, but an approximation of payload is given by missile weight W_F less 3500 pounds.)

The choice of thrust direction angle (θ) out of the initial satellite plane, and the in-plane angle (Φ) to apogee from equator naturally depend upon the minimum acceptable payload required to make the experiment worthwhile. Arbitrarily selecting 1000 pounds for this value, a maximum change in orbit inclination would be achieved of $\Delta i = 15.7$ degrees for $\theta = 90$ degrees, and $\Phi = -8$ degrees. If the constraint be imposed that $\theta = 60$ degrees, then $\Delta i = 4.4$ degrees, but the payload may be increased to 3300 pounds.

4. Launch-Time Problem

A launcher at Cape Canaveral is rotating in inertial space at a tangential velocity of 1342 ft/sec. At the instant the missile lifts off the pad, its initial position and velocity vectors are established in inertial space. Since these two vectors are time dependent prior to launch, any error in time of liftoff will cause them to be in error. The initial position and velocity vector errors represent initial-condition errors to the missile equations of motion. This results in errors in the solutions of these equations.

Geometrically, at the end of powered flight the probe's flight path is shaped like a planar conic (ellipse or hyperbola). Any error in launch time has the effect of rotating the conic about the earth's polar axis. This rotation will cause the position vector at any later time to rotate also. In particular, the position vector will be in error at impact time causing the probe to miss. Thus, in seeking methods of compensating for launch-time error, it is reasonable to choose methods which effectively re-rotate the conic in the opposite direction to a rotation about the earth's polar axis. This cannot be done directly but can be achieved by performing a combination of rotations. First, it is possible to rotate the conic about an axis passing through the launcher by varying launch azimuth. Second, it is possible to rotate the conic about an axis normal to its plane by varying the second third-stage coast period. This combination of rotations will restore the conic to the original space orientation it had before it was rotated due to launch-time error. Such a method of compensation is called the launch-azimuth/coast-time method.

A study was completed to determine the variation of launch azimuth and coast time as a function of launch-time error. These results are shown in Figures 85 and 86. Figure 85 is a plot of launch azimuth (σ_L) vs launch-time error assuming the initial launching was to occur at a

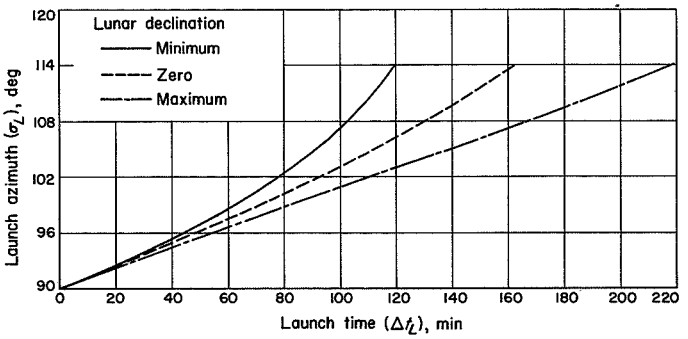

Figure 85. Launch azimuth vs launch-time error

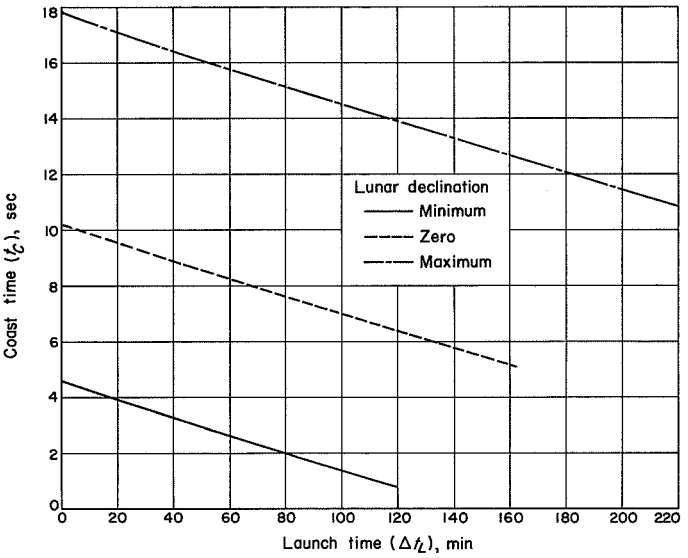

Figure 86. Coast time vs launch-time error

launch azimuth of 90 degrees. Cases of minimum, zero, and maximum lunar declinations are shown. Note that the required azimuth variations diminish for increasing lunar declination and a fixed launch-time error. For example, for a 120-minute launch-time error, the required launch-azimuth change is from 90 to 114 degrees at minimum lunar declination, but reduces to a change from 90 to 103 degrees at maximum lunar declination. In Figure 86, the coast time variation vs launch-time error is depicted. For a 120-minute launch-time error, the change in coast time is about the same for all lunar declinations because the slope of the three curves is nearly the same; i.e., 0.0525 minute of coast time per minute of launch-time error.

The advantage of using this method of launch-time error compensation is that total flight time remains relatively unaffected. However, a disadvantage is that the location of the injection point moves considerably. The effect is felt most strongly in longitude change. Figure 87 shows a plot of injection longitude vs launch-time error.

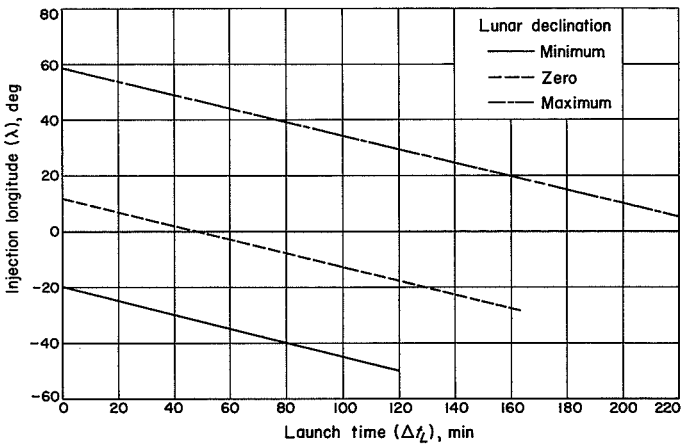

Figure 87. Injection longitude vs launch-time error

The longitude variation for a 120-minute launch-time error is very nearly a constant of 0.25 deg/min, which is the rotational velocity of the earth. Variation in latitude is slight (of the order of 2 degrees).

G. Trajectory Programs

1. Powered-Flight Trajectory-Computing Programs

a. General-purpose program. An existing, general-purpose computing program satisfies the major portion of the Laboratory's requirements for powered-flight trajectory generation. In this program, the vehicle is considered as a point mass with three degrees of freedom and has the capability of handling a maximum of six stages of powered flight with any amount of interstage coasting.

The equations of motion include gravitational, aerodynamic, and thrust forces. The gravitational forces are functions of latitude and earth-centered radial distance because the earth is considered as an oblate spheroid. Aerodynamic forces are computed separately as drag force and normal force. The aerodynamic-force coefficients may be stored either as tables or as cubic polynomials of the Mach number. When the polynomial form is used, provision is made to describe each aerodynamic coefficient by four polynomials for four different ranges of Mach number. The atmosphere is assumed to rotate as a rigid body. The ARDC Standard Atmosphere of 1957 is used for altitudes below 300,000 feet. Above this altitude the pressure ratio is described by a logarithmic equation, and the acoustic velocity is assumed to be constant. The magnitude of the thrust force is computed from the vacuum thrust reduced by the atmospheric back-pressure. A constant value of propellant consumption rate is generally assumed for each stage.

Several options are available for thrust-direction control in both the pitch and yaw planes. A zero-lift pitch program is available in which the thrust vector is maintained colinear with the velocity vector. Options are available to fly with either angle-of-attack or inertial attitude described by seventh-order polynomials in time. All of these options are available for control of both pitch and yaw.

The equations of motion are integrated in an inertial Cartesian coordinate system by a fourth-order Runge-Kutta routine. Suitable transformations are available to provide earth-fixed velocity and position. The primary coordinate system is chosen so as to be compatible with guidance-studies requirements. The origin is located at the launching pad, and the axes point vertically, downrange and crossrange. Transformations are made to both inertial and earth-fixed, earth-centered coordinate systems. The geocentric, earth-fixed coordinate system is a convenient branch point for computing tracking-station-referenced coordinates. The last-stage burnout position and velocity in the geocentric, inertial coordinate system are used as inputs to one of several available earth-satellite, lunar, or interplanetary-coasting trajectory programs. The tie-in between the powered-flight program and the coasting programs is completely automatic.

At the present time, the powered-flight program has only a 3 degree-of-freedom capability; however, 6 degree-of-freedom capability is easily attained by the inclusion of three moment equations.

b. Optimization of attitude during burning. For payload maximization, an available computing program, which computes in a nonrotating, spherical, earth coordinate system without atmosphere, determines (subject to various restrictions on end conditions) the optimum attitude during burning. Position is specified by two coordinates: the geocentric radial distance (r), and the downrange angle (θ). The integration of the equations

of motion proceeds from the initial conditions r_0, θ_0, $\dot{r}_0$, and $\dot{\theta}_0$. During the integration, iterative procedures are used to find the attitude which provides a maximization of burnout energy. Options exist for optimizing the attitude subject to various end-condition restrictions, which include specifying a burnout radial distance, a burnout-velocity pitch angle, and a specific value of $\Delta\theta$ during burning. These restrictions may be applied either one at a time or in any combination; however, as the number of restrictions applied increases, the speed of computation decreases.

c. Azimuth rotation program. A program exists which satisfies the frequent need to rotate an existing trajectory to a different firing azimuth. The existing trajectory is transformed point by point to a coordinate system which is natural to the launch-pad location and firing azimuth; i.e., one axis of the coordinate system lies along the firing azimuth. The effect of earth rotation on both position and velocity is removed at each point of the trajectory, which gives as an intermediate result, a nonrotating-earth trajectory. The reverse process is then applied to add the initial inertial velocity on the new firing azimuth. An option is available not only to rotate the firing azimuth but to move the location of the launch site as well. It is also possible to enter this rotation program at an intermediate point with a nonrotating-earth trajectory in order to produce a rotating-earth trajectory on any desired firing azimuth from any chosen launch location. This program is suitable for use with trajectories where the total downrange arc length is no greater than about 15 degrees.

2. Conic Interplanetary Coasting Program

a. Patched-conic program. An available interplanetary-coasting trajectory program, which calculates interplanetary trajectories by a patched-conic method, is three dimensional and generates planetary positions from stored orbital elements. As the computation is performed in a forward going (in time) conventional manner, it is particularly adaptable to being attached to the output of a powered-flight-trajectory computing program.

The computation begins with the specification of seven earth-fixed input parameters: injection time, three position coordinates, and three velocity components which are used to generate a geocentric hyperbola out to a geocentric distance of approximately 10^6 miles. At this point, the geocentric, hyperbolic trajectory is converted to a heliocentric ellipse.

A homing procedure, which is an integral part of this program, is guided by 21 partial derivatives of planet-miss-distance components with respect to the seven input parameters. The standard homing procedure allows the seven input parameters to so be adjusted as to achieve a near-miss at the target planet. As the partial derivatives or miss coefficients may be computed at any point on the trajectory, the program is a useful tool for investigating mid-course guidance corrections.

Basically, this program is a conic simulation of the precise integration procedures which are used to generate interplanetary trajectories. The program accepts the same type of input information as the integration program and uses the same type of homing procedures as are used with the integration program. The patched-conic program obviously does not have the accuracy of the integration program, but its clear advantage in computing speed makes it useful for studying and roughing-in trajectories.

b. Heliocentric transfer-ellipse program. A second existing interplanetary-coasting-trajectory program takes a rather unconventional approach to the problem. This program is three dimensional and uses a published planetary ephemeris.

The program is set into operation by the specification of target planet, desired arrival date, and desired heliocentric-transfer central angle as inputs, and the ephemeris is consulted for target-planet position and earth position at the arrival date. These positions are differenced to produce the communications distance which is an important trajectory design parameter. The heliocentric central angle, combined with target-planet position at arrival time, locates the position of earth at injection. The ephemeris is entered with this earth position in order to find the time at which earth is at this position; this determines a heliocentric ellipse. The various parameters of this ellipse are determined, particularly the required velocity at the heliocentric injection point. The difference between this required velocity and the earth velocity is the incremental velocity which is needed at heliocentric injection. The three components of heliocentric injection velocity and the heliocentric injection time specify the coupling conditions that must be met by the geocentric coasting trajectory and the powered flight.

Any trajectory in this program is a *hit* trajectory; i.e., the need for homing procedures is eliminated, which is a major advantage. It is another major advantage that only four injection conditions need to be matched by the geocentric trajectory as opposed to the seven which must be matched in the forward-going interplanetary program.

An option exists for automatically scanning the input-parameter heliocentric-transfer central angle to find the transfer ellipse which requires minimum incremental energy for any given arrival date. This option allows

tables and plots to be constructed which show all the significant trajectory parameters as a function of arrival date (communication distance) for the minimum-energy transfer which arrives at that date.

This program has been used to investigate heliocentric, elliptical transfer trajectories to Mars, Venus, and Mercury for the period 1960 to 1965. The arrival-time spans following the Mars 1960 opposition and the Venus 1961 conjunction have been investigated fully. For each arrival date, transfer trajectories have been generated at 5-degree intervals of heliocentric central angles throughout the entire elliptical range. Every significant trajectory parameter is listed for each case. This investigation has been extended to cover all the synodical periods of Mars, Venus, and Mercury during 1961 to 1965; however, this extended survey examines only the minimum-energy trajectory for each arrival date. Arrival dates were examined at 1-day intervals starting at the date of inferior conjunction for the interior planets and opposition for the exterior planets. The arrival-date span investigated is about 6 months for Mars and Venus and about 1 month for Mercury.

This program is to be part of a new, automatic, interplanetary-trajectory design program which will treat the powered-flight portion of the flight, the geocentric coasting hyperbola, and the heliocentric coasting ellipse. The Mars and Venus trajectories described previously have been stored on magnetic tape. From this tape a trajectory is selected by arrival date and heliocentric central angle with the choice being guided by the aforementioned minimum-energy trajectory-parameter plots. The tape lists the four heliocentric-transfer-point matching parameters for each trajectory. Because the trajectory-selection parameters have been chosen at such close intervals, simple interpolation routines may be used to select any trajectory. In effect, all reasonable heliocentric trajectories to Mars and Venus during 1960 to 1965 have been precomputed, catalogued, and are available in a form which permits their ready use.

3. Methods of Integration

For integrating the equations of motion, the JPL trajectory program uses a geocentric, space-fixed (space-orientation-fixed), rectangular coordinate system referred to the mean equator and equinox of 1950.0. The gravitational effects of the moon, the sun, and as many planets as are appropriate are brought in by using their ephemerides referred to the mean equator and equinox of 1950.0. Two oblateness terms for the earth are included in the equations of motion. The numerical integration is accomplished by a combination of a Runge-Kutta method (used for starting and changing interval size) and a Gauss-Jackson (second sum) method of the open formula type, with differences up to the seventh order retained (correct through h^{10}, where h is the integration step size). The input is normally in earth-fixed, spherical coordinates (radial distance, latitude, longitude, velocity magnitude, velocity azimuth, and velocity elevation angle), although space-fixed, rectangular coordinates can also be used. Outputs are available in the same two types of coordinate systems. Predicted values of observables include corrections for station anomalies, for atmosphere, and for time interval of transmission.

The Laboratory also has available the Themis program and a modified Space Technology Laboratory (STL) program. The modified STL program is divided into three phases, each using space-fixed, equatorial rectangular coordinates, but with different origins: geocentric, heliocentric, and planetocentric (Mars or Venus). Transfer from one phase to another occurs at pre-assigned distances from the earth and from the target planet. During the geocentric phase, only the disturbing effects of the sun, the moon and the oblateness of the earth are included. During the heliocentric phase, the earth-moon system, Jupiter, Venus, and Mars are the disturbing bodies. During the planetocentric phase, Jupiter and the sun are the disturbing bodies. In the geocentric phase, the ephemeris of the sun is referred to the mean equator and equinox of 1959.0, and the ephemeris of the moon is referred to the equator and equinox of date. In the other phases, all ephemerides are referred to the equator and equinox of 1950.0. In the geocentric phase, input and output may be in space-fixed, spherical or rectangular coordinates, or in earth-fixed, spherical coordinates. In the other two phases, input and output are in heliocentric or planetocentric coordinates, referred to the equator and equinox of 1950.0. The numerical integration procedure uses Runge-Kutta for starting and changing interval size, and a Milne predictor-corrector difference scheme which is useful in second-order equations not explicitly containing the first derivative; the Milne scheme is correct through h^5.

The Themis program is a double precision program in space-fixed, rectangular coordinates. It may be used in either geocentric or heliocentric form, but there is no automatic transfer from one phase to the other. When used in geocentric form, only the sun and the moon are disturbing bodies. When used heliocentric, the earth-moon system and all other planets except Mercury can be used as perturbing bodies. Input and output are

restricted to rectangular coordinates. The integration procedure is a Gauss-Jackson (second sum) method, retaining differences up to the tenth order, with a correction formula which may be applied as many as seven times. Starting values are obtained in this case by generating an approximate solution initially from the osculating elements at epoch and iterating on these with the correction formula to obtain accurate starting values.

For lunar satellites, there is being planned an additional system of equations obtained by translating the rectangular coordinate system of 1950.0 to the center of the moon and providing for a time-varying potential function for the moon treated as a rotating ellipsoid. Transformations are to be provided to obtain selenographic latitudes and longitudes relative to the mean central point of the visible disc and the mean equator of the moon.

4. Homing Programs

All of the homing programs are based on the use of vehicle parameters to satisfy the target conditions. Any useful combination of these parameters is generally available as a search option. Further, all of the procedures depend upon the solution of linearized equations in which the coefficients are developed by varying the search parameters one at a time. In general, if important nonlinearities are suspected, then the option is available to monitor the size of the increments to the search parameters so that they do not exceed values for which the method will converge. The further option of saving these coefficients for successive iterations is also available.

The homing procedure with the integrating program is based on specifying the target conditions in terms of two components of the impact parameter and closest approach time which are computed from the osculating conic about the target mass. One distance component lies in the equatorial plane and is perpendicular to the incoming asymptote to the local hyperbola; whereas, the other component is resolved along the direction mutually perpendicular to the incoming asymptote and the first component. The advantage of using this method of specifying the miss is that these components are relatively linear with respect to variations in the initial conditions.

A subroutine exists which computes the partial derivatives of the impact parameters with respect to the velocity coordinates at prescribed points along the trajectory. Since the direction of the velocity perturbation is pertinent, these partials are computed for each of seven directions, including that of each coordinate axis, the probe-earth line, and the probe-sun line. The so-called critical directions, in which the miss distance is most sensitive to velocity changes, are also determined. In addition, the program computes the velocity increments required to correct the miss.

A homing procedure is available for connecting the burning portion of the trajectory to the interplanetary transfer-ellipse program. This is accomplished by matching the right ascension, declination, magnitude of the heliocentric injection-velocity vector, and the time at heliocentric injection to the geocentric hyperbola generated by the burning program.

By adjusting the vehicle parameter selected for variation, the properties of the geocentric hyperbola are changed at the match-point. The matching can also be accomplished by using vehicle parameters in combination with variations in the heliocentric angle of the transfer ellipse.

5. Tracking

The reduction of tracking data is essentially the problem of filtering (by statistical analysis) the random observational errors and the systematic bias errors.

The basic procedure is as follows: A set of initial conditions is assumed or obtained from iterating within the program and is used to start the integration of the drag-free equations of motion, including the effects of the oblate earth, the moon, and the sun. The computed trajectory variables are transformed into station-referenced coordinates, and corrected for refraction and station anomalies. The difference between computed and observed values is used to determine those corrections in initial conditions which result in the minimum sum of squares of the differences between calculations and observations. The corrections in initial conditions are added to the previously employed initial conditions and this completes one iteration. Differential coefficients are computed by integrating a system of equations in which the partial derivatives are the dependent variables.

Prior to full acceptance of a data point into the tracking program, the difference between the computed and observed values is compared with a standard deviation which is either an externally specified number or one computed within the tracking program from earlier observation points. Measured values which differ from the computed values by more than three times the standard deviation are rejected.

Individual data points are weighted inversely as the variance of the deterioration in quality of the tracking data. The weighting used may depend on whether an

automatic tracking mode is used, on the signal strength, and on the elevation angle.

The differences between computations and observations, properly weighted, and the differential coefficients of the observations with respect to the initial conditions are fed into a number of least-squares-fitting routines. In the primary method, each data type is weighted inversely as the previously computed variances from the mean for that type and then is combined. Changes in the six initial conditions and in constant biases in the five possible observation types can be solved for. Thus, the maximum matrix size provided for is 11×11. The matrix size test which can, on option, presently be used is based on the ratio of the changes in initial conditions and biases called for and the computed standard deviation in initial conditions. The new initial conditions and biases obtained by adding the changes solved for are used as input for subsequent trajectory computations. Standard deviations from the mean and standard deviations in initial conditions are always displayed. Standard deviations of predictions are computed on option.

Least-squares routines are applied to each separate data type in order to obtain the changes in initial conditions called for by the various types. The initial conditions so solved for are used to obtain standard deviation from the mean for the optimum fit to each data type separately, and are called *noise* standard deviations. The separate changes in initial conditions obtained above are combined by weighting the results from each type inversely as the variance of that data type from the pointing trajectory. Standard deviations of the initial conditions obtained in this manner are also computed.

6. Ephemeris

The JPL program allows the possibility of introducing ephemerides for the moon, the sun, and all planets other than the earth. Currently, in addition to the sun and moon, only Venus, Mars, and Jupiter are being used. All five are available at 1-day intervals relative to the mean equator and equinox of 1950.0.

Present sources for Mercury and Mars are British planetary tables which do not contain as many significant figures as desired. Sources for the other planets as well as for the sun are the Themis tapes which correspond to the best available information from the Naval Observatory. The tables for the moon are relatively difficult to obtain in the 1950.0 coordinate system, and those currently available are not of the desired accuracy. Effort is being made to remedy the deficiencies in the Mars and moon data.

H. Flight Evaluation

The launch-to-injection tracking net described in *SPS 5* was designed to track rounds fired at azimuths between 44 and 66 degrees. This net, however, is not applicable to rounds fired along the southeast trajectories described in *Trajectory Studies* of this section. A tracking net for southeast firings is currently under study. It is planned to make use of the instrumentation which exists as part of the Atlantic Missile Range. The range of injection points for such southeast lunar trajectories is shown in Figure 78. The circle centered at Ascension Island represents approximately the span of injection points which can be seen by the FPS 16 radar at Ascension. The extent of coverage from Hartesbeesthoek, Union of South Africa, and from points near the west coast of Africa are also shown. Tracking during first- and second-stage burning can be accomplished from Cape Canaveral and from a number of islands in the Caribbean. The capabilities of the radar coverage available at these locations is currently being determined.

From the map it may be seen that the most difficult range of injection points to cover consists of those that occur when the moon is at negative declinations. If all firings take place when the moon is located between 0 and +18 degrees declination, most of the third-stage burning period can be seen by a combination of stations at Ascension Island and either at Hartesbeesthoek or near the southwestern coast of Africa. Whether the scientific missions planned are all compatible with positive declination of the moon is under study. The station in Africa will probably be at Hartesbeesthoek in order to make use of the facilities of the deep-space net which are planned for this location. On early rounds, the equipment used to observe powered flight and injection at this location will probably be that which had been planned for Newfoundland. Later, it may be possible to use the deep-space equipment for injection tracking and make the launch-to-injection station available for another site.

V. VEHICLE

During the last few months the objectives and boundary conditions for the *Vega* program have been reviewed and modified several times. The current schedule of missions calls for four development flights in 1961, two of which will carry lunar experiments, and two interplanetary attempts in 1962.

In order that some engineering progress could be made during the reprogramming exercises, the design of the launching vehicle and spacecraft was held relatively constant; the configuration as originally laid out still appears reasonably near optimum for the escape missions.

A. Structure

1. Vega Third-Stage Design

The third-stage structure of the *Vega* vehicle (Fig 88), consists of spherical fuel and oxidizer tanks supported by six longerons. The pressurization system helium bottles are suspended from the longerons between the fuel and oxidizer tanks. The forward hexagonal bracing ring supports the guidance compartment and spacecraft; the aft ring is supported on a space frame attached to the previous stage. The motor thrust and actuation forces are carried by a cone attached to the bottom of the fuel tank.

The size of the tanks was determined by the choice of a loaded propellant weight of 5300 pounds (*SPS 3*). The choice of double tanks was made because of the difficulties envisioned in making a reliable, lightweight, single tank with a diaphragm and a good differential pressure control system in the time available before the first vehicle had to be ready for flight. In the preliminary design phase of the *Vega* program, the present third-stage configuration was compared to a corrugated, magnesium-thorium alloy (HK 31A-H24) semimonocoque structure. The weight of these structures was about the same but the enormous increase in accessibility and the flexibility of arrangement inherent in the longeron-type structure, with an aerodynamic shroud carried on the previous stage, led to the present choice.

The longerons and rings in the third stage are made of 7075-T6 aluminum extrusions and the tie rods are made

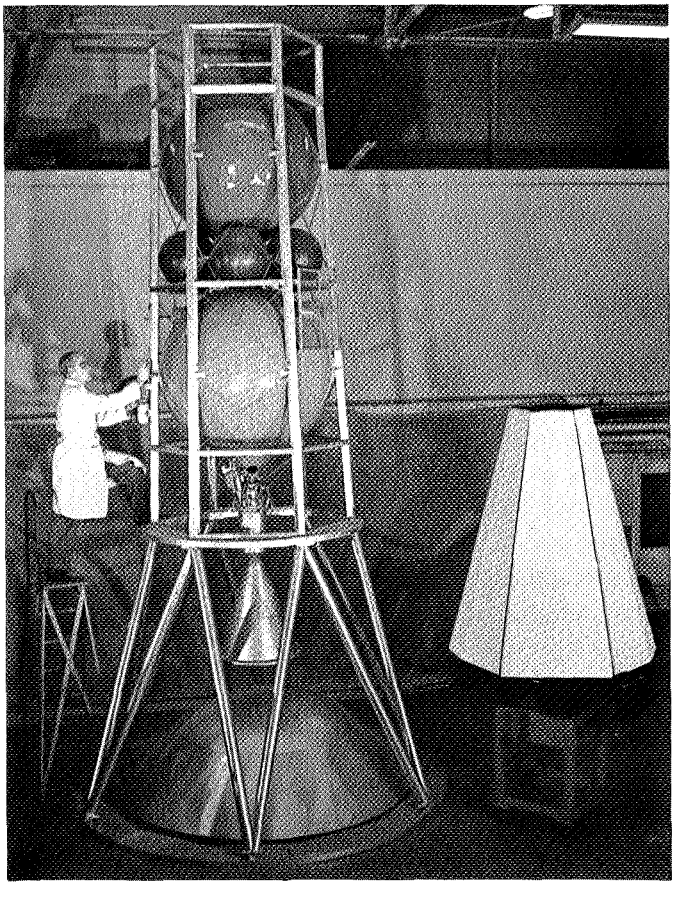

Figure 88. *Vega* third stage and spacecraft

of heat-treated 4130 steel. A cross section of the longeron is shown in Figure 89. The tie rods which provide shear stiffness are pre-stressed so that they are always acting in tension. The spacing of the tanks in the longerons has been chosen so that a cylindrical section can be added to the dome of each tank if it becomes necessary to increase the loaded propellant weight to 6000 pounds. The added length needed to accommodate this requirement is 4 inches and the penalty is only 2 pounds of longeron weight.

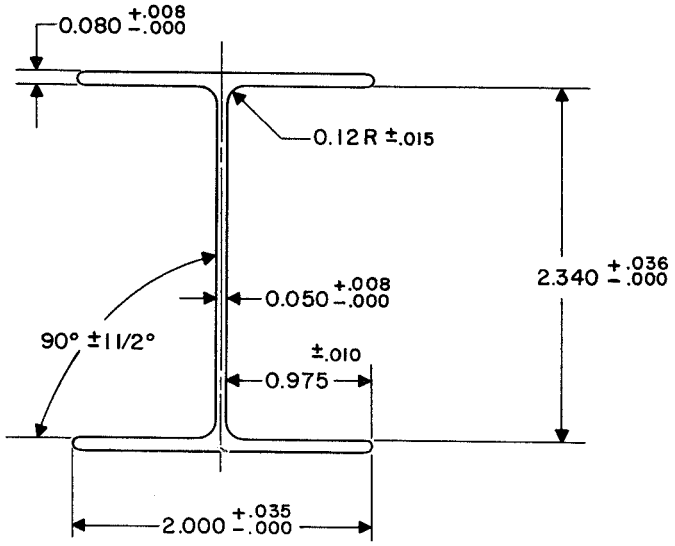

Figure 89. Longeron section

The propellant tanks are spheres with tangent cone bottoms, made of 2014-T6 aluminum. Some pertinent design information is given in Table 11. The weights shown do not include anti-slosh baffling, flow meters, or the motor mounting cone. The tank sizing is such that 5300 pounds of propellant can be carried at a mixture ratio varying from 0.91 to 0.97. If the tanks are lengthened so that the total loaded propellant weight is increased to 6000 pounds, then the total tank weight would increase by 38 pounds. Tank ullage was chosen so that, if the tanks are loaded at 70°F, sealed, and then have the bulk temperature raised to 130°F, the rise in tank pressure due to bulk temperature change and vapor pressure is 100 psi or less.

Table 11. Propellant tank design characteristics

Characteristic	N_2O_4	N_2H_4
Spherical radius, inches	23.80	26.75
Nominal volume at 70°F, cu in.	55,440	79,615
Tangent cone base diameter, inches	18	20
Nominal weight, pounds	83	113

Curves of pressure versus loaded propellant weight for various temperature changes are shown in Figures 90 and 91. The motor and actuators are mounted on a thrust cone which is bolted to the fuel tank with the fuel flow meter seated between the tank bottom and the lower end of the cone. As a result of this arrangement, the motor-actuator-fuel flow meter system can be removed from the rest of the structure with relative ease.

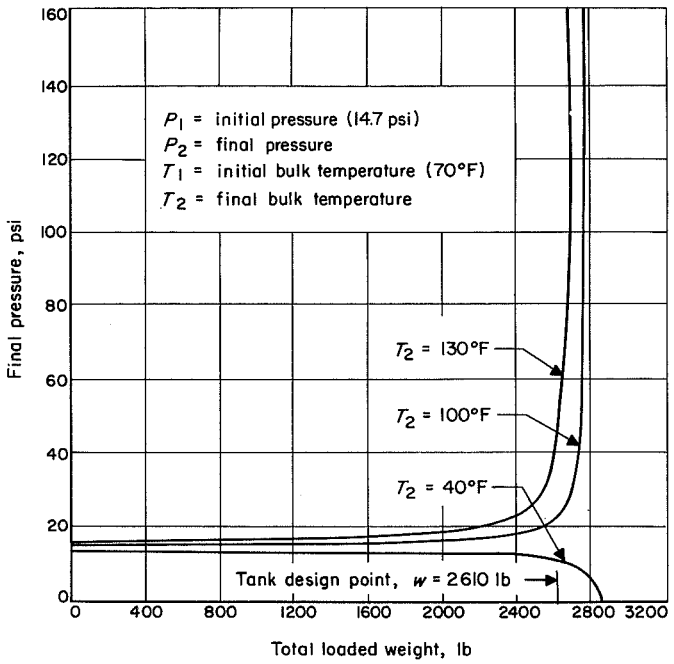

Figure 90. Final pressure vs loaded oxidizer weight

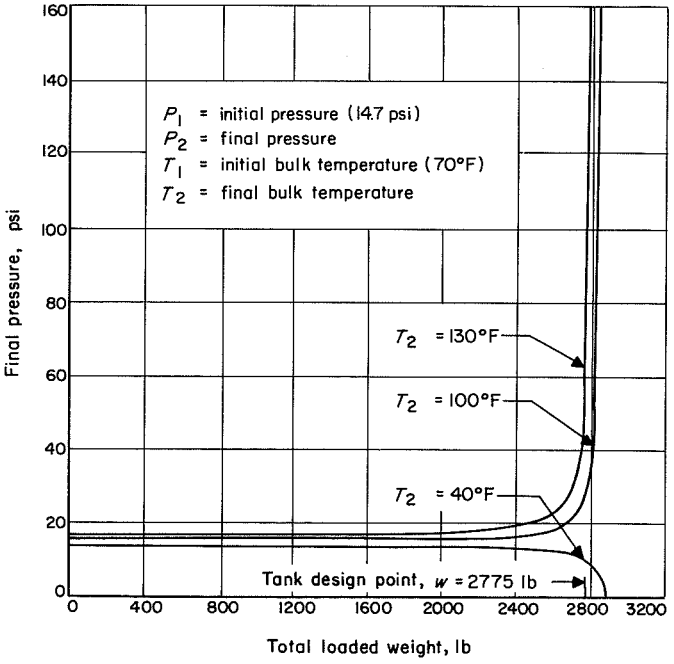

Figure 91. Final pressure vs loaded fuel weight

Among the unique problems associated with the third stage is providing adequate stiffness for the longeron structure at a minimum weight. Problem areas connected with the tanks stem from the use of welded 2014-T6 aluminum. This material is stronger, but more difficult to weld than 6061 aluminum, a more common tank material. The present tanks are not heat treated after welding; upset sections are provided to make up for the resultant loss in strength. The use of six concentrated supports on a thin wall pressure vessel involves some unique problems in local stress determination. Since the motor-actuator system is mounted on the bottom cone of the fuel tank, the question arises of determining the overall and local stiffness of the system, so that the dynamic problem of the motor-control system can be analyzed. Comparisons of the analytical and experimental investigations carried out in these areas will be presented in a future *SPS*.

The third-stage structural tests which have been completed to date include both a pressure test to failure of a prototype tank which is slightly larger and has a different bottom than the flight tanks (Fig 92) and an influence coefficient test to measure the stiffness of the motor mount system on a prototype fuel tank bottom which is slightly larger than the flight tank (Fig 93). Data reduction in these tests has not been completed, but preliminary results indicate that the tank design is satisfactory.

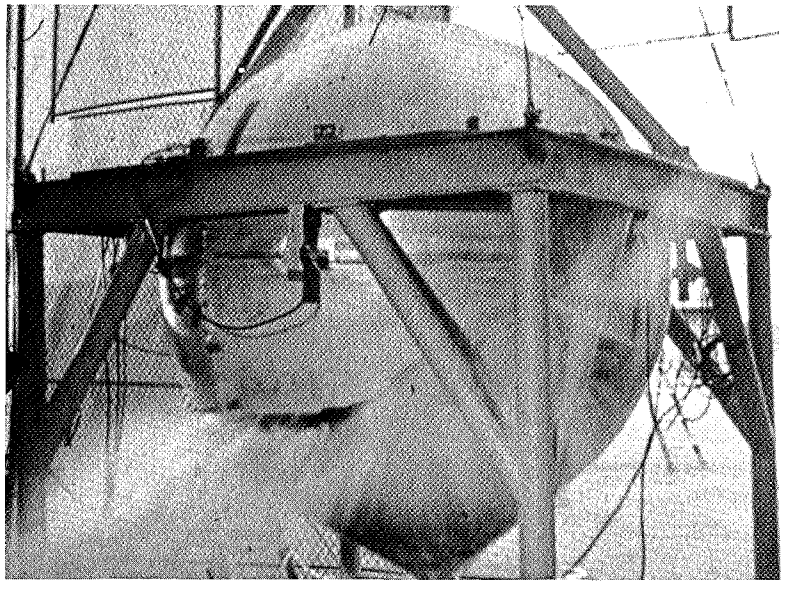

Figure 92. Prototype tank rupture

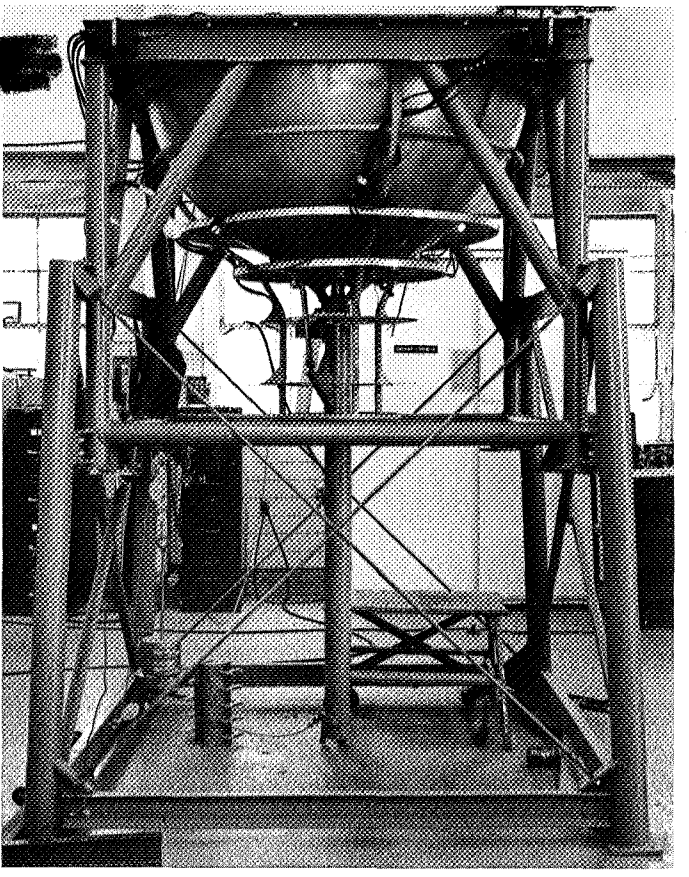

Figure 93. Prototype fuel tank test stand

2. Pressurization System

The helium pressurization system for the propellant tanks consists of six 6Al-4V titanium spheres operating at 3200 psia. This alloy of titanium was chosen because of its minimum weight and past experience with this material for pressure vessels.

The bottles are mounted by their bosses in an annular ring between the two propellant tanks. One boss on each bottle is plugged and mounted in a flexible support to allow for expansion, while the alternate bosses, in a fixed mount, are manifolded together into the supply line.

The bottles are designed for 3200-psia operating pressure, 3900-psia proof pressure and 4500-psia minimum burst pressure. Each bottle contains 2750 in.^{3} and weighs 23.5 pounds. Solder-type vent valves, similar to the *Sergeant* battery activator valves, are being incorporated into the system for ground emergency venting of the helium supply.

In addition, three retro-jets, under design, are located at the forward end of alternate longerons. The residual helium supply, after 6K burnout and physically disconnecting the spacecraft, will be vented via an explosive valve to supply a relative velocity between this stage and the spacecraft.

3. Umbilical Disconnect

A test facility is under construction to test for the reliable operation of the disconnecting sequence. The main umbilical cord consists of the four gas-pressurization and vent lines, a cooling air supply, and most of the elec-

trical cabling. This umbilical cord is pushed away from the vehicle by four interlocked pneumatic plungers to prevent jamming at X − 25 seconds. The secondary or emergency disconnect, containing only electrical wires, is unlatched by the 2-inch rise signal from the *Atlas* and falls clear by gravity. A lanyard is attached which will pull the disconnect clear should the latch release fail.

4. Flight Separation

The structural separation of the third stage consists of six redundantly wired explosive bolts located in magnesium fittings at the base of each longeron. These bolts are fired by a signal given at the same time as the 6K engine start signal. The bolt-to-bolt time variation is absorbed in the start transient of the 6K engine.

In a direct-ascent mission, with essentially full tanks, a period of 20 seconds is required after the shutoff command signal to the *GE-405* engine, to allow for the shutoff transient of the *GE-405* engine, to decrease the amplitude of sloshing waves in the 6K propellant tanks and to remove the gas bubbles from outlet pipe areas. During this period of time, the four 50 pound thrust H_2O_2 jets on the second stage are fired in order to provide a small positive g field for bubble settling. On missions requiring a coasting orbit, the H_2O_2 jets on the second stage will be fired for 60 to 80 seconds prior to igniting the 6K engine to remove gas bubbles from the tank outlets.

On either type of ascent, after ullage positioning, the third stage is ignited and leaves the launcher without external assistance. A summary of the weight, center of gravity, and moment of inertia of the third stage, less spacecraft is presented in Table 12.

Table 12. Summary[a] of third-stage weights, centers of gravity, and moments of inertia

Group	Item	Wt, lb	XCG[b], in.	YCG[b], in.	ZCG[c], in.
1	Structure	74.6	0	0	203.1
2	Tanks	242.9	0	0	190.2
3	Helium pressurization system	152.6	0	0	180.1
4	Propulsion system	162.0	−1.6	−1.1	249.4
5	Miscellaneous	57.0	2.7	2.0	177.3
6	Guidance compartment[d]	425.1	2.6	0.6	126.6
7	Fluids[e]	203.5	−0.2	0.3	207.5
8	Usable propellant, nominal	5150.0	0	0	186.0

Condition	Wt, lb	XCG[b], in.	YCG[b], in.	ZCG[c], in.	I_x	I_y	I_z
					10^5 lb-in.^{2}		
Step total dry (Groups 1–5)	689.1	−0.1	−0.1	202.2	13.2	13.0	2.84
Step wet at cutoff (Groups 1–5, 7)	892.6	−0.2	0.0	203.4	16.5	16.4	2.99
Stage at cutoff (Groups 1–7)	1317.7	0.7	0.2	178.6	35.3	35.2	5.00
Stage at liftoff (Groups 1–8)	6467.1	0.1	0.0	184.5	85.1	85.0	5.01

[a] The spacecraft is not included in any of these estimates.
[b] XCG and YCG are the locations of the centers of gravity of the indicated group or assembly along the X and Y axes, respectively.
[c] ZCG is the station of the center of gravity of the indicated group or assembly.
[d] Includes guidance and telemetry, roll jet assembly, and compartment and spacecraft support structures, but not the servoactuators. Both A and B telemetry and the radar beacon are included.
[e] Includes all He and N_2, and 150-pound nominal propellant reserve, plus engine and line holdup.

B. *Vega* Third-Stage Propulsion System

The Laboratory is engaged in the development of a 6000-pound-thrust helium-pressurized propulsion system employing the storable propellant system nitrogen tetroxide (N_2O_4) and hydrazine (N_2H_4). It is planned to employ this system in the third stage of the *Vega* vehicle. The developmental static firing of engines is presently being conducted on the Laboratory. Developmental static testing of the propulsion system is underway at the Edwards Test Station, Edwards Air Force Base, California. Previous reports on the 6K system development program have been presented in *CBS 68*, *RS 1* through *5* and *SPS 5*.

Development of the 6K stage was originally undertaken as part of the *Juno IV* project. The stage was intended first to comprise the second stage of a two-stage IRBM-based satellite vehicle. Later it was to become the third stage of a three-stage satellite and lunar vehicle. Due to program changes, the vehicle development program was terminated, but development of the 6K propulsion system was continued as a separate program until the *Vega* program was formulated. The design parameters of the stage have been changed to conform to the requirements imposed by use as the third stage of the *Vega* vehicle. The system has the following gross characteristics:

(1) Propellant combination: nitrogen tetroxide (N_2O_4) and hydrazine (N_2H_4).
(2) Vacuum thrust: 6000 pounds (nominal).
(3) Burned propellant weight: 5050 pounds (nominal).
(4) Burning time: 252.5 seconds (nominal).

A more complete listing of design parameters is presented in Table 13.

It is presently planned to use a helium-pressurization system in the early flights of the *Vega* vehicle. This pressurization system was selected on the basis of its simplicity and attendant reliability, as well as on the premise that a simplified pumping system would facilitate development and thereby better assure fulfillment of the *Vega* vehicle development schedule. Meanwhile, a more advanced pressurization system, utilizing gas-generation pressurization and called the *heated-hybrid* system, is currently under development. The helium pumping system offers a simple and reliable means of propellant transfer, and with minor alterations and refinements, it will allow on-off operations.

Since system reliability is the main goal in the 6K propulsion development program, the introduction of gas generation will not be made until this more advanced system has demonstrated a high degree of reliability in pumping tests. Such a feasibility demonstration has been undertaken. The heated-hybrid system is based on the use of monopropellant hydrazine decomposition gases to pressurize the fuel tank. The decomposition gases are cooled from the reaction temperature (1460°F) to 150°F by heat exchange with the oxidizer flow to the main engine. The helium (used to pressurize the oxidizer tank) is warmed to 150°F by heat exchange with the hydrazine decomposition gases. An appreciable decrease in propulsion system weight can be obtained by using the gas-generation system in lieu of the all-helium system. A payload increase of some 80 pounds can be realized if the heated-hybrid system is substituted for the current all-helium system.

1. Propulsion System Development

The 6K static test unit is presently undergoing firing tests on Stand D at the Edwards Test Station, California. There are three main goals of the static test program: (1) to demonstrate an upperstage propulsion system using the storable propellants nitrogen tetroxide (N_2O_4) and hydrazine (N_2H_4), (2) to prove the various components such as engines, valves, and regulators so that these parts can be used in actual flight rounds, and (3) to determine the characteristics of the overall propulsion system so that its flight behavior can be predicted.

Table 13. Nominal 6K design parameters

F_∞ = 6000 pounds	r = 0.95 $\frac{\text{lb oxidizer}}{\text{lb fuel}}$
I_{SP_∞} = 300 lb-sec/lb	P_c = 150.97 psia
W_P = 5050 pounds (total propellant burned)	f_t = 23.06 sq in. (throat area)
$\dot{w}_p$ = 20 lb/sec	ε = 20.54 (expansion ratio)
t_b = 252.5 seconds (burning time)	C_{F_∞} = 1.7235
c^* = 5600 ft/sec	f_c/f_t = 2.5 (contraction ratio)

Prior to the firing tests, the 6K static test unit underwent six water-pumping tests. The water-pumping tests indicated that the helium-pressurization system possesses a relatively high degree of stability and reproducibility. The nitrogen gas actuation circuits were found to have response characteristics adequate to insure reliable timing of the several valve operations. This data was used to evolve a satisfactory sequence for the firing tests; the only change required was the increase in nitrogen gas storage volume from 30 to 60 cubic inches. However, the sequence chosen involved the electrical sequencing of two signals during the starting period to avoid the flow of prepressurization gas and propellant vapors from the two propellant tanks into the common pressurization manifold. The mixing of the vapors in the manifold could be disastrous and must therefore be avoided. The sequence originally contemplated (all valves opening simultaneously) proved to have this shortcoming. In early system tests, the present helium regulator configuration would not raise the manifold pressure above the propellant tankage prepressurization pressure before the pressurization valves on the tanks were opened. Upon opening the valves, the higher tank pressures caused flow into the common manifold. In later tests, the sequence was changed to include a delay between the signal to start helium flow through the regulator and the signal to open the pressurization valves and the propellant valves.

Use of an electrically controlled sequence incorporating the necessary delay between signals was considered to be undesirable for the 6K flight propulsion system. An alternate scheme has been proposed wherein the helium pressure at 3000 psi, released to the regulator inlet by the explosive valve, would be used to open all gas-actuated valves. The time delay would be accomplished by a shuttle valve in the actuation line which would be opened when the pressurization manifold pressure reached a value great enough to burst a calibrated rupture diaphragm in the valve. All valves would be closed by 3000-psi nitrogen gas released from a 50 cubic inch vessel by an explosive valve. Work on this sequence and the delay valve is continuing.

Three firing tests using the electrically controlled sequence were made during October. Engine Assembly No. 1 (Table 14), consisting of a short, tube wall chamber, a flight-type propellant valve, and a development-model injector, was used for all three firings; this assembly had been previously fired in Pit F. The first test was programmed for 15 seconds of duration so that Stand D flame deflector could be checked for possible hot spots before a long duration firing was attempted. The coolant used was distilled water instead of hydrazine. A summary of the preliminary data from this and the other two firings is given in Table 15. Post-firing inspection disclosed no damage. Figure 94 shows the propulsion system in operation during the second water-cooled run.

The emergency cutoff valve (oxidizer), which failed to operate because of corrosion during the component checks, was replaced before the second firing. Water was used as a coolant again in the second firing, and a pre-fire purge was incorporated in the fuel side of the injector because difficulty had been encountered during the firing of another engine assembly in Pit F. Approximately 1 second

Table 14. Engine Assembly No. 1[a]

Characteristic	Value
Throat area, sq in.	21.164
L^*, inches	33.85
Contraction area ratio	2.705 to 1
Expansion area ratio	4.29 to 1

[a] Based on post-D-3 measurements.

Table 15. Performance summary

Parameter	Test D-1	Test D-2	Test D-3
Duration, second	15	200	200
Chamber pressure, psia	155	156	152
Propellant flow rate, lb/sec	19.14	19.12	18.89
Mixture ratio, O/F	0.86	0.85	0.97
c^*, ft/sec	5455[a]	5440[a]	5470[b]

[a] Based on pre-D-3 measurements.
[b] Based on post-D-3 measurements.

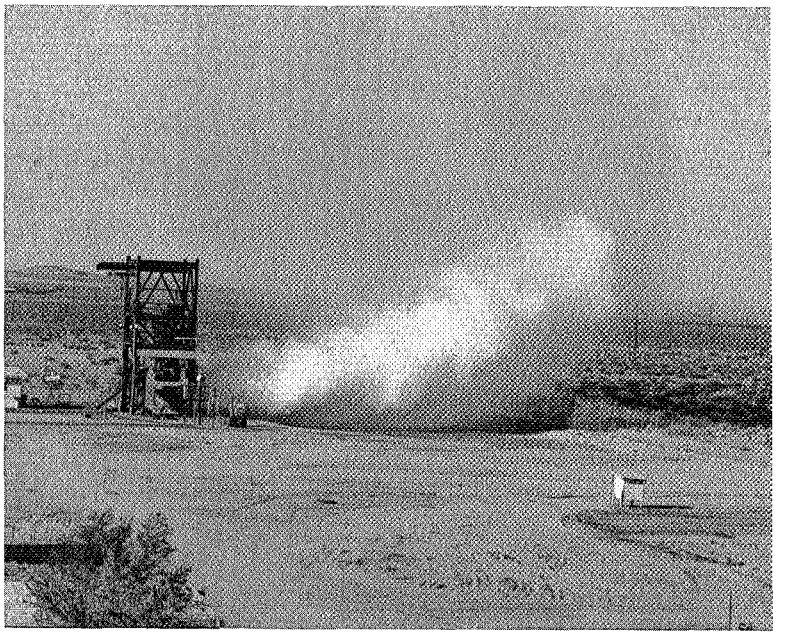

Figure 94. Firing test using water cooling

after start, periodic bursts of pressure oscillations occurred which continued until the end of the 200-second firing. The oscillations were sensed by three chamber pressure transducers and both the fuel and oxidizer injector manifold transducers. The probable cause of these oscillations is noted below. At 101 seconds after start, the tubing nut of the upstream chamber pressure tap split in two, releasing the tubing connected to the transducer; slight erosion of the tap resulted, but motion pictures disclosed that little or no flame issued from the open tap. The aluminum tubing nut was replaced with a stainless steel nut for the next firing.

The third test was a 200-second firing using the fuel (hydrazine) as a regenerative coolant. A new oxidizer flow meter was installed for this firing after discrepancies in the data from the second firing were noticed. The periodic bursts of oscillations appeared shortly after start, continued for approximately 34 seconds, and then ended after a particularly violent variation in the chamber and injector manifold pressures. At this time, the oxidizer injector manifold pressure transducer was ruined. From 34 seconds until approximately 70 seconds, a sinusoidal variation (16 to 18 cps) was apparent in the chamber and manifold pressure records. This sinusoidal wave was gradually damped out, and the remaining portion of the firing was relatively smooth. Post-firing inspection showed no hardware damage except for heating of the tubing close to the oxidizer injector manifold tap and a small weld crack joining the oxidizer and fuel injector manifolds. It is probable that propellant cross-flow through the crack caused the pressure oscillations in the second and third tests.

During the three firings, the silver-solder forming fillets between the thrust chamber tubes was being gradually eroded away, but at no location did the fillets entirely disappear. The chromium plating on the nickel injector face was removed from an annular area adjacent to the fuel orifice circle and around the center orifice. The splash-plate impingement areas had become burned and slightly eroded. Altogether, the condition of the engine assembly was judged to be fairly good and suitable for additional firings. The internal surfaces of the fuel-system hardware were partially coated with aluminum oxide which was judged to be a result of the water flushes used in the system after each test.

2. Thrust Chamber Development

As described in *SPS 5*, the thrust chamber for the 6K engine has been designed expressly for the propellant combination of nitrogen tetroxide and anhydrous hydrazine. As predicted on the basis of past research at JPL, hydrazine can be successfully used as a rocket-engine coolant provided that the proper precautions are observed. The heated hydrazine must be prevented from coming in contact with surfaces which will catalyze the hydrazine decomposition or which are readily reducible. Due to the fact that hydrazine will spontaneously decompose at high temperature, it is also necessary to eliminate all stagnation zones where the coolant could become overheated.

In order to satisfy these requirements and also to fabricate a thrust chamber in the shortest possible time, a tube-wall method of construction was selected as the primary approach. An alternate method of construction called the welded-rib type showed promise of lighter weight and is being pursued as a state of the art improvement on a longer development schedule.

Tube-wall thrust chamber. The tube-wall thrust chamber is composed of 111 Type 347 stainless steel tubes of 0.020-inch wall thickness. The tubes are formed, by a combination of spinning and drawing, to the proper diameter at each station and then sized to the cross sections shown in Figure 95. The tube is flattened in the chamber and convergent section in order to reduce the total heat-transfer surface area and to increase the local coolant velocity. The crescent-shaped cross section of the tubes in the divergent area of the nozzle results in a large reduction in tube weight and propellant holdup. The wire wrap, which is attached to each tube, prevents the concave surface of the tube from buckling outward under internal pressure.

As described in *SPS 5*, early models of the thrust chamber were assembled by hand using a silver-copper alloy for the braze material. In order to increase the uniformity and corrosion resistance of the thrust chamber, present units are being brazed in a furnace with nickel-based alloys. Two thrust chambers of 4:1 and one of 20:1 expansion ratio have been successfully furnace-brazed. One 4:1 chamber and one 20:1 chamber have completed the second braze cycle of the three which are normally required. Figure 96 shows a furnace-brazed thrust chamber of 20:1 expansion. A new tube design for both the 4:1 and 20:1 chamber has been completed and the tubes are being fabricated. This new design involves a greater flattening of the tubes in the areas just upstream and downstream of the throat and will result in a high coolant velocity and therefore a greater burnout margin.

A successful test firing of 40-second duration was made on the first furnace-brazed thrust chamber, using water as the coolant. However, a test firing using hydrazine cooling terminated with a thrust chamber burnout at 6 seconds. The exact cause of this failure has not yet been

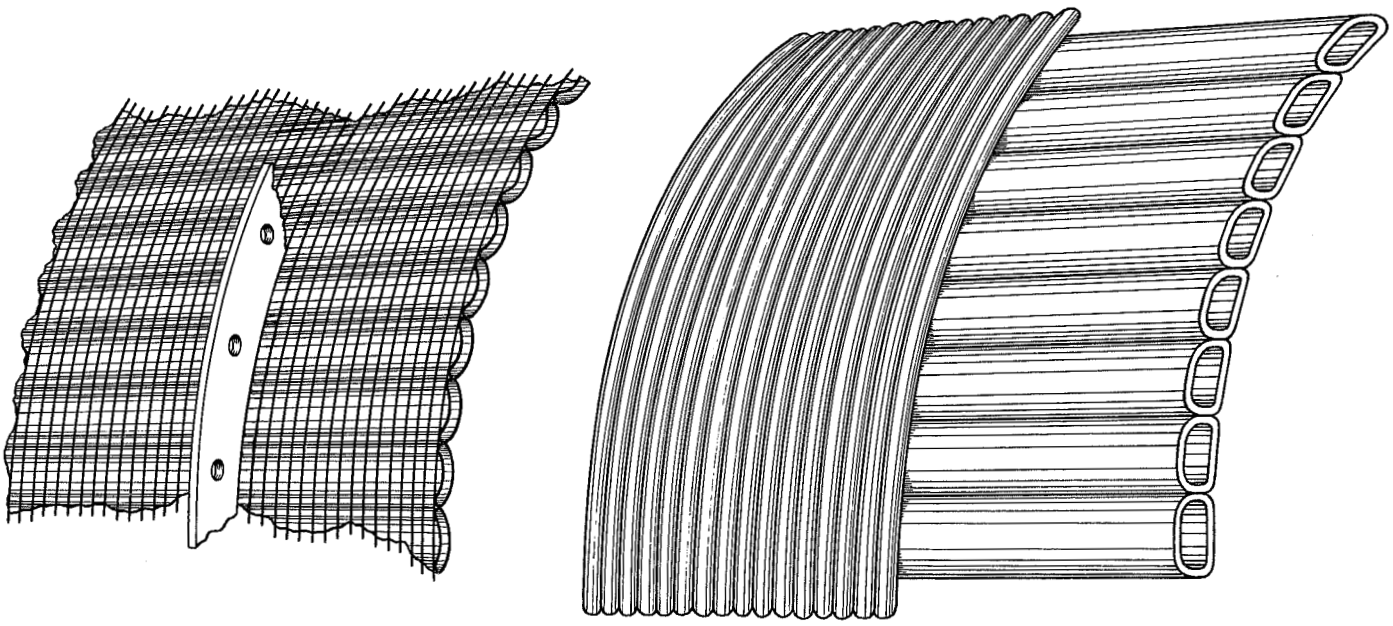

Figure 95. Cross section of thrust chamber

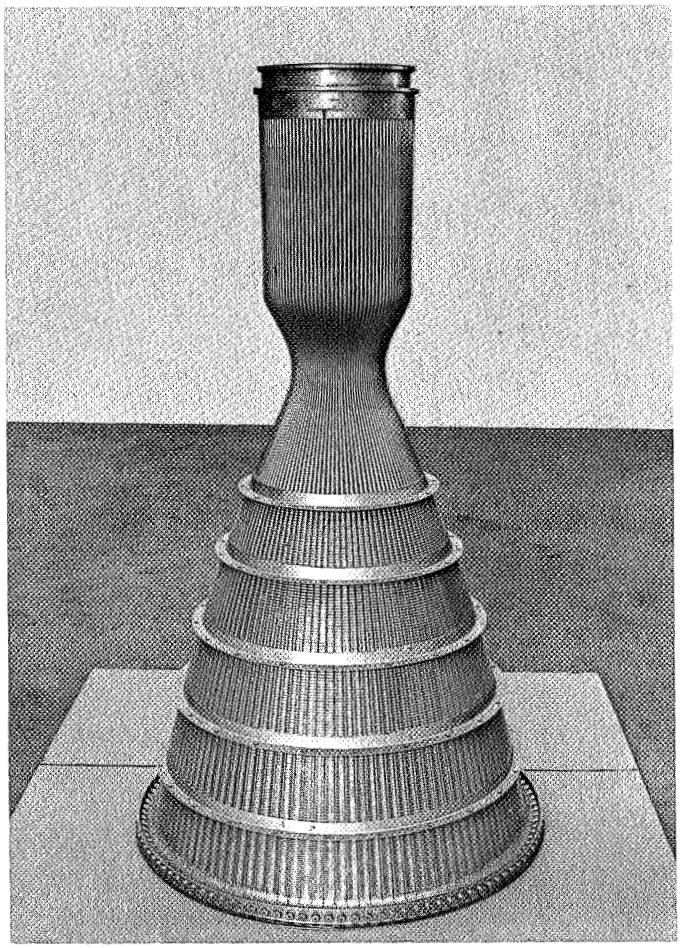

Figure 96. Tube wall thrust chamber, 20:1 expansion ratio

determined, but it is believed that maldistribution of heat flux caused by poor injection symmetry was responsible. The injector embodied minor modifications from those previously used and was test-fired for the first time using heated fuel in the test in which failure occurred.

A silver-brazed thrust chamber, which had been proof-fired with the prototype flight propellant valve and injector at the JPL Pasadena facility, was delivered to the Edwards Test Station and incorporated in the 6K static test unit. Two test firings (employing water cooling) of 15-second and 200-second duration were made, and were followed by a successful firing test (employing fuel cooling) of 200-second duration. The engine was then disassembled and inspected and is now being prepared for additional hot firings at the Edwards Test Station.

3. Propellant Valve Development

The *JPL-6K* propellant valve (Fig 97) is of the spherical plug type. The integral aluminum body contains two ported balls which are linked together and driven by a single rotary actuator. The linkage arrangement insures that the oxidizer ball will open ahead of the fuel ball to give a smooth controlled starting transient. On closing, the fuel ball closes first to prevent a residual accumulation of fuel in the thrust chamber. The seals are spring-loaded Teflon, and the balls are heat-treated 17-4PH stainless steel. The valve also acts as a structural load-carrying member in that the thrust and gimbal actuating forces are transmitted directly through it.

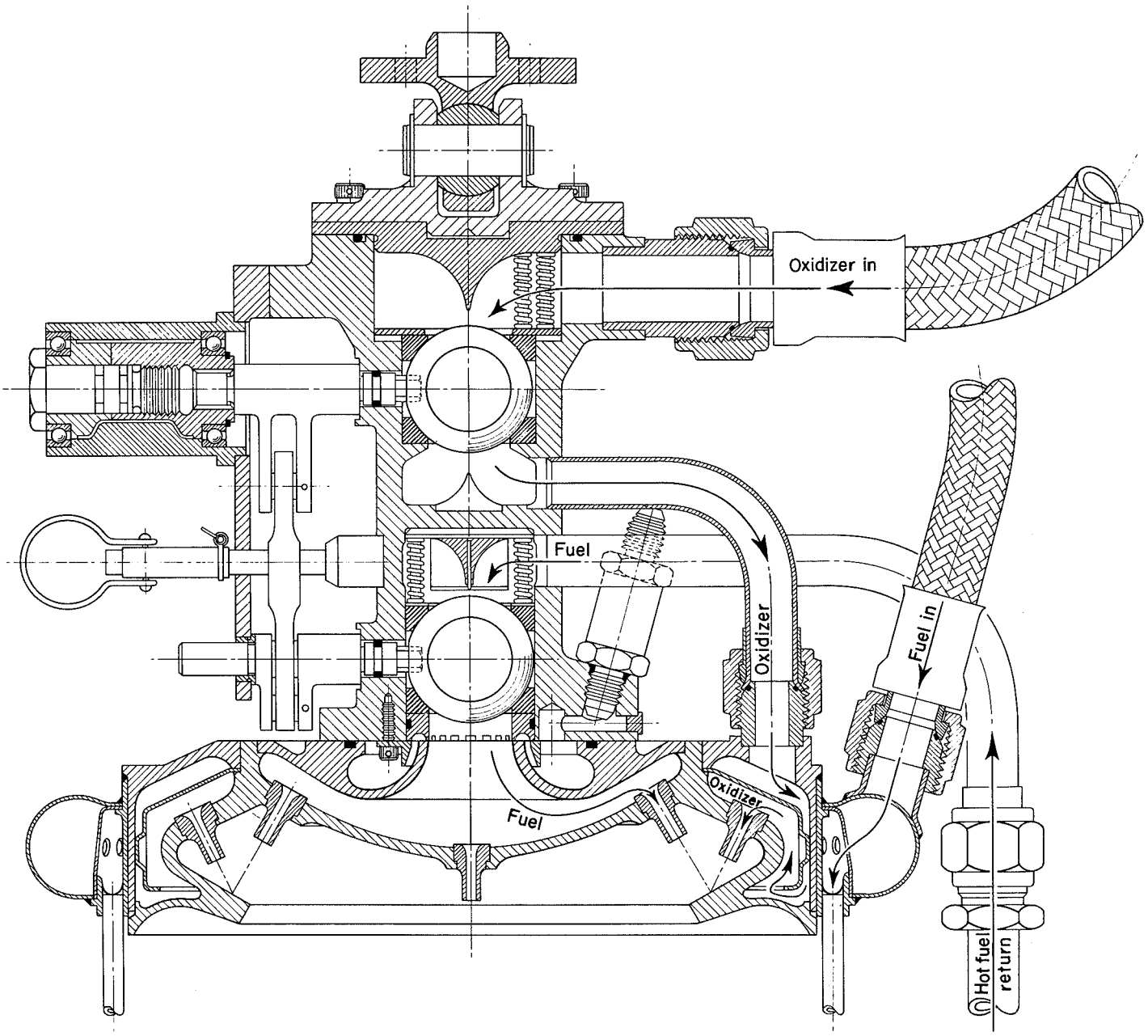

Figure 97. Head end of flight type engine

Although the operation of the propellant valve during system testing at the Edwards Test Station was without fault, some malfunctions have developed during static proof firing at the Laboratory. In two of the proof-firing tests, the valve opened rather slowly, and a post-firing inspection revealed that the drive shaft was twisted. In a third test, the operation of the valve was so slow that oxidizer splashed back through the fuel orifices and accumulated in the injector fuel manifold. When the fuel ball opened, the resulting combustion destroyed the injector and damaged the propellant valve. A post-firing inspection of the third test revealed that the actuation drive shaft was twisted.

These valve malfunctions have been attributed to the increased break-away torque resulting from a high fuel-tank pressurization level. The system pressure drop in the test cell used for proof firing requires fuel-tank pressures of about 340 psia, while the heavy-weight system at the Edwards Test Station operates with a prepressurization level of about 240 psia. Further testing has revealed that the valve break-away torque is far more sensitive to pressure when hydrazine rather than water is used as the pressurized fluid. The actuation drive shaft has been redesigned to carry a higher torque load, and the test cell will be modified to allow the use of lower fuel-tank pressures.

4. Injector Development

The injector which is being developed for the *JPL-6K* engine is of the splash-plate type with 16 oxidizer-on-fuel impinging doublets. The heated face and splash plate of the injector are made of Type 9 nickel alloy and all other parts are of Type 347 stainless steel. The thrust and pressure loads on the injector are carried by webs which are welded to the propellant valve. These webs have been omitted from the head-end layout (Fig 97), but may be observed in Figure 98. The nickel splash plate is cooled by the propellant streams which impinge upon it and by the oxidizer which flows within it.

Recent developments in injector design have included the elimination of swirl-jets from the oxidizer orifices and of screens from the fuel orifices. The swirls and screens were originally believed to improve the properties of the impinging streams. However, further investigation revealed that they had very slight, if any, effect on performance. Injector performance without the use of swirls or screens has been excellent in test firings employing ambient hydrazine (c^* approximately 5690 ft/sec at $r = 0.9$). In the first firing test with the new orifice configuration employing hot hydrazine, the thrust chamber burned out at about 6-second duration. The total heat rejected to the coolant during the 6 seconds was less than predicted and the performance was the highest yet obtained with heated hydrazine ($c^* = 5550$ ft/sec at $r = 1.04$). The injector face showed signs of overheating, and the thrust chamber, signs of localized hot spots. A water flow test of the injector after the firing revealed a mass flow unbalance among the 16 oxidizer jets. This unbalance was not observed during the flow testing which preceded the firing test. An internal inspection was made and no reason for the change in flow properties of the injector has been found.

The injector used in system testing at the Edwards Test Station has now had a total of 563 seconds of operation. The face and splash plate show slight signs of erosion, but the injector is still suitable for further firing tests (Fig 99).

5. Heated-Hybrid Generated-Gas Pressurization System

Concurrent with the development of the helium-pressurized 6K propulsion system for the *Vega* program, considerable effort is being expended to improve the payload capabilities of the vehicle by minimizing propulsion system weight. One such development project is the heated-hybrid generated-gas pressurization system. Progress in this program has previously been described in *CBS 68*, *RS 1* through *5*, and *SPS 1*. Henceforth, the development of this system will be described only in the *SPS*.

The project has been termed a heated-hybrid system since a monopropellant-hydrazine catalytic gas-generator system supplies decomposition gases to pressurize the fuel tank and a compressed-helium system supplies gas

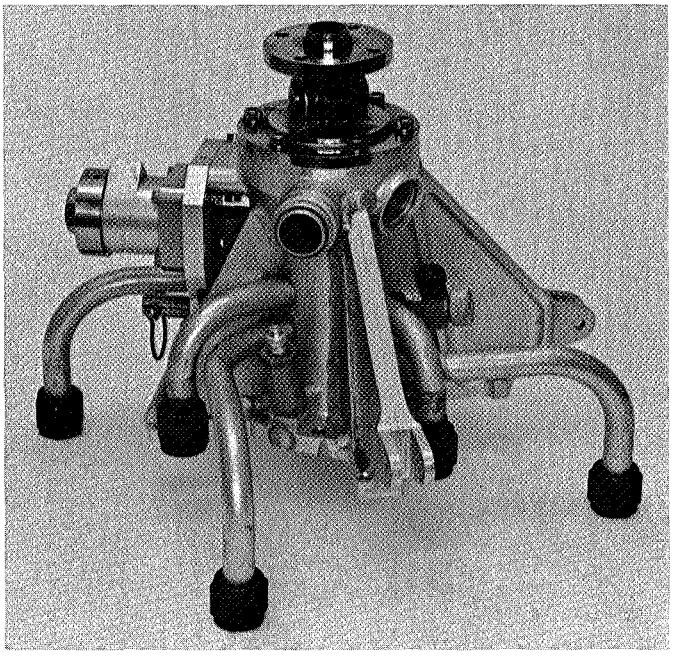

Figure 98. Flight type propellant valve

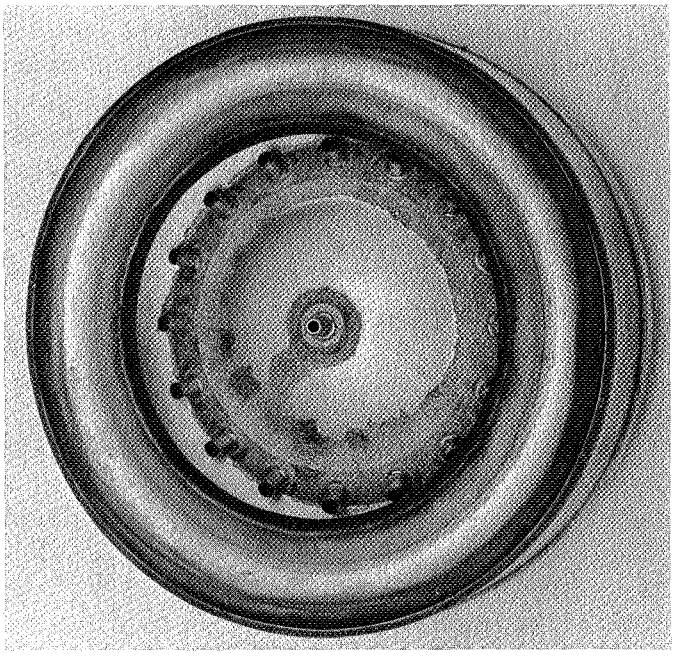

Figure 99. Flight type injector after test

to pressurize the oxidizer tank. The monopropellant decomposition gases, which are quite hot when generated, are cooled before entry to the fuel tank by interchange first with the helium gas, thus warming the helium, and finally with the liquid nitrogen tetroxide supplying the rocket engine.

The separate subsystems are mated through a suitable control device into a unified system. (A schematic of the system appears in *CBS 68*.) It is expected that a saving of approximately 50% in pressurization system weight can be obtained through the substitution of the heated-hybrid system for the compressed-helium pressurization system employed in the present model of the 6K propulsion system.

Activities during this report period have been centered upon full-scale system tests utilizing the pseudo-vehicle flow system where water, rather than actual propellants, is pumped from the vehicle tanks. This series of tests was directed toward the evaluation of: (1) the influence upon the system starting transient of propellant-tank prepressurization level, tank ullage volume, and time delay in propellant valve opening; (2) the increase in the efficiency of the helium-gas expansion process afforded by warming of the helium by interchange with the hydrazine decomposition products; and (3) the detailed behavior and stability of system parameters at operating levels and over the operating durations anticipated in typical *Vega* missions. A total of 18 full-scale tests was made; good data was obtained in all of the tests although in two of the tests a facilities power failure caused premature termination.

The system-starting transient was discussed briefly in *RS 4*. Typically, in keeping with the operating philosophy of the *Vega* program, the propellant tanks are prepressurized before startup of the propulsion system. At ignition, all systems valves are open. This means that the gas generator products are entering the tank while the engine is being fed propellants by the expansion of the prepressurized ullage. The transient is due to (1) the time required for the gas generator to come up to full chamber pressure, (2) the time required for the gases to reach an equilibrium temperature, and (3) the fact that the gas generator capacity is limited by system pressure drop.

A typical total flow-rate variation immediately after ignition for a test without valve sequencing is shown in Figure 100. The specific flow-rate variation for several different conditions, with the nomenclature as shown on Figure 100, is contained in Table 16.

The values used for each parameter are based upon the current system characteristics and/or operating philosophy of the 6K propulsion unit for *Vega*. It is of interest

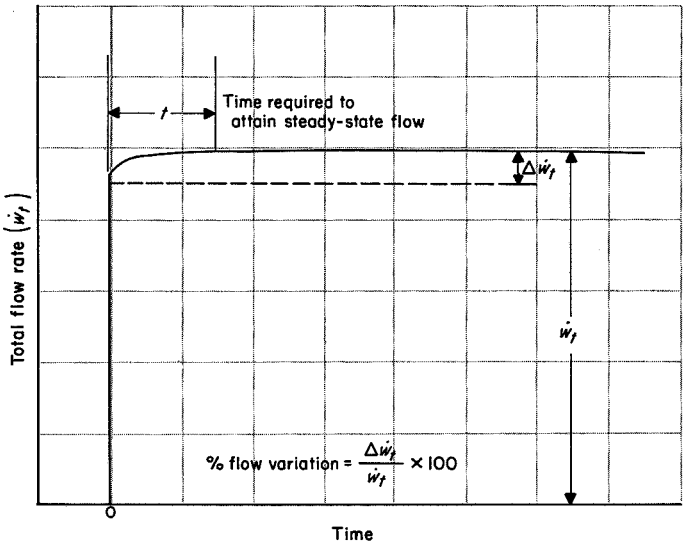

Figure 100. Typical flow rate variation

to note that, with the proper time delay in propellant valve actuation, the effects of any of the stated conditions of prepressurization level and ullage can be entirely eliminated without attendant difficulty. It should be noted, however, that an inherent limit in the duration of valve delay time exists because of the presence of stagnant nitrogen tetroxide in the heat exchanger which normally cools the decomposition products. The total delay time available is on the order of 5 seconds. When no valve sequencing was used (except at very low prepressure levels and at the largest ullage) the total propellant flow rates were below nominal by 5 to 6% (maximum), a value not considered detrimental to the operation of the rocket engine or the overall propulsion system.

Table 16. Effect of various pressurization and ullage values upon heated-hybrid pressurization system performance

Test No.	Prepressurization, psia[a]	Ullage, in.^{3}	Variation between total flow at $t = 0$ and steady-state flow,[b] %	Time required to obtain steady-state flow, sec	Time delay before flow valves open, sec
33	247	2000	−2	30	0
37	248	6900	0.2	—	0
38	214	6900	−6	60	0
39	214	2000	−6	60	0
40	214	6900	1.4	—	3.8
41	139	2000	−31	60	0
42	214	2000	−3	20	1.5
43	220	6900	0.7	—	3.6
47	220	6900	0.4	—	3.5
52	220	6900	0	—	2.8

[a] Nominal tank pressure is 250 psia.
[b] An explanation of these parameters is given in Figure 100.

In the heated-hybrid pressurization system, the high-temperature gases from the monopropellant gas generator must be cooled before entry into the fuel tank. This cooling is necessitated by considerations of compatibility with the hydrazine fuel, tank-wall stress levels, and gas-pressure stability. A portion of this waste heat can readily be employed to raise the temperature of the compressed helium used to pressurize the oxidizer tank. The helium is stored at approximately 3000 psia and cools down materially as a result of the expansion process in the helium tank. In the prototype system, the temperatures of the helium reach approximately −100°F in the course of the expansion proceeding from 3000 to 250 psi.

By using some of the heat available from the decomposition gases, the temperature and, hence, the efficiency of the helium system can be raised materially. The quantity of heat which can be transferred to the helium is temperature-limited at 275°F by the allowable tank-wall stress levels and gas-pressure stability considerations. As the compressed helium temperature at the heat exchanger inlet drops during a test, the outlet helium temperature drops from 275 to approximately 225°F.

The relation between the helium volume requirements and the operating parameters of the system is given by the following relationship (Ref 1):

$$\gamma' = \frac{V_R (P_i - P_f)}{(V_P) P_R}$$

where

V_R = volume of reservoir
P_i = initial reservoir pressure
P_f = final reservoir pressure
V_P = volume of propellant tank filled with gas
P_R = regulated pressure

In this relationship γ' is a measure of the heat transfer taking place during the gas-expansion process. For an expansion where no heat transfer is involved, the process is adiabatic and γ' equals the specific heat ratio of the gases. For an isothermal process, γ' equals unity.

For the prototype heated-hybrid pressurization system, experimentally determined values of γ' for the overall system (i.e., the pressure reservoir expansion, the regulator throttling process, and added heat from the decomposition gases) are shown in Table 17. From these values it is evident that the performance of the overall system approaches that of an isothermal process.

A typical set of operating data obtained in a full-duration operation of the heated-hybrid system is shown in Figures 101 and 102. Particularly noteworthy is the

Table 17. Pumping efficiency of preheated helium

Operating parameters	Test No. 41	Test No. 42	Test No. 43
Initial reservoir pressure, psia	2966	2984	2907
Final reservoir pressure, psia	246	253	245
Initial reservoir temperature, °F	74	69	73
Final reservoir temperature, °F	−97	−92	−99
Helium temperature at heat exchanger exit,[a] °F	250	256	264
Helium temperature in oxidizer tank[a]	129	129	134
Effective specific heat ratio γ'	1.13	1.12	1.07

[a]Steady-state values.

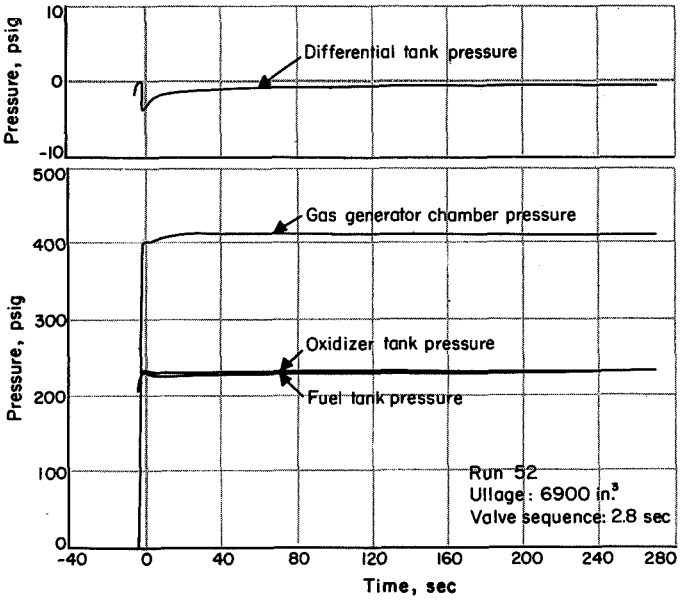

Figure 101. Typical pressure data from pumping test

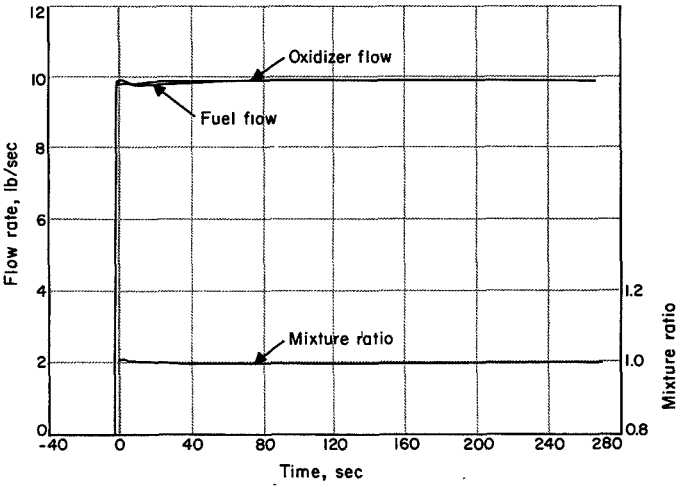

Figure 102. Typical flow and mixture ratio data, Pumping Test 52

general stability of the propellant-tank pressure levels, the propellant flow rates, and the mixture ratio.

Present project activity is being centered upon the vibration testing of the critical system components and readying the prototype system for a series of full-scale full-duration tests using a prepressurization level, ullage, etc., most likely to be the nominal values encountered in the *Vega*. It is anticipated that several complete tests will be made using the same conditions each time in order to evaluate the stability of the system to consistently reproduce its performance.

6. Instrumentation

A complete instrumentation system (Fig 103) for testing the 6K-thrust storable-liquid propulsion system has been installed at Edwards Test Station. This system was constructed under contract to Consolidated Systems Corporation, Monrovia, California, and is now undergoing final acceptance tests. Although the present system furnishes instrumentation only to the new Test Stand D, in which the 6K propulsion system is located (*SPS 5*, p 40), provisions for the use of the common instrumentation components of the system by several other test stands will be made in the future. A large additional program patchboard will be used for connecting the other test stand circuits and existing Test Stand D circuits to the common instrumentation equipment.

The proposed system when completed will provide sufficient independent instrumentation for each test operation to permit transducer calibrations and a complete prerun checkout of the system undergoing test. After a satisfactory checkout has been performed, connections will be made to the common equipment in the data recording center, electrical calibrations of this system will be made, and the test performed. The common equipment may then be disconnected, allowing it to become available for other test-stand operations, or for data reduction or maintenance. Following are the equipment lists for the three areas associated specifically with Stand D operations and also for the common-equipment area:

(1) Test Stand D junction boxes (2)
  (a) Channel capacity:
    60—4-Arm bridge terminations
    48—Thermocouple terminations
    14—Position-potentiometer terminations
    12—Turbine meter flow terminations
    12—Accelerometer terminations
    1—6-Channel accelerometer pre-amplifier, Dynamics Inst. Co., Mod 2690
  (b) Equipment:
    1—24-Channel 32°F reference junction, Cr-Al, Pace Inst. Co.
    1—24-Channel 150°F Cr-Al/Cu-Con/Fe-Con, Pace Inst. Co.
  (c) Transmission line to terminal room, 45-ft length:
    10—25, 2-Conductor twisted pair shielded No. 22 PVC-PVC insulation (250 circuits)
    2—6, 2-Conductor twisted pair shielded No. 22 PE-PVC insulation (12 circuits)

(2) Terminal room for Stand D
  (a) Equipment:
    42—Excitation power supplies for bridges, position pots, and tc calibrator, Video Inst. Co.
    40—4-Arm bridge balance and calibration circuits
    48—Channel thermocouple calibration system
    12—Channel turbine flowmeter calibrator
    1—DC preamplifier and digital voltmeter, Kin Tel 114A and Non-linear Systems 481
  (b) Transmission line to blockhouse control area, 580-ft length:
    104—2-Conductor twisted pair, shielded No. 22 PVC-PVC insulation

(3) Blockhouse control area for Stand D (Fig 104)
    11—366-Jack monitoring patchboard
    6—DC amplifiers, KinTel 111BF
    6—Speedomax recorders with retransmitting slidewires
    1—36-Channel oscillograph CEC 5-119, with Datarite *quick-look* record magazine
    1—3-Channel turbine flowmeter converter
    20—Monitor meters (indicators)
    1—14-Channel position balance unit
    2—Closed-circuit TV monitors, KinTel
    2—High-frequency pressure measuring systems, Photocon DG101

(4) Blockhouse common equipment area
    1—3264 pin program patchboard, A-MP
    1—60-Channel MicroSADIC digital recording system
    24—DC amplifiers, KinTel 111 BF
    36—Low-pass filters for amplifiers, 10 cps at 3 db down
    10—DC amplifiers, Neff 100-C, for thermocouple signals
    1—40-Channel time-share commutator for Neff amplifiers (20 channels can presently be used with the 10 Neff amplifiers)

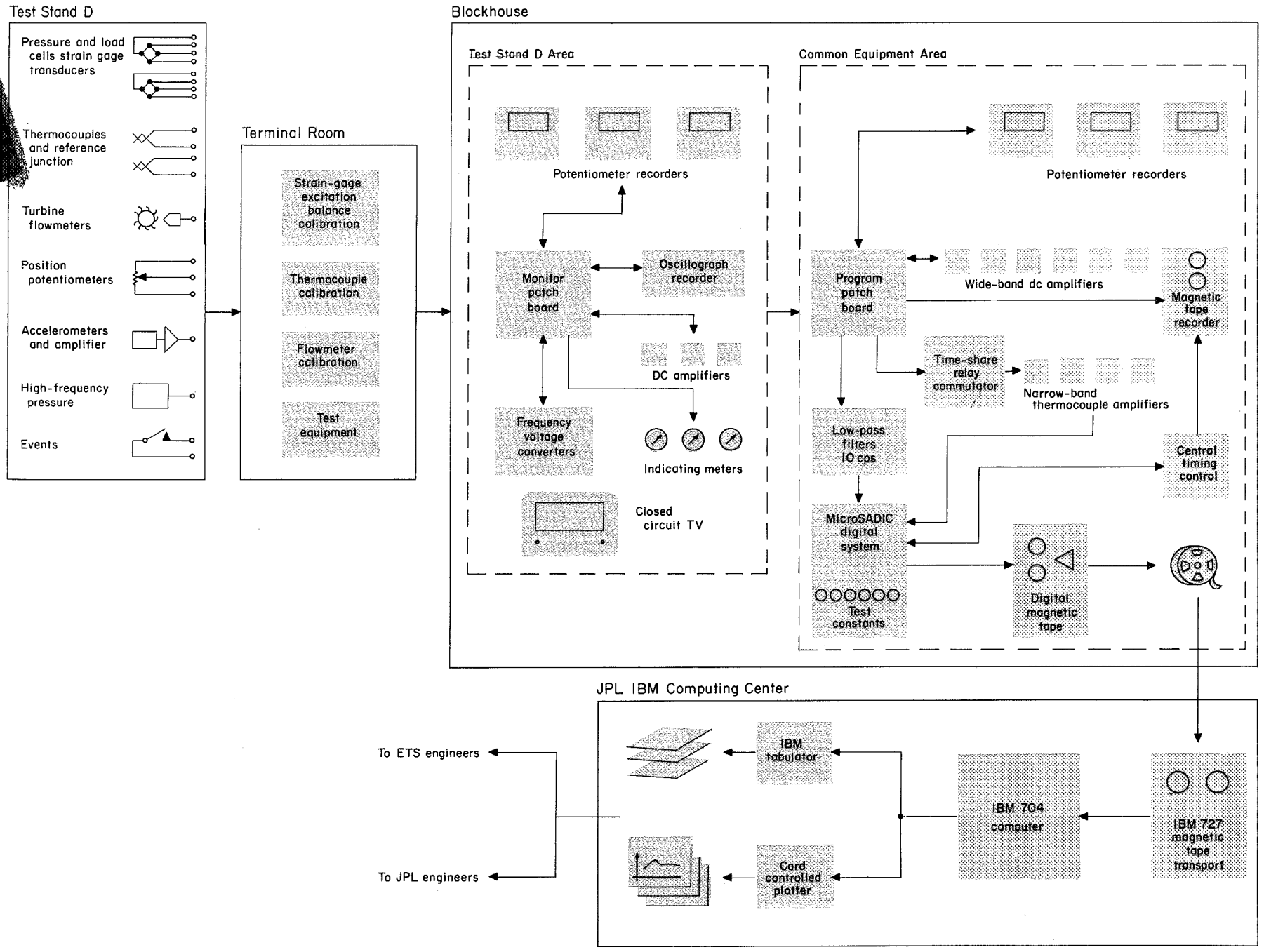

Figure 103. Instrumentation system for Edwards Test Station

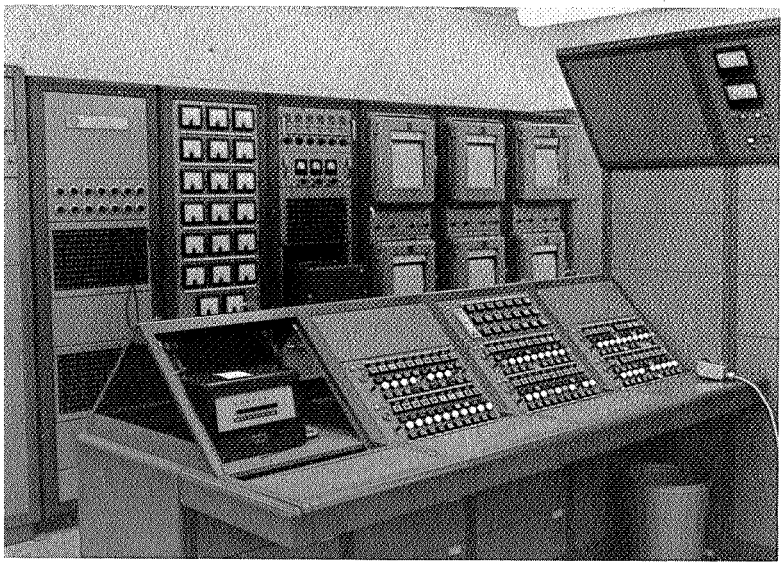

Figure 104. Control area for Stand D

1—14-Channel magnetic tape recorder, CEC 5-752, containing 4 direct-recording channels, 10 FM recording channels, 4 direct-reproducing channels, and 4 FM reproducing channels

12—Speedomax recorders with retransmitting slidewires

1—Control console, including instrumentation system control functions, and digital system calibration functions

1—Communication center (10-station dial telephone exchange)

An important feature of the ETS instrumentation system is the high-speed, transistorized MicroSADIC digital recording equipment (Fig 105) which prepares digital magnetic tapes suitable for entry into the JPL IBM computers, either the 704 or the forthcoming 7090.

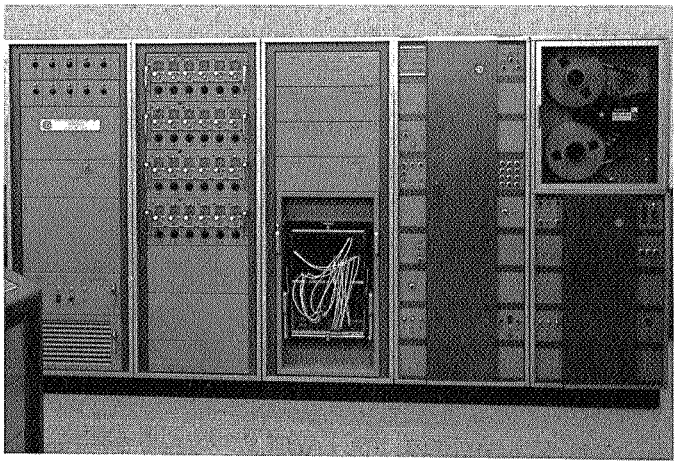

Figure 105. MicroSADIC, program patchboard, amplifiers, filters, and low-speed commutator

The MicroSADIC has a capacity of 60 channels, and a total sampling rate of 6666 samples/sec. The scan rate varies with the requirements of the sampling program selected for a particular test. The program variables include: the number of channels to be sampled, a choice of the use of low-level multiplexing of thermocouple signals, magnetic-tape recording using a blocked or continuous format, and selection of a minimum sampling rate consistent with data reduction program requirements. For example, if it is assumed that the full 60 channels are to be scanned plus 12 digits of time identification, then the continuous mode provides 100 scans/sec and the sampling rate per channel is 100 samples/sec. Using the blocked format, the scan rate is approximately 50 scans/sec. The usable scan rate for thermocouples when using the low-level multiplex is appreciably lower than the above figures due to the narrow bandwidth of the thermocouple dc amplifiers. The time-share relays are therefore cycled at a 10 cps rate allowing each thermocouple to be sampled 5 times/sec. This low sampling rate is consistent with the frequency response of thermocouple channels.

Higher-frequency channels, such as those from strain-gage pressure and load cells, are amplified through wide-band dc amplifiers. Before being sampled by the MicroSADIC, the signals are filtered by 10-cps low-pass filters. The 10-cps cutoff and 50-sample/sec sampling rate combine to reduce folding or aliasing errors.

The nominal input to the MicroSADIC required for a full scale count of ± 999 is ± 1 volt dc, and the time required to perform the analog-to-digital conversion is 93 microseconds. The specified accuracy of the digital system, including amplifiers, exciters, commutators and analog-to-digital converters is 0.25% of full scale for 99% of the measurements.

Digital recording systems are commonplace in rocket motor testing facilities, and their usefulness in large-scale and prouction testing is well established. The advantages to be gained in a development program such as that being carried out at Edwards Test Station are less evident, however, and the following is therefore noted: (1) Automatic digital recording is in general more accurate than analog recording, both in the record itself and in the handling and processing of the record. (2) By use of digital computer processing, the reduced data can be quickly tabulated in desirable engineering units. (3) The availability of digital magnetic tape records opens the possibility for more sophisticated data analysis using the large digital computer now available at JPL; such

analyses include: statistical studies, correlation and power spectral density studies, and stability studies. (4) For a large number of data channels, digital recording is cheaper and simpler than analog recording and personnel required are fewer. (5) Being automatic, there is less likelihood of human error in the data recording and reduction process.

The obvious problems associated with digital recording are: (1) Since all data is routed through the digital-recording apparatus, it is necessary to back up some key channels with conventional analog recorders and to have adequate safeguards that the digital recorder is functioning properly. (2) The digital magnetic tape output is of no use to the testing engineers until the tape can be processed, and typed records and plots obtained. This involves serious time delays.

The two problem areas noted above were studied during the procurement of the ETS data system, and the following solutions adopted: (1) Critical data channels will be backed up by an array of strip-chart recorders, oscillographs and a conventional magnetic-tape recorder. In addition, the MicroSADIC has a feature called a Quality Analyser which checks the performance of the equipment up to and including the digital tape record. (2) Quick-look facilities will be added to allow selected portions of the raw data to be tabulated and plotted. Equipment is presently under development by CSC and other manufacturers. Furthermore, the capability of the JPL IBM computing center will be extended in the area of data reduction. This involves the procurement of fast-magnetic-tape controlled *x-y* plotters to supplement the present punched-card controlled plotting equipment, and the procurement of the new IBM-7090 equipment in 1960. The IBM-7090 has fast-interrupt capabilities which will allow routine data handling without interference with higher priority scientific calculations and, therefore, tape can be processed immediately on arrival at JPL.

Since the bridge-transducer output voltages are amplified to 1-volt full-scale level for recording or digitizing by the use of unbalanced-input dc amplifiers, the input circuits have no capability for rejecting common-mode noise inputs. Therefore, floating-type transducer exciters are used which are highly shielded from the 120-volt ac line so that less than 5-microvolts peak voltage is introduced into a 350-ohm transducer bridge circuit from this source. The effect on the transducer circuits of the common-mode voltage which exists between transducer and the blockhouse recording center is reduced greatly by floating the entire blockhouse rack system with respect to the local earth or power-system ground, and connecting these racks to test-cell earth-ground by use of a bus-bar. Isolation transformers are used for supplying power to the common equipment area, and for each test-stand terminal room and control area (Fig 106).

All analog recorders or indicators, such as recording potentiometers, oscillographs or oscilloscopes, magnetic-tape recorders, and indicating meters are driven from amplifier outputs when amplifiers are used as part of the instrumentation circuit. If a measurement is needed only for monitoring purposes, or if it is not to be recorded by the MicroSADIC, it may be recorded by potentiometer only. In this event, the recorder may be viewed directly, or its output may be retransmitted by slidewire to a remote meter in the control area.

Since the primary 60-cycle ac power at ETS is subject to extended disturbances of a periodic nature which are severe enough to adversely affect the instrumentation

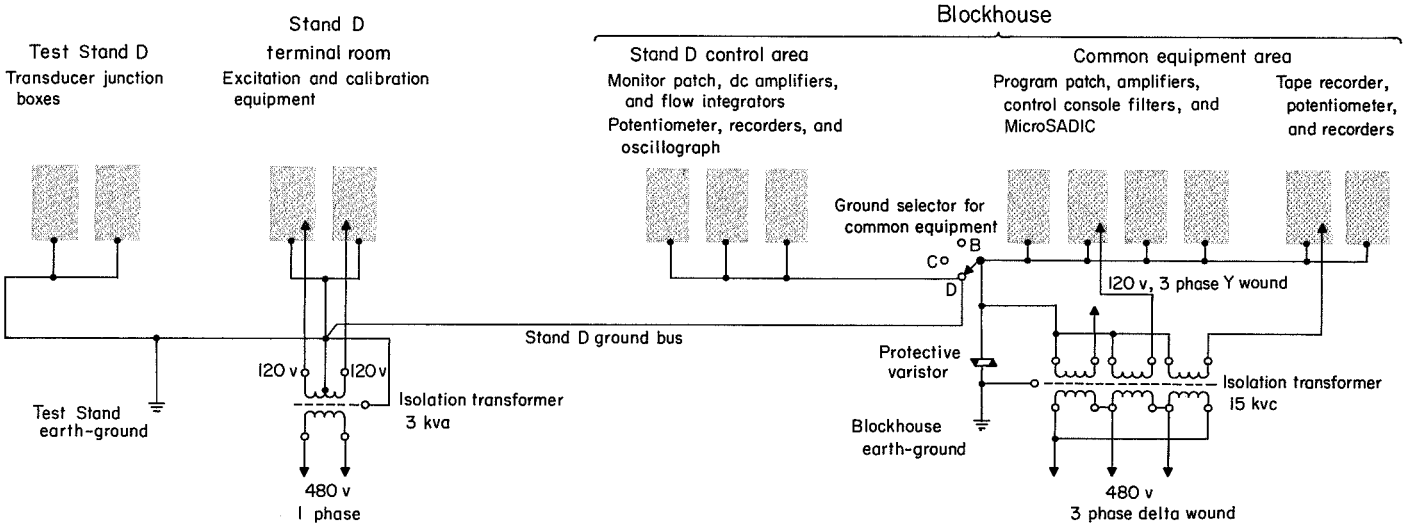

Figure 106. Mock ground system

system performance, an emergency engine-driven alternator of 15-kva capacity is available to operate the instrumentation system when the public-utility power is unsatisfactory. A Varistor connected between the bus-bar and the local earth-ground in the blockhouse is used to prevent excessive rack-to-ground voltage in the event of a lightning discharge near the test stand.

C. Instrumentation

1. Vega Third Stage

a. High-accuracy measurement. The *Vega* third-stage A and B telemetering systems are FM/FM systems and are therefore subject to the fundamental accuracy limitations of any analog measurement process. These limitations are the result of disturbances throughout the system which affect the measured quantity. These disturbances fall in both the random and systematic categories. The systematic, or instrumentation errors are reduced through the use of more stable modulation and demodulation devices and through inflight calibration of the system. The information, however, is still distorted by certain characteristics of the frequency multiplexing scheme and by noise sources in the communication system. Simple direct modulation of the subcarrier oscillator by the information signal, therefore, is not feasible where high accuracy is required. For these *Vega* third-stage measurements requiring accuracies to 0.2 to 0.4% of full scale, a scale expansion technique will be used prior to modulation. This will reduce the effects of system error relative to the full-scale deviation of the measured quantity in order to provide the desired accuracy.

The scale expansion is accomplished by determining which of N equally spaced levels the information voltage exists in, and then transmitting both the information in the level, expanded by the factor N, and the level number n where $n = 1,2,3 \cdots N$. If no error were introduced in amplification, the percent of full-scale telemetering error is then $1/N$ its previous contribution.

In the *Vega* application, this technique will be mechanized through quantization of the information signal into $N = 16$ levels. The level information will be carried on IRIG Channels 8 and 9, the expanded signal information on Channel 10. The quantization and amplification device is called *Vernitel* (Hoover Electronics Company, Timonium, Maryland).

The Vernitel quantizes the information signal into 16 discrete levels by continuous successive comparison of the signal voltage with four voltages weighted in binary fashion at 0.5, 0.25, 0.125 and 0.0625 of full scale or 8, 4, 2, and 1 parts in 16. If the voltage at the comparator is greater than the weighted value, this value is subtracted from the signal and the remainder is compared with the next less significant weighted value. The final remainder is a voltage proportional to the signal within one of 16 levels. This, amplified by 16, is the expanded information voltage. A block diagram of the Vernitel operation is shown in Figure 107.

The level number n can be represented by discrete voltage levels for modulation of the subcarrier oscillator. If a single subcarrier channel were used to carry the level information, 16 discrete voltage levels are required. Assuming equally spaced levels, a combined telemetering system and detection error (peak value) of $1/(N-1)$ or $\pm 3.33\%$ is allowable in determining the level transmitted. Coding the discrete levels for optimum modulation of two subcarrier oscillators (four levels per channel) the allowable error is $\pm 16.7\%$. In the Vernitel, equally spaced voltage levels weighted 0, 4, 8, and 12 and 0, 1, 2, and 3 modulate two subcarrier oscillators, the sum of the two outputs corresponding to the level n. The level number can be determined by the states of the comparison circuits. The discrete voltages are generated by interrogating these states and summing the corresponding weighted voltages.

Although the accuracy improvement is expensive in terms of bandwidth, the added airborne instrumentation requirements are minimal in terms of size, weight and

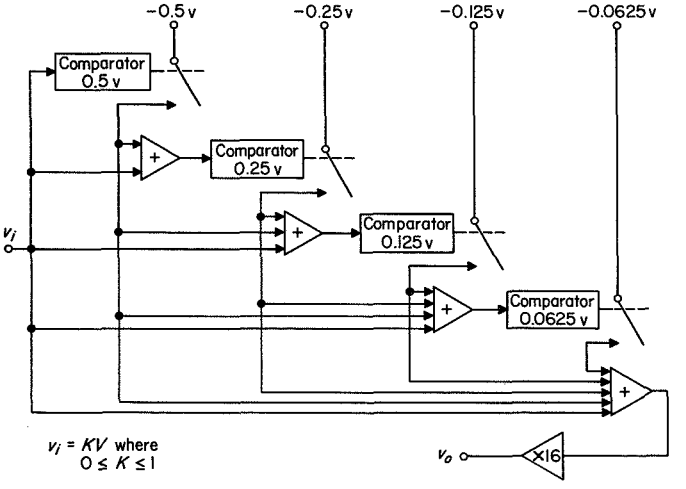

Figure 107. Vernitel operation

power required. The scale expansion technique also permits flexible accuracy capability within a single unit and does not alter the basic advantages of the FM/FM communication system. The improvement in the accuracy which is realized is a function of the telemetering system error and the Vernitel device error for a given demodulation scheme. At threshold received power, that is, maximum system error, an rms error of 0.25% of full scale is expected using scale expansion. Using direct modulation, a 3.3% rms error would result. The error reduction is therefore approximately 13 to 1 under these conditions.

b. Telemetering system data block diagram. Mechanization block diagrams of both the A and B systems are shown in Figures 108 and 109 respectively. Extensive use of time division multiplexing is being made especially in System B. System A contains the Vernitel, its associated multiplier, and the three subcarrier oscillators used to transmit the quantized level and expanded signal information. Each system has its own power supply and transmitter although a common antenna system is being used. To couple the outputs of the two telemetry transmitters into one antenna system, a diplexer is being used.

c. System threshold vs data accuracy. A test was recently conducted to demonstrate the threshold capability of a prototype telemetry station with a specified telemetry flight package and channel assignment. The purpose of the test was to measure the lowest RF signal level at which useful data could be recovered. It was intended that the test results serve as a basis for comparison of the threshold capability of different telemetry communication system configurations. The definition of useful data and the means to apply the definition posed a problem. The need to expedite the test forced the acceptance of an interim solution, that of recording the data on an oscillograph and judging when the data became unusable by inspecting the records.

Consideration of the problem led to the conclusion that percent error should be the criterion for data quality. It was further concluded that it would be useful to determine how data accuracy varied with signal strength

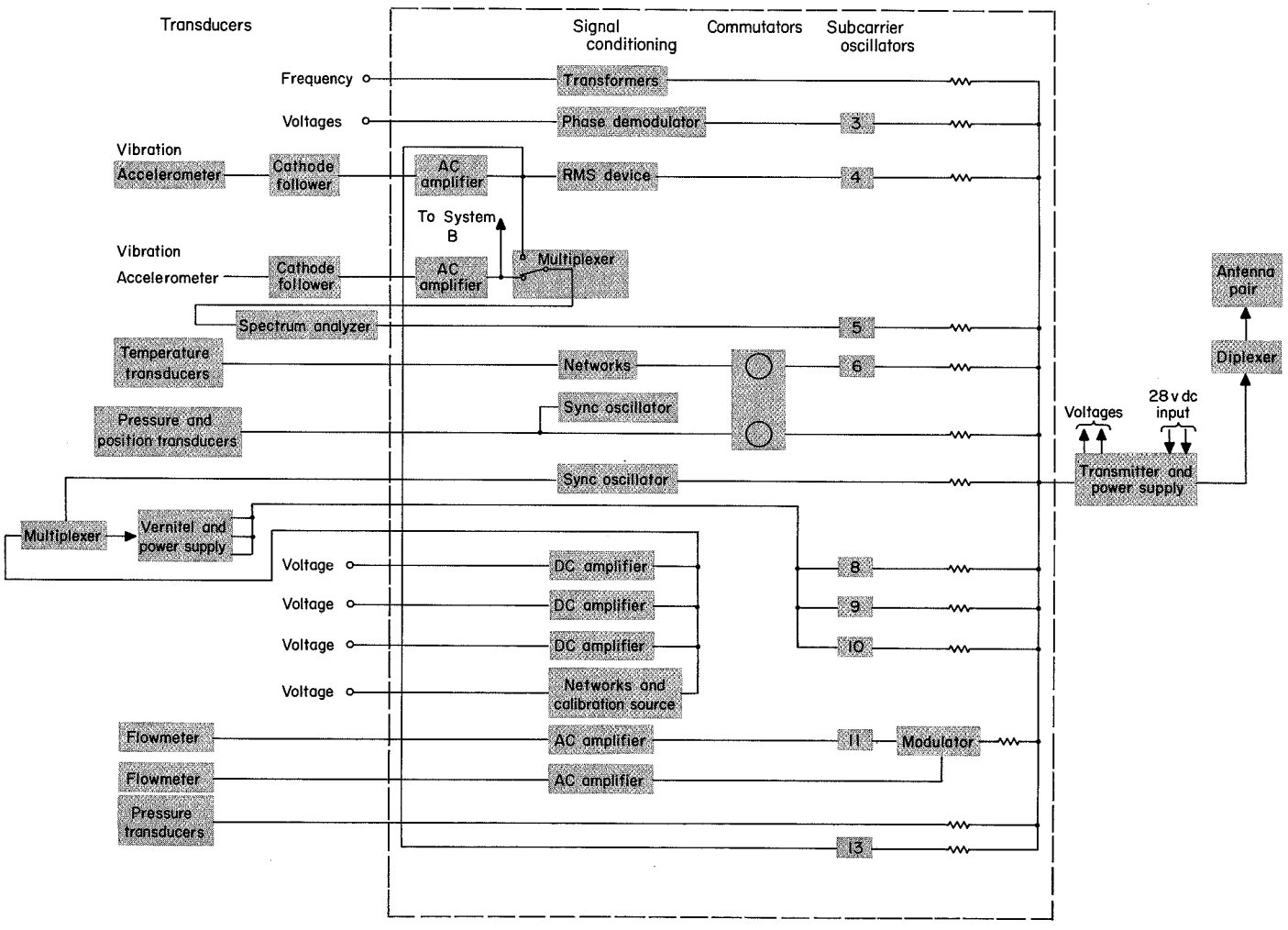

Figure 108. Telemetry System A

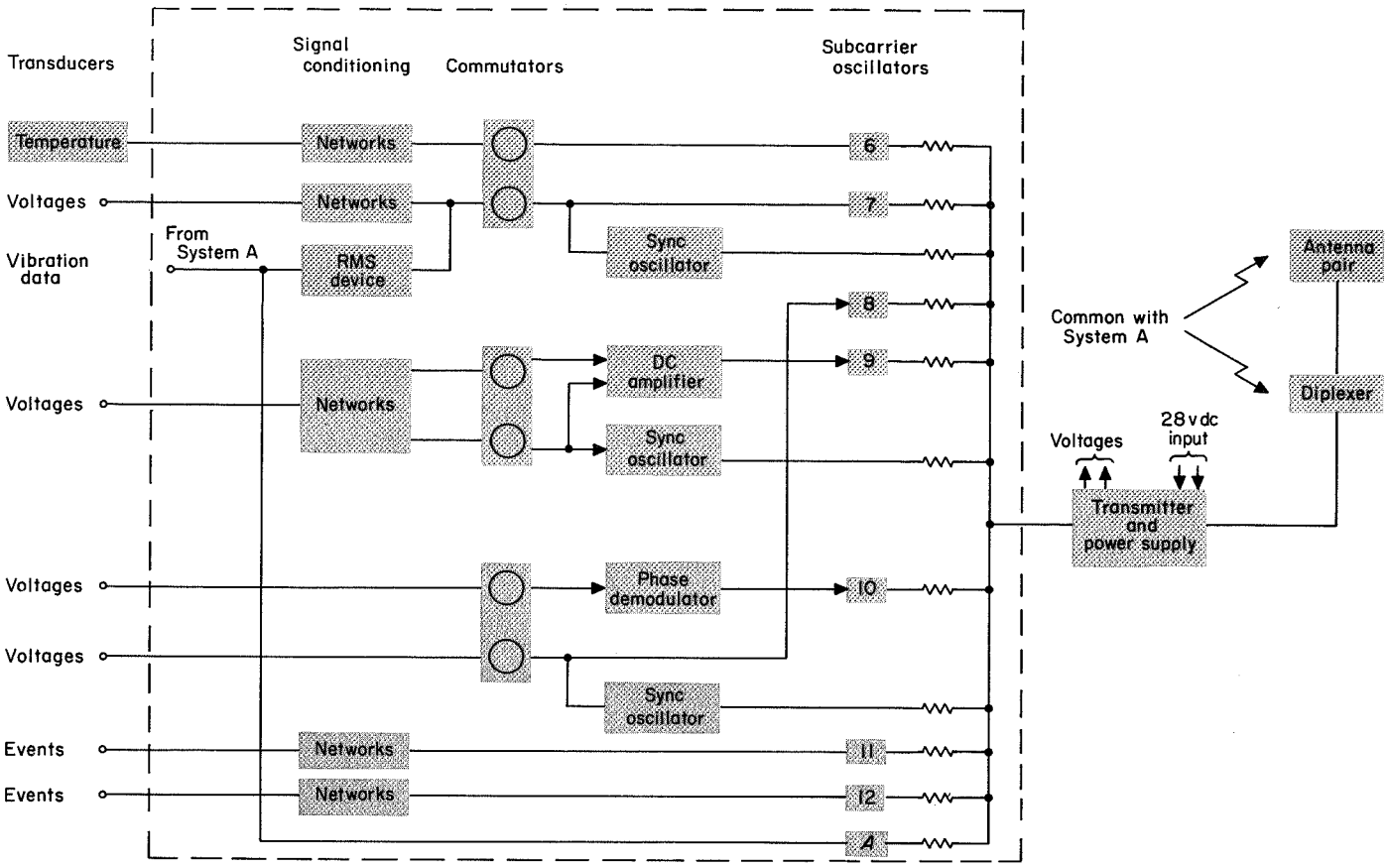

Figure 109. Telemetry System B

rather than define and measure one point on the curve of data degradation versus decreasing signal strength. A special piece of test equipment is useful to facilitate measurement of data error, and this instrument is being developed. The instrument has been given the name telemetry error detector (TED).

The basic operation of the TED is illustrated in Figure 110. The special test instrument is used as prescribed below:

(1) Adjust the RF attenuator such that a strong signal is applied to the telemetry station.

(2) With S_1 open, measure the output (rms) from the TED with a VTVM. Adjust the TED input attenuation for a 1-volt indication on the VTVM.

(3) Close S_1, adjust the gain and phase-shift controls for a null output indication on the VTVM. The output from the TED is now the instantaneous data error.

(4) Systematically reduce the RF signal strength applied to the station and record the corresponding VTVM indication. (10 millivolts corresponds to 1% error (rms) in the recovered data.)

The first prototype of the TED will have a useful frequency range of from 5 to 5000 cps. The nature of the phase-shift network requires the data to be a pure sinusoid.

The TED output (instantaneous data error) could be recorded directly if this information were of interest in a particular situation. Measurement of the phase shift of noisy recovered data would also be facilitated by the TED.

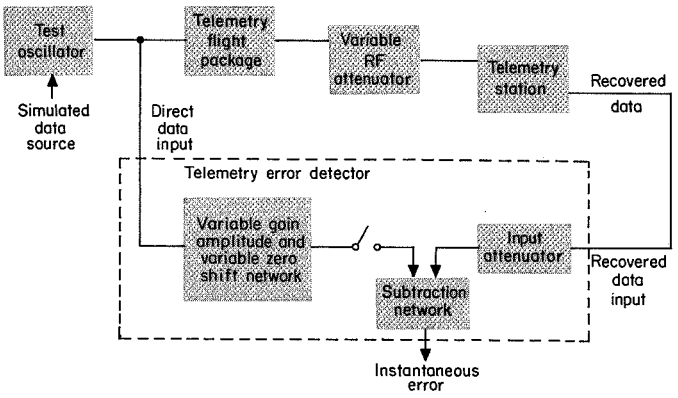

Figure 110. Basic operation of TED

An improved model of the TED utilizing a variable time-delay network in place of the variable phase shifter may be useful to evaluate the transient response of telemetry systems. The problems associated with providing long time delays would probably severely limit the low-frequency capability of this instrument.

D. Electrical Power

The *Vega* first-, second-, and third-stage electrical power systems will all have a battery power source. Power at 400 cps will be provided by a rotary inverter on the first stage, and by static inverters on the second and third stage. The third-stage static inverters will also provide regulated dc, 4.2 kc, and 8.4 kc power. A motor-driven power transfer switch is used on all three stages.

Convair-Astronautics is providing the first-and second-stage electrical power systems, whereas JPL is responsible for the third-stage power. Technical liaison has been established between JPL and Convair-Astronautics electrical power system personnel.

1. First Stage

The first-stage *Vega* electrical power system uses a remotely-activated battery to provide 28-volt dc power. A block diagram of the first-stage electrical system is shown in Figure 111. A 3000-va rotary inverter operates from the 28-volt battery to provide 3-phase, 400-cps power with a frequency accuracy of $\pm 1\frac{1}{2}\%$ and a voltage regulation of $\pm 1\frac{3}{4}$ volts. No dc or ac voltage other than the basic 28 volts dc and 400-cps power is provided by the *Vega* first-stage electrical power system. All other voltages which may be required by the guidance equipment are generated by self-contained, regulated power supplies. A motor-driven switch provides changeover from external to internal power.

2. Second Stage

The *Vega* second-stage electrical power system as planned by Convair-Astronautics will have a manually-activated battery that provides 28 volts dc power. A 3-phase, 300-va static inverter will provide 400-cps $\pm 0.02\%$ power. This inverter will probably incorporate silicon controlled rectifiers. A block diagram of the second-stage electrical power system is presented in Figure 112. As in

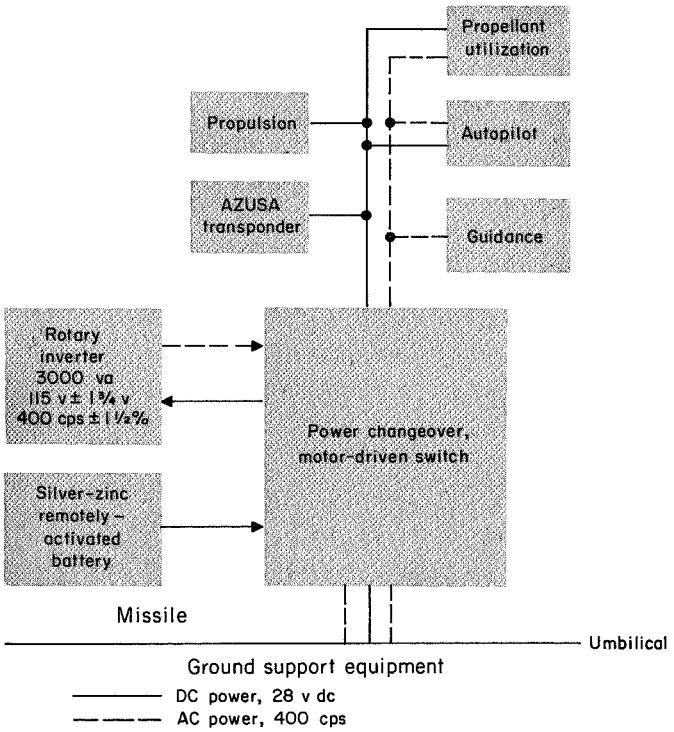

Figure 111. First-stage electrical power

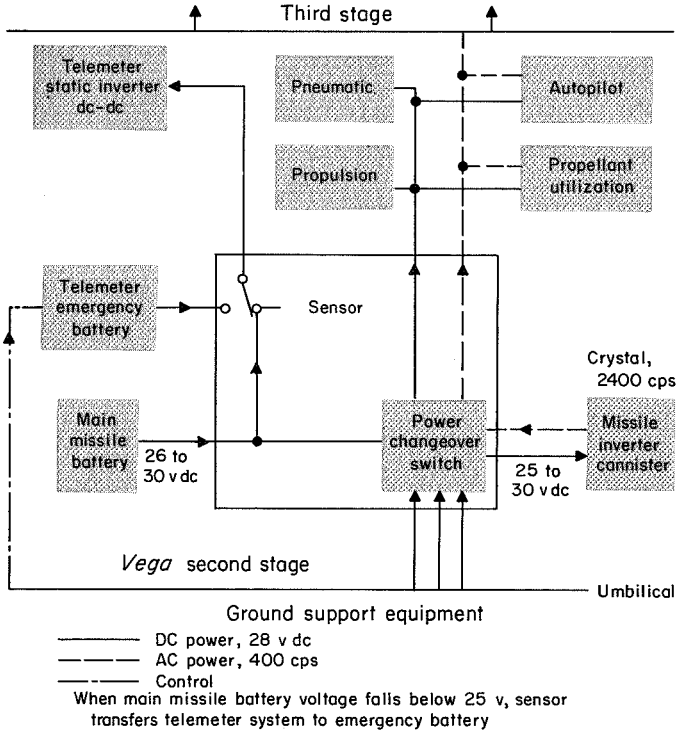

Figure 112. Second-stage electrical power

the first stage, a motor-driven power changeover switch accomplishes the transfer from external to internal power. In addition, a telemetering emergency battery as well as a separate dc-dc static inverter is provided. A voltage sensor will switch over the telemetry power system from the main missile battery to the emergency telemetry battery in the event voltage falls below 25 volts dc.

3. Third Stage

The third-stage power system has been previously described in *Space Programs Summaries 3, 4,* and *5. Vega* missions will fly both direct ascent trajectories and will have coasting times as long as 35 minutes. Because of the recent possibility of the 35-minute coasting-time interval, use of the leave-behind battery has been re-examined. Because substantially better watt-hr/lb performance can be obtained from batteries that have long discharge times, such as 45 minutes instead of only 10 minutes, the weight saving of the leave-behind battery does not justify the decrease in reliability that would accompany its use and the required power transfer switch. Table 18 presents a comparison of the design alternates considering the leave-behind battery which will be placed in the adapter between the second and third stages. Figure 113 is the current estimated load-time curve with the maximum coasting time incorporated. Many detailed load changes have occurred, but the average battery load remains at approximately 1100 watts.

Table 18. Leave-behind pattern weight comparison

Design alternate	Second stage	Third stage		
	Battery	Battery	Switch box	Total
Leave-behind battery in adapter of second stage supplies power to third stage until separation	21.3 lb (46 min, 40 watt-hr/lb)	10.4 lb (10 min, 20 watt-hr/lb)	2.0 lb	12.4 lb
No leave-behind battery	—	21.0 lb (50 min, 50 watt-hr/lb)	—	21.0 lb

A silver-zinc cell has been selected which is typical of the size to be used in the primary battery of the third stage. These cells have been tested in the laboratory under the following test conditions:

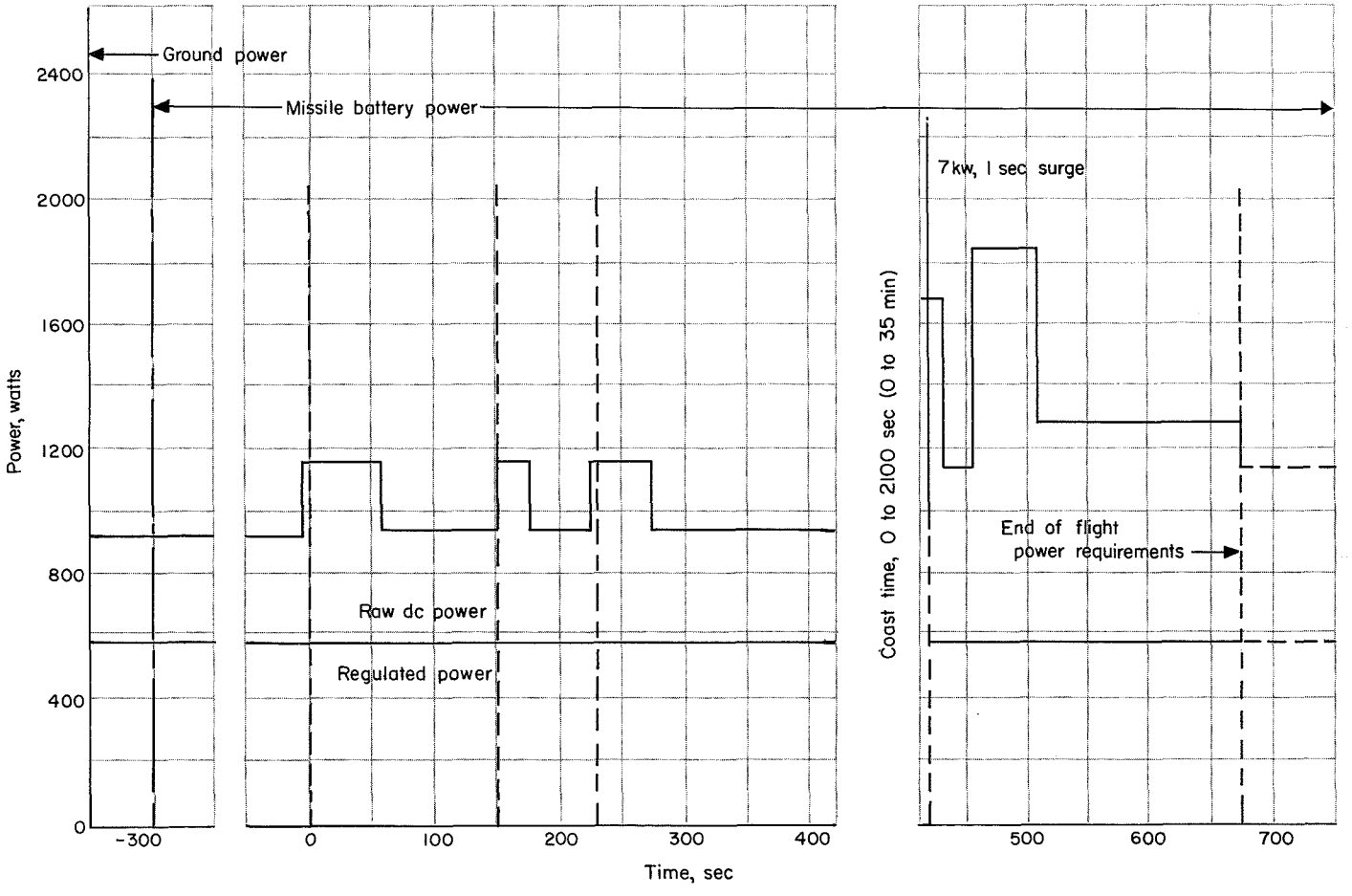

Figure 113. Third-stage battery power requirements

(1) Stand time of 24 hours (18 hours at 70°F followed by 6 hours at 130°F) and discharged under a programmed load curve.
(2) The above same test with a 6-hour stand at 139°F followed by 18 hours at 70°F.
(3) Low-temperature tests to determine the minimum stabilized temperature at which satisfactory operation will be assured.

A battery package has been designed based upon a group of 20 of the above cells. The dimensions of this cell will be 11 × 5.5 × 5.5 inches and it will weigh about 22 pounds. Batteries and cells from different sources have been ordered for testing of the time power requirements of the propulsion squib activation battery. This battery is estimated at this time to be 2 × 1.5 × 1.5 inches and weighs 2 pounds.

Table 19 is a summary of the various regulated and unregulated voltages and their respective power requirements. The total losses for the power converters and associated equipment are estimated to be 146 watts. The ±150-volt supply, ±65-volt supply, and the 6.3-volt supply design details and mechanical layout have been completed, and the contractor for these supplies is starting assembly of the prototype converters. The laboratory is studying the various proposals for the required 400-cps power inverters. Since the writing of *Space Programs Summary 5*, a requirement has arisen for a 1-watt, 4-kc voltage. A breadboard of this supply has been built and cooperative tests with the user of the 4-kc voltage are underway to ascertain the optimum filter required to provide both the minimum necessary harmonic reduction and a 70-degree phase shift between the 4-kc square wave (used in the demodulator) and the psuedo sine wave used in the modulator.

The 40-volt propulsion squib and controller magnetic reset converter has been designed and built in a prototype form using both silicon and germanium power switching transistors. These circuits have been optimized as to circuit details but packaged almost identically. Following proof testing at the required −10 and 82°C ambient temperature at atmospheric pressure environment, overall efficiency and transistor stud temperature and radiator temperature will be monitored during a simulated deep-space environment test in an attempt to determine the relative suitability of silicon vs germanium switching transistors in space power applications.

Table 19. *Vega* third-stage power supply summary

Unit	Weight, pounds	Input, volts	Input peak nom min amperes	Input peak nom min watts	Output, volts	Output peak nom min amperes	Output peak nom min watts	Noise spikes, mv	Frequency
DC-DC regulated power supply									
Computer	4.1	31-23	1:8[a]	50	150	0.240	36	20	DC
	4.2	31-23	1.45	40	−150	0.190	28.5	20	DC
Autopilot	4.3	31-23	2.3	64.5	65	0.685	44.5	50	DC
Controller	4.3	31-23	0.83	34	−65	0.350	22.8	50	DC
Inertial platform stabilizer	7.5	31-23	5.5	156	6.3	18	116	50	DC
					18	0.056	1	2	DC
					−18	0.056	1	2	DC
DC-AC static inverter									
Acc demodulator	0.5	31-23	0.95	21.5	115	0.110	12.6	NA	8.4 kc
		20	(reg from 8.4 supply)		26	0.058	1.5	NA	4.2 kc
Inertial platform[b]	10	31-23	—	143	115	0.228	52	2%	400 cps
Gyros[c]					26	1.1	48	2%	400 cps
Actuators[d]					6.3	0.24	1.5	2%	400 cps
DC-DC unregulated power supply									
Magnetic reset squibs	2	31-23	2.1	60	42-32	1.5[e]	48.7	100	DC
Third-stage battery	22	NA	NA	NA	31-32	71-38[a]	1839-920	2000	
Leave-behind battery	Not required for first three flights								
Prelaunch power supply[g]	100 ampere peak capability								

[a] At 28 volts.
[b] Two-phase supply, 1 watt at 26 volts and 90 degrees.
[c] Three-phase supply; 0.3 power factor.
[d] Chopper supply.
[e] At 32 volts.
[f] 5-kw 80 ms load at X_3 — 1.5 minutes.
[g] 28 to 34 volts adjustable in 1-volt steps.

VI. FIELD OPERATIONS

A. *Juno II*, Round AM-19A

On 13 October 1959, *Juno II* Round AM-16A (19A) was launched successfully and resulted in placing a 91.5-pound multi-experiment satellite (Fig 114) into a satisfactory orbit. This Laboratory was responsible for the fabrication, assembly, test, field operation, and reliability of the cluster of three solid-propellant stages. This launching represented the second attempt to achieve this mission, the first attempt in July (AM-16) ending in failure because of a malfunction in the booster electrical system. Launching was delayed 12 days because of damage sustained by the booster during the firing of *Jupiter* Round AM-23 on 16 September 1959. Discounting this delay, the preflight assembly and test operations were carried out in a very satisfactory manner.

1. Preflight Preparation

Cluster Number 13, used for this flight, had been in storage at AMR since April. It was scheduled for use with a lighter payload and hence was not capable of supporting this heavier payload. It was determined that the cluster could most easily be modified by stiffening the fourth-stage motor case. However, it was desired that the modification not be directly attached to the fourth stage since this would subtract directly from payload weight. It was therefore decided to rivet a stiffening cylinder (Fig 115) to the third-stage cone which would support the forward end of the fourth-stage motor case. An adapter (Fig 116) on the fourth-stage motor case could then transfer the radial support to the head end of the cylinder. The adapter was fabricated and attached to the third and fourth stages without requiring any other major cluster changes.

The modification successfully accomplished, final assembly and checkout of the cluster started on 28 August 1959 at AMR. Visual inspection and pressure check of the motors gave no indication of any damages due to shipping or the long storage period. After the installation of each assembly in the launcher, alinement and balance were checked and reduced to a minimum. After the entire cluster was balanced and shear-pinned, the runouts taken on the head end of the fourth-stage motor were less than 0.001 inch, both in perpendicularity and concentricity.

On 16 September 1959, *Jupiter* Round AM-23 was fired. Shortly after liftoff, difficulties in the missile necessitated its destruction, which, in turn, caused some damage to the Round AM-16A booster already erected on the next pad. Work was suspended on the cluster while awaiting word as to when the damage could be repaired. Operations got underway again on 28 September upon receiving word that the launching had been rescheduled for 13 October. Payload integration and final preparation prior to moving to the pad were satisfactorily completed.

a. RF interference test. On 7 October 1959, the cluster was mated with the booster and preparation made for the RF interference test. This test performed with all RF equipment operating and the cluster spinning did not show up any interference difficulties. Upon examination of the telemetering records it was noticed, however, that the armature current on one of the cluster drive motors was excessive during cluster acceleration periods. This condition was improved by deliberately unbalancing the field currents of the two motors. During the spin test, satisfactory operation of the cluster accelerometers was also indicated.

b. Flight test. The final countdown commenced at 2150 hours, 12 October at X − 700 minutes. In addition, a 1-hour hold was scheduled at X − 31 minutes in order to assure launching during the alotted 2-hour firing window. The countdown operations progressed with only minor difficulties although the presence of several lightning storms in the general area caused considerable

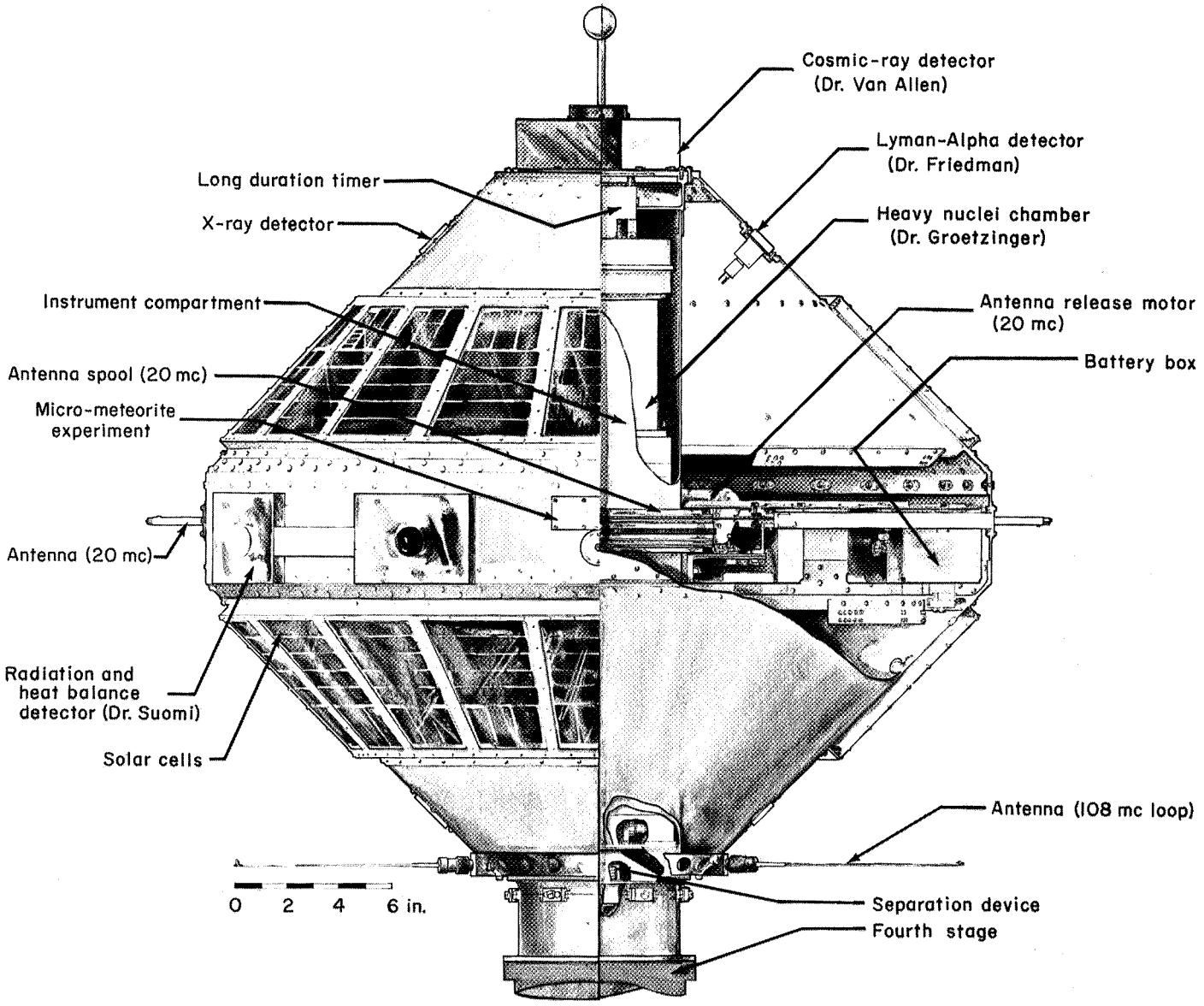

Figure 114. Payload Round AM-19A

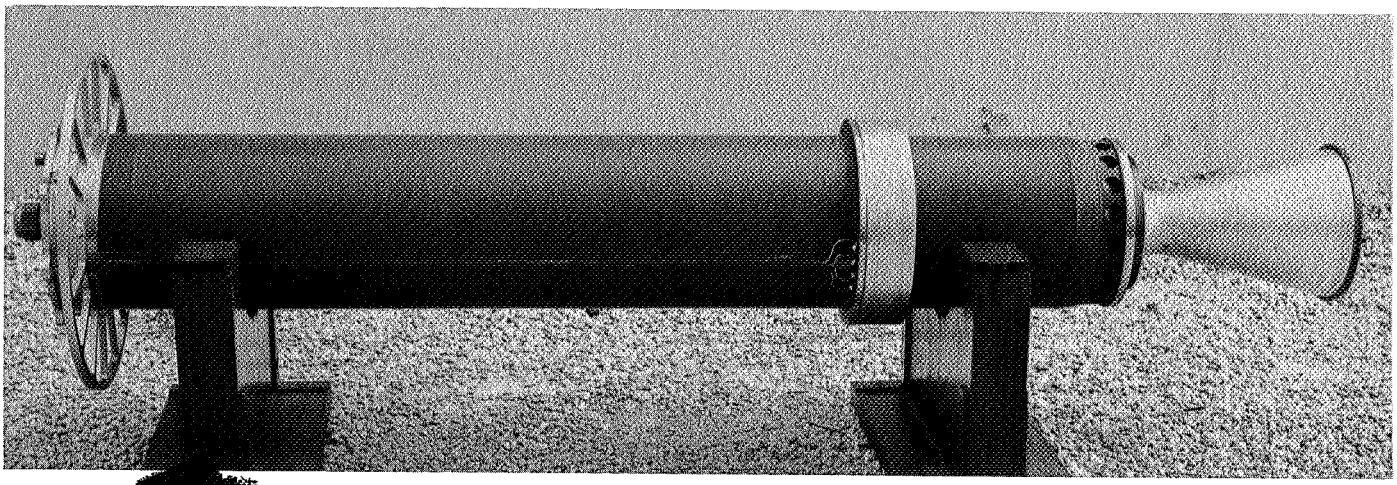

Figure 115. Modified fourth stage

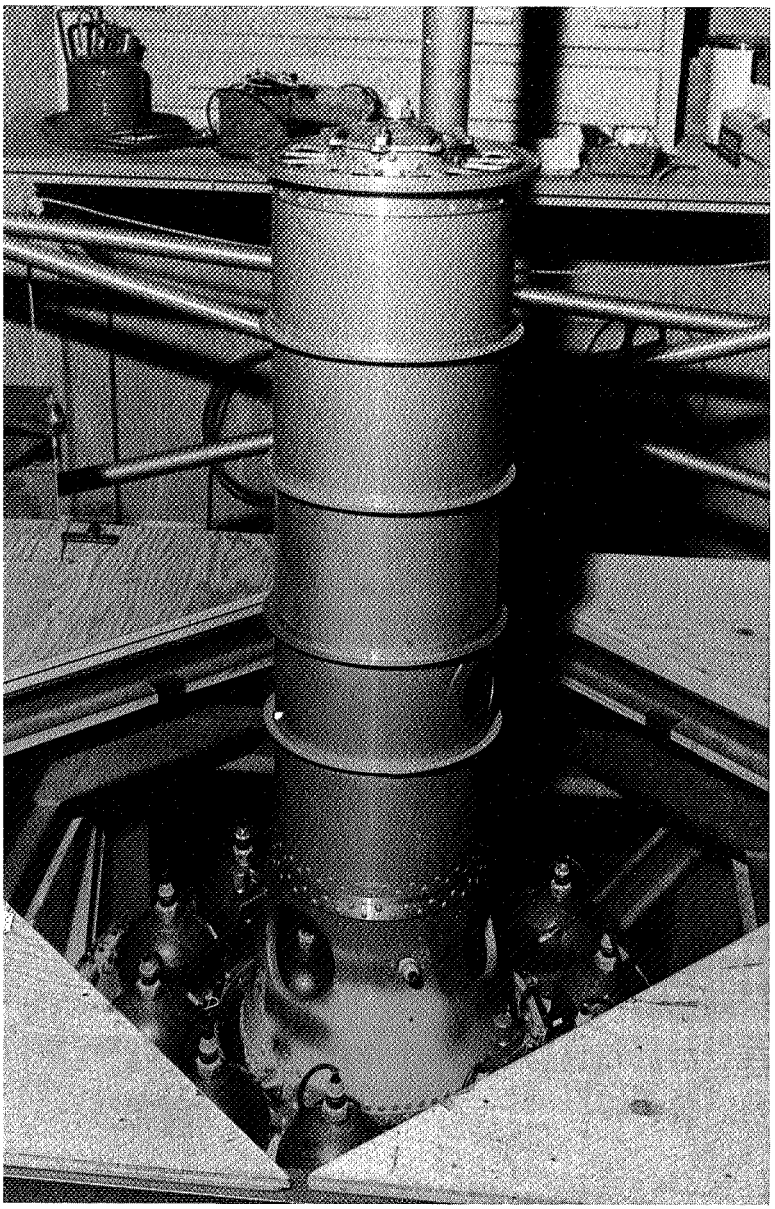

Figure 116. Modified third stage

apprehension as to whether it would be necessary to stop work. Fortunately, the disturbances did not move in closer than the 1.5-kilometer safety radius and therefore countdown operations continued. At X − 45 minutes, 4 minutes of the built-in hold were utilized in order to clear the pad area prior to turning on all RF again. The remainder of the hold was used at the scheduled time of X − 31 minutes. No further holds were necessary and liftoff occurred at 10:30:04.25 EST.

c. Results. Preliminary information indicated that all flight operations were successful with only minor deviations in velocity and angle. This was later confirmed by the early orbit determination at ABMA. The latest information from ABMA (based upon injection conditions that were obtained by fitting all doppler data available from launch and the first two orbital passes, Goldstone angle data from the second pass, and optical sighting from San Fernando, Spain, and Woomera, Australia) is shown in Table 20.

2. Dispersion Study

Round AM-19A which contained a satellite with numerous experiments (similar to that attempted on Round AM-16) was fired on 13 October 1959. The first stage performed normally as expected, providing a greater signal strength than that of the previous round. However, commencing at second-stage ignition and for the duration of the measurement, signal strength dropped slowly from 1400 to 350 microvolts. About the time the aft bulkhead passed the lip of the tube, signal strength jumped to a level of 1100 microvolts where it remained for about 90 milliseconds before dropping to 350 microvolts. This malfunction was apparently caused by the flame around the telemetering antennas located on the sides of the guidance compartment.

The data (Fig 117) from this round indicates an initial shock in the vicinity of Motor 5 and a saturation level bump (approximately 50-millisecond duration) in the vicinity of Motor 2. This bump started shortly after the machined-surface release and ended shortly before the mid-bulkhead passed the tube lip, with the trailing wires breaking shortly after this point.

The nature of the structure at the points of accelerometer mounting is such that a great deal of ringing can be expected during motor burning. Granting that the amplifier can be driven to saturation in this way, it is out of character for it to recover in the sudden manner exhibited on the records without a shock of opposite polarity to that driving it into saturation.

There is no indication of equipment failure in either case, although the measurements should have been less sensitive.

Table 20. Orbital characteristics

Parameter	Actual value	Predicted value
Semi-major axis, km	7199.2	7212.2
Eccentricity	0.037466	0.041047
Period, minutes	101.3	101.6
Inclination, degrees	50.447	50.27
Perigee, km	556.5	546
Apogee, km	1096	1138

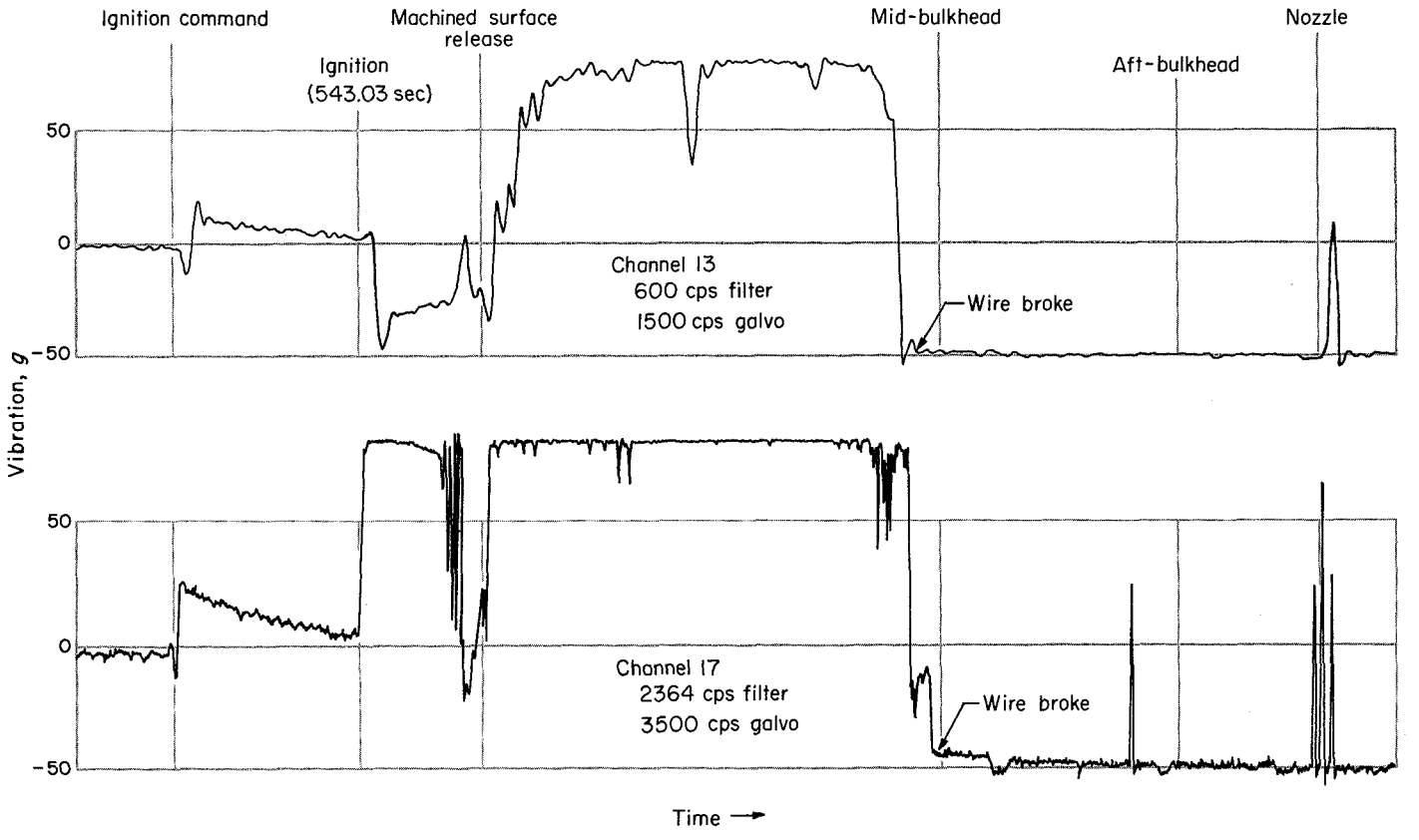

Figure 117. Vibration data, Round AM-19A

B. *Juno II*, Round AM-19B

The purpose of the inflatable sphere experiment was to determine the characteristics of the upper atmosphere in the region between 100,000 and 500,000 feet. To aid in the gathering of data an inflated sphere having a minimum lifetime of 40 days was to be used. The payload preparation started early in March, 1959, and ran through the middle of July. However, a completed payload had to be available early in June for environmental testing.

The payload (Fig 118) was a cylindrical configuration, having a diameter of 7 inches and a length of 31.5 inches. The major components were the payload shell, the beacon assembly, the pressure vessel, the squib-actuated valve assembly, the bellows and piston assembly, and the inflatable sphere. A prototype payload and three flight units were fabricated. However, only two flight units were readied for launch date (14 August 1959).

Liftoff occurred at 1931:00.7 EST. The velocity of the first stage was determined to be approximately 5 to 10% low. To aid in optical tracking, a series of flares were to be fired from the guidance compartment. The first flare was fired at X + 180 seconds; after which time, no further flares were observed or recorded. After X + 203 seconds, telemetering records indicated a rapid reduction in the pressure within the guidance compartment. Pressurization of the guidance compartment is normally accomplished by a pressurized nitrogen bottle. This nitrogen bottle also serves as a gas supply for the guidance gyros bearing and the attitude control jets. Due to the loss of guidance and the reduced velocity of the first stage, the velocity increments of the high-speed stages failed to put the payload into orbit.

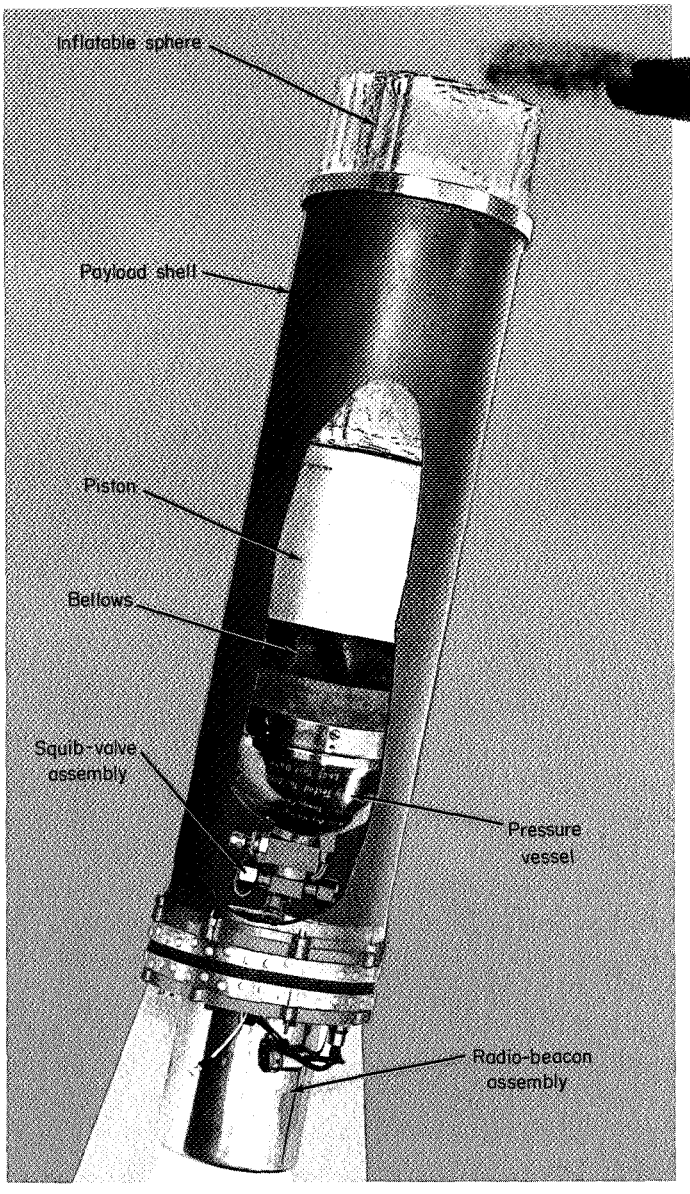

Figure 118. Payload Round AM-19B

1. Payload Design

Beacon assembly. The beacon assembly (Fig 119) consisted of a beacon RF transmitter assembly, a telemetry subcarrier oscillator assembly, a battery pack, and an antenna assembly. The power of the beacon exceeded 50 milliwatts and utilized a battery pack containing 12 Mallory RM12-RT2 mercury cells.

The transmitter consisted of a crystal-controlled, transistorized oscillator operating at approximately 54 mc. The oscillator was used to feed a transistorized power amplifier serving as a frequency doubler (108.03 mc) which, in turn, fed the antenna. The modulation signal was derived from two transistorized subcarrier oscillators operating Channels 3 and 4. Channel 3 was a resistance-controlled oscillator, having its frequency controlled by a thermistor located so that it would measure the transmitter temperature. This channel was also used to telemeter the inflatable sphere's ejection; this was accomplished by superimposing a step function of approximately 10 cps upon the temperature information. Channel 4 was a current-controlled oscillator used to telemeter the firing of the squibs which were to activate the pressure valve. The frequency step for this function was to be approximately 50 cps.

Balloon package. The inflatable sphere package consists of a pressure vessel and squib-actuated valve, a bellows and piston assembly, an inflation and release valve, and an inflatable sphere. The inflatable sphere was constructed of laminated Mylar (1 mil thick) sandwiched between two layers of aluminum foil (0.45 mil thick).

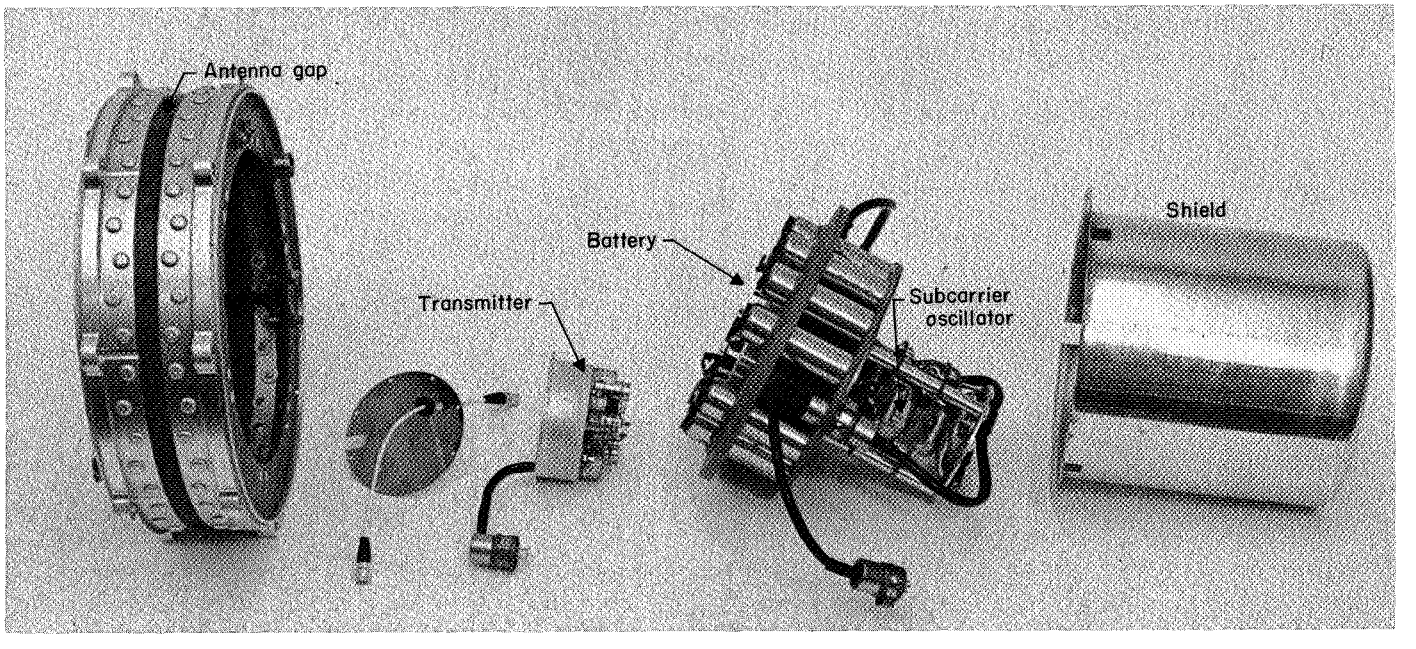

Figure 119. Beacon assembly

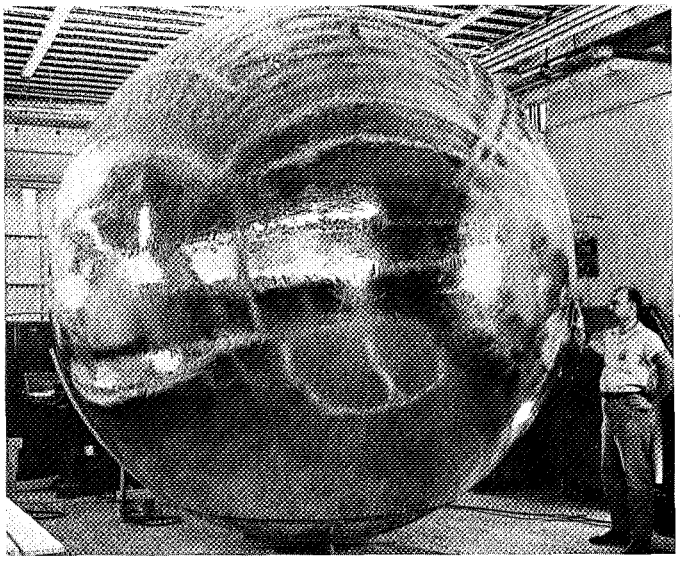

Figure 120. Inflatable sphere, 12 foot

The Mylar served as a gas barrier for the inflation process and as a support to which the aluminum foil layers could be bonded. The aluminum foil layers supplied the structural rigidity required to preserve the balloon's spherical shape after the inflation gases were bled off. The foil also provided a highly reflective surface for optical tracking. (It should be noted that this sphere was not dependent upon internal pressure to retain its shape.) The designed rigidity of the inflated sphere was several times greater than the amount of structural inflexibility necessary to resist the orbital environment loads to which it was to be subjected. Figure 120 shows the inflated sphere fully formed, with its internal pressure normalized to atmospheric pressure.

The sequence of the inflation and release valve assembly is shown in Figure 121. The Position 1 condition shows the valve assembly just prior to the ejection process. The first event in the ejection process is the firing of the two squibs which actuate the pressure vessel valve. (This event is telemetered through Channel 4 by the current-controlled oscillator sensing the electrical impulse which fires the squibs.) The pressure vessel valve then permits the pressurized nitrogen to expand the bellows, forcing the bellows piston to expel the packaged sphere. The extreme forward travel of the piston is then stopped by a wire rope attached to the inflation and release valve (Position 2). The valve spring, then free to release part of its compression, draws the valve stem forward, opening the ball cock outlet port, and pressurized nitrogen begins to flow from the bellows, through the valve stem into the sphere (Position 3).

The valve assembly components remain in this relationship until the sphere is completely inflated. The entire quantity of nitrogen is required to inflate the sphere, resulting in the draining off of the pressurized nitrogen in the bellows. In this condition the internal face of the bellows piston exerts a forward-moving force of about 3 pounds. Being compressed between the outer sleeve and the valve stem, the valve spring overcomes the 3-pound force of the bellows piston and pushes the outer sleeve back to its starting position. The valve spring, now free to release, pulls the valve stem out of the inflation and release valve assembly, simultaneously imparting a separation energy to the satellite, and moving it ahead of the payload (Position 4). Equalization of the internal pres-

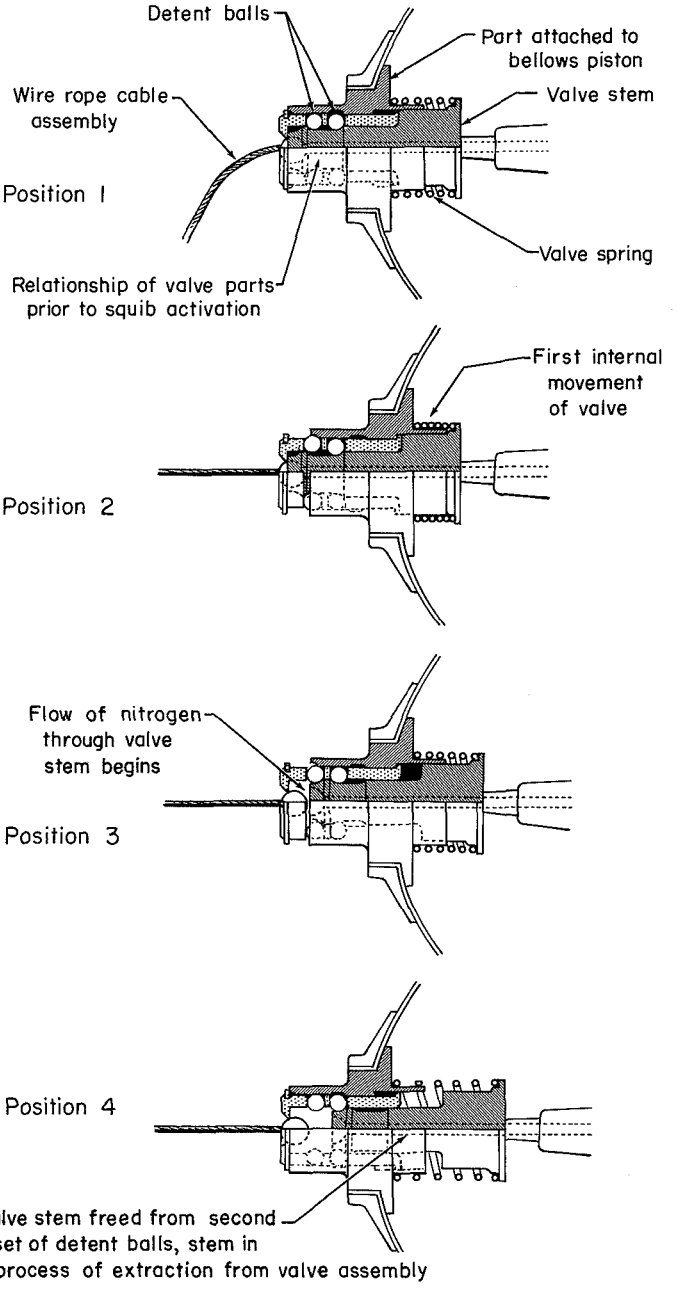
Detent balls
Part attached to bellows piston
Wire rope cable assembly
Valve stem
Position 1
Valve spring
Relationship of valve parts prior to squib activation
First internal movement of valve
Position 2
Flow of nitrogen through valve stem begins
Position 3
Position 4
Valve stem freed from second set of detent balls, stem in process of extraction from valve assembly

Figure 121. Inflation role sequence

sure of the satellite to that of the external environmental pressure is provided through the open-valve stem of the satellite.

2. Dispersion Study

Telemetry data has been taken during recent *Juno II* firings for the purpose of studying possible causes of trajectory dispersion due to mechanical interference. The mechanization of this study has been presented in *SPS 2* and *4*.

Because the guidance compartment and cluster was tumbling at the time of the second-stage ignition, a poor telemetering signal was received. The vehicle antenna pattern was such that all stations except the TLM-18 teletemetering station on the Cape lost the signal at the time of second-stage ignition. This station regained the telemeter signal at low level 2 seconds before and lost it 8 seconds after ignition. Consequently, the data during this period was quite noisy. (Received signal strength records were not obtained for this round.)

Evaluation of this data (Fig 122) indicated an initial ignition shock in the vicinity of Motor 10, and a saturation level bump in the vicinity of Motor 2. The bump with a duration of approximately 30 milliseconds started shortly after the machined-surface release and ended shortly before the mid-bulkhead passed the lip of the tube. The data from this point until trailing-wire breakage (approximately the time the aft bulkhead passed the lip of the tube) indicated a vibration which was difficult to evaluate because of the noise level. This vibration level, however, stayed within the measurement range of ± 50 g peak.

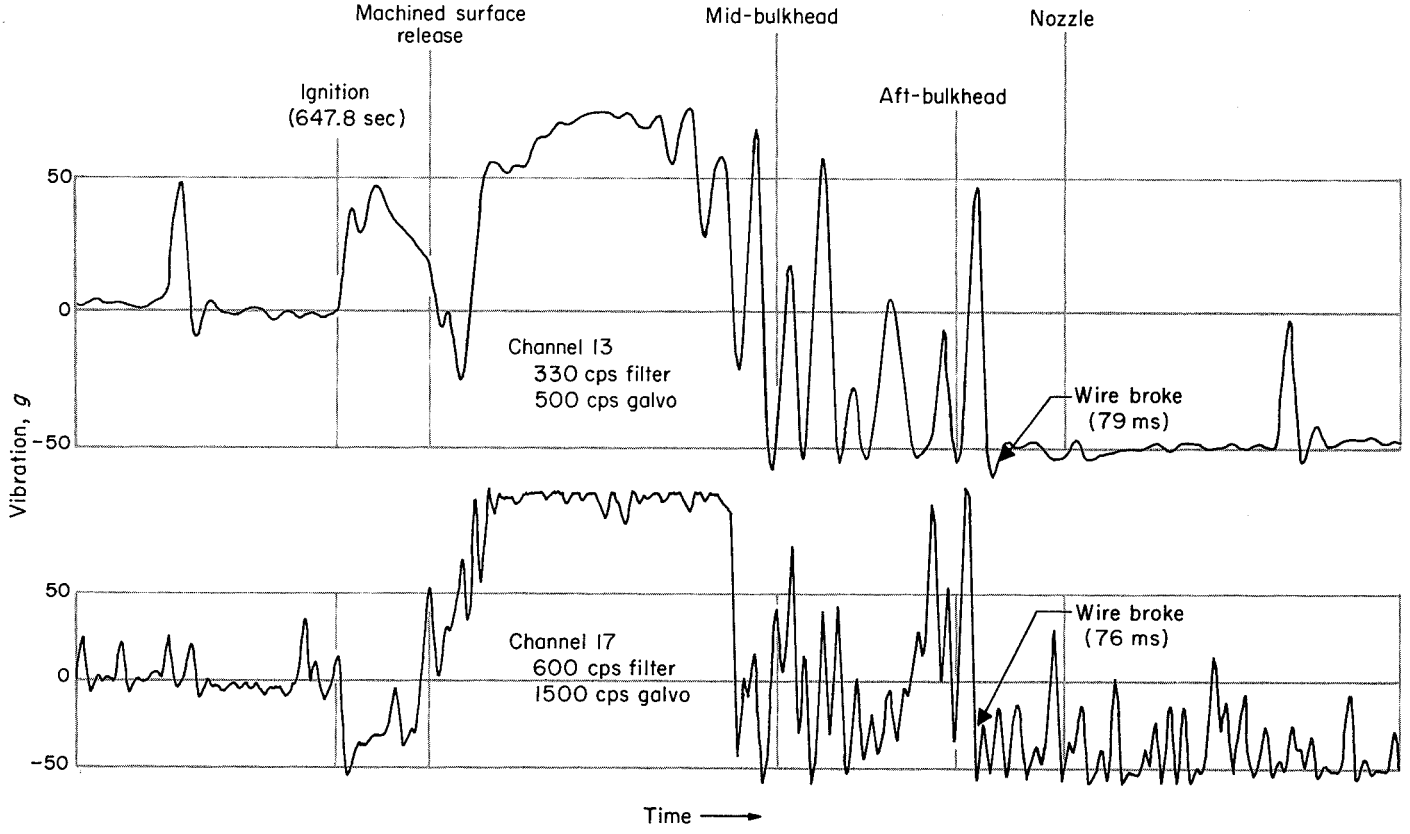

Figure 122. Vibration data Round AM-19B

VII. ASSOCIATED STUDIES

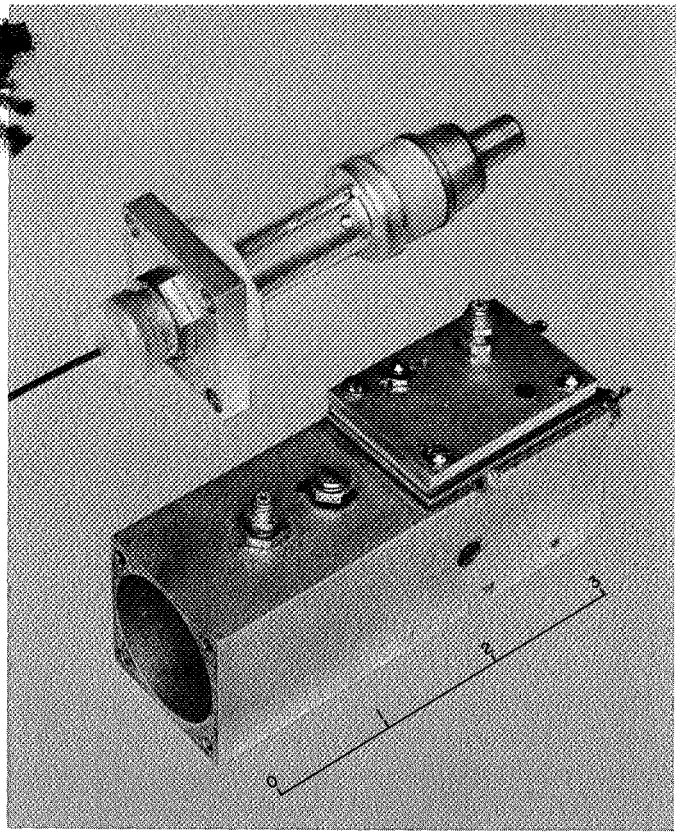

Figure 123. UHF cavity amplifer

A. Communication Techniques

1. RF Power Amplifier

A survey of a number of possible 960-mc airborne transmitter configurations was presented in an earlier report (*SPS 2*). Some of these units provided RF power output capability in the range from 0.01 to 125 watts. Subsequently, specifications were prepared for the development of three UHF cavity power amplifiers to provide nominal RF power output levels of 3, 25, and 125 watts. The major design objectives were high efficiency, light weight and high gain. An evaluation of the 3-watt UHF amplifier was presented in *SPS 5*. The 25-watt cavity development is reported herein.

Two of the nominal 25-watt triode amplifiers developed by Spectralab Instrument Company have now been submitted to JPL for evaluation. Figure 123 shows the cavity amplifier partly disassembled. A stripline sandwich section is used to obtain an accurate match at the input terminal. The inner plate line clamps the tube anode very tightly, and the assembly is pulled clear of the grid and cathode contacts during tube removal. The triode is a General Electric GL-6897 modified by Spectralab for conduction cooling (Fig 124). This modification permits the tube to perform efficiently in a small cavity and at the same time provides adequate thermal conduction for cooling the plate electrode. Additional heat sinking was provided external to the cavity body to insure safe tube

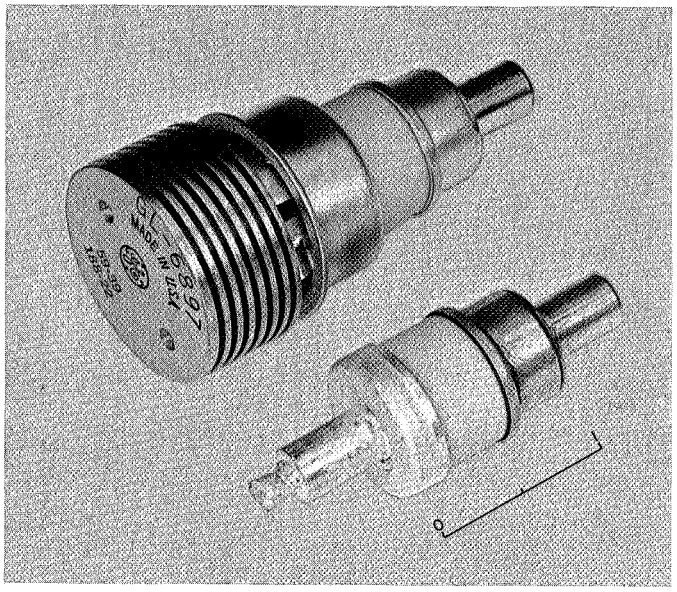

Figure 124. UHF triode modified for conduction cooling

operating temperatures. The performance tests described in this report have been made with an aluminum heat sink as shown in Figure 125. The weight of the heat sink is 4.5 pounds; the total surface area, 190 sq in.; and the cavity contact area, 4.5 sq in. Measured performance data is compared with the JPL major design specifications in Table 21 where it will be noted that the overall efficiency exceeds even the objective specification. Table 22 compares tube operation levels in the 25-watt cavity with the manufacturer's rated maximum levels.

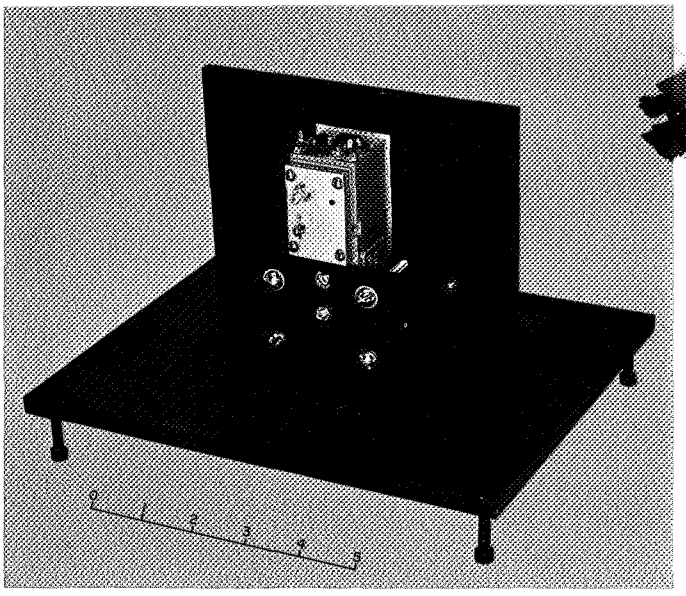

Figure 125. Cavity amplifier heat sink

One of the more difficult parameters to determine at UHF is grid dissipation which has a significant effect on tube life. For low-frequency linear operation, the power output for a grounded grid amplifier is

$$P_{out} = \frac{(\mu + 1)\, E_g \cdot i_p}{2}$$

Table 21. JPL major design specifications and measured data for 25-watt Spectralab amplifier

Parameter	Firm specification	Objective specification	Spectralab unit
Overall efficiency including heater power, %	30	40	47
Weight, ounces	15	12	8
Gain at 25-watt drive level, db	9	11	10.5

Table 22. Operation of GL-6897 triode in 25-watt cavity amplifier compared to manufacturer's maximum ratings

Characteristic	Maximum ratings	25-watt cavity	Percentage of maximum
Heater voltage, volts[a]	6.3	5.5	0.87
Heater current, amperes	1.05	0.95	0.90
DC plate, volts	1000	700	0.7
DC cathode current, milliamperes	125	75	0.6
DC grid current, milliamperes	50	20	0.4
Peak positive RF grid, volts	30	10	0.33
Peak negative RF grid, volts	400	35	0.09
Plate dissipation, watts	100	25	0.25
Grid dissipation, watts	2.0	1.0	0.50
Maximum temperature of anode seal, °C	250	125	0.50

[a]Set for most stable operation.

assuming a matched load. Thus the RF signal source supplies a small fraction of the power developed across the load.

For Class C nonlinear operation at UHF, the power gain is greatly reduced with a corresponding reduction in the effective μ of the tube. Additional losses at the input also occur due to grid current and transit-time loading (Fig 126). The net effect is that a much greater proportion of the drive power appears in the output circuit, and a high percentage of the drive power is dissipated in grid circuit losses. For the GL-6897 tube at a 2.5-watt level, the estimated transit-time loss is 0.85 watt and the dc loss is 0.15 watt. At this drive level approximately 1.5 watts, or 6% of the output power, is effectively transferred directly from the input generator to the load.

Figure 127 presents performance data with the amplifier optimally adjusted at the 25-watt level. Figures 128 and 129 indicate the power supply control required to maintain power output within ± 0.25 db. Figure 130 shows the RF power variation with time and temperature and indicates the temperature range that may be expected with a heat sink comparable to that illustrated. Vibration tests at a 4-g (rms) level have produced less than 0.4-deg/g incidental phase modulation over a range of 50 to 2000 cps. Considerably more attention must be paid to operating procedures for the 25-watt amplifier than is customary with lower powered units in order to (1) avoid damage to the tube, (2) obtain maximum efficiency, and (3) insure stable operation.

This triode 25-watt cavity amplifier has demonstrated the feasibility of lightweight, medium-powered UHF amplifiers having an overall efficiency of the order of 50%. Further refinements in cavity design and improved tube cathodes and electrode structures should enable still higher efficiencies to be obtained at UHF frequencies.

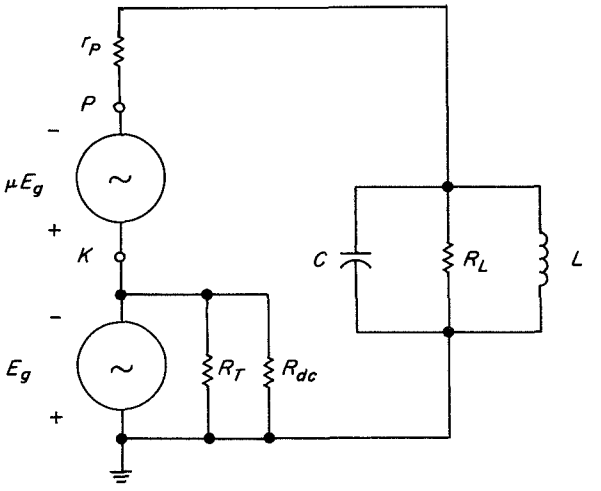

Figure 126. Grounded grid UHF amplifier

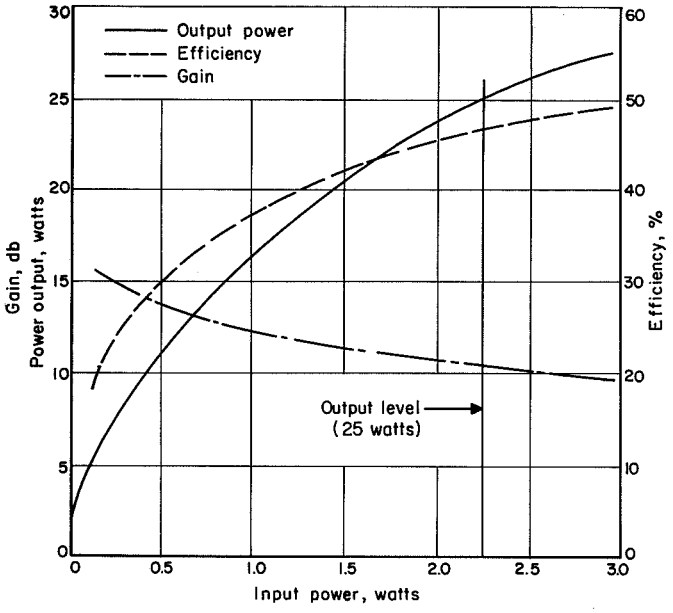

Figure 127. UHF amplifier characteristics

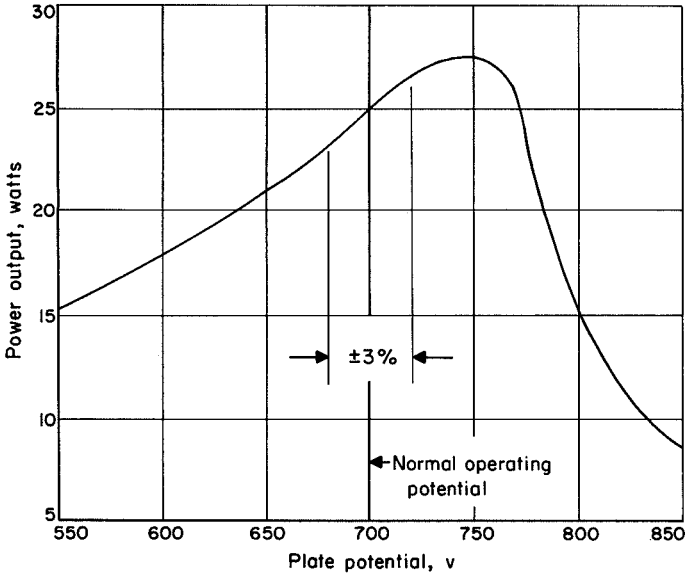

Figure 128. Power output vs plate potential

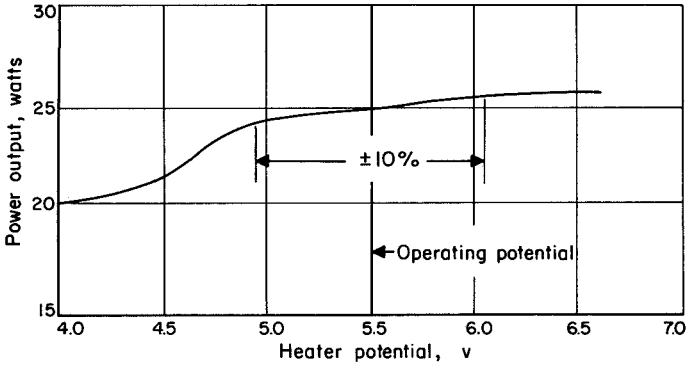

Figure 129. Power output vs heater potential

2. Low-Noise Amplifiers

a. Solid-state maser. The solid-state maser is a low-noise amplifier principally because of its low operating temperature. However, because it is a regenerative type of amplifier it is sometimes difficult to realize the low-noise performance in a receiver system. In particular, it is difficult to match impedances at the terminals of a maser because the resistive component is negative.

In an effort to gain better understanding of these problems a series of noise-figure measurements of the receiver system using a maser preamplifier were made. After some experimentation it was decided that two L-band circulators would be necessary for good performance. The present setup which performs quite well is shown in Figure 131. The line tuners A, B, and C are used to match impedances at all the terminals of the circulator. The following procedure has been found to be satisfactory: (1) With pump power to the maser *off*, tuners A and C are tuned for maximum signal transfer. (2) Tuner B is then tuned for minimum signal transfer. This latter adjustment implies that virtually all of the signal power is being absorbed in the maser crystal. When pump power is applied to the maser, the reflection coefficient changes from a small fraction to a value greater than one depending on the gain. It has been found that

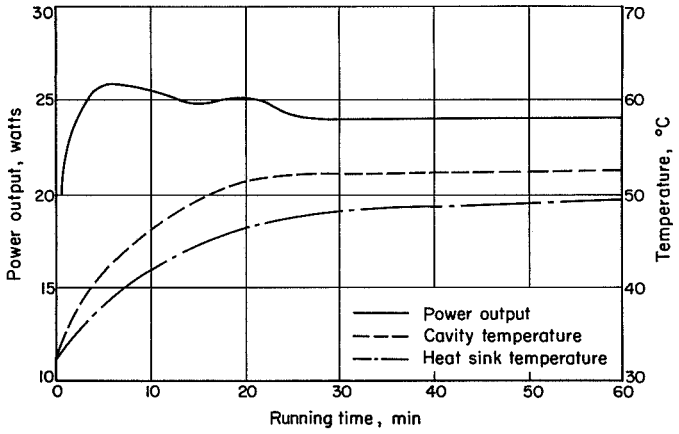

Figure 130. Power output and temperature characteristics

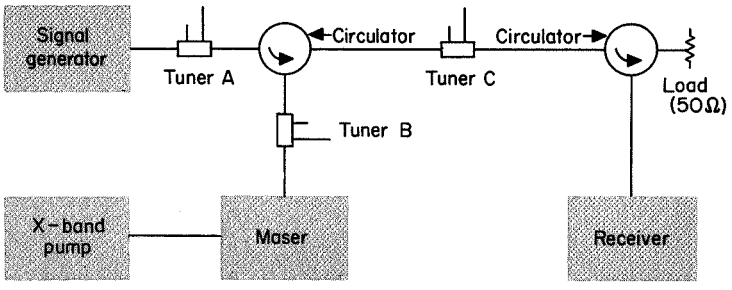

Figure 131. Maser test setup

only minor readjustment of tuner B is necessary for optimum performance. The change in noise-power output as a function of input resistor temperature has been observed by replacing the signal generator with a 50-ohm resistor and varying its temperature.

The second circulator is used as an isolator and serves two purposes: First, the input impedance of the receiver (a diode mixer) is dependent on local oscillator power and is only approximately constant; therefore the isolator is used to maintain the load impedance for the maser at a constant value. Second, local oscillator power is prevented from getting into the maser at high levels since most of it is dissipated in the 50-ohm dummy load.

b. Parametric amplifier. Two negative-resistance 900-mc parametric amplifiers have been operated in cascade. The advantages include improved gain stability and greater gain bandwidth product. Performance is listed in Table 23. The disadvantage of operating in cascade is the added complexity of equipment and operating procedure. A better solution is one parametric amplifier of low gain (5 to 15 db) feeding a low-noise amplifier. To date the low-noise mixer built for this purpose when preceded by a lowpass filter and isolator has a single-channel noise figure of 8 db. A 4-db noise figure was obtained with a parametric amplifier gain of 10 db.

Table 23. Principal parameters of 900-mc negative-resistance parametric amplifier

Type of amplifier	Gain, db	Bandwidth, mc	Gain change with 10% source impedance change, db
Single stage	10	2	1.45
Single stage	5	5	0.2
Two-stage cascade	5[a]	3	0.2

[a]Value given for each stage.

3. Attitude Control

An experimental research effort is in progress to study and to test in the laboratory, advanced techniques for attitude sensing of a space vehicle (*SPS 5*). This effort will supply concepts and techniques which may, in the future, apply to the development of specific space-vehicle attitude-control systems.

The general category of attitude-control systems being investigated is that in which attitude sensing is achieved by means of radio frequency signals and, when appropriate, other forms of electromagnetic energy.

The tentative design of a specific laboratory model attitude-control system was described in *SPS 4*. This model, or vehicle simulator, will have dimensions on the order of 2 feet, will weigh about 50 pounds and will be supported on an extremely low-friction spherical gas bearing. The vehicle simulator will contain an X-band transmitter, a monopulse parabolic antenna, airjet attitude actuators, optical actuator and optical command detectors, and an optical attitude collimation system.

a. Design modifications. In *SPS 4* tentative transmitter, receiver, and angle-detector block diagrams were presented. Further study indicated that certain changes in these block diagrams are necessary for correct system operation. In particular, in a system where coherently related modulation signals are used to detect and differentiate between the reference and two error patterns of a transmitting monopulse antenna, it is necessary that the error pattern modulation frequencies are made harmonics of the reference frequency. This is done to prevent phase ambiguities in the receiver angle-detector system. In view of the harmonic relationship between the weak error signals and the strong reference signal, it is most important to keep harmonic distortion in the receiver to a minimum. The present transmitter and receiver block diagrams are shown in Figures 132 and 133, respectively.

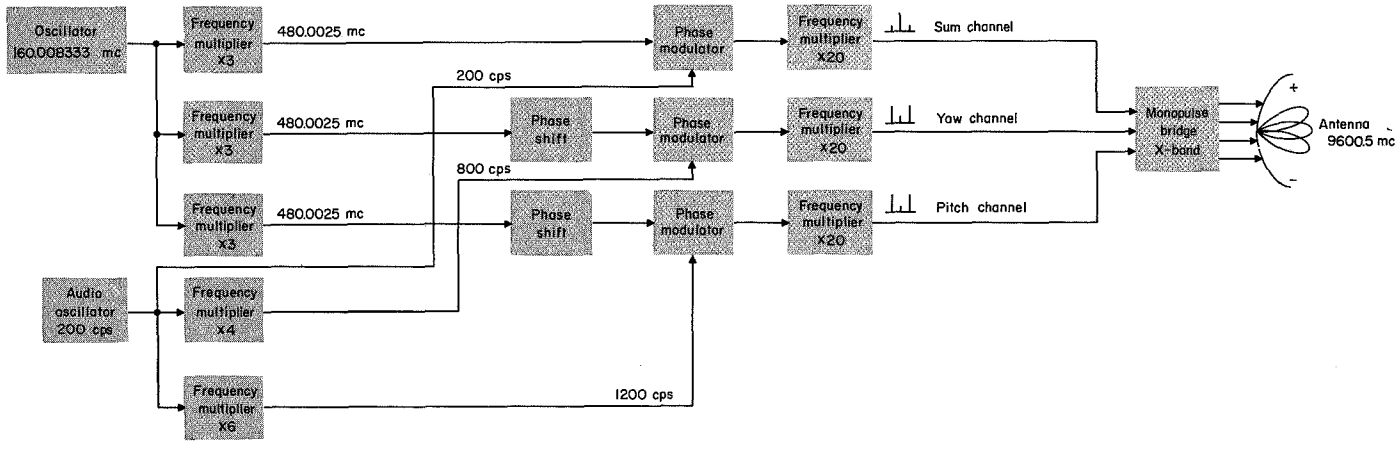

Figure 132. Vehicle transmitter

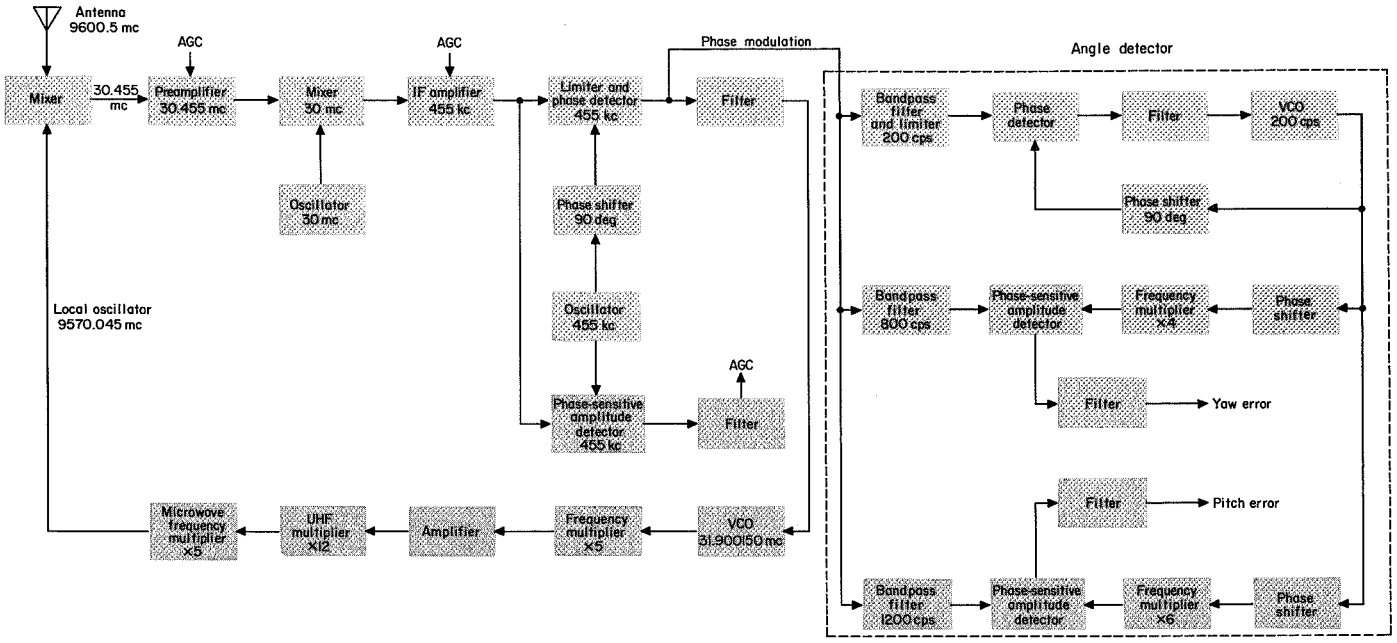

Figure 133. Ground receiver and angle detector

Even harmonics are utilized in the error modulation, since even-harmonic distortion tends to be suppressed in the receiver 455-kc phase detector.

b. Component development. The transmitter multiplication chains have been completed. The first multiplication from approximately 160 to 480 mc is accomplished by a varactor (Type MA-460E), placed between suitable resonant circuits. The 480-mc output is fed through an isolating resistor to a diode (Type HPA 2800) shunting a resonant circuit, the diode being used as a phase modulator. The isolating resistor helps to reduce crosstalk between the three transmitter channels. The 480-mc phase modulated output is multiplied to 9600.5 mc in a standard waveguide detector mount by a Type 1N23 diode. The error-channel phase modulators provide the necessary 2.5 radians of modulation at X-band for carrier suppression.

The monopulse antenna has been tested and found to perform satisfactorily. As shown in Figure 134, the antenna is a parabolic reflector 6 wavelengths in diameter illuminated by a set of four turnstile antenna elements in front of a circular ground plane. The antenna bridge network is described in detail in *SPS 5*. It is constructed of microstrip-type printed circuitry. Four hybrid junctions of the ratrace variety are used to perform the necessary signal additions and subtractions in the bridge. The measured sum-channel antenna gain is 16 db above isotropic. The measured antenna patterns for two different polarizations are shown in Figure 135. The rather high level of the first sidelobes in the patterns is consistent with the high degree of aperture blocking caused by the antenna feed assembly.

The 9600.5-mc phase-lock receiver has been completed. Construction of the audio section comprising the angle detector has been completed; performance checks on this unit are in progress.

Fabrication of the gas bearing, the vehicle simulator platform, and the gas jet actuator system is in progress. It is presently planned to use commercially available components for the optical collimation system and the actuator command system described in *SPS 4*.

c. Preliminary system check. As a means of checking the soundness of the block diagram design depicted in Figures 132 and 133, a preliminary electronic system

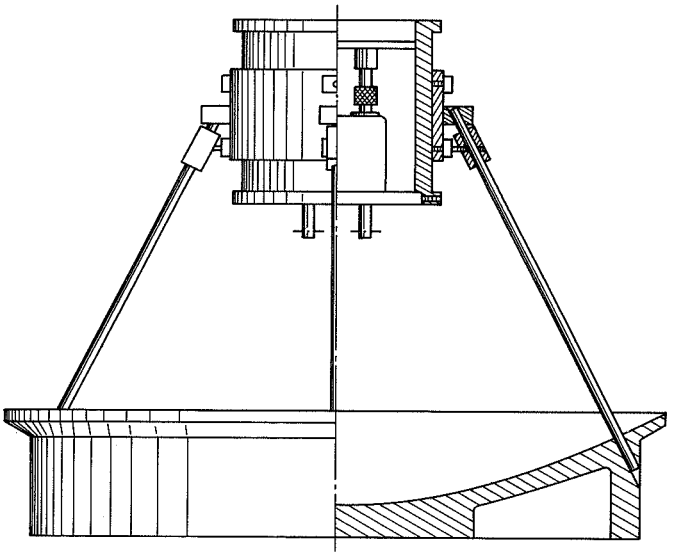

Figure 134. Monopulse antenna

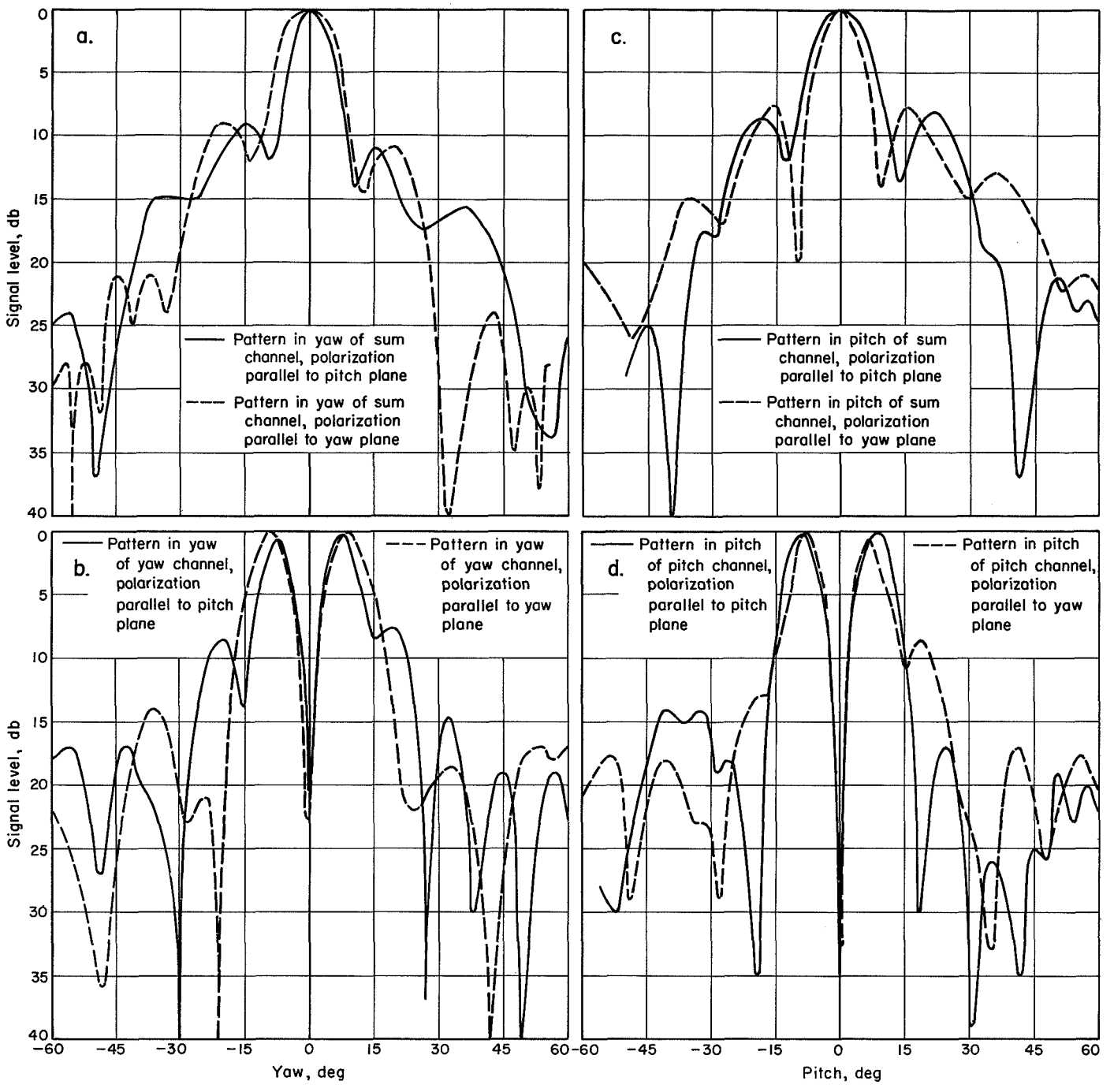

Figure 135. Monopulse antenna patterns

bench test was undertaken. The setup used for this test is shown in Figure 136.

For these tests, only the pitch error channel was used. The polarization produced the error antenna pattern depicted in Figure 135; i.e., the polarization was parallel to the pitch plane. The signal level used was such that the receiver was operating about 15 db above threshold. The transmitted error-channel spectrum is shown in Figure 137a. The transmitted X-band sum-channel spectrum is shown in Figure 137b; this also is the approximate received spectrum when the antenna is alined on axis. The composite observed received signal for an angular antenna displacement of 3 degrees is shown in Figure 137c. The scale is linear in voltage.

Although the preliminary system check was more qualitative than quantitative in nature, the system performance was as had been expected, and further studies of the system's performance are to be made.

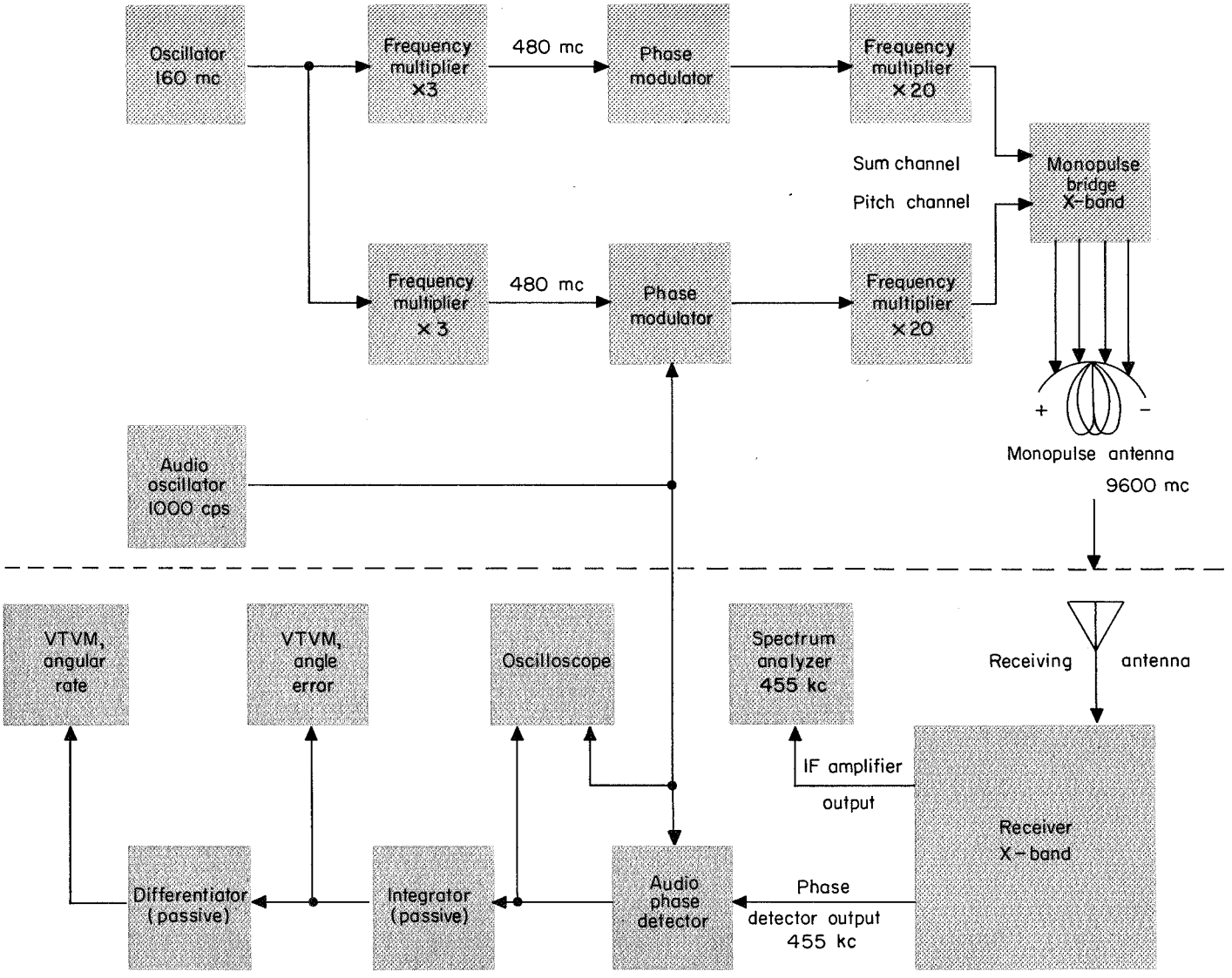

Figure 136. Preliminary system check block diagram

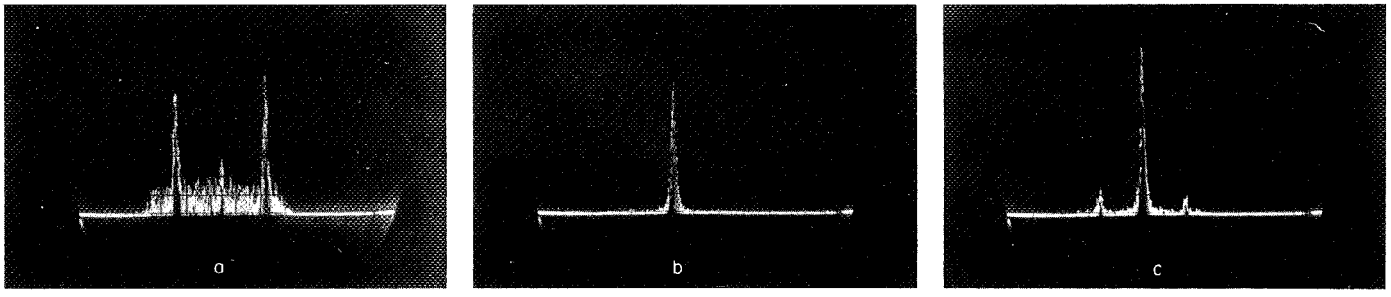

Figure 137. Spectrum of received signal

B. Space Guidance

Correlated velocity vector. In *SPS 5* the derivation of a correlated velocity vector was described. This correlated velocity vector is the velocity vector which would be required by the vehicle at a specified position and time along the powered portion of the trajectory such that if the thrust of the rocket motor were terminated at that instant, the vehicle would still be capable of performing its intended mission.

Although in theory the actual values of the components of the correlated velocity vector $\vec{V}_c$ could be calculated from the position of the vehicle, it is more practical to calculate the components by means of an expansion made around the nominal shutoff point of the vehicle. If the nominal position of the vehicle at shutoff is identified by the coordinates (X_s, Y_s, Z_s) and the guidance system measures the true position (X, Y, Z) of the vehicle and forms the difference between true and nominal position, then the components of the correlated velocity vector could be calculated from the following expansions:

$$V_{cx} = B_0 + B_1\delta X + B_2\delta Y + B_3\delta Z + B_4(\delta X)^2 + B_5(\delta Y)^2 + B_6(\delta Z)^2 + B_7\delta X\,\delta Y + B_8\delta X\,\delta Z + B_9\delta Y\,\delta Z + B_{10}\delta t \quad (1)$$

$$V_{cy} = C_0 + C_1\delta X + C_2\delta Y + C_3\delta Z + C_4(\delta X)^2 + C_5(\delta Y)^2 + C_6(\delta Z)^2 + C_7\delta X\,\delta Y + C_8\delta X\,\delta Z + C_9\delta Y\,\delta Z + C_{10}\delta t \quad (2)$$

$$V_{cz} = D_0 + D_1\delta X + D_2\delta Y + D_3\delta Z + D_4(\delta X)^2 + D_5(\delta Y)^2 + D_6(\delta Z)^2 + D_7\delta X\,\delta Y + D_8\delta X\,\delta Z + D_9\delta Y\,\delta Z + D_{10}\delta t \quad (3)$$

where the δQ's appearing in the expansion are defined as $\delta Q = Q(t) - Q_s(t_s)$. A second-order expansion is used so that greater variations in the path of the vehicle can be tolerated without increasing the system error. The coefficients B, C, and D appearing in the expansion are chosen so as to minimize the rms error over the expected range of coordinate deviations at shutoff. In the example appearing in Table 24, coordinate deviations of $\pm 200{,}000$ feet in each of the three variables δX, δY, and δZ were assumed with a resulting rms error in the calculation of V_{cx}, V_{cy}, and V_{cz} of approximately 0.03 ft/sec. A first-order expansion for the same range of coordinate deviations resulted in rms errors of 1 to 2 ft/sec in the components of $\vec{V}_c$. The coefficients which appear in the expansions

Table 24. Coefficients in expansion of components of correlated velocity vector

First-order expansion				
i	B_i (V_{cx})	C_i (V_{cy})	D_i (V_{cz})	Units
0	$-0.66166893 \times 10^{4}$	0.37472018×10^{5}	0	ft/sec
1	-0.433833×10^{-3}	4.714424×10^{-3}	0	sec^{-1}
2	0.714439×10^{-3}	0.186904×10^{-3}	0	sec^{-1}
3	0	0	0.184164×10^{-2}	sec^{-1}
Second-order expansion				
0	$-0.66170017 \times 10^{4}$	0.37472218×10^{5}	0	ft/sec
1	-0.433697×10^{-3}	0.714313×10^{-3}	0	sec^{-1}
2	0.714356×10^{-3}	0.186954×10^{-3}	0	sec^{-1}
3	0	0	0.1841669×10^{-2}	sec^{-1}
4	-0.1703×10^{-10}	0.2463×10^{-10}	0	$ft^{-1}\ sec^{-1}$
5	0.1059×10^{-10}	-0.2230×10^{-10}	0	$ft^{-1}\ sec^{-1}$
6	0.7028×10^{-10}	-0.5019×10^{-10}	0	$ft^{-1}\ sec^{-1}$
7	0.4765×10^{-10}	0.2149×10^{-10}	0	$ft^{-1}\ sec^{-1}$
8	0	0	0.1408×10^{-9}	$ft^{-1}\ sec^{-1}$
9	0	0	-0.1021×10^{-9}	$ft^{-1}\ sec^{-1}$
10	0.2005×10^{-2}	-0.3020×10^{-3}	0.6216×10^{-2}	ft/sec^{2}

for V_{cx}, V_{cy}, and V_{cz} were calculated for the particular Venus mission used as an example in *SPS* 5. The expansions were carried out in a launcher-centered coordinate system with the X axis directed along the firing direction, the Y axis along the plumb line vertical and the Z axis in a right-handed relationship to the X and Y axes. The nominal values of position and velocity of the vehicle at shutoff are shown in Table 25.

Velocity-to-be-gained vector. In addition to the correlated velocity vector $\vec{V}_c$ it is also desirable to define a velocity-to-be-gained vector $\vec{V}_g$ as the vector difference between the correlated velocity vector $\vec{V}_c$ and the velocity vector $\vec{V}$ of the vehicle (Fig 138); i.e., $\vec{V}_g = \vec{V}_c - \vec{V}$. The three components of the velocity-to-be-gained vector $\vec{V}_g$ are calculated by a comparison of the components of the correlated velocity vector $\vec{V}_c$ with the components of the velocity $\vec{V}$ of the vehicle, i.e.,

$$V_{gx} = V_{cx} - \dot{X} \tag{4}$$

$$V_{gy} = V_{cy} - \dot{Y} \tag{5}$$

$$V_{gz} = V_{cz} - \dot{Z} \tag{6}$$

The velocity to be gained is thus the additional velocity required by the vehicle in order to accomplish a successful mission in the absence of further thrust. The desired condition which should then be satisfied at shutoff is that the magnitude of the velocity-to-be-gained vector be zero.

$$|\vec{V}_g| = 0 \tag{7}$$

In order for the magnitude of the velocity-to-be-gained vector to be zero, it is necessary that each component go to zero simultaneously,

$$V_{gx} = V_{gy} = V_{gz} = 0 \tag{8}$$

The guidance system in the vehicle must then perform two functions: first, it must provide steering commands in pitch and yaw so as to insure that all three components of the velocity-to-be-gained vector go to zero simultaneously; and second, it must detect when the components go to zero and provide a shutoff command to the rocket engines at that time.

Present studies are being made in order to determine the optimum method for deriving the shutoff and steering commands. The method by which the commands are generated from the components of the velocity-to-be-gained vector will be discussed in the next *Space Programs Summary*.

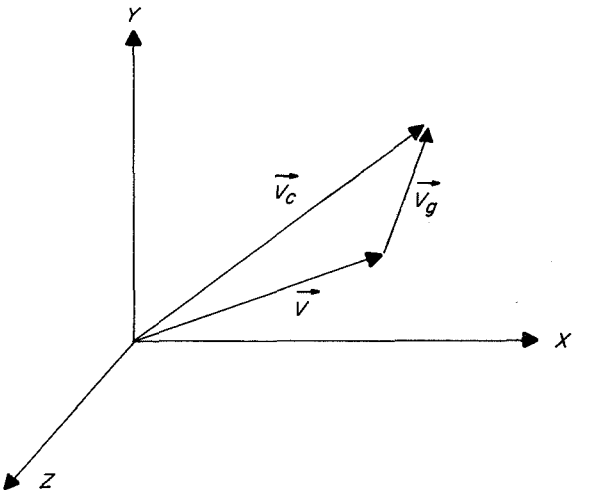

Figure 138. Velocity-to-be-gained vector

Table 25. Nominal values of position and velocity

Nominal values of position and velocity at shutoff	
X_s, feet	−21,695,845
Y_s, feet	−22,568,285
Z_s, feet	0
$\dot{X}_s$, ft/sec	−6,617.012
$\dot{Y}_s$, ft/sec	37,472.283
$\dot{Z}_s$, ft/sec	0
Characteristics of the desired hyperbola	
Semi-major axis, a, feet	−91,345,842
Direction cosines of $\vec{S}$	
s_1	0.63517796
s_2	0.77236582
s_3	0

Note: $\vec{S}$ is a unit vector in the direction of the outgoing asymptote of the desired hyperbola.

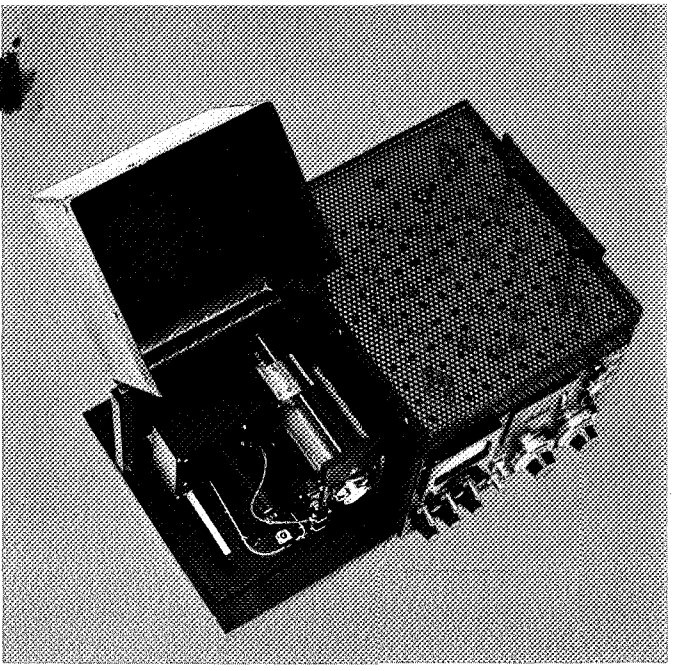

C. Photographic Experiment

The basic photographic film camera facsimile receiver has been previously described in *SPS 3*. Changes in the design philosophy of this experiment have led to the development of a new facsimile receiver (Fig 139) possessing the following characteristics:

(1) At least one megabit picture resolution.
(2) A flyback time less than 6% of the line-scan time.
(3) Accurate speed control based on the spacecraft camera motor variations.
(4) Picture format of 200 to 1000 lines with 1200 line-pair resolution referred to the camera.
(5) Minimum printout time of 30 minutes for a 200-line picture.

Figure 139. Facsimile receiver

Two major changes in the facsimile receiver are: first, the position synchronization of the film drum to the film scanner; and second, the generation of a 60-cps pulse-width-modulated (PWM) signal independent of the cell sync frequency (Fig 140). The theoretical receiver resolution is determined by PWM which drives the glow modulator. For the new facsimile receiver this resolution is 600 line pairs per line of scan (or 600 line pairs per

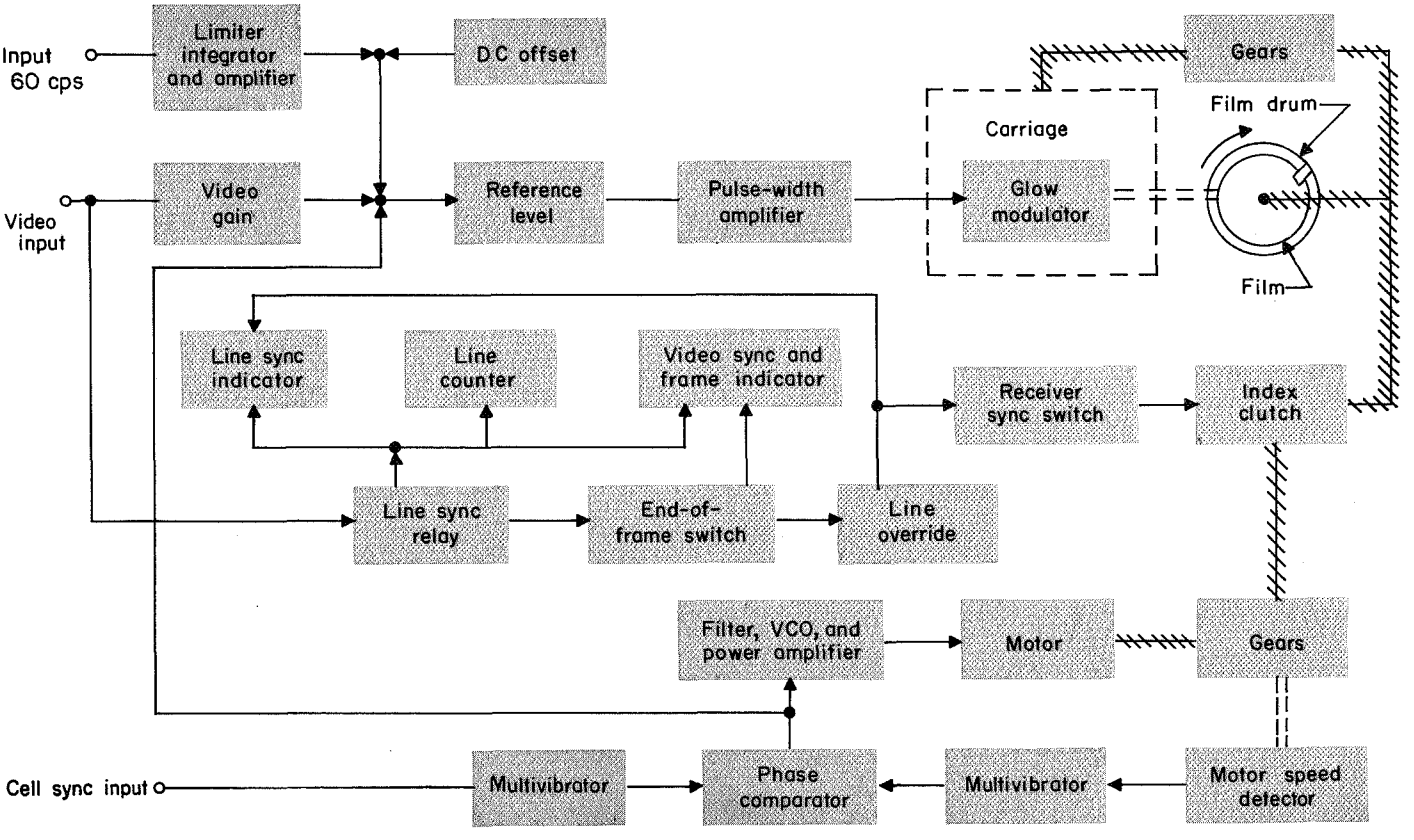

Figure 140. Block diagram of facsimile receiver

inch referred to the camera film). This figure exceeds the best camera film resolution (520 line pairs per inch) achieved to date (Fig 141).

The signal to the glow modulator is generated by mixing the video signal with a 60-cps triangular-wave and a variable offsetting dc voltage. The resulting composite waveform is compared to the reference voltage for polarity. The time duration and polarity of the resulting signal determines the pulse width of the glow modulator light output.

The picture is generated by exposing film to the series of light pulses from the glow modulator, while slowly rotating the film drum. Since the pulse repetition frequency is 60 cps, the typical light pulse may vary from 0 to 16 milliseconds. This length is determined by the average level of the video signal during that period of time. For visual purposes, the individual pulses exposing the receiver film along a line of scan will not be seen; only the integrated effect of varying film density will be observed. The receiver film is processed in the normal manner for optimum image quality. The system uses a 200-line scan due to telemetering constraints. A 500- to 1000-line scan is available by a suitable gearing change in both camera and receiver.

The dc offset control determines the picture contrast and is the only adjustment necessary during the operation of the receiver. Usually this can be set up in the first few minutes of a run. Line sync is impressed on the video signal in the camera and is telemetered as a zero voltage signal, which then sets the level for the line sync gate. Receiver synchronization by the video signal is achieved by operation of the receiver sync control.

Receiver tracking of the camera scanner is accomplished by phase-locking the receiver motor to the telemetered cell sync signal which is generated, by a multivibrator in the camera, as a function of the scanner motor speed. The output of the motor speed detector drives a second multivibrator at the same rate as the cell sync input frequency. The outputs of the multivibrators are then compared, and the phase difference between the two signals is then used to determine the output frequency of a voltage-controlled oscillator (VCO). Normally, cell sync frequency is 10 pps and the VCO output is 400 cps. The VCO output, when suitably amplified, drives a hysteresis synchronous motor.

Tests have shown the system to phase-lock when the cell sync (at 10 cps) leads the internally generated sync by 90 degrees. A variation in the input cell frequency varies the dc level from the phase comparator to the VCO. Therefore, the VCO output can be shifted in proportion to the input cell sync frequency. Phase angle tracking is maintained by keeping the receiver synchronized to the camera scanner.

An interesting effect was observed in early tests on the receiver. A periodic background variation in density was observed on the film whenever the camera motor was periodically cycled about the running speed. The speed variation induced in Figure 142 was −20 to 10% of the

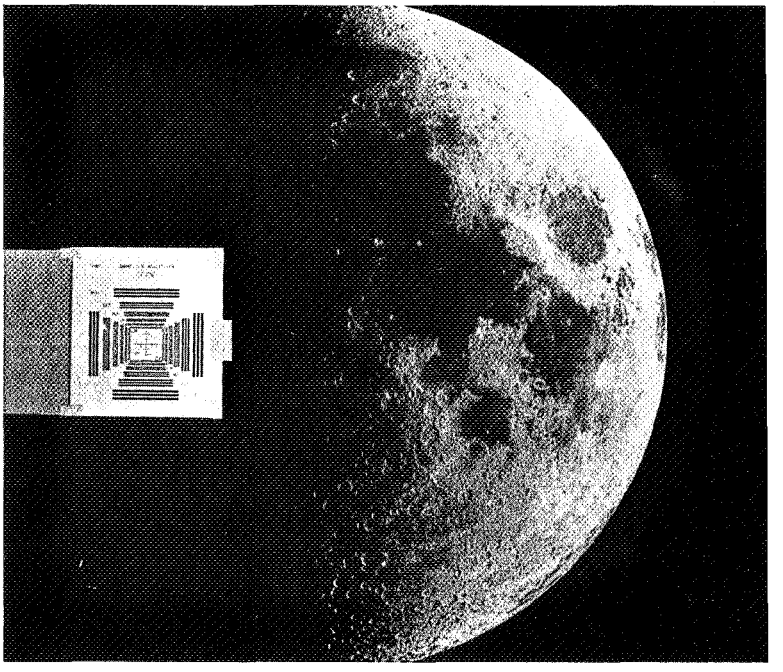

Figure 141. Lunar photograph with a 600 line pair scan rate

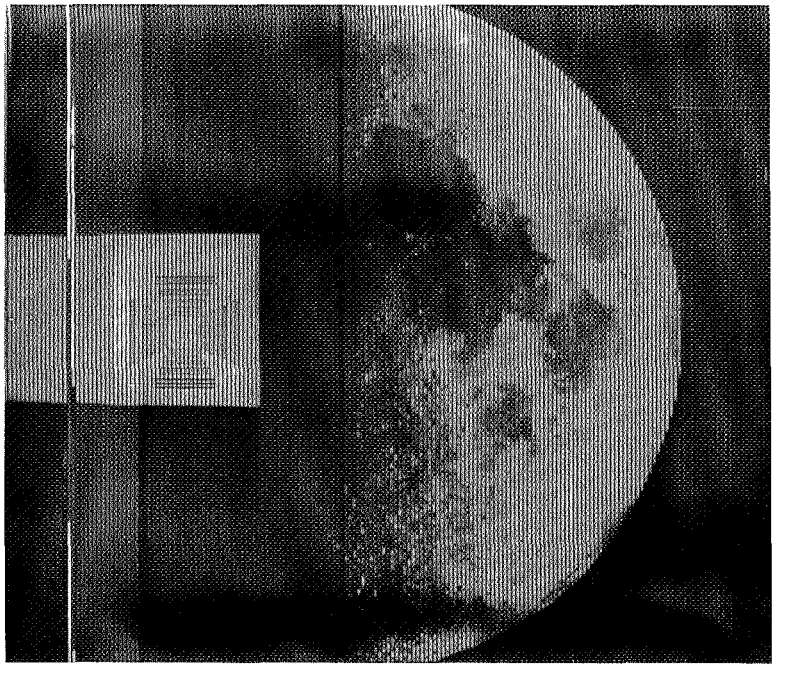

Figure 142. Lunar photograph with variations in the camera motor running speed

normal scanning speed. The resultant pattern showed spreading and compression of the light pulses on the film from the glow modulator. This was corrected by the addition of a small portion of the error control signal to the video input from the phase detector. This signal shifts the video bias or film background density in proportion to the speed of the receiver.

The line sync relay and associated sync switches perform a number of functions. At the end of each scan line, the line sync switch indicates receiver sync, whereas the video sync indicator shows the input sync pulse from the camera. Position of the glow modulator carriage during a run is indicated by the line counter. The end of a picture results in the stopping of the receiver.

D. Lunar Magnetic Field

Soon after their recent moon-impact, the Soviets announced (Ref 2) that the magnetometer on the vehicle had detected no evidence of a lunar magnetic field. It is known also that (1) the Soviet instrument was capable of detecting fields only down to 6×10^{-4} gauss, (2) the impact occurred on the sunlit side of the moon, and (3) the final magnetometer reading before impact presumably was obtained at a lunar altitude of the order of a kilometer (or more).

There is not sufficient evidence from this data alone, however, to conclude that the general lunar magnetic field is weaker than 6×10^{-4} gauss on the surface. It is suggested that, if a general lunar magnetic field existed, it would be confined by the solar corpuscular radiation, or solar wind, to a thin layer above the sunlit surface, but it *could extend* a considerable distance beyond the surface on the side *away from the sun.*

An upper limit to the strength of magnetic field which can be pushed around by the solar wind can be obtained by a calculation of the momentum of the solar corpuscular radiation. If it is assumed that the proton density n is 500 cm^{-3} and that the average particle velocity v is 1000 km/sec, the momentum flux per unit area, or pressure, in the solar wind is $nMv^2 = 8 \times 10^{-6}$ dynes/cm^2. A pressure of this magnitude is capable of compressing a magnetic field until the magnetic pressure $B^2/8\pi$ builds up to this size ($B^2/8\pi = nMv^2$); the magnetic-field strength corresponding to this pressure then is $B = (8\pi \times 8 \times 10^{-6})^{1/2} = 1.4 \times 10^{-2}$ gauss.

Recent observations by N. A. Kozyrev and by J. Dubois (Ref 3) of both the energy content and the time variations of the luminescence of some parts of the lunar surface indicate that this luminescence is, in large part, caused by solar corpuscular radiation incident on the lunar surface rather than by solar electromagnetic radiation. As the luminescence is observed only in sunlit regions of the lunar surface, it can be argued that the solar corpuscular radiation must have travelled essentially straight into the moon's surface without being appreciably deflected by either a lunar or an interplanetary magnetic field. As pointed out in the argument in the preceding paragraph, the solar corpuscular radiation could not have reached the lunar surface if the moon's surface magnetic-field strength were greater than $\sim 10^{-2}$ gauss.

These observations and their interpretation are consistent with the estimates of the strength of a possible lunar magnetic field based on various theories of the formation and history of the moon; these estimates (Ref 4) range from zero to several hundred gamma (1 gamma = 10^{-5} gauss).

Let it be supposed that, in the absence of the solar wind, the lunar magnetic field (B_0) would be a few hundred gamma or less on the surface. The protons and electrons in the solar corpuscular radiation are deflected by this field so as to set up a current; the field resulting from this current tends to cancel the moon's field above the lunar surface and to add to it below the surface. The equilibrium properties of a magnetic boundary layer such as this can be calculated for the case of a cold plasma normally incident on a one-dimensional "moon" from the equations for such a plasma given by Davis, Lüst, and Schlüter (Ref 5). If all the dependent variables except the magnetic field strength are eliminated from these equations, there results the differential equation

$$\frac{d}{dx}\left[(1-\beta^2)\frac{d\beta}{dx}\right] = \frac{4\pi e^2 n}{m}\beta$$

where

$$\beta^2 = \frac{1}{nMv^2}\frac{B^2}{8\pi}$$

M and m are the proton and electron masses, respectively, and x is the distance from the lunar surface (measured negatively out from the surface so that the plasma flow is in the positive x direction). This equation can be solved

subject to the boundary conditions that the magnetic field strength is $2B_0$ at the surface of the moon and zero at $-\infty$ with the result that

$$\left(\frac{4\pi e^2 n}{m}\right)^{1/2} x = -\left\{\left[1-\frac{(\beta^*)^2}{2}\right]^{1/2} - \left(1-\frac{\beta^2}{2}\right)^{1/2} + \ln\frac{\beta^*}{\beta} + \ln\frac{1+\left(1-\frac{\beta^2}{2}\right)^{1/2}}{1+\left[1-\frac{(\beta^*)^2}{2}\right]^{1/2}}\right\}$$

where

$$(\beta^*)^2 = \frac{1}{nMv^2}\frac{(2B_0)^2}{8\pi}$$

For small values of β ($B_0 << 7\times 10^{-3}$ gauss), this expression can be approximated by

$$B = 2B_0 e^{-(4\pi e^2 n/m)^{1/2} x} = 2B_0 e^{-4.2x(\mathrm{km})}$$

Thus, if the moon had a surface field strength of less than ~700 gamma in the absence of the solar wind, the field would, according to this model, drop to $1/e$ of this value at ~500 meters above the surface on the sunlit side; this height is much less than the altitude of many of the lunar mountains. Even for an undistorted surface field as large as 700 gamma, the transverse displacement of the protons is only 8 meters.

This model is not completely realistic in many ways: For a three-dimensional moon, the current layer is curved; thus, the field strength at the surface is not exactly $2B_0$. Furthermore, the solar corpuscular radiation is not a cold plasma and, thus, a random velocity distribution will be superimposed on the flow previously described. Collisions between particles in the plasma were neglected; however, the mean free path for large angle collisions is orders of magnitude greater than the calculated boundary-layer thickness. All reflection of charged particles from the lunar surface has been neglected, as has any contribution from the solar magnetic field which may be trapped in the solar corpuscular radiation. Furthermore, a steady-state solution was found and all plasma oscillations were ignored. It is believed that corrections for these effects would either be small or would lead to a smaller boundary-layer thickness than that calculated.

References

1. Powell, Walter B., *Gas Feed Pressure Systems and Pressure Regulators*, Project Note 1-29, Jet Propulsion Laboratory, Pasadena, February 28, 1945.
2. JPL/AI Translation No. 12, *Pravda*, September 21, 1959, Translated by J. L. Zygielbaum, November 1959.
3. Kopal, Z., "Does the Moon Possess a Magnetic Field?", *Space Journal* (p 3), September 1959.
4. Vestine, E. H., "Utilization of a Moon-Rocket System for Measurement of the Lunar Magnetic Field," RAND Corporation, RM-1933, July 9, 1957.
5. Davis, L., Lüst, R., and Schlüter, A., "The Structure of Hydromagnetic Shock Waves, I. Non-linear Hydromagnetic Waves in a Cold Plasma," *Zietschrift für Naturforschung*, 13a, 916-936, 1958.